Condition Monitoring of VSD-fed Induction Motors

Prepared by

LEBOHANG RALIKALAKALA

Department of Electrical Engineering

University of Cape Town

January 2023

Submitted to the Department of Electrical Engineering at the University of Cape Town in partial fulfilment of the academic requirements for a Master of Science degree in **ELECTRICAL ENGINEERING**

Declaration

This dissertation is submitted to the Department of Electrical Engineering in the Faulty of Engineering and the Built Environment, University of Cape Town, in fulfilment of the requirements for the degree of Master of Science.

I know the meaning of plagiarism and declare that all the work in the document, save for that which is properly acknowledged is my own. This thesis has been submitted to Turnitin module (or equivalent similarity and originality checking software) and I confirm that my supervisor has seen my report and any concerns revealed by such has been resolved with my supervisor.

Lebohang Ralikalakala

Signed by candidate

10 January 2023

Acknowledgements

First and foremost, I would like to thank the Almighty God for the gift of life and His grace that has enabled me to successfully complete this study. I am also grateful to UCT management for providing a conducive platform for learning and to the Mastercard Scholars Foundation at UCT for the financial support during the course of study.

My gratitude also goes to my supervisor, Professor Paul Barendse, for his endless academic support, guidance, and inspiration. His endless suggestions, attention to detail and availability/accessibility greatly helped to shape this work.

I am also grateful to my parents, Mr. Mpho and Mrs Mathabiso Ralikalakala, and to the love of my life, Mats'epo Ralikalakala, and our two children Ts'epo and Eric Ralikalakala for believing in me so much, even beyond how much I believed in myself. I am appreciative to their support and prayers. I am grateful to my little sister, Nthabiseng Ralikalakala, for her emotional support too.

I would like to extend my heartfelt thanks to Mr. Maysam Soltanian and his team of laboratory technicians for their invaluable support, their technical assistance and providing electrical equipment and maintenance of the test rig used in this study.

Finally, I am grateful to Akshay Jankee, John Mushenya, Esther Hamatwi, Boniface Chigozie, Surprise Mahlangu, Musa Thokwe and other AMES members who have contributed to this research project. I am really grateful to them all.

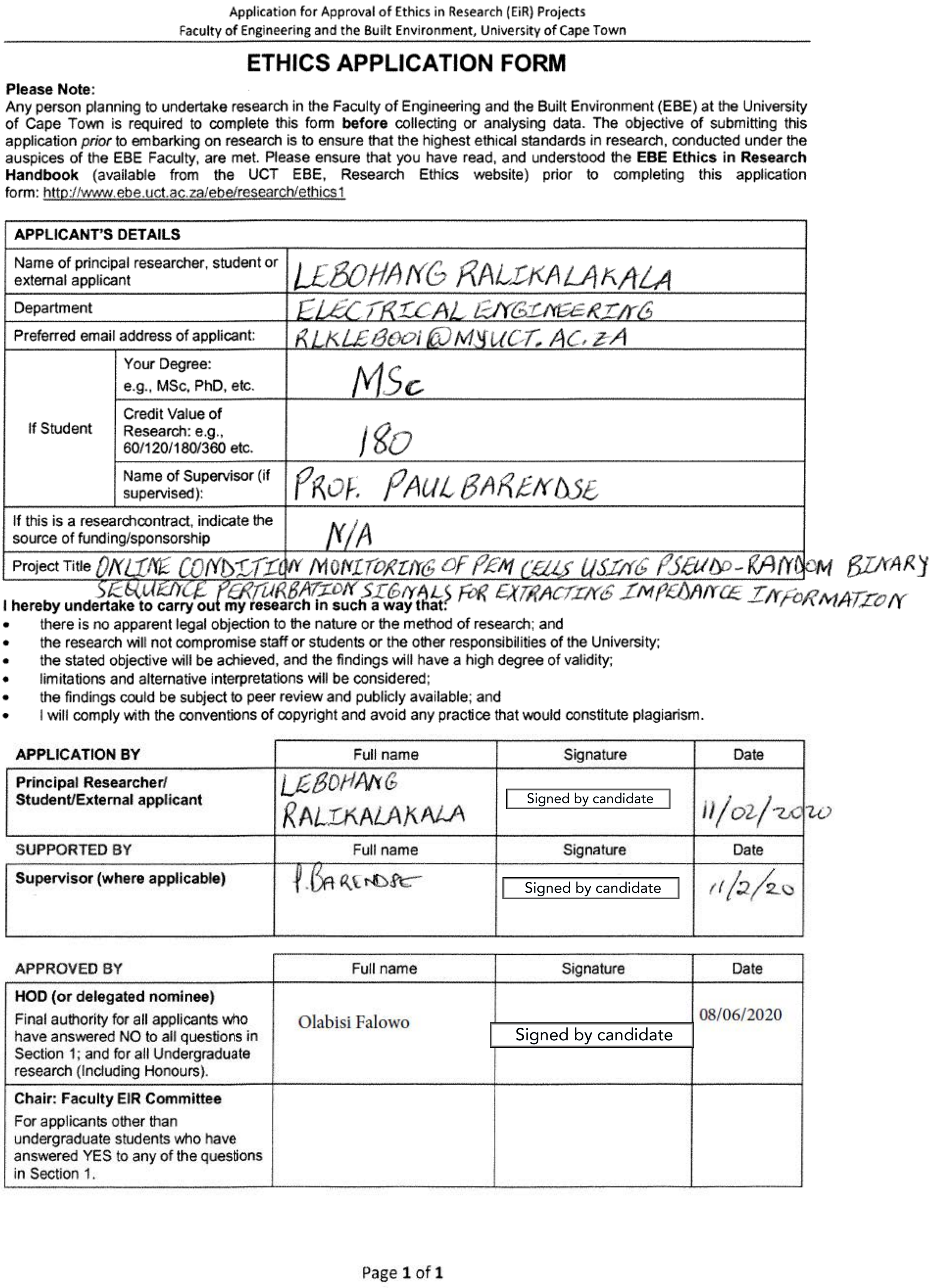

ETHICS APPLICATION FORM

Please Note:
Any person planning to undertake research in the Faculty of Engineering and the Built Environment (EBE) at the University of Cape Town is required to complete this form **before** collecting or analysing data. The objective of submitting this application *prior* to embarking on research is to ensure that the highest ethical standards in research, conducted under the auspices of the EBE Faculty, are met. Please ensure that you have read, and understood the **EBE Ethics in Research Handbook** (available from the UCT EBE, Research Ethics website) prior to completing this application form: http://www.ebe.uct.ac.za/ebe/research/ethics1

APPLICANT'S DETAILS		
Name of principal researcher, student or external applicant		LEBOHANG RALIKALAKALA
Department		ELECTRICAL ENGINEERING
Preferred email address of applicant:		RLKLEB001@MYUCT.AC.ZA
If Student	Your Degree: e.g., MSc, PhD, etc.	MSc
	Credit Value of Research: e.g., 60/120/180/360 etc.	180
	Name of Supervisor (if supervised):	PROF. PAUL BARENDSE
If this is a researchcontract, indicate the source of funding/sponsorship		N/A
Project Title		ONLINE CONDITION MONITORING OF PEM CELLS USING PSEUDO-RANDOM BINARY SEQUENCE PERTURBATION SIGNALS FOR EXTRACTING IMPEDANCE INFORMATION

I hereby undertake to carry out my research in such a way that:

- there is no apparent legal objection to the nature or the method of research; and
- the research will not compromise staff or students or the other responsibilities of the University;
- the stated objective will be achieved, and the findings will have a high degree of validity;
- limitations and alternative interpretations will be considered;
- the findings could be subject to peer review and publicly available; and
- I will comply with the conventions of copyright and avoid any practice that would constitute plagiarism.

APPLICATION BY	Full name	Signature	Date
Principal Researcher/ Student/External applicant	LEBOHANG RALIKALAKALA	Signed by candidate	11/02/2020
SUPPORTED BY	Full name	Signature	Date
Supervisor (where applicable)	P. BARENDSE	Signed by candidate	11/2/20

APPROVED BY	Full name	Signature	Date
HOD (or delegated nominee) Final authority for all applicants who have answered NO to all questions in Section 1; and for all Undergraduate research (Including Honours).	Olabisi Falowo	Signed by candidate	08/06/2020
Chair: Faculty EIR Committee For applicants other than undergraduate students who have answered YES to any of the questions in Section 1.			

Abstract

Induction motor drives are presently the most fully fledged technology amidst the various motor drives not utilising commutators [1]. They consist of an induction motor (IM) fed from a variable frequency AC inverter. They are mostly used in applications which need good dynamic and steady state performance over a large range of speeds [2]. The induction motor is often referred to as the workhorse of the industry due to its predominance in the industry – constituting around 90% of all the motors in the industry [3], [4]. Its admired features include relatively low cost, high efficiency, robustness, and ease of maintenance [5], [6]. These motors are of two types, the wound-rotor and the squirrel cage [1], [5], with the three-phase squirrel cage induction motor being the most common, constituting over 80% [7], [8]. On the other hand, variable frequency AC inverters are also of two types, the voltage source inverter (VSI) and the current source inverter (CSI). VSI is used for most induction motor drive applications due to its simpler control and efficient operation in addition to its low weight, cost, and volume.

Despite their high reliability and robustness, induction motors are still prone to faults [9] due several factors such as being subjected to diverse, continuous, and harsh conditions [10], being subjected to frequent start-stop cycles leading to wear and cracking of machine elements, or being subjected to continued motor overload for long periods required by some industrial processes, resulting in increased thermal stress [11]. Studies have shown that one category of faults that an induction motor may suffer from is the rotor faults [12]. Of these, the broken rotor bar fault in squirrel cage induction motors is the most common [13], constituting 5-10% of all induction motor faults [14]. Besides the induction motor, the state of health of the driving inverter is also important to the overall reliability, integrity, and availability of the induction motor drive system. The power electronic converter (inverter) constitutes about 82.5% of all the faults that occur in the inverter-fed motor drives [15] and of this, 38% occur due to failures of the power electronic switching transistors [16], [17]. These faults include short circuit faults, open circuit faults and intermittent gate-misfiring faults [18]. Open switch faults and short circuit faults are very common in inverters. Consequently, the continuous monitoring of the induction motor drive components (e.g., the induction motor or inverter) is crucial for an early and timely detection of faults to avoid the propagation of the faults and the total breakage of the drive or part of the drive. This will in turn reduce the risk of reduced output, increased emergency maintenance costs and out-of-service problems [10].

The process of continuously monitoring the condition or state of health of a system is called condition monitoring. It is very indispensable in electric drives. One condition monitoring technique commonly used for the detection of broken rotor bar fault is the motor current signature analysis (MCSA), which is focused on the application of the Fourier transform to machine's stator current under steady state operating conditions [7]. The MCSA assumes that the motor is sufficiently loaded and operating under steady state conditions [19]. Despite its robustness, this fault diagnostic tool suffers nonnegligible drawbacks, especially when applied in the industry, where there are many real-time factors such as speed variation or load changes which affect the operation of the induction motor. Similarly, diagnostic variables technique

(DVT) is a condition monitoring technique commonly used in the detection and diagnosis of inverter open switch faults. Contrary to MCSA, it uses diagnostic variables and current average values to detect and localise open switch faults [17], [20], [21]. This method can detect both single open switch and double open switch faults [21].

The objective of this study is to design and develop an open-loop volts-per-hertz controlled induction motor drive for study of faults across the various parts of the drive. In particular, the study focuses on the broken rotor bar fault on the motor-end of the drive and the inverter open switch faults on the converter side of the drive. It commences with investigation of the impacts of the various inverter open switch faults (single switch open circuit, single phasing, and double switch open circuit faults) on the performance of the induction motor, before performing fault detection and diagnosis of these faults to validate the diagnostic variables technique. Then it experimentally establishes some of the shortcomings of MCSA in the detection of the broken rotor bar fault of a Class B inverter-fed 250 W, 190 V, 50 Hz and 2-pole, star-connected three-phase squirrel cage induction motor. Finally, it proposes a complementary broken rotor bar fault detection technique, for inverter-fed induction motor, that is premised on the variation of impedance with rotor position at standstill to supplement MCSA.

The results for investigation of the impact of open switch faults show that both simulation and experimentation produced results with high concordance. They show that double switch open switch fault results in the largest increase in distortion and in DC offset voltage and current than the other two faults, while relatively less changes on these parameters are observed for single phasing fault. A similar trend is observed in speed and torque pulsations of the motor under the respective faults. Similarly, the method of diagnostic variables has proven valid for both simulation and experimental results and is able to detect and localise inverter open switch fault for single and double switch fault. Furthermore, the MCSA is shown to be incapable of detecting broken rotor bar fault under no-load conditions because the sideband harmonics overlap the fundamental component. Likewise, inverter switching harmonics mask and interfere with higher ordered sideband harmonics in the case of inverter-fed motors, thus decreasing the confidence level in this technique. Finally, the proposed standstill impedance variation test shows large change, to the value of 9.59% of average impedance, in impedance as function of rotor position, and this is used to characterize the broken rotor bar fault. The inverter harmonics and switching noise do not impact on this variation in impedance. Further exploration of the standstill impedance variation approach in inverter-fed induction motors showed that it is possible to detect anomalies within the motor due to broken rotor bar fault by utilizing the geometrical orientation of the three-phase stator windings instead of changing the rotor position. That is, by manipulating the inverter switching such that the pulsating flux is aligned with each of the three magnetic axis of the three-phase stator windings, three impedances (one along each magnetic axis of the windings) are obtainable. The average of the absolute differences of these three impedances is large enough to characterize the broken rotor bar fault except when the rotor is positioned at 30°, 70° and 150° relative to the chosen reference position. These positions are referred to as critical rotor positions since the difference in impedance at these positions is very small and can lead to the possible misdiagnosis of the fault (false negative indication of the fault). It is noteworthy that this extension of the standstill

impedance variation test is only applicable to 2-pole machines only since their mechanical degrees is equal to their electrical degrees.

Table of Contents

Chapter 1: Introduction

1.1 Background to the Study

An induction motor is the most commonly used motor in industry [22], hence it is known as the workhorse of the industry. Its popularity births from factors such as its relatively low cost, high efficiency, robustness, and ease of maintenance [6], [23]. Induction motors range from small single-phase motors, used for household appliances like blenders, washing machines, and lawn mowers, to large three-phase induction motors used in industrial applications such as paper mills, printing press, and conveyors. They are essentially constant speed machines. Nonetheless, the industrial need is quite diverse and often requires different speeds or a range of variable speeds in some applications. Traditionally, DC motors were used for such adjustable-speed applications, but they are expensive and have high maintenance costs [5]. In addition to this, there was a surge in high performance drive applications such as electric transportation which necessitated accurate speed control. To overcome these, solid-state controllers were used in conjunction with the induction motors to achieve accurate speed control application. Using inverters, variables such as voltage and frequency are varied to control the speed of the induction motor. Different control mechanisms such as vector control and constant V/F control are used to control the speed of the induction motor.

Despite their robustness and widespread use, induction motors are not immune to faults. Usually, such faults start as small incipient faults but eventually aggravate to become more catastrophic to the overall health and integrity of the machine. This can in turn cause huge financial losses due to downtime arising from machine breakdowns. Although inverters provide a mechanism for variation of speed in induction motors, they inherently introduce other problems of their own. First, inverters are, just like the induction motors, susceptible to faults such as open-switch (open circuit) and short-circuit faults. These faults impact on the motor performance by drastically changing parameters such as motor speed and torque in addition to subjecting the machine to thermal and mechanical stress. Secondly, high switching noise due to the inverter places additional mechanical and electrical stress on the induction motor, while also masking the fault harmonics in the stator current of the motor. When the fault signatures are obscured by the inverter switching noise, it is difficult to detect and identify faults at their incipient phase using techniques such as Motor Current Signature Analysis (MCSA) [24], [25]. It is for this reasons that condition monitoring of inverter-fed machines is still attracting research attention.

1.2 Problem Statement

Induction motors have been and are still being studied extensively. Their operation under normal conditions and under faulty conditions is still of great interest. The aim is to improve their integrity, reliability, and availability. Several condition monitoring techniques have been proposed and employed to study induction motor faults and their detection. The most common technique which is considered as the most effective in grid-connected induction motors is the non-invasive MCSA. Alongside, several signal processing techniques have been proposed and used to detect and identify fault signatures in faulty induction motors.

On the other front, the need for high performance motor drives has compelled the development and use of inverter controllers in this field to control the speed of induction motors to suit the diverse industrial need. While they may successfully address the issues of speed control, they are also problematic. First, they may suffer short-circuit faults or open-circuit faults. Secondly, high inverter switching increase the voltage stress on the stator insulation leading to its accelerated deterioration. Also, inverter switching noise mask fault harmonics in the stator current, making the fault identification process using MCSA very difficult. It is therefore imperative that further research is done in the condition monitoring of inverter-fed induction motors and different fault detection techniques are explored for their effectiveness in detecting faults.

This research investigates the impact of inverter open switch faults on the voltage, current, speed and torque parameters of the motor. It then validates the method of diagnostic variables used in the detection and localisation of inverter open switch faults. Finally, it experimentally establishes the shortcomings of MCSA in detecting a broken rotor bar fault in an inverter-fed induction motor before proposing a new technique to supplement MCSA, based on variation of impedance in different radial paths through the rotor due to asymmetry caused by the broken rotor bars. This technique switches the inverter in a manner to observe the changes in impedance across different magnetic paths through the rotor, despite the presence of inverter harmonics, due to broken rotor bars.

1.3 Research Questions

This research investigates fault conditions across the different sub-components in an inverter-fed induction motor drive. It focuses on four specific aspects of inverter-fed squirrel cage induction motor: 1. the effects that one or two open-switch faults will have on the overall performance of the induction motor, 2. the diagnosis and localization of these open switch faults using diagnostic variables technique, 3. shortcomings of MCSA in detecting broken rotor bar fault in inverter-fed induction machines, and 4. proposition and validation of an alternative technique to supplement MCSA in detecting such faults, based on machine impedance variation at standstill due to rotor asymmetry as a function of the rotor position. It should be noted however that, unlike MCSA which is an online diagnostic technique, the proposed alternative technique requires the motor to be at standstill.

The following questions are addressed by this research:

1. If one of the two switches on one of the three legs (bridge arms) of an inverter is opened, and fails to close, what is the effect on the terminal voltage, line currents, speed, and torque of the connected motor?
2. If two switches on the same bridge arm of the inverter are open circuited, what is the effect on the terminal voltage, line currents, speed, and torque of the motor?

3. If two switches on two separate legs of three-legged inverter simultaneously fail to close, and remain open, what is the effect on the terminal voltage, line currents, speed, and torque of the connected motor?
4. Can each of the fault in 1 – 3 above be successfully detected and localised using the method of diagnostic variables?
5. Does the MCSA successfully detect broken rotor bar fault for both loaded and unloaded grid-connected motor?
6. Is the MCSA able to detect broken rotor bar faults at 0% and 100% load conditions when inverter-fed?
7. If the induction motor is unloaded and taken offline, two phases manually shorted, and a single-phase grid supply impressed between the shorted-phases and the third phase, and rotor position varied, will the impedance variation with the rotor angle be large enough to characterize the broken rotor bar fault?
8. If the inverter is configured to output a single-phase and thus effectively shorting two of the three-phases of the motor, what will be the impact of inverter switching harmonics on the ability to detect the changes in impedance at different rotor positions? Can this be used to supplement the MCSA in inverter-fed induction motors with broken rotor bar faults?
9. Suppose (7) above is true, if the rotor is fixed but the shorted phases changed such that the orientation of the pulsating flux is changed, will the average of the absolute impedance difference be sufficient to be used for fault detection?

1.4 Objectives of the Research

The aim of his research project is to design and develop an open-loop volt-per-hertz controlled induction motor drive for study of faults across the various parts of the drive. Focus being on the study on the broken rotor bar fault on the motor-end of the drive and the inverter open switch faults on the converter side of the drive. The research objectives are as follows:

1. To establish standstill impedance variation of a broken rotor bar induction motor with respect to the rotor position for grid-connected squirrel cage induction motor. This will be used for benchmarking the inverter-fed case of the same scheme.
2. To design and develop a variable frequency induction motor drive for fault detection application, as well as a three-phase LC filter for interfacing the inverter to the induction motor.
3. To implement open loop constant Volts/Hertz (V/F) control on the inverter using a microcontroller in conjunction with MATLAB Simulink.
4. To implement open-circuit inverter faults by using a microcontroller for controlling the switches and investigate their impact on the motor voltage, current, speed and torque.
5. To perform fault diagnosis of these inverter open switch faults and valided the method of diagnostic variables.
6. To investigate broken rotor bar fault detection using MCSA alone in inverter-fed induction motor.
7. To explore the impact of switching harmonics in the detection of changes in impedance of inverter-fed broken rotor bar induction motor at different rotor positions.

1.5 Scope and Limitations of the Research

The study presented here is limited to the detection of broken rotor bar fault in an induction motor under steady state condition, and inverter open-switch faults. Diagnosis of inverter open switch faults consider a single open switch faults, single phasing, and double open switch faults. The machine under study is a star-connected squirrel cage induction machine with a floating neutral, and it is considered only in motoring mode. The study covers both grid-connected and inverter-fed induction motors. The grid-connected cases are only for benchmarking the inverter-fed cases. For the online fault detection tests, 0%, 50%, 75% and 100% load conditions were considered in this study. Condition monitoring techniques considered in the broken rotor bar fault detection were the MCSA and the standstill impedance variation test, and the monitoring signals were limited to stator current and terminal voltage signals on the drive-end of the induction motor. For the inverter open-switch faults, shaft speed and torque signals were monitored in addition to stator current and voltage signals.

1.6 Organization of the thesis

Going forward, this thesis is organized as follows:

Chapter 2 presents a comprehensive review of induction machines and inverters, their most common faults, and the need for condition monitoring of induction motor drives, along with the most common condition monitoring techniques used in induction motors and inverters.

Chapter 3 provides signal classification and processing and feature extraction that is used in induction machine fault diagnosis.

Chapter 4 presents Motor Current Signature Analysis and its shortcomings when used in grid-connected and inverter-fed induction motors. It also describes the phenomenon of rotor pseudo-saliency introduced by broken rotor bars and explains how the resulting impedance change could be used to characterise the broken rotor bar fault. Finally, it describes common inverter faults impacting the performance of the machine for inverter-fed induction motors and presents their diagnosis using diagnostic variables method.

Chapter 5 presents the design and development of variable frequency drive for induction motor fault diagnostics. It also provides some of inverter control techniques. Finally, it presents inverter drive circuit, modulation scheme and microcontroller used in this research.

Chapter 6 presents experimental set-up, testing, measurement, and data acquisition used to carry out the various tests.

Chapter 7 Represents both simulation and experimental results.

Chapter 8 finally draws conclusions based on the obtained results and provide recommendations for carrying out similar work.

Chapter 2: Literature Review on Induction Motors, Inverters, their Common Faults, and their Condition Monitoring Techniques

2.1 Introduction

This chapter provides a literature review of induction machines, inverters, their common faults and as well as the subject of condition monitoring of these devices. It commences with constructional features and operational aspects of induction motors, and their most common faults before further considering the voltage source inverters (VSI), their constructional features and working principles alongside their common failures. It further dwells on the aspect of condition monitoring of these devices. It emphasizes the need for condition monitoring of induction motor drives before specifically reviewing condition monitoring techniques used for fault detection and diagnosis in these machines and inverters.

2.2 Induction Machines

An electric machine is defined as an energy converter that continuously converts electrical input to mechanical output or vice versa [5]. Converters known as induction machines play an indispensably role in a variety of industries [9], operating as either motors – converting electrical energy into mechanical power, or generators – converting mechanical energy into electrical energy. Small single-phase induction motors are often used in household applications [26] such as blenders, lawn mowers and washing machines whereas large three phase induction machines are used in pumps, fans, compressors, and paper mills among others [5], [12]. Like other machines, an induction motor consists of a stationary part called the stator and a rotating part called the rotor, separated from each other by an air-filled space called the airgap [27]. As opposed to other types of machines (DC and synchronous machines), in an induction machine, both the stator (carrying the field winding) and rotor (carrying armature winding) carry alternating current. However, the AC current is supplied to the stator winding directly whereas it is supplied to the rotor by induction [5]. Induction machines are also called asynchronous machines, since their rotor speed is never equal to the synchronous speed [5], [28].

Induction motors account for more than 85% of all motors used in industry and domestic applications [28]. This is partly because they are preferred to DC motors for variable-speed drives as they are cheaper and easier to maintain and do not require commutators and brushes for mechanical rectification [28]. Commutators and brushes become worn out over long use and need to be regularly maintained. Another reason why induction machines have dominated the electromechanical energy conversion sector is due to their reliability, low cost and high performance [26]. So, they make the best cut at meeting industrial needs in this highly technically demanding world, because of their unmatched versatility.

2.2.1 Construction Features of Induction Motor

The stator of an induction machine is often hollow and cylindrical in shape as shown in Fig. 1.1(b). The walls (called core) are made of high-grade steel laminations clamped tightly together. Slots are cut within the inside wall/surface of the stator, in which three phase windings are inserted. These three phase windings may be inserted into the slots such that all windings of a phase are concentrated into two slots (called concentrated winding) or all the windings of a phase may be distributed over several slots (called distributed windings). Distributed windings possess the advantage of producing a smooth sinusoidal MMF in the air gap, and hence a smooth electromagnetic torque of the machine when current flows in the stator windings. On the contrary, concentrated windings produces air-gap field filled with harmonics and hence a pulsating torque [5]. For three phase induction machines, the stator is not only wound for three phases but also has a fixed number of poles [28].

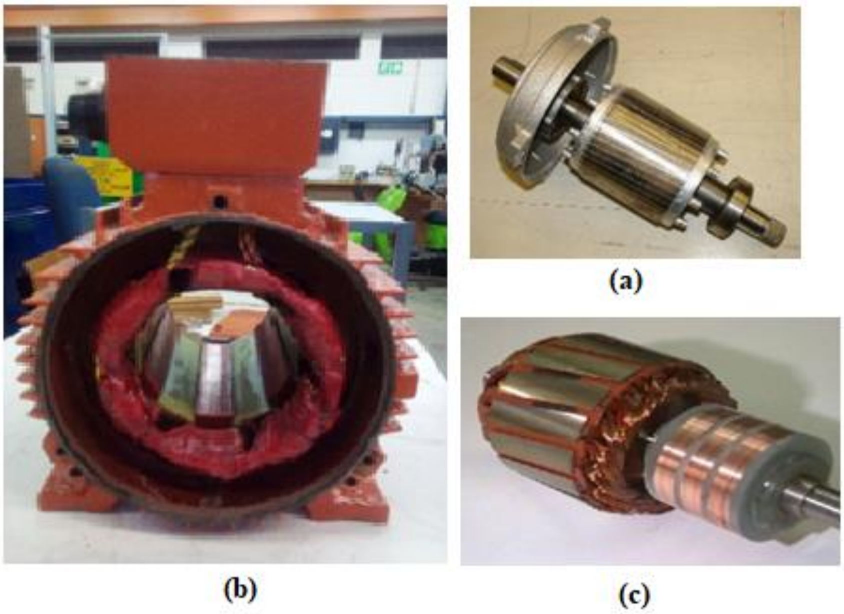

Fig. 1.1: **(a)** Squirrel cage rotor, **(b)** stator and **(c)** wound rotor

Conversely, the rotor is a solid cylinder, small enough to fit into the hollow stator, leaving a small air-filled space called the airgap, and mounted on bearings. The rotor is also made of a ferromagnetic material. The rotor may be one of the two types: squirrel cage rotor or wound-rotor type as shown in Fig. 1.1(a) and (c) respectively. Copper (or aluminium) bars are embedded into the rotor core and shorted on both ends by copper or aluminium end rings in a squirrel cage rotor. Contrarily, slots are cut on the outer surface of the rotor and three phase windings inserted on the slots in a similar fashion to the stator in the case of wound-rotor type machine. For wound-rotor type, one end of each rotor phase wind is connected to its own slip ring on which a carbon brush makes sliding contact and when the rotor rotates, the three brushes slip over the three rings and provide a connection with an external three-phase circuit [28]. The other three ends of the phase winding may be connected for Y-wound machine, or each end may be connected to the beginning of the next phase for Delta-wound machine. The squirrel cage rotor is more rugged and robust [28] and hence it is most widely used in many industrial applications [18]. For this reason, most of the induction machines in industry are squirrel cage induction machines. On the other hand, wound-rotor type possesses the unique advantage of a high starting torque as opposed to squirrel cage induction motors which has a low starting torque. This is because in the case of a wound-rotor machine, it is possible to connect a 3-phase external resistance to the rotor so that the overall rotor resistance is increased, thus decreasing the phase angle between voltage and current. Thus, the overall starting torque is increased.

2.2.2 Principle of Operation

Connecting a balanced three phase supply to the stator's three phase winding will result in the flow of three phase currents in the stator winding. These stator currents in turn produce a rotating magnetic field that is sinusoidally distributed in the airgap and has a constant amplitude [27]. The angular speed of rotation of this magnetic field is called synchronous speed, n_s, and is given by the formula:

$$n_s = \frac{120}{p} f \qquad (2.1)$$

where, f is the frequency (Hz) of the power supply and p is the number of poles of the machine. It should be noted that each of the three phases produces its own magnetic field into the airgap since current is flowing in each phase. However, these three magnetic fields (or MMF's) produce a resultant magnetic field which is seen to be rotating in the airgap [5].

The rotating field in the air-gap due to stator's three-phase currents induce voltages on the rotor windings [27]. This is in accordance with Faraday's First Law of electromagnetic induction, which explains that voltage will be induced in a conductor (rotor windings in this case) in a region of varying magnetic field. Magnetic field variation could be its change in direction or amplitude. Therefore, if there is a relative motion between the stator's air-gap field and the rotor windings, there will always be voltage induced in the rotor conductors. If the rotor circuit is left open circuited, the rotor will remain stationary although there are voltages induced in its bars/windings. This condition is called the standstill operation [5] of the machine. However, if the rotor circuit is closed, the induced rotor voltages will start to drive currents around the rotor circuit. These currents will in turn produce their own magnetic field into the airgap. It is the interaction (the need to align) of this field with the stator's airgap field that produces mechanical torque that tends to rotate the rotor.

The rotor will rotate in the direction of the rotating airgap field in accordance with Lenz's Law [28]. It's speed, denoted by n_r, will gradually increase from 0 rpm to a value close (but not equal) to the synchronous speed at steady state operating conditions. This small difference in speed between the rotor and the rotating field (synchronous speed) is called slip, s, and is very important in determining most of the quantities associated with the machine such as the torque developed. Slip of an induction machine is calculate as:

$$s = \frac{n_s - n_r}{n_s} \qquad (2.2)$$

The voltage, and hence the current, induced in the rotor during running mode are different from those at standstill. This can be expected since the voltage induced in a conductor is depended not only on the size of the magnetic field linking the conductor but also on the speed at which the magnetic field is moving relative to the conductor. So, during the running mode, the speed of the rotating field relative to the rotor is less than that at standstill, hence, we can expect the voltage induced in the rotor windings during running mode to be less than that at standstill. Consequently, the frequency of these induced quantities is also depended on the relative speeds of the rotor and the rotating field. The frequency of the rotor circuit, f_2, can be expressed in terms of the supply frequency as in the following equation:

$$f_2 = sf \tag{2.3}$$

An induction machine has three modes of operation, namely, motoring, generating, and plugging mode [5]. In a motoring mode, the induction machine delivers mechanical power (by applying an electromagnetic torque) to a load coupled to its rotor by a shaft. It has already been pointed out that wound-rotor type machines have high starting torque whereas squirrel cage induction motors have low starting torque. The starting current is however much larger than the rated value – about 5 to 8 times the starting current [5]. This may often present problems in cases where the starting time of the motor is large since the high starting current would have to flow for the duration of this time before steady state is reached [29]. This could lead to problems such as overheating and insulation breakdown.

The electromagnetic force, F_e, exerted on each rotor conductor, which is ultimately responsible for the exertion of torque on the rotor shaft, is described as:

$$F_e = Bli \tag{2.4}$$

where B is the airgap stator magnetic field, l is the length of the rotor bar/conductor and i is the rotor current. However, the induced rotor current depends on the speed of the rotor. This in turn means that the electromagnetic torque of an induction motor varies with speed. Fig. 2.2 [5] shows that, upon starting the machine, the electromagnetic torque starts at some low value and increases as the speed increases until the maximum (pull-out) torque is reached. Beyond this, the torque starts decreasing when speed further increases towards the synchronous speed.

In this context, $n_{syn} = n_s$, is the synchronous speed. An induction machine can either be connected directly to the mains supply (direct online, DOL) or it can be connected via an inverter (inverter-fed) depending on the application.

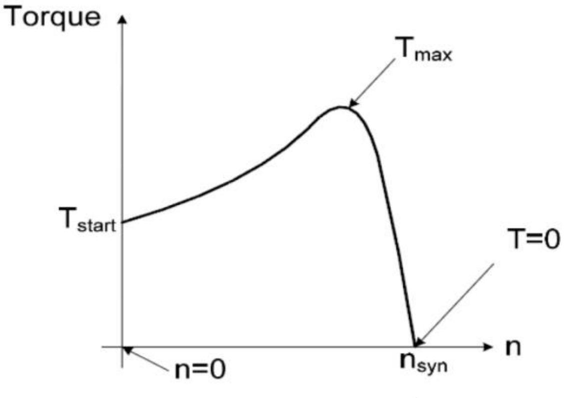

Fig. 2.2: Torque-speed characteristics of an induction motor

2.2.3 Inverter-fed Induction Motors and Speed Control Methods

As already mentioned, induction motors (IMs) have been the backbone of industrial applications for several decades now [30], owing to their many industrial merits – more robust, high reliability, low cost, low inertia, and high transient torque capacity [31] – than other types of machines. Nonetheless, individual industrial applications have various individual and collective needs. For instance, certain industrial processes may require constant or variable speed operation, or constant or variable torque operation. As such, induction machines should be versatile enough to accommodate most of these industrial applications' needs. In this regard, important performance characteristics (in steady state) such as efficiency, power factor, current, starting torque, maximum (or pull-out) torque [5] must be considered and possibly controlled with easy to fulfil the requirements of industrial applications. In the previous section, a graph of torque vs speed was shown for an induction motor.

Sen [5] derived the following formula for mechanical speed, ω_{mech} and electromagnetic torque, T_{mech}:

$$\omega_{mech} = (1 - s)\omega_{syn} = \frac{n_s}{60} 2\pi(1 - s) \qquad (2.5)$$

where s is slip, ω_{syn} is synchronous speed in rad/s and n_s is the synchronous speed in rpm, and

$$T_{mech} = \frac{1}{\omega_{syn}} \frac{V_{th}^2}{\left(R_{th} + \frac{R_2'}{s}\right)^2 + (X_{th} + X_2')^2} \frac{R_2'}{s} \qquad (2.6)$$

where V_{th}, R_{th} and X_{th} are Thevenin voltage, resistance, and reactance, respectively, of the IEEE equivalent circuit of an induction machine shown in Fig. 2.3, $R_2{}'$ and $X_2{}'$ are rotor referred resistance and reactance respectively. It should be noted that this is per phase electromagnetic torque developed.

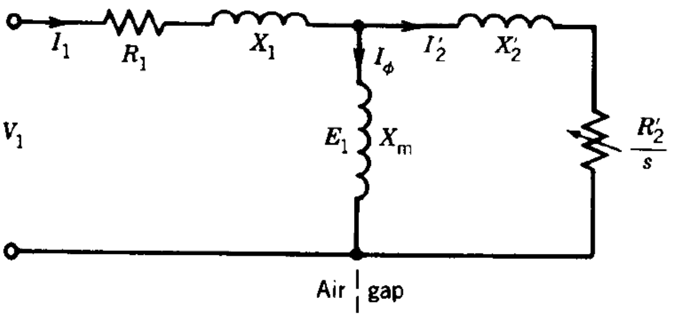

Fig. 2.3: The IEEE-recommended equivalent circuit [5]

These equations show that the mechanical speed of the rotor and the torque developed by the machine depend on, among other quantities, the synchronous speed, n_s, and the Thevenin voltage. The Thevenin voltage in turn depends on the supply voltage V_1. In fact, if the voltage-drop across the stator impedance, $R_1 + jX_1$, is appreciably small, such that the stator induced voltage $E_1 \approx V_1$, then $V_{th} \approx V_1$ [5]. Consequently, it is conclusive, based on these equations, that induction motor will run at constant speed and produce a constant torque if supplied from a constant-voltage supply with a constant frequency. This may be adequate for some industrial applications but not for others, which require variable-speed or those whose load torque need to be varied over a given range. It is therefore, of the utmost importance that a mechanism be put in place for smooth variation of speed or torque requirements of an induction motor.

Speed variation of induction motor can be achieved in different ways such as pole changing or using solid-state controllers such as inverters. In pole changing, the speed of the motor is changed by changing the number of poles of the machine, which inherently changes the synchronous speed of the motor hence the speed of the shaft. Alternatively, an inverter is used to control the speed and the torque of an induction machine. An inverter in the context of power-electronics refers to a class of power conversion circuits that operates from a dc voltage source or a dc current source and converts it into ac voltage or current [32]. Thus, an inverter does the opposite of a rectifier – it reverses dc power back to ac power. Most often, the inverter is used in conjunction with a rectifier as shown in Fig. 2.12. The diode rectifier is used to convert the AC source such as the grid into DC, and this DC voltage is converted back to AC with the desired amplitude and frequency by the inverter. The rectifier and the inverter are connected via a dc-link capacitor which is responsible for filtering the DC output of the rectifier [30]. Detailed review on inverters is presented later in this chapter.

From equation 2.6, it follows that the torque-speed in Fig. 2.2 can be modified by varying the voltage while keeping the supply frequency constant. This relationship of supply voltage and torque is depicted in Fig. 2.4.

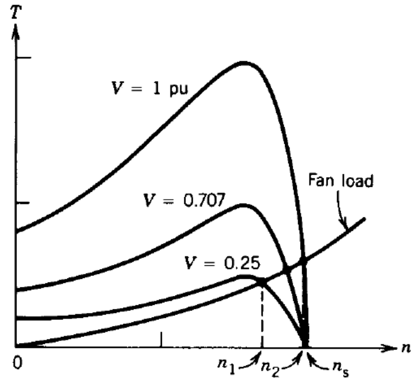

Fig. 2.4: Torque-speed characteristics for various terminal voltages [5]

It may be recalled that electromagnetic torque developed is proportional to the square of the terminal voltage [5], which is what is seen on the graph. According to Fig. 2.4, torque decreases as the voltage decreases for any given speed. It should be noted that the fan load torque graph is given as a demonstration load and, shows that the speed may be varied from some value n_1 to n_2 by increasing the terminal voltage from 25% of the rated value to the rated value.

A. Methods of Induction Motor Speed and Torque Control

From the torque speed characteristics in Fig. 2.2, it is observed that at any rotor speed the magnitude and/or frequency of the supply voltage can be controlled to obtain a desired torque [33]. There are various methods for the speed control of an induction motor, and they are [28], [5]:

i. Pole changing
ii. Variable Supply Frequency Control
iii. Variable Supply Voltage Control
iv. Variable Rotor Resistance Control
v. V/f Control
vi. Slip Recovery
vii. Vector Control

Some of these methods are described below:

i) **Variable Supply Frequency Control**: Here, supply frequency is varied at constant voltage supply. In an induction motor, the airgap flux will remain at the rated value if the voltage and frequency are also at their rated values. However, maintaining voltage at the rated value while reducing the frequency well below its rated value will increase the flux. This is because voltage is proportional to the product of flux and frequency (since $V_1 \propto \emptyset f$) [28]. An increase in airgap flux beyond its rated value drives the machine into saturation, thus invalidating motor parameters for determination of torque speed characteristics. Low frequency also results in a decrease in machine reactance, causing a detrimental rise in motor current, and this may damage winding insulation. Consequently, this method is seldom used [34].

ii) **Variable Supply Voltage Control**: This method involves the variation of stator voltage at constant supply frequency. It is a simple speed control method in a cage-type induction motor. This method is commonly used for “soft start” of the induction motor to limit the stator current during periods of low rotor speeds [33]. The torque-speed characteristics curve is shown in Fig. 2.5 below.

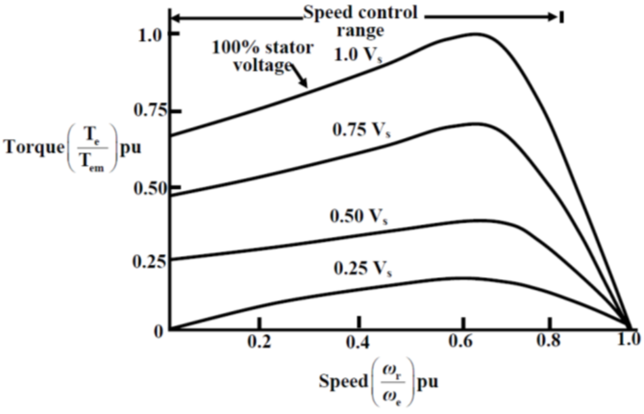

Fig. 2.5: Torque-speed curves at variable supply voltage [33]

iii) **V/f Control:** The rotating airgap flux induces voltage, E_1, on the stator windings, and it is such that $E_1 \propto \Phi f$, where Φ is the air-gap flux, and f is the supply frequency. Given that the stator is wound such that the stator impedance is very small, then the stator voltage drop is negligibly small. Under this assumption, we make the approximation: $E_1 \approx V_1$, where V_1 is the terminal voltage. Therefore, $V_1 \propto \Phi f$. Consequently, if frequency is reduced without changing the supply voltage, the air-gap flux will increase, driving the machine into saturation, which is undesirable. Therefore, frequency should be varied when terminal voltage is also varied, so that V/f ratio remains constant. This avoids driving the motor into magnetic saturation and thus affecting the torque produced by the machine [35]. That is, by maintaining a constant V/f ratio, the maximum torque of the motor becomes constant for changing speed [28]. Fig. 2.6 [33] shows torque-speed characteristics under this mode of control. Note that since the airgap flux of the motor is kept constant at the rated value, the torque per ampere is high. Moreover, the supply frequency is lowered at low speeds, allowing the machine to operate at low slip always. This ensures that the efficiency of the machine does not deteriorate [33], since the efficiency of an induction machine ideally depends on the slip (which in turn depends on speed), according to equation 2.7 below [5].

$$Eff_{(ideal)} = \frac{P_{out}}{P_{in}} = 1 - s \tag{2.7}$$

So, the lower the slip, the higher the efficiency of the machine.

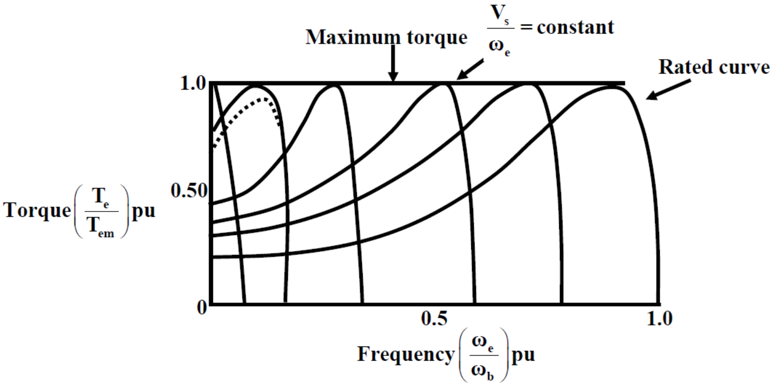

Fig. 2.6: Torque-speed curves at constant V/f

Constant V/f control is the most popular control method and is widely used in industrial and domestic applications because of its, among other advantages, simplicity and ease-of-implementation [28], [35], [36], [37].

iv) Vector Control

Included in the vector control is the field-oriented control (FOC) and the direct torque control (DTC). The main difference between FOC and DTC lies in linearity. FOC employs a linear controller and PWM to regulate fundamental components of the motor voltage whereas DTC is nonlinear and directly generates the voltage vectors without the need for a modulator [38]. Both these vector control methods have pros and cons [39] and the choice of one over another is a result of a careful consideration of these pros and cons with respect to the specifications of the application being implemented. However, vector control is often used in applications requiring increased performance with improved accuracy [37]. Its popularity stems from its simplicity and ease of implementation over other control strategies.

2.3 Common Types of Induction Motor Faults

Despite their high reliability and robustness, induction motors are still susceptible to faults [9] due several reasons, including:

- being subjected to diverse, continuous, and harsh conditions [10], incorrect operation and/or even manufacturing defects [9].
- being subjected to frequent start-stop cycles, leading to wear and cracking of machine elements [11].
- operation of the motor in poorly ventilated environments, breeding motor efficiency reduction and likelihood of rotor bar breakage [11] due to thermal stress.
- continued motor overload for long periods required by some industrial processes, resulting in increased thermal stress [11].

These unfavourable working conditions exert stress such as thermal stress, electrical stress and mechanical stress on the motor and motor elements. These stress components in turn cause machine deterioration and faults. These faults, gradual deterioration, and failures may lead to motor interruption, if left undetected, and their resulting unplanned downtime is very expensive [9].

In [40], multiple components of an electrical drive system that can deteriorate include motor bearings, mechanical gears, insulation, winding faults, eccentricity, opens or shorts of inverter switches, gate driver deterioration and malfunction, and demagnetization of magnets.

Induction motor faults are categorized into internal and external faults that are further classified into mechanical, electrical, and environmental faults as shown in Fig. 2.7. The most prominent mechanical faults are the bearing and broken rotor bar faults, and most electrical faults arise from power quality issues supplied by AC grid; such as frequency variations, voltage disturbances, over or undervoltage conditions, etc [26].

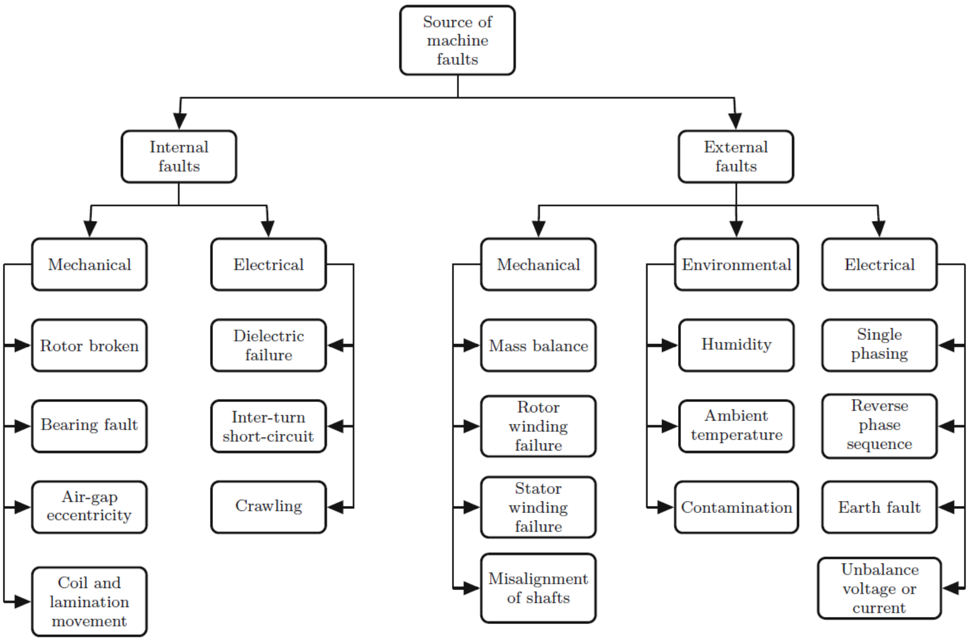

Fig. 2.7: Classification of faults in induction motor [12]

An induction motor fault may be classified as either rotor, stator, bearing or another mechanical fault depending on where it occurs in the machine. Faults like bearing problems, broken rotor bar, eccentricity abnormalities, and stator winding faults cause variation in amplitude and frequency of the motor current signature [26]. This is what characteristically separates a faulty motor from a healthy motor.

2.3.1 Stator Faults

As already mentioned, three-phase induction motors have high starting current. This starting current subjects the induction motor to continuous electrical and thermal stresses. Mechanical stress also increases as the windings vibrate about their fixed positions when the large stator current flows through them. These stresses cause deterioration of stator winding insulation, leading to gradual development toward inter-turn, phase-to-phase, and phase-to-ground faults. Other factors such as voltage unbalance and over-voltage causes the winding temperature to increase. If undetected in time and addressed, these incipient faults lead to hazardous motor failure, translating to large losses on financial investment [41].

A stator fault may be a fault in stator winding, winding laminations, or the frame of the stator. However, stator winding faults are the most frequently occurring fault in the stator [12]. Commonly, upon inception, the interturn short circuit fault in the stator winding will quickly advance to inter-coil fault, phase winding fault, and single line to ground fault, resulting in the total breakdown of the motor. Hence, its early detection ensures corrective measures may be taken to repair the machine by rewinding it or, in large motors, displacing short-circuited coils [26]. Also, the increase in variable-speed drives in industry increases the probability for stator faults because the high rates of voltage changes produced by inverter switching increases stator winding stress [41].

Fig. 2.8 shows the various stator winding faults such as turn to turn, coil to ground faults, coil to coil, phase to phase.

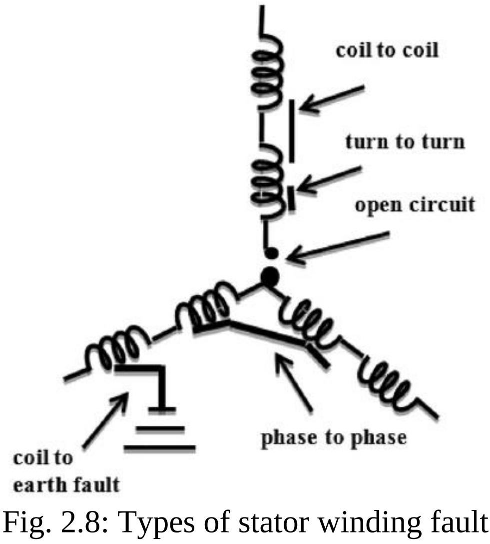

Fig. 2.8: Types of stator winding faults [12]

In reference to Fig. 2.8, it is worth noting that stator winding faults occur mainly due to turn-to-turn, phase-to-phase, and winding-to-ground short circuits, and that the phase-to-phase and phase-to-ground faults start with turn-to-turn short circuit and if undetected leads to major faults [42]. Consequently, turn-to-turn short circuit faults should be detected and diagnosed as early as possible.

2.3.2 Rotor Faults

As already demonstrated, the rotor of squirrel cage induction motor is made up of copper or aluminium bars embedded axially along its outer surface and connected on both ends by aluminium or copper end rings. During operation, it is exposed to different types of stress that threaten its state of health and may lead to its failure. Such failures are classified into crack/breakage of rotor cage bars, crack/breakage of end rings and rotor bow [9]. Fig. 2.9 shows a rotor with one of its bars broken.

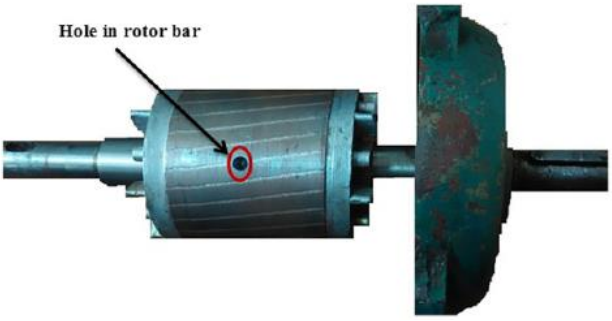

Fig. 2.9: Single broken rotor bar of induction motors [12]

Both increased thermal and mechanical stresses cause expansion and eventual breakage of rotor bars, the bar to end ring, and/or end ring segments. The cause of these stresses could be large start-up currents or high torque transients [40]. Rotor bar breakage translates to increment of current in the neighbouring healthy bars. Consequently, net airgap flux distribution is no longer uniform. On the other hand, non-uniform thermal distribution of the rotor during operation may bow the rotor, causing unsatisfactory alignment in the motor [9], and further non-uniform airgap flux distribution.

According to EPRI and IEEE, rotor faults occurring in induction motor operation, are 8% and 9% respectively [12]. Although rotor faults have been extensively studied in recent years, this area still needs more research because of the complexity of the motor during the runtime [9].

2.3.3 Bearing Faults

Bearings are indispensable components of electrical rotating machinery. For induction motors, bearings provide support to the rotating shaft, and they are placed at both ends of the rotor. Like other machine elements, bearings are susceptible to defects due to stresses (such as mechanical stress) imposed on them. One of the most common faults in induction motor is the bearing failure. Induction motor bearing defects are classified into localized and distributed faults [12]. The causes of bearing failure include radial and axial loads, bearing currents, vibrations, contamination and increased operating temperature [9].

Spalling on raceway surface, improper mounting, manufacturing errors and corrosion presents some of the most dominant mode of the rolling element bearing failure, although they are subjected to a variety of influences that affect their service life. As per the survey conducted by the IEEE and EPRI on induction motors, the bearing fault occurring in induction motors during operation are 41% and 42% respectively [12]. Different bearing faults are depicted in Fig. 2.10 [12].

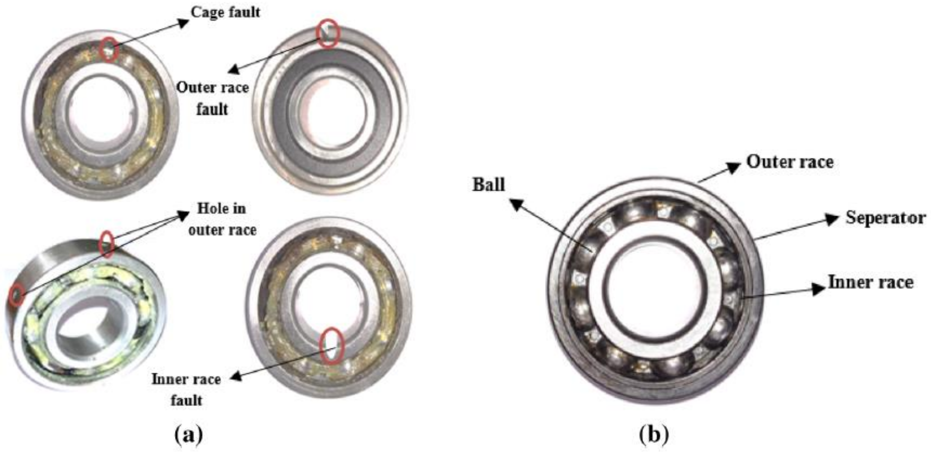

Fig. 2.10: Structure of ball bearing. **(a)** bearing defects and **(b)** healthy

2.3.4 Air-gap eccentricities

The rotor is centre-aligned in the stator in a free-fault machine, resulting in a uniform airgap. This means the rotation centre of the rotor is the same as the geometric centre of the stator bore. Consequently, the rotor symmetrical axis (C_r), stator symmetrical axis (C_s), and rotor rotational axis (C_g) coincide with each other, and hence, magnetic forces are balanced in opposite directions. Rotor eccentricity, displacement of the rotor from its centred position in the stator bore, produces an asymmetric airgap. Causes of eccentricities include elliptical stator core, wrong placement of the rotor or stator at the setup or subsequent of maintenance, incorrect bearing positioning, bearing deterioration, shaft deflection, housing imperfection, end-shield misalignment, excessive tolerance, and rotor weight or pressure of interlocking ribbon, to mention but a few [9]. Of these, the most common cause of eccentricity is the bearing fault, which contributes approximately 42% of induction motor faults. Three types of eccentricity faults are static, dynamic and mixed eccentricity (a combination of both static and dynamic eccentricities) [12]. These are demonstrated in Fig. 2.11, where R_s is the stator radius and R_r is the rotor radius.

Eccentricity produces unbalanced radial magnetic force on the rotor shaft, which also pulls away the rotor from the stator bore centre, thus imposing extreme stress on the motor [9]. This also causes an uneven airgap flux density, resulting in the introduction of harmonics in the stator voltage and current. Other than harmonics, eccentricity puts a heavy load on bearings, leading to an avalanche phenomenon which aggravates their degradation [40]. Nonetheless, eccentricity is commonly present in rotating machines, but the maximum permissible level is set, which is 5 or 10% of the airgap length. Should it exceed this level, it will doubtlessly damage the windings, stator core and rotor core in the motor due to timely rubbing of the rotor against the stator [9].

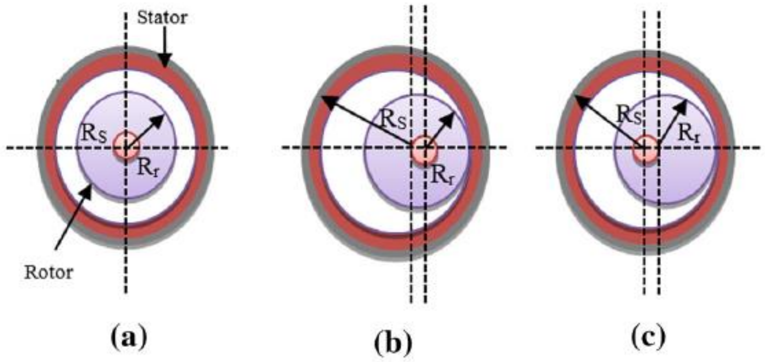

Fig. 2.11: Cross-section of induction motor **(a)** normal (concentric), (**b)** static eccentricity and, **(c)** dynamic eccentricity [12]

2.4 Voltage Source Inverter (VSI)

Inverters are broadly classified as Voltage Source Inverters (VSI) and Current Source Inverters (CSI), depending on their operation. Sharma and Tali [43] assert that a CSI is supplied with adjustable current from a DC source of high impedance – a stiff DC current source, whereas VSI is fed from DC source with a negligible impedance – stiff DC voltage source.

2.4.1 Construction and Working Principle of VSI

The standard 3-phase induction motor drive is shown in Fig. 2.12, adopted from [44]. It consists of a three-phase diode rectifier, two DC-link capacitors, the classical 2-level 3-leg VSI, comprising six transistor switches, two on each leg and the induction motor. Isolated base drive amplifiers are normally used to control the semiconductor devices (transistors) [15]. Transistor switches, such as MOSFET's, require appropriate gate voltage to be applied between the gate and source terminals to drive the transistors into saturation mode and achieve the low on-state voltage mode. This control voltage is generated by the isolated base drive amplifiers (gate control drive circuit) [45].

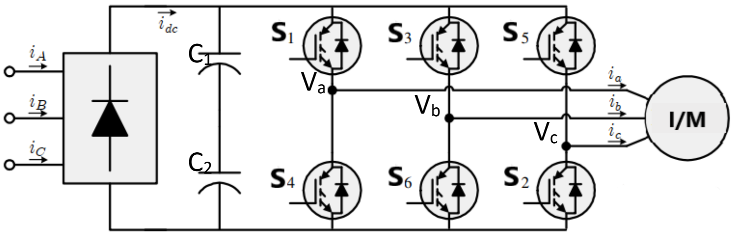

Fig. 2.12: VSI induction motor drive

The switching function for any one arbitrary leg (bridge arm) of the inverter may be defined as shown in Fig. 2.13 [45], where j is the phase (e.g. $j = \{a, b, c\}$ for three-phase system), and variables p and n represent the top and bottom switches respectively. The closed and open states of a switch is represented by state symbols "1" and "0" respectively. The top signal (i.e., gate control voltage signal of the top switch), S_{jp}, is responsible for the positive current (positive half-cycle) in that phase, whereas the bottom signal, S_{jn}, is responsible for the negative current of the same phase. In reference to the first bridge arm in Fig. 2.12, which supplies phase a current, i_a, the signals S_{ap} and S_{an} are controlling the positive and negative half-cycles of i_a, respectively.

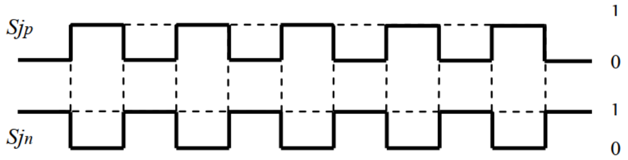

Fig. 2.13: Gate signals of one leg of a healthy inverter

It is noteworthy that the switching signals (gate control voltages signals) for the two switches on the same bridge arm are complimentary, which means, when the top switch (e.g., S1) is closed (state = 1), the bottom switch (e.g., S4) is open (state = 0). Consequently, the eight possible switch state combinations and the resulting output line-to-line voltages are as shown in Table 2.1.

Table 2.1: Switching Possibilities for 2-phase VSI

S1	S3	S5	V_{ab}	V_{bc}	V_{ca}
0	0	0	0	0	0
0	0	1	0	$-V_{dc}$	V_{dc}
0	1	0	$-V_{dc}$	V_{dc}	0
0	1	1	$-V_{dc}$	0	$-V_{dc}$
1	0	0	V_{dc}	0	$-V_{dc}$
1	0	1	V_{dc}	$-V_{dc}$	0
1	1	0	0	V_{dc}	$-V_{dc}$
1	1	1	0	0	0

To understand how Table 2.1 is constructed, we first note that V_{dc} denotes the DC bus voltage, which is voltage across the two filtering capacitors C_1 and C_2. For any arbitrary switch state, say 001, S1 and S3 are off, which means pole voltages V_a and V_b are both 0 V while S5 is on, resulting in pole voltage V_c = V_{dc}. Then the line voltages are calculated as:

$$\begin{gathered} V_{ab} = V_a - V_b = 0 - 0 = 0 \\ V_{bc} = V_b - V_c = 0 - V_{dc} = -V_{dc} \\ V_{ca} = V_c - V_a = V_{dc} - 0 = V_{dc} \end{gathered} \tag{2.8}$$

These are the voltages on the second switch states combination (3rd row) in Table 2.1. The same procedure is followed for all other switch states and Table 2.1 is populated. It should be noted that only two switch states result in all three line-to-line voltages taking a value of 0 V, and that is the states 000 and 111 for the three switches. Otherwise, two of the line-to-line voltages are always non-zero in each switch state. To generate a given waveform, the inverter transition from one state to another [45]. Another factor to be noted is that, for a healthy inverter case, line-to-line voltages take both negative and positive values as observed from the table.

With this basic understanding of construction and operational features of the VSI, focus may now be turned to faults it may develop. Any one of the four components of the drive system shown in the drive system of Fig. 2.12 is prone to operational failure. The following section focus on the faults that may occur in the six semiconductor switches constituting the inverter.

2.4.2 Common Inverter Faults – Overview

Cui [15] remarks that the faults that occur in the power electronic converter constitute about 82.5% of all the faults that occur in the inverter-fed motor drives. Of this, 38% occur due failures in the power electronic switching transistors [16], [17], [18], [45], [46], [47]. These faults include short circuit faults, open circuit faults and intermittent gate-misfiring faults [18]. If one (or more) of the isolated base drive amplifiers generating the gate control voltage malfunctions, then the corresponding switch(es) will be deprived of the base drive voltage. The result is the manifestation of the inverter open-switch fault. On the contrary, the short circuit fault could be caused by several factors, including reverse breakdown of the device, insulation breakdown of the leg or if the sucking circuit paralleling with the device is shorted. The short circuit fault is the most severe and to limit damage to the inverter, the base drive feeding the healthy transistor of the same leg is removed to prevent a shoot-through fault [15]. However, if the faulty switch on one leg is open circuited, the fault isolation is done by removing the gate drive signal from the switches of that faulty leg [45].

2.5 Condition Monitoring of Induction Motor Drives

2.5.1 What is Condition Monitoring?

Condition monitoring of induction motor drive means continuous observation of the health of the drive. The aim is to improve productivity, efficiency, cost reduction and to increasing system availability [12]. Condition monitoring uses incipient fault detection and diagnostic techniques. It changes maintenance from corrective maintenance to preventive maintenance [10]. According to [48], this change is accelerated by the rapid increase in the need for high-quality, low-cost products and safe production. Conventional methods such as scheduled maintenance and redundancy have been used in industries to prevent severe defects in induction motor drives. However, scheduled maintenance is not reliable as the drive may break ahead of the scheduled maintenance period. On the other hand, redundancy prevents unexpected shutdowns, but not failure. It also leads to high maintenance cost and physical space required for motor drives due to implantation of preventive measures [12]. Condition monitoring addresses these drawbacks of conventional methods of maintenance.

The best condition monitoring techniques rely on the knowledge of the characteristics of the electric motor drives in both fault-free and faulty situations. In the event of a fault, some parameters of the drive change subject to the fault degree. The fault identification schemes are based on capturing the changes in drive parameters, followed by signal processing. Each fault can then be detected via a specific feature present in the measured signal of a faulty motor drive when compared to a fault-free one [9].

Condition monitoring in electric drives can be grouped into two methods, namely, model based and feature based methods. The former method is also known as failure detection method. Here a precise computational model is found and used to correlate the observational signatures of abnormal structures with analytical or quantitative models to detect faults. On the contrary, the latter method is performed by first extracting features from the signal and then making decisions based on these features. Time-domain features, frequency-domain features, time-frequency domain features, and spatial domain features all constitute features that can be used for extraction [49].

The intention of fault detection is to detect the fault at the beginning stage and shut off the drive immediately to avoid failure due to the large fault current [26]. This ensures prolonged health of the drive and continued productivity.

2.5.2 The Need for Condition Monitoring of Induction Motor Drives

Induction motor drives form part of the backbone for majority of the industrial applications. Meanwhile, they often operate in continuously harsh and unfavourable operating conditions due to the diverse and critical needs of the industry. As a result, they are susceptible to several types of faults and subsequent failure that could affect their normal operation. However, in the industry, the normal and reliable operation of an induction motor drive is a necessity. A failure of any kind may result in a loss of revenue, reduced output, emergency maintenance costs and out-of-service problems [10]. Therefore, an early detection of irregularities in these drives is vital. A proper fault detection scheme will help to stop the propagation of failure, and thus it prevents unscheduled downtimes that cause loss of production and financial income [9].

Condition monitoring of induction motor drives is indispensable in industry for several reasons, including the following:

1. Conventionally, induction motor maintenance is carried out at fixed time intervals. However, environmental factors and operating conditions often deteriorates machine performance at irregular intervals. This necessitates online monitoring of the machine if the integrity of the system is to be maintained [12].

2. A typical industrial plant will consist of many installed electric motor drives. Monitoring the health of individual motor drives is an integral part of ensuring the health of the entire arrangement of machines. Hence, early fault diagnostics is crucially important for avoiding the deadly effects of sudden failure of the overall electric drive systems [10].

3. Fault occurrence in an electric motor drive constituting a critical industrial process leads to emergency interruptions, leading to production process losses and product quality losses. Therefore, early fault detection is mandatory to identify incipient fault presence in the drive so that these problems may be avoided [11].

4. Unlike scheduled maintenance, the condition-based monitoring improves the performance and efficiency of motor drive, enhances its life and productivity, and reduces drive damages. Consequently, condition monitoring and fault detection of induction motor drives is indispensable to stop the unexpected breakdowns [12].

5. To ensure continued production process and quality, reliability of the electric drive system becomes the absolute necessity. Detection, diagnosis, and severity of the fault are the first and the most integral steps in a multi-step process that leads to increased reliability of a system. This improvement is achieved by maintenance. This in turn secures continuation of operation [40].

[50] indicated that the most important and encompassing objective in the maintenance of wide industrial systems is the detection of incipient faults in induction motor drive as soon as possible to perform the repairs during the maintenance period, without stopping the working process. This will not only minimise maintenance cost but will also ensure that production/process schedules are met and adhered to.

2.5.3 Common Condition Monitoring Techniques for Induction Motors

Different types of faults that may occur in an induction motor were discussed in 2.3. When the motor is subjected to any of these faults, then some of its parameters like current, flux, vibration, temperature, voltage, acoustic emission, airgap torque, etc. are subject to variation. The various condition monitoring techniques use these parameters to detect and isolate faults, and may be online or offline. The online techniques perform motor diagnosis and fault detection while the motor is in operation. Conversely, offline techniques perform motor fault diagnosis while the motor is at standstill. Logically, online techniques are preferred over offline techniques because they reduce the total downtime [48].

It is noteworthy that some of these techniques require the use of expensive sensors and hence their overall cost may be high. An efficient condition monitoring scheme will provide warnings of a fault and predict it at early stages. To achieve this, the system will collect primitive data from the motor using signal processing or data analysis techniques [12]. Some of these techniques include:

A. Vibration Monitoring

Motors vibrate during operation because of electromagnetic forces on the motor parts. In this technique, signals are captured, non-invasively, using vibration sensors mounted on the machine. Then the vibration spectrum of these signals are analysed for signatures which are indicative of specific faults. Usually, vibration harmonics from a healthy motor are weaker compared to those from a faulty motor which have larger amplitudes. So, to detect a fault, vibration spectrum in a healthy and a faulty motor are compared when they are in operation.
These signals may be detected in the form of velocity or acceleration or displacement in relative or absolute value. Effective signal analysis techniques are used to extract this vibration signature that is embedded in the raw vibration signals [12].

B. Acoustic Emission Monitoring (AE)

This condition monitoring technique uses ultrasonic and audible frequencies. When the wave travels through the medium of interest, AE signals generate complexity in areas of interest. The drawback of this technique is that it requires knowledge of the wave characteristics, and the properties of the medium through which the wave travels. AE monitoring system involves two integral elements namely, a material deformation – the machine, and transducers that receive the stress signals generated. Like with other condition monitoring techniques, actuators and sensors are used to acquire primitive data from the models [12].

C. Airgap Torque Monitoring

Three-phase stator current flowing in the three-phase windings produce airgap magnetic flux which in turn produces airgap torque. This torque is reliant on the current and flux linkages. It is possible to measure the airgap torque, from the instantaneous power distribution when the induction motor is in running. This could be used to monitor the condition of the motor. Nonetheless, it is quite exhaustive to measure the air-gap torque in electric rotating machines directly, hence finite element analysis have been proposed for estimating the air-gap torque in [12].

D. Motor Current Signature Analysis

Motor Current Signature Analysis (MCSA) is a common technique used for detecting various machine faults. It is both non-invasive and cheaper than most other techniques. It uses Fast Fourier Transform (FFT) of the motor stator current for fault detection and diagnosis. This current is acquired by means of a meter or a sensor from any one phase (or each) of the three phases of the stator [24]. Once the frequency spectrum of the motor current is obtained from the Fourier analysis, then the fault features are extracted from the analysis of the spectrum [42]. Fig. 2.14 depicts how the MCSA technique is employed in condition monitoring of an induction motor.

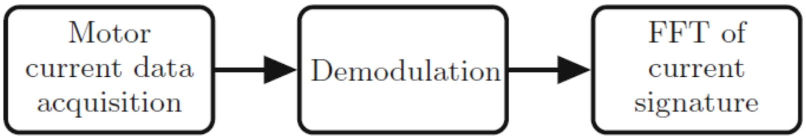

Fig. 2.14: General procedure for MCSA [12]

In the ideal case, the current spectrum for a healthy electric machine contains a dominant component corresponding to the supply frequency along with other harmonics from the supply and the machine's own time-space harmonics due the winding distribution. However, the presence of any asymmetries in the machine will produce other frequency components in the power spectrum profile of the stator current. These other frequency components are diverse and differ according to each specific fault, and they are referred to as the fault signatures for the different faults. So, MCSA simply analyses the stator current signal to detect the presence of any fault signature in the electric machine [9].

E. Infrared Thermography (IRT)

Electric machines usually experience temperature surges at a faulty region because of high fault currents or increased friction. These high temperature zones are used to detect the regions and severity of the faults [31]. IRT technique, as the name implies, uses infrared waves captured by a thermal camera. Data acquisition from the machine using IRT can be done in continuous operation without any physical contact with the machine [12]. So, it is a non-invasive analysis technique. IRT needs less instrumentation compared to other techniques, hence it is widely accepted as matured condition monitoring tool for temperature measurement.

2.5.4 Common Condition Monitoring Techniques for VSIs

As already shown, the VSI is an integral part of induction motor drive. Just like the induction motor itself, the VSI is also prone to faults as shown in section 2.4.2 of this report. However, the reliability and availability of the VSI is important for the overall reliability of the entire induction motor drive. Therefore, it is important that the condition of the VSI be continuously monitored during operation to minimize catastrophic faults and downtimes. Several condition monitoring techniques for VSI's exists in literature. Khater *et. al* [51] developed a rule-based fuzzy logic system derived from voltage spectra and able to identify the type of inverter switch fault and the location of the switch. Their technique uses a matrix to provide fault condition based on a database status. Meanwhile, an online switch fault detection technique is proposed by [52] in which mode detection is used to estimate the switch states based on GARRs generated from HBG model of the system. Reyes-Malanche *et. al* [53] introduced an open-switch fault detection technique that perform time-domain analyses of phase currents directly from the VSI and utilizes three rotary reference systems and basic arithmetic operations to detect inverter open-switch faults. Similar to [53], Mala *et. al* [54] introduced a diagnostic variable technique for the detection of inverter open-circuit faults. This technique uses diagnostic variables along with average current values to detect and localise both a single and multiple switch open-swich fault.

Chapter 3: Signal Processing, Feature Extraction and Classification for Induction Motors

3.1 Introduction

Integral to the art of induction motor drive condition monitoring is signal processing and fault feature extraction. After deciding which machine parameter (e.g., stator current, torque, flux) will be continuously observed for condition monitoring, the next step is the data acquisition. It involves the use of sensors or transducers to obtain the values of the monitored parameter(s) from the machine. It is advantages for this to be done as non-intrusively. Once the data is captured, the next step is the signal processing and feature extraction. The real challenge in signal processing is finding the technique capable of making features of interest to be more prominent and easily observable from the usually noisy and complex data captured. Another factor that adds to the complexity of condition monitoring is that different fault detection techniques require the use of different parameters and require different signal processing techniques [55]. A suitable signal processing technique will enhance fault signatures while vehemently suppressing the dominant system dynamics and noise [56]. This section summarizes the most common signal processing techniques used in condition monitoring of induction motor drives.

3.2 Signal Processing Techniques for Diagnostics

Several signal processing techniques are used in the detection of faults. The common ones are classified into three broad categories, namely, standard digital signal processing techniques, advanced digital processing techniques and artificial intelligence (AI) based techniques [57]. Discrete Fourier transform (DFT), fast Fourier transform (FFT), short-time Fourier transform (STFT) and higher order spectra (HOS) are all examples of standard digital signal-based techniques. These tools are widely used in electric machines diagnostics. They can either be used in the time domain or frequency domain. Time domain analysis uses statistical properties whereas the frequency domain makes use of the Fourier methods for signal transformation from the time domain to the frequency domain [57]. Amongst the advanced digital signal processing-based techniques are the continuous wavelet transform (CWT), discrete wavelet transforms (DWT), wavelet packet transform (WPT) and wavelet neural network (WNN) [57]. Time domain or frequency domain does not provide features such as localised analysis or transient analysis. The advanced techniques do provide access to this information. The artificial intelligence techniques are expert systems (ES), support vector machine (SVM), fuzzy logic, genetic algorithm (GA) and neural networks (NN). In AI, system conditions are analysed using computational models. It is an impeccable tool for solving intricate engineering problems, which need human intelligence [57].

Signal processing is an indispensable component in fault detection. It effectively represents the signal as a simple transform of the originally acquired signal, making it easy to extract dominant features from the signal for use in fault detection.

3.3 Signal Classification

For a given application, there are many signal processing techniques to choose from. There are also many different types of signals in this field, ranging from simple signals to complex signals. However, different signals will have different characteristics which are important in deciding how different signals are analysed. So, for effective signal analysis, it is important to be familiar with the signal to be analysed. This way, an appropriate signal processing technique may be effectively chosen for optimum and accurate results.

Signals may be classified as deterministic or non-deterministic signals [58], [59].

- **Deterministic** signals: If there is no uncertainty with respect to the value of the signal at any given instant of time, then such a signal is deterministic [58]. This kind of signal can be defined precisely by mathematical expression. Fig. 3.1 shows an example of a deterministic signal.

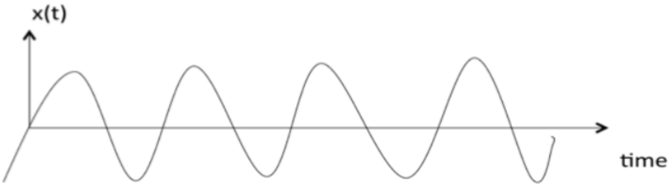

Fig. 3.1: Deterministic signal [60]

- **Non-deterministic** signals: Some signals cannot have their values predicted at some future time. There is an uncertainty with respect to the value of the signal at some instant in time [59]. Such a signal is non-deterministic or **stochastic**. Non-deterministic signals are random or irregular. Random signals cannot be described by an analytical expression but can be modelled in probabilistic terms. Gaussian noise is an example of a random signal. An irregular signal cannot be modelled statistically or stochastically. They are neither deterministic nor random [60]. Fig. 3.2 shows one example of a non-deterministic signal.

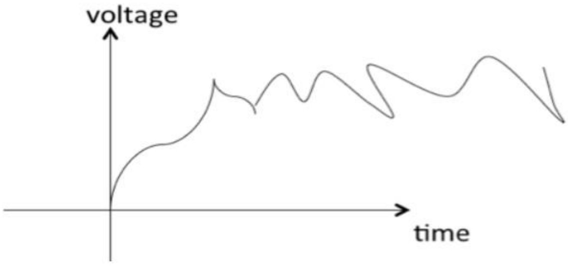

Fig. 3.2: Non-deterministic signal [60]

3.4 Common Signal Processing Techniques

An early and reliable machine fault detection will always require an improved signal processing method. These signal processing methods are divided into three categories based on which domain the analysis is performed – time domain, frequency domain and time-frequency domain [61]. The following sections briefly describe these signal processing methods.

3.4.1 Time-Domain Analysis

In this analysis, the signal is described as a function of time. The signal value is known for all real numbers if the signal is a continuous-time signal, otherwise, it is a discrete-time signal, and its value is known at various distinct instants [61]. Statistical analysis is one fault detection approach which is often performed in the time-domain. Some of the common statistical parameters used in fault detection include mean, variance, skewness, and kurtosis. For instance, crest factor is commonly used to detect bearing faults in time-domain analysis, despite its limitations in detecting defects which are localized [62]. To demonstrate the mathematical descriptions of these statistical parameters, that can be used in incipient fault detection in induction motors, an N-numbered data set $(x_1, x_2, x_3, \ldots, x_n)$ is considered. Then the parameters are defined as [62]:

1. The mean, μ, is the first moment of the data and is defined by the equation:

$$\mu = \frac{1}{N}\sum_{n=1}^{N}(x_n) \tag{3.1}$$

2. The variance, σ, is the second moment of the data and is defined as:

$$\sigma = \frac{1}{N}\sum_{n=1}^{N}(x_n - \mu)^2 \tag{3.2}$$

3. The skewness, sk, is the third moment of the data and is defined as:

$$sk = \frac{\frac{1}{N}\sum_{n=1}^{N}(x_n-\mu)^3}{s^3} \tag{3.3}$$

4. The kurtosis, kur, is the fourth moment:

$$kur = \frac{\frac{1}{N}\sum_{n=1}^{N}(x_n-\mu)^4}{s^4} \tag{3.4}$$

where s, is the square root of the variance, or the standard deviation, defined by

$$s = \sqrt{\sigma} \tag{3.5}$$

So, all the above statistical parameters are used in time domain, and they are derived from moment of the data. Other than measure of measurements, some dimensionless quantities of the data may also be used for fault detection. These include the crest factor, impulse factor, margin factor and shape factor. These are mathematically described as follows [63].

5. Crest factor, X_{cf}, is the ratio of peak value to the RMS value of the signal [62].

$$X_{cf} = \frac{\max(|x_n^2|)}{\left(\frac{1}{N}\sum_{n=1}^{N}x_n^2\right)^{\frac{1}{2}}} \tag{3.6}$$

6. Impulse factor, X_{if},

$$X_{if} = \frac{\max(|x_n|)}{\frac{1}{N}\sum_{n=1}^{N}|x_n|} \tag{3.7}$$

7. Margin factor, X_{mf},

$$X_{mf} = \frac{\max(|x_n|)}{\left(\frac{1}{N}\sum_{n=1}^{N}\sqrt{x_n}\right)^2} \tag{3.8}$$

8. Shape factor, X_{cf},

$$X_{cf} = \frac{\left(\frac{1}{N}\sum_{n=1}^{N} x_n^2\right)}{\frac{1}{N}\sum_{n=1}^{N}|x_n|} \tag{3.9}$$

This time domain parameters are often used to the detect the presence of incipient faults in electrical machines. They are used to quickly observe changes in the signal’s statistical behaviour. Although these parameters cannot distinguish between the different fault signatures, they are able to estimate the severity of a fault from the changes in the amplitude of the signal of the parameter being observed [63].

3.4.2 Frequency-Domain Analysis

Time-domain analysis is not enough for all applications. It does provide direct analysis of the signal and provides some useful information about the signal. However, for periodic signals, it does not clearly depict what frequency components are in the signal nor does it provide any information about the amplitude of such frequency components. Frequency domain analysis such as Fast Fourier transform (FFT) addresses the drawbacks of the time domain analysis. FFT is a real time analysis that transforms a function or signal from time domain to frequency domain or vice versa [55].

Fig. 3.3 below shows how the Fourier transform works, whereby a time-domain signal is decomposed into constituent sinusoids of varying frequencies. This transform is extremely important when a signal’s frequency content is of interest because it shows the different frequency components present in the signal, which cannot be identified in the time domain. Fourier transform gives Fourier coefficients, F(ω), which in turn give the constituent sinusoidal components of the original signal when multiplied by a sinusoid of frequency ω [64]. Fig. 3.4 shows how the time domain signal is decomposed into several sinusoids.

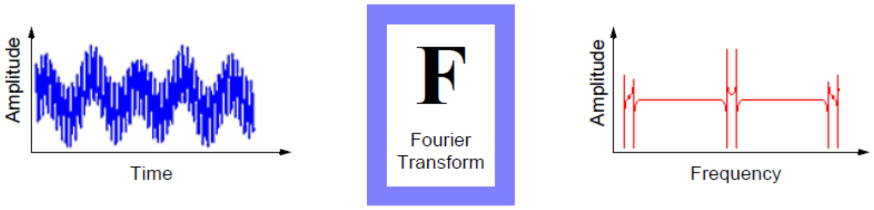

Fig. 3.3: Fourier Transforming a time-domain signal [64]

So, Fourier Transform (FT) simply measures and estimates the relative percentages of the different frequency components, called the power spectrum, of a time-domain signal. There is the forward and the inverse FT available to a signal analyst. For the forward FT the signal is transformed from time-domain to frequency domain. The inverse FT does the exact opposite [49]. The most common Fourier transforms include the Fast Fourier Transform (FFT) and the Discrete Fourier Transform (DFT). Mathematically, DFT, $F[k]$ of the sampled signal, f[n], is described as

$$F(k) = \sum_{n=0}^{N-1} f[n]e^{-j2\pi nk/N} \tag{3.10}$$

where k = 0, 1, 2, 3, … N – 1. Its inverse discrete Fourier transform is

$$f[n] = F^{-1}\{F(k)\} = \frac{1}{2\pi}\sum_{k=0}^{N-1} F(k)e^{j2\pi kn/N} \tag{3.11}$$

where, $n = 0, 1, 2, 3, \dots N - 1$ [27]. On the contrary, fast Fourier transform, $F(\omega)$, of the continuous signal f(t) is given by [64],

$$F(\omega) = F\{f(t)\} = \int_{-\infty}^{\infty} f(t)e^{-j\omega t}dt \tag{3.12}$$

and, its inverse Fourier transform, $f(t)$, is given by

$$f(t) = F^{-1}\{F(\omega)\} = \frac{1}{2\pi}\int_{-\infty}^{\infty} F(\omega)e^{j\omega t}d\omega \tag{3.13}$$

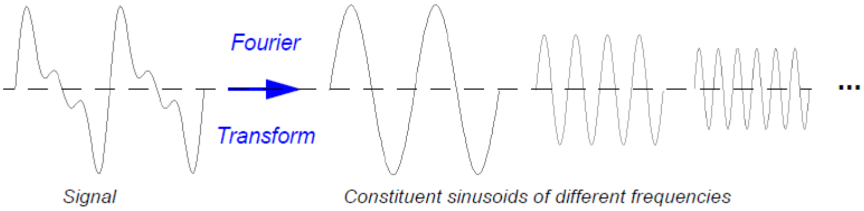

Fig. 3.4: Decomposing a signal into sinusoids [64]

It is easy to perform and effectively analyse stationary signals, for a finite time. This time interval over which FFT is performed is termed "time window" of analysis. During digitization of FFT, it is imperative that a correct sampling frequency is chosen to avoid aliasing, which introduce false frequency components. This sampling frequency is chosen according to Nyquist theorem - the sampling frequency should be so chosen that it is at least twice the maximum frequency present in the signal. FFT is extensively used and is even applied in other signal processing techniques. For instance, it can be used to estimate the power spectrum and cepstrum [49].

3.4.3 Frequency-Time Domain Analysis

Most of the real-world signals are nonstationary in nature, which means their spectra varies with time. Likewise, some signals generated by an electrical machine in operation, such as vibrations signals, can have different frequencies at each time instant. More precisely, when a process or a system is starting up, motor signatures captured are nonstationary [65]. Although FFT can depict the frequency components present in the signal, it comes short when the characteristics – trends, drift, sudden changes, beginning and end of events [64] - of the signal being analysed is changing with time. It fails to depict the changes in frequency of the signal. It is not possible to tell when a given event occurred in the signal by looking at the Fourier Transform of the signal [64]. This is where frequency-time domain analysis receives its significance over frequency domain analysis. Frequency-time analysis technique characterizes the signal into a two-dimensional representation, frequency against time, simultaneously. This is achieved by comparing the signal with elementary functions like the frequency modulated Gaussian functions. Several frequency-time methods exist and are used extensively in research works and in the field. These mainly differ in terms of how they handle the uncertainty, since the uncertainty principle states that ‘‘one can’t simultaneously have good frequency resolution and good time resolution’’. Frequency-time domain signal processing techniques include short-time Fourier transform (STFT), Wigner–Ville distribution (WVD), and wavelet transform (WT) [55]. These are described in the following sections.

A. Short-Time Fourier Transform

This signal processing technique addresses the shortcomings of the FFT. STFT is nothing other than the extension of FFT such that it can analyse nonstationary signals. Here, the initial signal is split into small time windows, whereby the Fourier transform is applied to each time window. The result is the FFT of the signal in that time segment, representing variation in frequency content within the time interval. It gives absolute bandwidth analysis, identifying harmonic components in the signal within that time interval. It represents the signal in two dimensions and provides a constant resolution, without due regard to the signal’s actual frequency. The accuracy of STFT is dependent on the size of the window – the smaller the window size the higher the time resolution and the lower the frequency resolution, and vice versa [55]. Fig. 3.5 below shows how windowing is performed on a signal during STFT.

Fig. 3.5: STFT of a signal [64]

Here, once a time window is chosen, its length is fixed for all the frequencies. This technique of using Fourier transform on a small section of the signal by selecting a time-window is called windowing technique [64]. The mathematical description of STFT of a time domain signal $x(t)$ is,

$$S(f,\tau) = \sum_{t=0}^{N-1} x(t)\,\omega(t-\tau)e^{-j2\pi ft} \tag{3.14}$$

where, $\omega(t)$ is the window function centred around τ. STFT can also be demonstrated by Fig. 3.6 below [64]:

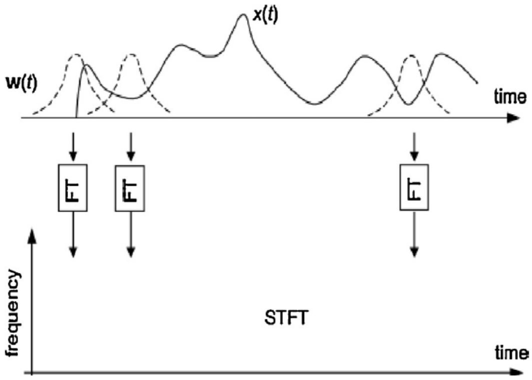

Fig. 3.6: Short-time Fourier transform

B. Cohen’s Class

STFT still faces some limitations, such as low-resolution due to the small window, failing to portray dynamic and transient behaviour accurately. The WVD offers a suitable substitute for STFT. The WVD is a distribution which belongs to a larger group of distributions called the ‘Cohen’s class’ of time-frequency distributions. The Cohen’s class distribution is generally a technique used for the evaluation of energy of systems which vary with time. The WVD invalidates the uncertainty principle by offering an exceptional resolution for analysis of the signal in both domains. It perfectly substitutes STFT because of its simplicity, great accuracy, and best resolution regardless of the window effects [55]. For a real signal $s(t)$, its WVD is defined as [65]

$$W_s(t,f) = \int_{-\infty}^{+\infty} s(t+\tau/2)\bar{s}(t-\tau/2)e^{-j2\pi f\tau}d\tau \tag{3.15}$$

where $s(t)$ = the time signal, $\bar{s}(t)$ = the conjugate of $s(t)$, t = time index, f = frequency index, and τ = the radius extending from time *t*.

This equation demonstrates that the WVD provides the instantaneous power of the signal at time *t* and frequency *f*.

C. Wavelet Transform (WT)

Wavelet analysis provides a time-frequency analysis with optimum balance between frequency and time resolutions. Unlike STFT, which transforms a signal from time domain to frequency domain using complex cosine and sine functions, WT involves the use of elementary functions called wavelets, which can independently be scaled or shifted. The two most common wavelet transforms are the continuous wavelet transform (CWT) and the discrete wavelet transform (DWT). The main difference between these two lies in the nature of the scaling factor. In DWT, the scaling factor is a power of two, and it is implemented by passing the signal through a pair of lowpass and high-pass filters. On the other hand, in CWT the scaling factor is selected by means of convolution or arbitrarily. At high frequencies, WT generally provides optimum time localization, leading to the analysis of the signal at a constant percentage bandwidth. This is one other aspect that makes WT better than STFT. Because of this, WT is also good at detecting sudden changes in the signal being analysed [55]. Fig. 3.7 [64] shows an overview of what happens when a signal is transformed by wavelet transform.

Fig. 3.7: An overview of wavelet transform

Wavelet analysis use time-scale region instead of frequency vs time, as shown in the diagram above. Hence, it uses longer time intervals for more precise low-frequency information and uses shorter ones to depict high-frequency regions. It should be noted that, there is a correspondence between wavelet scales and frequency, since scale simply measures how stretch or compressed the wavelet is. So, the low scale means that the wavelet is compressed, which in turn means high frequency (due to rapidly changing details) and vice versa [64]. This relation can be demonstrated in diagram as shown in Fig. 3.8 below.

Fig. 3.8: Relation of scale to frequency [64]

As already mentioned, wavelet transform uses wavelets as basic functions of transformation, instead of complex sinusoids used by the Fourier transform. By definition, a wavelet is a waveform whose duration is limited, and whose average value is zero. A wavelet does not extend to infinity and is irregular and asymmetric as opposed to a sinusoid which extends to infinity and is rather smooth and predictable [64]. Fig. 3.9 below clarifies the difference between wavelet and sinusoid.

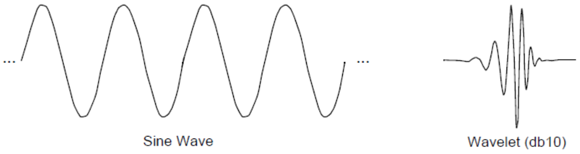

Fig. 3.9: Nature of Sinusoids and wavelets [64]

The figure also clarifies why wavelets are suitable for the analysis of rapidly changing events, and why they are best at performing localized analysis as compared to Fourier analysis. There are many wavelets transforms in use, but the most common ones include:

(a) Continuous wavelet transformation (CWT)
(b) Discrete wavelet transformation (DWT)
(c) Wavelet Packet decomposition transformation (WPT)

(a) Continuous wavelet transformation (CWT)

CWT is the sum over all the time, of the product of the signal and the version of the wavelet which has been both scaled and shifted. The result of CWT on a time domain signal is many wavelets coefficient, denoted by C, and all of which are defined from the scale and the position of the (mother) wavelet used. This definition can be presented mathematically as

$$C(scale, position) = \int_{-\infty}^{\infty} f(t)\psi(scale, position, t)dt$$

where $f(t)$, is the time domain signal being analysed. It should be the case that multiplying each wavelet coefficient by an appropriate scaled and shifted wavelet function gives the constituent wavelets of the signal being analysed [64].

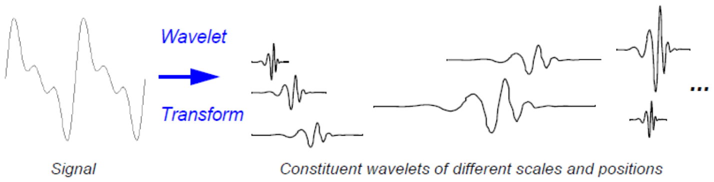

Fig. 3.10: Decomposition of a signal into scaled and shifted wavelets [64]

CWT can be represented pictorially as in Fig. 3.10, which is a similar but not identical process to the Fourier transform, discussed earlier.

Continuous wavelets transform basically consists of first taking a wavelet and comparing it to the first section of the signal being analysed. Then, a number C is calculated, which is a representation of how closely correlated is this section of the signal and the wavelet. Then, the wavelet is shifted along the length of the signal, and at each shifting, C is calculated. This will result in a vector of coefficients C's, corresponding to that scale of the wavelet. Then, the wavelet is scaled, and the process is repeated, until all coefficients at all the scales have been calculated [64]. This is shown in Fig. 3.11 [64].

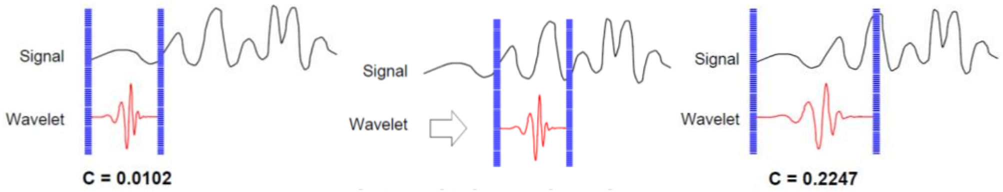

Compare Shift Compare

Fig. 3.11: Demonstration of CWT coefficients calculation

The detailed mathematical description is of continuous wavelet transform $\omega(m,n)$ of the time domain signal f(t) is as follows:

$$\omega(m,n) = \int_{-\infty}^{\infty} f(t)\psi_{m,n}^{*}(t)dt \tag{3.22}$$

* means complex conjugate, and $\psi(t)$ is a wavelet, and

$$\psi_{m,n}(t) = 2^{-\frac{1}{2}}\psi(2^{-m}t - n) \tag{3.23}$$

where, m and n are the dilation/scale and translation, which are employed in transforming the original signal to a new one with smaller scales, in accordance with high frequency components.

(b) Discrete Wavelet Transform

CWT requires the calculation of wavelet coefficients at every scale, and at each scale, the analysing wavelet is shifted smoothly throughout the domain of the signal that is being analysed. This is computationally extensive with large amounts of data generated. This is where the Discrete wavelet transform gains its importance. It uses only a subset of scales and positions at which to perform the transform, instead of using the entire scales and positions. It so happens that if scales and positions are selected based on powers of two, the analysis is more efficient than in the case of CWT, yet equally accurate. This is known as dyadic scales and positions. In 1988, Mallat developed an algorithm to implement DWT using filters [64]. Mathematically, DWT of an input signal $x(n)$ is described as,

$$DWT(m,k) = \frac{1}{\sqrt{a_0^m}}\sum x(n)g\left(\frac{k-nb_0a_0^m}{a_0^m}\right) \tag{3.25}$$

where $g(n)$ is the mother wavelet, "a" and "b" are scaling and translation parameters respectively, and they are functions of the integer m [66].

For most signals, it is the low-frequency content that carries the more important information about the signal. The low-frequency, high-scale signal components are called approximations, whereas the low-scale but high-frequency components are called details. To obtain approximation and detail of the signal S, it is passed through two filters, which are compliments of each other as shown in Fig. 3.12. However, the outputs of the two filters are down sampled (a process called down sampling), so that the length of the signal remains the same as that of the original signal [64].

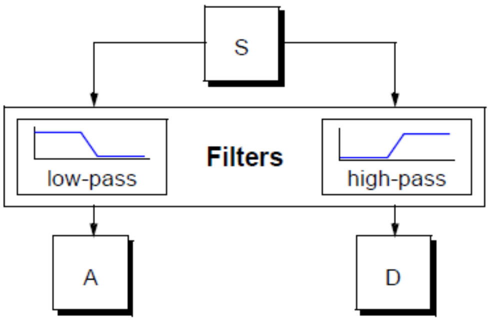

Fig. 3.12: Filtering mechanism in DWT [64]

The process of decomposition can be iterated with each successive approximation, until the required analysis level is reached [66].

3.4.4 Other Signal processing techniques

Some other signal processing techniques that are often encountered in the fault diagnosis of rotating machinery are described in the following sections.

A. Cepstrum Analysis

The inverse Fourier Transform of the log power spectrum is defined as power cepstrum. It is extensively used for finding periodic structures that exists in spectra. Each structure is identified by a unique peak that corresponds to the spacing of the harmonics and sidebands in the spectrum. This technique finds its application in machine diagnosis to spot the modulating frequencies and in gear diagnosis. Rotational frequency harmonics in gear vibrations have overlapping families of sidebands, as a result, they are difficult to analyse. However, cepstrum analysis offer prognostic monitoring by compressing the frequency domain information so that it is in a form easier to understand [55]. Mathematically, this analysis, x_c, is represented as the inverse Fourier transform (F^{-1}) of the log power spectrum or amplitude spectrum. This is shown in the equation below [49]:

$$x_c(\tau) = F^{-1}\{\ln[X(\omega)]\} \tag{3.26}$$

where,

$$X(\omega) = F\{x(t)\} \tag{3.27}$$

B. Hilbert–Huang Transform

The ±π/2 phase shift operator was proposed in 1905 by David Hilbert, and it is a basis of Hilbert transform. This transform is just a convolution between a function and the Hilbert transform. It is implemented in two steps. First, decomposition of data into intrinsic mode functions (IMF) by the main part of HHT, EMD. IMF is comprised of multiple band-limited and quasi-stationary functions which a complete – adaptive and nearly orthogonal – representation of the signal that is being analysed. Secondly, applying the Hilbert spectral analysis to each IMF either gives the local energy of all instantaneous frequencies or, it gives its amplitude and phase angle from the non-linear or nonstationary signals. The advantages of this technique include non-involvement of any convolution and less computation time [55].

Mathematically, the Hilbert transform, $\tilde{x}(t)$, of the signal x(t) is a convolution between the Hilbert transformer, $\frac{1}{\pi t}$, and the function, x(t), itself.

$$\tilde{x}(t) = H\{x(t)\} = x(t) * \frac{1}{\pi t} = \frac{1}{\pi} \sum_{\tau=0}^{N-1} x(\tau) \frac{1}{t-\tau} \tag{3.28}$$

From this, the amplitude and the phase are respectively calculated as follows:

$$|x(t)| = \sqrt{x^2(t) + \tilde{x}^2(t)} \tag{3.29}$$

$$\theta_i(t) = \tan^{-1}\left[\frac{\tilde{x}(t)}{x(t)}\right] \tag{3.30}$$

This means that, the signal can analytically be expressed in a rectangular form, with real and imaginary part as follows:

$$x_a(t) = x(t) + j\tilde{x}(t) \tag{3.31}$$

This signal processing technique still faces several drawbacks, despite its application machine vibration analysis. Firstly, the IMFs produced by EMD at low frequencies are undesirable, which may cause the results to be misinterpreted. Secondly, the frequency range is wide, making the mono-component property of the IMF unobtainable. Finally, the EMD drastically fails to distinguish the signals of low frequency elements [49].

C. Power Spectral Density (PSD)

It is a non-parametric time series method for identifying and quantifying the amplitude of oscillatory functions with respect to frequency [49]. It is the best tool used for demonstrating the strength of variations in relation to frequency. It identifies the amplitude of oscillatory signals in time-series data, it measures this amplitude and then reveals the frequencies at which the variations are strong or weak. It requires a small amount of processing power, making it suitable for use in fault diagnosis of induction machine. This technique can either be calculated by FFT or by transformation of the autocorrelation function. It is therefore defined as the autocorrelation function divided by 2p, over a large time interval. When the PSD function is integrated over a range of frequency, the result is the mean square value (msv) of the random function and energy [55].

Power spectral density, S_x, is defined, mathematically, as the Fourier transform of the autocorrelation function, R_x, multiplied by 1/2π, taken over a large time T, tending to go towards infinity. Autocorrelation function is a function obtained by correlating a function, say $x(t)$, with itself [49].

$$S_x(\omega) = \frac{1}{2\pi} \sum_{\tau=0}^{N-1} R_x(\tau) e^{-i\omega\tau} \tag{3.32}$$

The inverse of power spectral density is R_x, given by

$$R_x(\tau) = \sum_{\omega=0}^{N-1} S_x(\omega) e^{i\omega\tau} \tag{3.33}$$

where, τ is the function of delay function, and R_x is defined from the original signal as:

$$R_x(\tau) = \lim_{T\to\infty} \frac{1}{T} \int_{-T/2}^{T/2} x(t)x(t+\tau)dt \tag{3.34}$$

3.5 Windowing and Zero Padding

In practical applications, captured signals are always definite or limited in the time domain. Unless the sampled signal has a length that is an integer multiple of the signal period length, the first and the last values of the signal are different. So, there will be discontinuities in the boundaries of the observing interval. On the other hand, the FFT algorithm assumes the captured signal is periodic throughout or at least it starts and end at the same value. Consequently, when the FFT is applied to a finite signal with discontinuities at the boundaries, a phenomenon called spectral leakage manifests [67]. This means that the frequency content is smeared over the full range of the DFT coefficients because the discontinuities at the boundaries results in the spectral power of a specific frequency leaking out of the main lobe to the nearby side lobes, on either side of the main lobe [68], which is undesirable. Also, the decrease of power in the main lobe due to leakage leads to increase of power in the sideband harmonics which can lead to false diagnosis in the case of fault analysis.

Spectral is impeded – and not eliminated – by the application of a window function, a process called windowing. A window function often contains a weighted trigonometric function which starts at zero and ends at zero, hence they are sometimes called tapering functions. So, windowing reduces spectral leakage by reducing abrupt discontinuities at the boundaries of the viewing window. There are many window functions in use to date, differing in strengths and drawbacks. These include rectangular, Hanning, Blackman and Kaiser window functions. In this work, Hanning window will be used as it reduces the side lobes a lot and has a better frequency resolution than the other window functions [67].

Zero padding on the other hand, is the processes of enlarging data sequence, such that its length is equal to the next power of two. This is done by adding zeros to the end of the input sequence so that the total number of samples are equal to the next higher power of two. In this way, a longer FFT can be used resulting in longer FFT vector. So, in essence a zero padded signal has the DFT assumption of periodicity lifted and superseded by the truncated DTFT assumption, which is a DTFT of signal calculated with all signal values outside the known ranged assumed zero. Zero padding only increases frequency resolution without adding any new information to the signal [69].

Chapter 4: VSI Faults, MCSA in Inverter-fed Induction Motor and Impedance Variation due to Broken Bar Rotors

4.1 Introduction

In this chapter, the impacts of inverter open switch faults on the overall performance of the induction motor, with particular focus to the changes in voltage, current, speed and torque of the motor are reviewed. Fault diagnosis of these inverter open switch faults using diagnostic variables method is also reviewed. Furthermore, MCSA and its shortcomings in its application to the broken rotor bar fault detection is discussed before finally discussing the standstill impedance variation technique and its viability in broken rotor bar fault detection in inverter-fed induction motors.

4.2 Impacts and Fault Diagnosis of Inverter Open Circuit Faults

4.2.2 Impacts of Inverter Open Circuit Faults

The effects of open switch faults of the inverter feeding the induction motor on its performance is presented here. However, the analysis of the impacts of the various inverter open-switch failure modes draws back from understanding the switching mechanism employed in a six-switch 2-level inverter. Under open switch fault, one (or more) of the switches is deprived of its gate control voltage signal. In this case, the switch function of Fig. 2.13 become modified as depicted in Fig. 4.1(a) and (b) for top and bottom switch fault respectively.

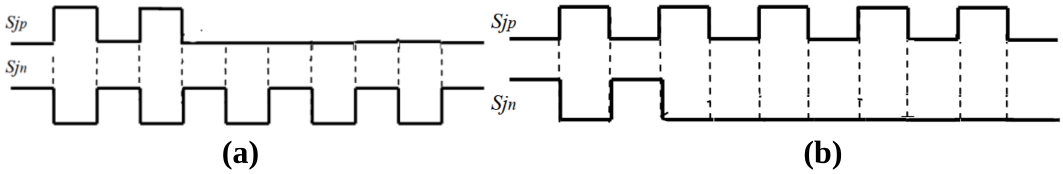

(a) **(b)**

Fig. 4.1: Gate signals with open-circuit fault in the **(a)** top, **(b)** bottom switch

Fig. 4.1 shows that when open circuit fault occurs in a switch, the state of that switch remains at 0 throughout. It can be deduced from Table 2.1 that under this fault, if the fault involves the top switch, say S1 in the first bridge arm, then the line-to-line voltage calculated with respect to that bridge arm, V_{ab} in this case, is either zero or negative but never positive. So, if S3 is open circuited, its state remains '0' throughout, and V_{bc} is either 0 or $-V_{dc}$. The same is true for open circuit fault in S5. Consequently, it can be concluded that when this type of the fault occurs in one of the top switches, the positive half-cycle of the current is eliminated as it drops to zero (because the voltage becomes zero) and negative half-cycle remains, resulting in a negative (DC) current in that phase. The opposite is true if the open circuit fault occurs in one of the bottom switches. Therefore, [45] concluded that an open-circuit fault makes the current in the affected phase be zero for either the positive or negative half-cycle depending on whether the fault occurs on the upper or lower switch. They further noted that the occurrence of this fault does not take the motor out of operation, but greatly degrades its performance with the presence of nonnegligible torque pulsations.

Salem *et al.* [70] remark that there is no positive current flow into phase A following an open switch fault in switch S1, the upper switch of phase A, resulting in a DC current in this phase. They say this DC current, which is then divided into the two remaining phases, causes excessive heat in the windings of the motor in addition to causing torque pulsations.

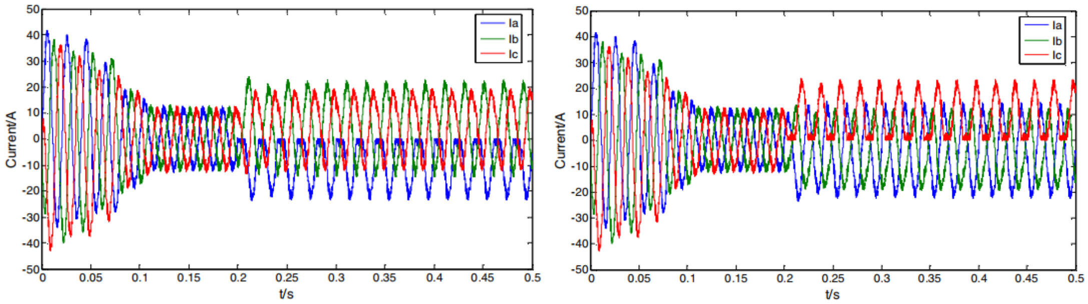

(a) **(b)**

Fig. 4.2: Stator current response with **(a)** top, **(b)** bottom swich open circuit [15]

Cui [15] simulated open switch circuit fault of VSI feeding an induction motor in MATLAB Simulink environment. Their results are shown in Fig. 4.2(a) and (b) for top switch (S1) and bottom switch (S4) fault respectively.

Fig. 4.2 confirms [45]'s claim that when the top switch is open circuited, the positive half-cycle of the current of the affected phase drops to zero, leaving only the negative half-cycle, while the faulty bottom switch leads to the elimination of the negative half-cycle of the current waveform, leaving the positive half-cycle. Cui [15] further studied the torque response of the motor under the influence of this fault. Their results are shown in Fig. 4.3(a) and (b) for faulty S1 and S4 respectively. It is observed from their results that, no matter whether it is the top switch or bottom switch that is open circuited, the torque response is the same – the torque relinquishes its steady state regime and start pulsating substantially.

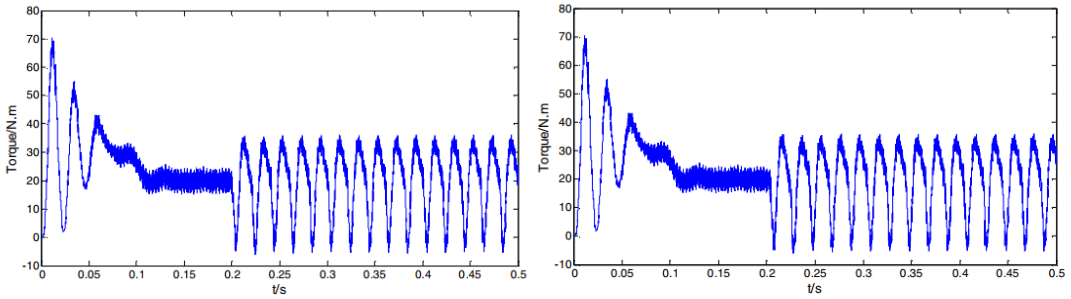

(a) **(b)**

Fig. 4.3: Torque of the system under **(a)** top, **(b)** bottom switch open circuit fault

It is observed that prior to the occurrence of the fault, the torque had reached a steady state value of 20 Nm. However, when the fault occurs at t = 0.2 s, the torque drops slightly and starts to pulsate significantly. Sujo [46] further confirms that this type of fault degrades the motor drive performance by causing discontinuity in one of the phase currents, and so causing an unbalanced conditions in the motor current. This causes distortion not only in the torque, but also in the speed of the motor. They further assert that in addition to studying time domain response, the variations in parameters including voltage and current, caused by open-circuited switches, may further be studied in the frequency domain by using THD analysis. Khater *et al.* [51] showed that when there is an open switch fault on top switch, say S1, the voltage spectra showed a slight decrease in the fundamental component of the other phases (phases b and c), while phase a drops by almost half. They further showed that even harmonic components are present in all phases, with phase a having the highest second order harmonic than the other phases.

So, the performance of the SCIM is greatly affected by the open-switch faults. The fundamental value of the current changes from its nominal value in each respective phase, and thus putting the machine under enormous mechanical, electrical, and thermal stress. Also, the voltage becomes distorted and constitutes additional harmonics. Finally, the torque and speed of the motor starts oscillating significantly on occurrence of this fault. So, the effects of this fault are better understood by performing analysis of the switching pattern and the corresponding change of the line-to-line voltage levels and current during the switching times. This is done for both healthy and faulty conditions, for comparison. The time domain and frequency domain analysis are performed on both current and voltage to discriminate the fault condition. So, one of the aims of this research is to investigate the changes in voltage, current, speed and torque of the test motor due to the occurrence of inverter open switch faults.

4.2.3 Fault Diagnosis of Inverter Open-switch Faults

It is also desirable and worthy to perform diagnosis of these inverter faults, so that they can be detected early and then addressed before they could become aggravated, causing secondary failures in the drive. Several diagnostic techniques have been proposed, in the literature, for fault diagnosis of inverter open switch faults. However, most of these methods are complex and computationally intensive [70].

An open switch fault detection method based on the use of diagnostic variables and current average values is developed and presented in [17], [20], [21], [70]. However, only [21] extended the diagnosis to double open switch faults. All others only focused on a single open switch fault. The method uses the stator current for inverter open-switch fault detection and diagnosis [15]. The schematic of this detection method is shown in Fig. 4.4 [21].

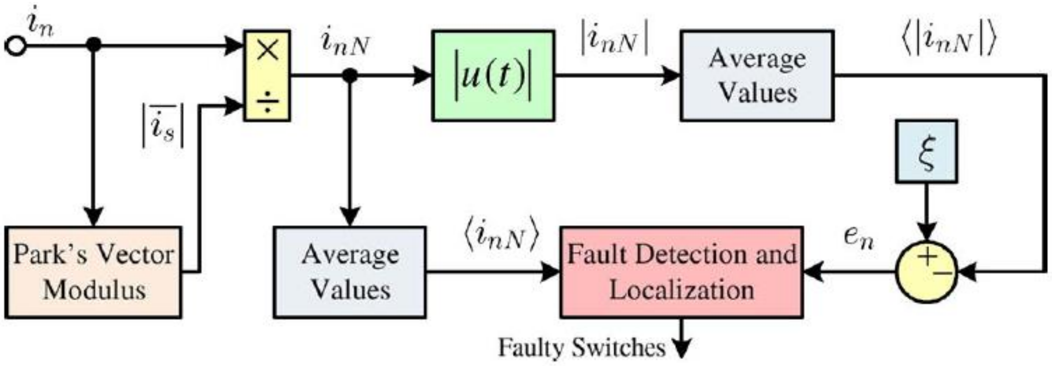

Fig. 4.4: VSI open switch fault diagnostic method

It uses motor phase currents, denoted as i_n. For a three-phase system, $n = a, b, c$, for phases a, b and c respectively. The advantage here is the fact that these currents are already used in the diagnosis of the motor broken rotor bar fault. So, this means no additional sensors or additional set ups are required for the diagnosis of inverter open switch fault. The diagnosis uses average current values and the average absolute values of the normalised motor currents. The normalisation is to ensure reliability of the diagnostic method, especially under fast dynamic cases, and it is done using Park's modulus vector ($|i_m|$) [70]. To normalise the currents, the Park's vector components, i_{qs} and i_{ds}, are first calculated as,

$$i_{qs} = \sqrt{\frac{2}{3}}i_a - \frac{1}{\sqrt{6}}i_b - \frac{1}{\sqrt{6}}i_c \tag{4.1}$$

$$i_{ds} = \frac{1}{\sqrt{2}}i_c - \frac{1}{\sqrt{2}}i_b \tag{4.2}$$

From the vector, the Park's modulus is calculated as

$$|i_m| = \sqrt{i_{qs}^2 + i_{ds}^2} \tag{4.3}$$

So, to normalise the phase currents, the currents are simply divided by the Park's modulus vector as follows,

$$i_{nN} = \frac{i_n}{|i_m|} \tag{4.4}$$

Alternatively, [21], [20] and [70], claim that if the motor is fed from a healthy inverter generating perfectly balanced three phase currents, with a peak value of I_m, then Park's modulus vector is defined as

$$|i_m| = I_m\sqrt{\frac{3}{2}} \tag{4.5}$$

They further showed that the average absolute value of the normalised phase currents for a healthy inverter is constant and calculated as,

$$\xi = \omega_s \int_0^{1/\omega_s} |i_{nN}|dt = \frac{1}{\pi}\sqrt{\frac{8}{3}} \approx 0.5198 \tag{4.6}$$

The diagnosis uses the average absolute values of the normalised motor currents, $\langle |i_{nN}| \rangle$, and the average motor currents, $\langle i_{nN} \rangle$, to detect and localise the open switch faults, respectively. When the inverter is healthy, and outputting, ideally, balanced three-phase currents, then the average values of the currents are zero (because they are perfect sinusoids). The average absolute values of the normalised currents are constant at 0.5198. However, under open switch fault conditions, either the positive or negative half-cycle of the current drops to zero, depending on whether the fault is on the top or the bottom switch. The result is a DC current in that phase. This DC current is shared between the two remaining phases. Consequently, the average value of each phase current, $\langle i_{nN} \rangle$, becomes either negative or positive but not zero as in the case of healthy inverter. Likewise, the average absolute values of normalised currents change for each of the phase currents and is no longer 0.5198.

The diagnostic variables e_n are defined as the errors of average absolute values of the normalised currents for healthy and faulty cases, as follows,

$$e_n = \xi - \langle |i_{nN}| \rangle = 0.5198 - \langle |i_{nN}| \rangle \tag{4.7}$$

It can be deduced from this equation that the diagnostic variables equal to zero under healthy operating conditions. However, when open-switch fault occurs in the inverter, one of the diagnostic variables assumes a positive value.

To locate which switch is open circuited, the diagnostic variables are used together with the current average values $\langle i_{abcN} \rangle$. This is achieved by defining the following symptom variables and compiling Table 4.1 [21].

$$E_n = \begin{cases} N & if\ e_n < 0 \\ 0 & if\ 0 \leq e_n < k_f \\ P & if\ k_f \leq e_n < k_d \\ D & if\ e_n > k_d \end{cases} \tag{4.8}$$

$$M_n = \begin{cases} L & if\ \langle i_{nN} \rangle < 0 \\ H & if\ \langle i_{nN} \rangle > 0 \end{cases} \tag{4.9}$$

Therefore, d_n is the diagnostic variable of phase n, and $\langle i_{nN} \rangle$ is the average of the normalised phase n current. The threshold k_f is directly related to any open switch fault detection. In their work, they assigned it the value $k_f = 0.08$.

Table 4.1: Fault Signatures for the Faulty Switch Identification

Faulty Switches	E_a	E_b	E_c	M_a	M_b	M_c
S1	P	N	N	L	-	-
S2	N	N	P	-	-	H
S3	N	P	N	-	L	-
S4	P	N	N	H	-	-
S5	N	N	P	-	-	L
S6	N	P	N	-	H	-
S1, S4	D	-	-	-	-	-
S3, S6	-	D	-	-	-	-
S2, S5	-	-	D	-	-	-
S1, S3	P	P	N	L	L	H
S4, S6	P	P	N	H	H	L
S3, S5	P	N	P	L	H	L
S2, S6	P	N	P	H	L	H
S1, S5	N	P	P	H	L	L
S2, S4	N	P	P	L	H	H

Likewise, the threshold value k_d plays an indispensable role in double switch fault in the same inverter phase (i.e., same bridge arm). It was assigned the value $k_d = 0.32$. These thresholds are usually established by analysing the variables' behaviour for various faulty operating conditions [21].

Merabet *et al.* [20] studied open switch failure in which S1 was open circuited at t = 0.4s by building and simulating a model of the VSI fed induction motor system in MATLAB/SIMULINK environment. Their three-phase currents, the diagnostic variables and current averages values are shown in Fig. 4.5.

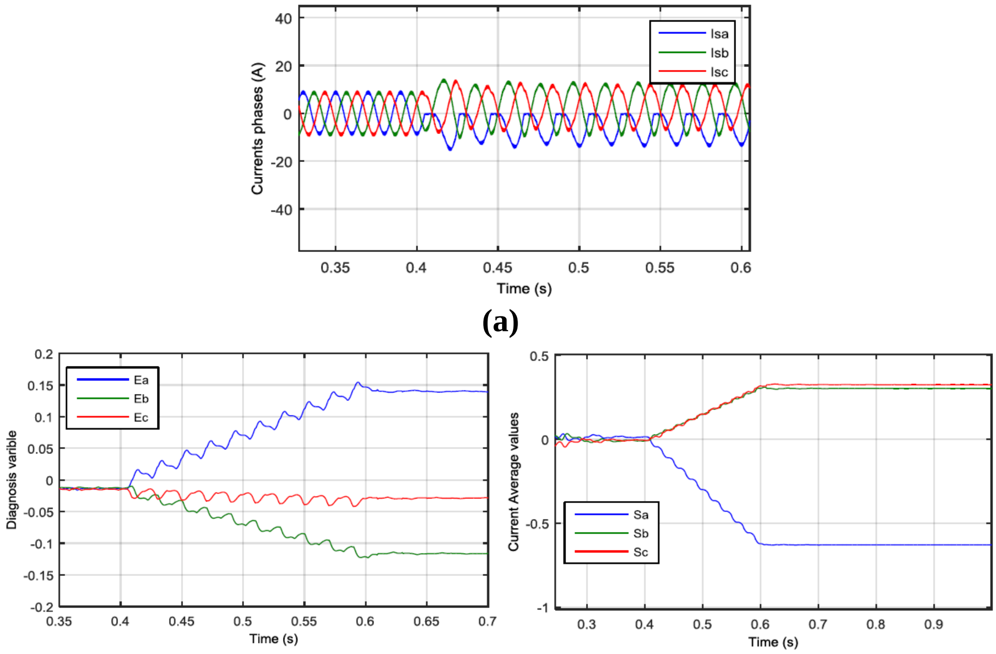

(a)

(b) **(c)**

Fig. 4.5: **(a)** 3-phase currents, **(b)** diagnostic variables and **(c)** current average values for case of S1 open circuited

The results show that when the fault occurs at t = 0.4 s, the currents become unbalanced and the positive half-cycle of phase a is diminished to zero. Despite the slight difference in notation, it is evident that average current values (denoted by S_a, S_b and S_c) are zero under healthy conditions. However, the average value of phase a current becomes negative while the average values of the currents in other phases become positive on occurrence of the fault. Similarly, the diagnostic variables (here denoted as E_a, E_b and E_c) remained zero under healthy operation. Nonetheless, only diagnostic variable for phase a became positive and converged to a value of approximately 0.15 (greater than $k_f = 0.08$) while the other diagnostic variables dropped and assumed negative values. This is characteristic of an open switch fault. To localise the fault, it is noted that, while the diagnostic variable for phase a is positive, the average current value for the same phase is negative. This combination satisfies the second row of Table 4.1. Thus, the faulty switch is S1.

On the other hand, Estima and Cardoso [21] conducted simulation studies and experimental work to detect and diagnose, among others, two open switch fault types: single-phasing fault and double open switch faults. Fig. 4.6 shows their simulation results for single-phase open circuit fault in phase a. It is observed that when both switch S1 and S4 are deprived of their gate control voltage signal, phase a current drops to zero, while the other phases become distorted but are still sinusoidal. Therefore, the average current values for all the phase currents remain zero even after the fault as shown in Fig. 4.6(c). However, the diagnostic variable for phase, e_a, becomes positive and increases until it converges at a value of 0.49, which is greater than $k_d = 0.32$. The other diagnostic variables drop from zero and assume negative values.

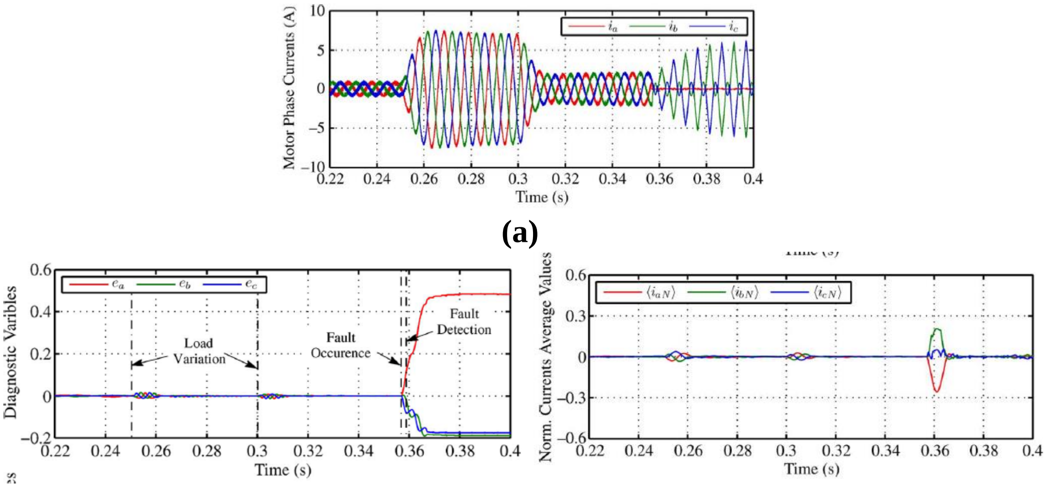

(b) **(c)**

Fig. 4.6: **(a)** 3-phase currents, **(b)** diagnostic variables and, **(c)** current average values for case of single-phase open-circuit fault in phase a

It is noted that at the instant when the fault occurs, there are some transients generated on the average current values, but these quickly die out as the averages converge back to zero. The results for the double open switch fault on S1 and S3 are shown in Fig. 4.7(a) and (b), for simulation and experimental results, respectively. Both simulation and experimental results show that when this fault occurs, the two affected phases (a and b) lose their positive half-cycle of current as it drops to zero in these phases. Consequently, the current average values for these two affected phases become negative, while that of phase c becomes positive. Two diagnostic variables corresponding to phase a and b become positive while, that of c drops and converge to a negative value. This indicates that there is a fault in phases a and b. To localise the fault, it is observed that these combination of current average values and diagnostic variables corresponds to row 11 in Table 4.1. Hence, both S1 and S3 are open circuited.

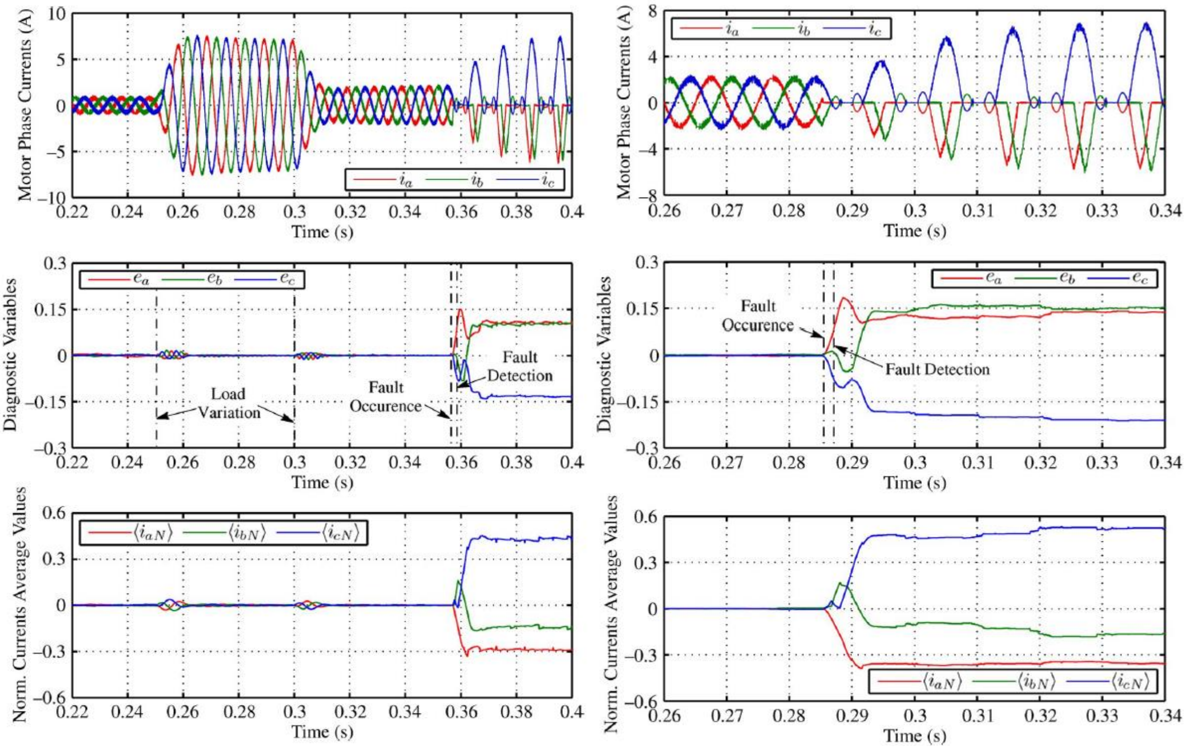

(a) **(b)**

Fig. 4.7: **(a)** simulation, **(b)** experimental, 3-phase currents, diagnostic variables and, current average values for case of double open-circuit fault in S1 and S3

So, another focus of this research is to validate this diagnostic method for inverter open switch faults by first building the system in MATLAB/Simulink environment and simulating the fault, and then building this system and emulating the faults experimentally in the laboratory.

4.3 Broken Rotor Bar Fault Detection Using MCSA

Of all the rotor-related failures, broken rotor bars are the most common [13], constituting 5-10% of all induction motor faults [14]. When a bar breaks, the rotor loses its symmetric properties [71] and this is reflected as amplification of certain harmonic components in the stator current. The most prominent components amplified by the fault – known as sideband harmonics [72] – are those located on either side of the fundamental component. These current components, characteristic of the broken bar fault, are located at,

$$f_{brb} = (1 \pm 2ks)f \qquad (4.10)$$

where f is the frequency of the fundamental component, s is the slip and $k = 1, 2, 3 \ldots$ [65], [71], [73].

Under healthy state, the three-phase stator windings excited at frequency f produce a rotating flux of constant amplitude in the airgap of the machine. This flux induces rotor currents at frequency sf. However, bar breakage (asymmetry) results in rotor currents being induced at frequency $-sf$, causing a backward rotating component of flux. This induces a stator EMF at frequency $(1-2s)f$ causing speed and torque ripple. The ripple is reflected to the stator as line current oscillations at frequency $(1+2s)f$. The current component at frequency $(1+$

$2s)f$ in turn induces rotor currents at $\pm 3sf$. This ripple effect continues until filtered by the inertia of the rotor [71]. Li and Mechefske [65] remarked that the first-order sidebands (for $k = 1$) are of great importance in the diagnosis of broken rotor bar faults, and further state that the left sideband $(1 - 2s)f$ is the one which surfaces from rotor electric or magnetic asymmetry caused by the broken rotor bars, whereas the right sideband $(1 + 2s)f$ arises from speed ripples/variation, which is also affirmed by Gyftakis *et al.* [14] and Asad *et al.* [74].

It is then asserted in [19] that a-less than 50 dB amplitude difference between the fundamental frequency and the left sideband harmonic is indicative of broken rotor bar fault. On the other hand, by virtue of being speed (and hence load) dependent (because of the slip factor), the positions of the sidebands in the spectrum shift outwards when load is increased [65], and as [74] remarked, a growing value of k also shifts the positions of the sidebands outwards (increases their frequency) while decreasing their amplitudes [75].

While broken rotor bar faults do not necessarily cause catastrophic failure of the machine right away [14], it is imperative that it is detected at an early stage before it produces secondary failures. If not discovered early, the fault propagates as increased current in the neighbouring healthy bars, leading to increased electrical and thermal stresses in the machine [56]. The ability to detect this kind of fault at an incipient phase requires a reliable fault detection technique, alongside an appropriate signal processing technique to detect and isolate the fault successfully and explicitly. MCSA is the most used fault detection technique in the diagnosis of broken rotor bar fault in induction machines [13], [56] and is employed in most commercial induction motor monitoring devices [76].

This classical technique is focused on the application of the Fourier transform to machine's stator current under steady state operating conditions [7]. The fault detection is done by observing amplified sideband harmonics that appear on either side of the supply frequency on the frequency spectrum of the stator current. Broken rotor bar fault detection with this technique is premised on four main assumptions: the load is constant, the speed is also not changing and is known, the stator fundamental frequency is kept constant and the machine is sufficiently loaded [19].

MCSA gains its popularity from some of its advantages: it is a robust fault diagnostic tool, which uses simple acquisition system and software [6]. Also, it is non-invasive, which is a very desirable feature for a typical fault detection technique. MCSA also demands the least number of sensors and has a variety of agreeable diagnostic algorithms that can be used [74]. Despite its robustness, this technique suffers serious drawbacks, especially when applied in industry, where there are many practical factors which affect the operation of the induction motor. Other than the fact that MCSA is only applicable in steady stead operating conditions, it also comes out short in the following 3 ways.

4.3.1 False Positive Indication of the Fault

This is a case where through MCSA, the machine is diagnosed as faulty, yet it is healthy. This is highly undesirable in industry as the cost of inspection of this motor may be tremendously high, let alone if it is a large motor, in which the cost of handling, detachment, installation of a spare motor, rental of the handling equipment like cranes will extremely be high. The cost increases further if the loss of production is included [76]. So, in short, to mistakenly diagnose a healthy machine as being faulty will have immense economic implications on the company. Some of the phenomena which may eventually lead to false positive diagnosis of the motor include:

A. Load Torque Oscillations

The presence of load torque oscillations introduces into the spectrum, frequency components that are very similar to those caused by the broken rotor bar fault [76]. As it can be observed, Fig. 4.8(b) could possibly lead to the conclusion that the motor is faulty, while in fact it is healthy. As [6] admittedly remarked, any external factor capable of introducing speed or torque oscillations will cause the appearance of harmonics in the spectrum of current that can erroneously be diagnosed as broken rotor bar fault harmonics. Similar results to Fig. 4.8 showing the presence of sideband harmonics in a healthy induction motor driving a pulsating load are presented in [76].

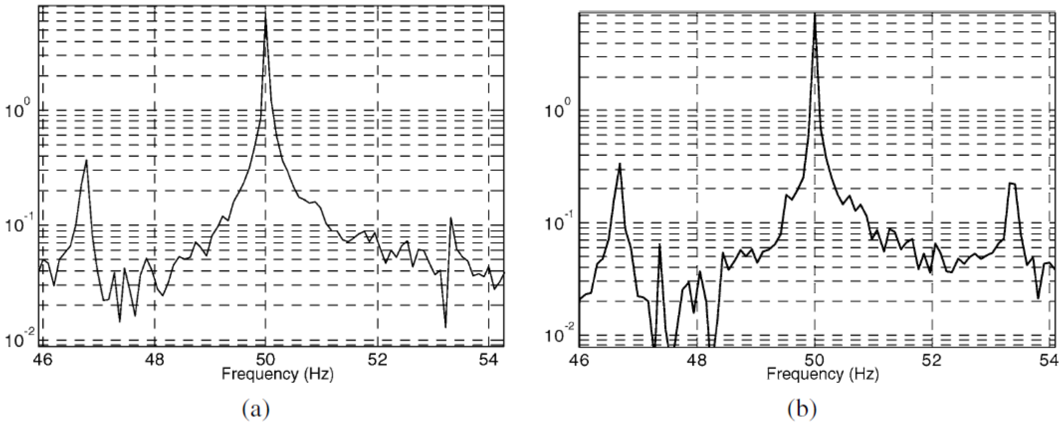

Fig. 4.8: **(a)** Sideband components due to broken bars, **(b)** Frequencies due to fluctuating torque in healthy machine [6]

B. Cooling Rotor Axial Ducts

It is remarked in [14] that several cases of broken rotor bar fault false-alarms have been reported in induction machines with axial cooling ducts. This is affirmed by [76] that when the number of ducts and number of poles are equal, which is often the case in large induction motor, frequency components similar to those produced by broken rotor bar fault are introduced in the spectrum of the stator current. [76] further presents MCSA results for two samples (labelled A1 and A2) extracted from a healthy 6.6kV, 2400kW induced draft fan motor with 8 cooling ducts and 8 poles. These results are shown in Fig. 4.9.

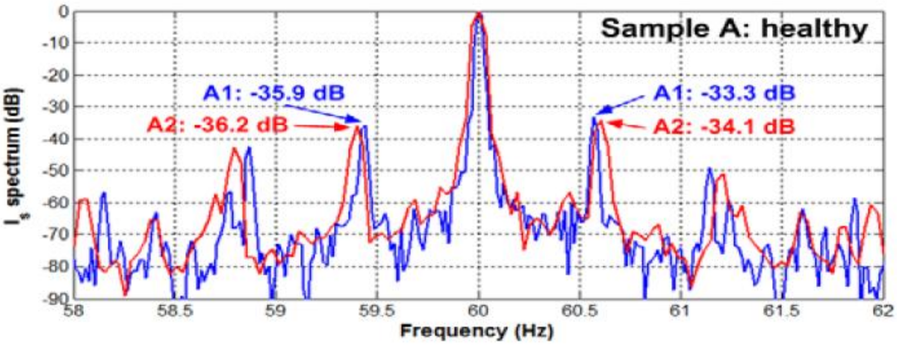

Fig. 4.9**:** MCSA of two samples for healthy induced draft fan motor [76]

As it can be observed, MCSA shows strong amplitude for the sideband harmonics, such that the amplitude difference between the fundamental harmonic and these sideband harmonics is less than 50 dB and hence the machine may be falsely diagnosed as having a broken rotor bar fault. It is further stressed in [76] that even in the event of the presence of broken rotor bar fault, the presence of cooling ducts can still cause a decrement in the amplitude of broken rotor bar fault harmonics, which can lead to difficulty in deciding if the machine is faulty or not, especially if the machine is fed through an inverter, where the decreased fault harmonics may be buried in the inverter switching noise.

4.3.2 False Negative Indication of the Fault

In this case, contrary to false positive case, is where, through MCSA technique, the machine is diagnosed as healthy, yet it has broken rotor bar(s). False negatives, as can be expected, have dangerous consequences because, if not detected in time, the broken rotor bar fault propagates to the neighbouring healthy bars [76] because of the increased current in those bars. This could lead to the eventual total breakdown of the machine, which undoubtedly invokes unplanned production shutdowns, the consequence of which has financial implications. False negatives defeat the objective of condition monitoring, which is detection of machine faults at their incipient phase, and hence prevents unexpected production shutdowns. Some of the phenomena which may eventually lead to false negatives during the diagnosis of the motor include:

A. Faulty Motor Diagnosed under Reduced Slip

When the motor is lightly loaded or unloaded altogether, it runs at a speed close to the synchronous speed. Consequently, the slip, s, is very small. In these operating conditions, the faulty sideband harmonics overlap the fundamental component [6], [11], [74], [76]. This will make identification of faulty harmonics very difficult, and hence the faulty machine may be falsely diagnosed as healthy. The cases in which the machine may be run at low slip include testing the machine in repair workshops or in the plant, just before the machine is put into service [76]. Fig. 4.10 shows the current signal spectrums obtained from FFT technique for a motor with one broken rotor, both under no-load and fully load conditions.

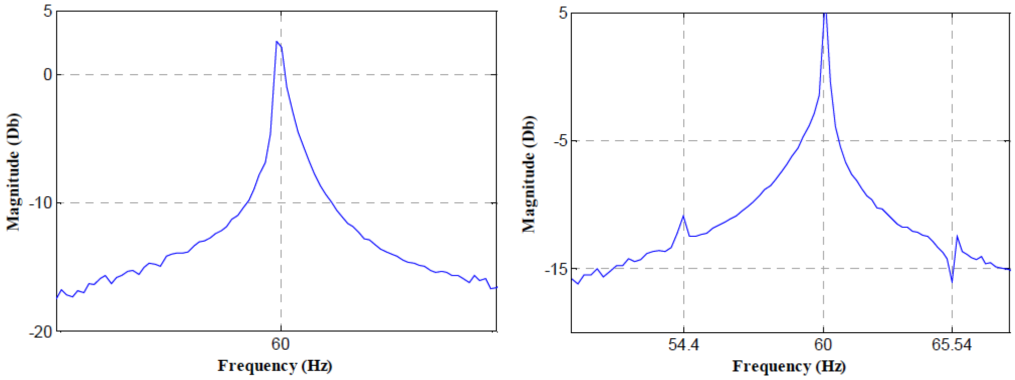

Fig. 4.10: MCSA results for a broken rotor bar motor on **(a)** No-load, **(b)** full load [11]

As it can be observed from Fig. 4.10(a), it is difficult to identify the presence of the sideband harmonics. This could lead to erroneous conclusion that the machine is healthy, while indeed it is faulty. However, when the machine is loaded, as in Fig. 4.10(b), the sideband harmonics become visible. Similar results are presented in [6] and [76], all of which confirm that the sideband harmonics are unidentifiable for unloaded or lightly loaded machines.

The FFT of the stator current usually shows a small amplitude of the sideband harmonics. This is due to several factors, including the fact that while the analysed current signal has fixed duration, the FFT algorithm is designed for infinitely long-time period. As a result, there is spectral leakage caused by signal truncation. This is where logarithmic scale comes into play, as it makes spatial and fault frequencies with low amplitude to be noticeable in the spectrum [74]. An alternative approach is to use other forms of MCSA like the Power Spectral Density (PSD).

B. Double Cage Rotors – Outer Cage Breakage Detection

Double-cage induction motors have very small circulating current flowing in the outer-cage under steady state conditions. Hence, online FFT-based techniques fail to detect broken rotor bar(s) in the outer cage, since the distortion in airgap MMF will be very low [77]. This failure is more prominent in inverter-fed induction motors since this reduced fault sideband harmonics are likely to be masked by inverter switching noise. Double-cage rotors are used in high-starting torque machines, and their design features larger outer bar resistance coupled with large inner bar leakage inductance, resulting in relatively large current flowing in the inner cage, and very little in the outer cage during steady state [76]. Fig. 4.11 shows the degrading ability of MCSA to detect broken rotor bar fault as it is applied from single cage to double cage rotor.

As Fig. 4.11 depicts, MCSA does not show much of an increment in sideband harmonics in the case of outer cage bar breakage, which may lead to incorrect diagnosis that the machine is healthy while it has a broken rotor bar in the outer cage.

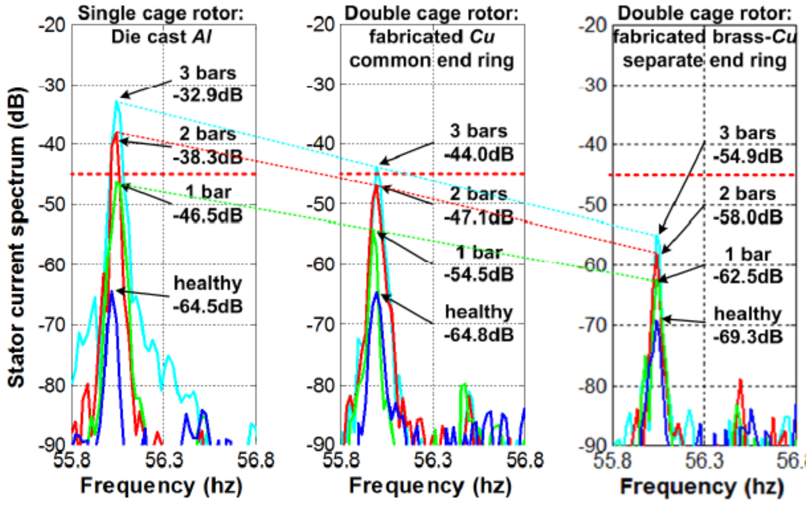

(a) (b) (c)

Fig. 4.11: Application of MCSA in **(a)** single cage deep bar Al, die cast rotor, double-cage fabricated **(b)** Cu common end-ring rotor, **(c)** brass-Cu separate end ring rotor [76]

4.3.3 Fault Identification in Inverter-fed Induction Motors

Application of MCSA in the detection of broken rotor bar faults in grid connected induction motors operating under steady stead operating conditions is, to a large extent, a success (provided those assumptions stated earlier in this chapter are met). However, in practical industrial applications involving induction motors, there are often continuous load changes, or voltage variations or manifestation of unacceptable frequency components [78] which violate the steady state requirements of MCSA and degrades its credibility as a fault detection tool. This is more so if the induction motor is fed through an inverter. Inverter-fed motors sometimes operate in nonstationary conditions depending on the particular needs of an industrial application [79] in which the motor is used. Akar [80] affirms that in inverter-fed motors, speed changes continuously, meaning both amplitude and frequency of applied voltage and current through motor windings are changing as well. Consequently, MCSA becomes insufficient as a broken rotor bar fault detection technique.

Apart from introducing nonstationary conditions in the motor, the inverter also introduces other harmonics; another factor negatively impacting the efficiency of MCSA. [81] and [82] remarked that, no matter how accurate the switching PWM is, the inverter inherently produces harmonic distortion in the voltages and currents it sources. So, since the current is rich in harmonic content and switching noise (signal to noise ratio is low), the broken rotor bar fault harmonics can possibly be masked by the inverter harmonics if they overlap [24], [25], [78]-[82], making their detection and diagnosis very difficult. These – inverter switching noise and overlapping inverter harmonics – reduces the effectiveness of MCSA as a fault detection tool in inverter-fed induction motors.

4.3.4 Concluding Remarks on MCSA

It has been shown here, from the literature, that the classical MCSA, although it has some advantages over other condition monitoring techniques, has major drawbacks which could potentially be detrimental in its industrial application. It is shown that it is difficult to deduce the state of health of an inverter driven induction motor from the stator current (MCSA) because fault signatures could be masked by other signatures arising from load oscillations, low slip, inverter, and other nonstationary conditions existent during operation. Hence, one of the objectives of this work is to experimentally establish some of these shortcomings of MCSA in detecting broken rotor bar faults when the motor is unloaded, and when it is fed through at inverter at various loading levels. The shortcomings of MCSA call for alternative approaches of detecting broken rotor faults in inverter-fed induction motors to supplement the classical MCSA. One such alternative is the standstill impedance variation test for broken rotor bar fault, presented in the following section.

4.4 Impedance Variation Due to Broken Rotor Bars

4.4.1 Implications of Rotor Asymmetry on Motor Impedance

Except for some manufacturing imperfections, the rotor of a squirrel cage induction motor is both magnetically and electrically symmetrical. In the case of a healthy rotor, the stator's magnetic flux passes through a small uniform airgap into the symmetrical and ferromagnetic rotor structure. Because of this rotor symmetry, the magnetic flux ideally encounters the same magnetic reluctance through any path passing radially through the rotor structure. That means if the magnetic flux was to be fixed and kept pulsating along an arbitrary axis, say the x-axis, and the rotor was then slowly rotated, the magnetic flux would experience the same reluctance across any chosen radial path through the rotor, and hence the motor would show a constant impedance for any rotor position.

On the contrary, rotor bar breakage introduces asymmetries within the rotor structure. Current stops flowing in the broken rotor bars [83], and instead it increases in the neighbouring healthy bars. The result of this is an asymmetric distribution of rotor MMF. Airgap MMF is the resultant of both rotor and stator MMFs, which means it also becomes distorted and differs from that of ideal symmetric rotor [73], [83]. Effectively, the rotor becomes salient-like [73], [84] due to the cracked bars, and this magnetic asymmetry changes both resistance and inductance parameters, in both d- and q-axis. Ambrozic *et. al.* [73] presented the results of measurements of resistance and inductance as a function of rotor position (rotor angle) of a healthy and faulty motor (with 7 out of 44 rotor bars broken). Fig. 4.12(a) and (b) show these results for resistance and inductance, respectively.

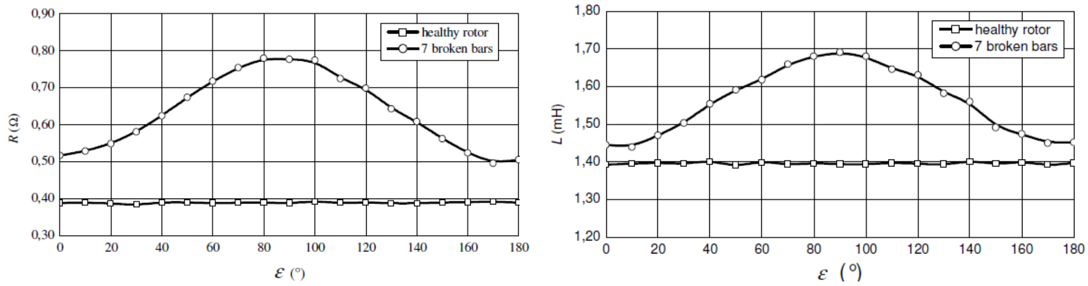

(a) **(b)**

Fig. 4.12: Measured **(a)** resistance, **(b)** inductance, versus position for healthy rotor and rotor with 7 broken rotor bars [73]

As observed in Fig. 4.12, both resistance and inductance vary sinusoidally with rotor angle, and the authors remarked that rotor resistance and inductance vary depending on the number of broken rotor bars. In fact, the same authors carried out additional work later in [85], and concluded that no matter the broken rotor bar fault configuration, both rotor parameters (resistance and inductance) take a quasi-sinusoidal shape that depends on the rotor angle.

The rotor asymmetry can be used to tell if there is rotor breakage, by simply monitoring the changes in impedance of the machine as a function of rotor position and comparing the results with that of a healthy machine.

4.4.2 Standstill Impedance Variation Test in Grid-connected Motors

The simplest approach to identify impedance variations due to rotor pseudo-saliency caused by rotor bar breakage is to perform the following test at standstill. Fig. 4.13 [11] shows the schematic for the wiring configuration of the stator.

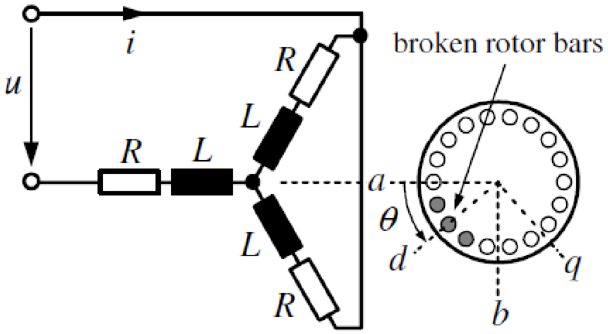

Fig. 4.13: Schematic of offline impedance variation test

The test procedure is carried out while offline, with the rotor at standstill. Two phases are manually shorted together, and a single-phase AC supply impressed between these shorted phases and the third phase. In this configuration, no torque is produced, and the magnetic field is not rotating but is pulsating along a particular axis [84]. This is an injection method since the single-phase voltage does not turn the motor. With magnetic field fixed and pulsating along this axis, the rotor position is changed and for each rotor position (from 0 to 360 deg.), the impedance of the machine is determined from the captured current and voltage signals. The observed change in impedance behaviour between the healthy machine and the one with broken rotor bar is characteristic of the fault. This procedure is implemented in this work to validate its viability for the test induction motor in the laboratory, and also to be used as a benchmark for evaluating the application of the procedure to inverter-fed squirrel cage induction motors.

4.4.3 Standstill Impedance Variation Test in Inverter-fed Motors

This work further proposes the implementation of the scheme mentioned in section 4.4.2 above but using the inverter for inverter-fed machines. The advantage here is that the connections to the machine do not need to be reconfigured, simply the switching scheme adapted. However, the purpose of the work is to investigate its applicability in identifying changes in impedance due to the broken rotor bar since the additional switching noise will have an impact on the measurements as in the case of MCSA. As mentioned, only the switching strategy within the controlling microcontroller is changed and configures the switches in such a way that the inverter supplies a single-phase output to the machine. It is in this configuration that the rotor can be moved to different positions and in each position the impedance of the machine is determined [75].

The use of an inverter further allows the possibility of an advancement of the scheme to simply change the switching configuration to vary the axis of the pulsating magnetic flux, thereby not requiring the physical movement of the rotor into different positions. However, under this modification, the objective will be to find the critical rotor orientation/position where the variation in impedance is minimum, leading to the possible misdiagnosis of the fault. This advancement can be described with reference to Fig. 4.14 which shows the schematic of magnetic axis of each winding of a three-phase 2-pole induction motor.

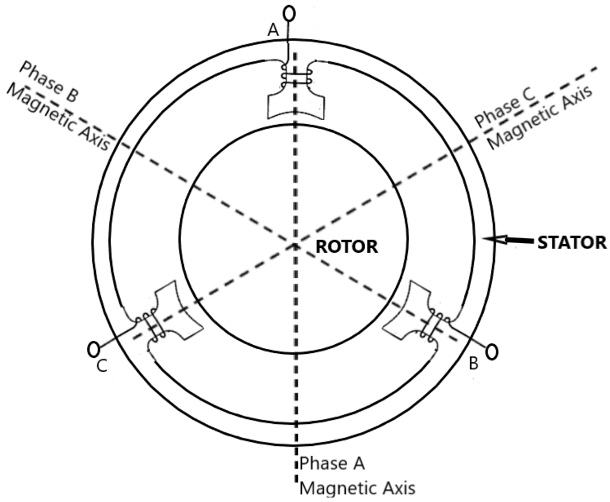

Fig. 4.14: Illustration of magnetic axis of a 3-phase 2-pole machine

Suppose phases B and C are first shorted and current supplied through phase A. The result is a pulsating magnetic flux along the magnetic axis of phase A windings. If the switching configuration is changed such that phases C and A are shorted and current supplied through phase B, the result is a pulsating flux along the magnetic axis of phase B windings. However, since this is 2-pole machine, the electrical degrees are equal to mechanical degrees and the magnetic axis of the phases are 120° apart. Therefore, the axis of the pulsating flux rotates by 120° when the switching configuration changes from shorting phases A and B to shorting phases C and A, because the phase windings are 120° apart. The same logic is true if phases A and B are shorted and current supplied through phase C. So, in essence, for a single rotor orientation/position, three orientations of the pulsating flux are obtained. Three respective impedances, Z_a, Z_b and Z_c, are then determined. If this is repeated for different orientations of the rotor, a series of three sets of impedances, $\{Z_{a1}, Z_{b1}, Z_{c1}\}$, $\{Z_{a2}, Z_{b2}, Z_{c2}\}$, $\{Z_{a3}, Z_{b3}, Z_{c3}\}$ ..., are obtained for rotor orientations 1, 2, 3…. In each set, the three impedances are 120º out of phase as shown in Fig. 4.15(a), assuming a sinusoidal variation of impedance with rotor position as remarked by [73], [83] and [84]. The average of the absolute values of the difference in impedances obtained for each rotor orientation is calculated and plotted as shown in Fig. 4.15(b). The rotor position/orientation with minimum difference is then identified as critical –

cycled red in Fig. 4.15(b). The viability of this technique in broken rotor bar fault detection is also explored and presented in this work.

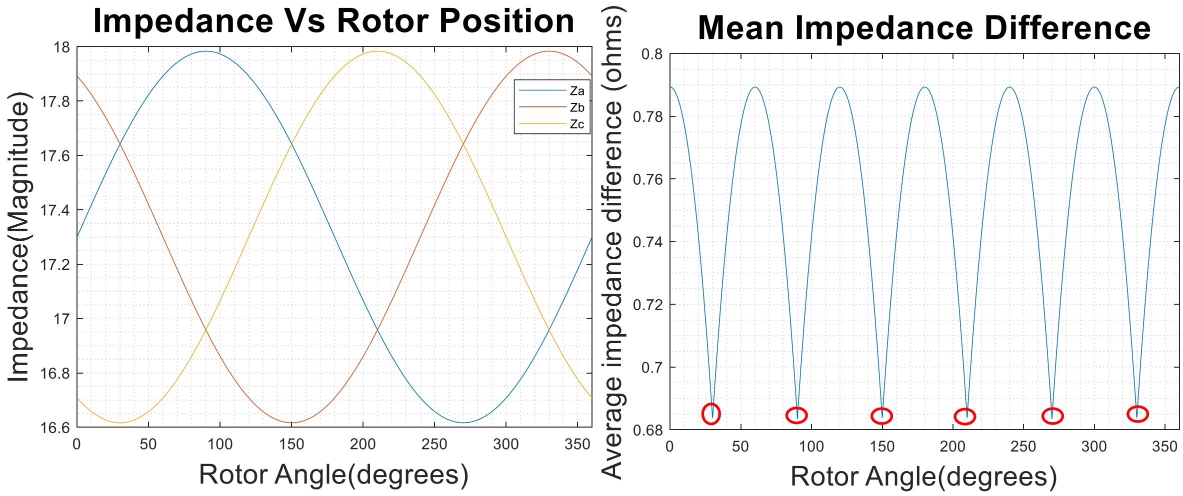

(a) **(b)**

Fig. 4.15: **(a)** Three sets of impedances and **(b)** the average of their absolute differences at each rotor position

To configure the inverter to supply the motor with a single-phase supply, one of the three top switches (Sw1, Sw3, Sw5) and two of the three bottom switches (Sw2, Sw4, Sw6) or vice versa, are switched on at the same time in Fig. 4.16, adapted from [15]. Fig. 4.16 shows an example of current flow in which phases B and C are shorted and current flows from A, by switching on switches Sw1, Sw6 and Sw2 at the same time. To have the current reverse direction so that it flows into A from both B and C, switches Sw4, Sw3 and Sw5 are both switched on at the same time.

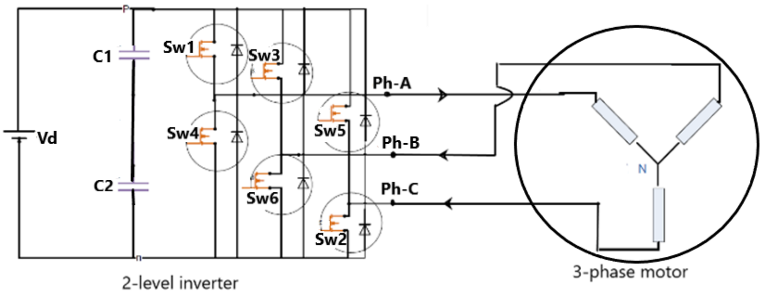

Fig. 4.16: Current flow when phase B and C are shorted

The practical application of this fault detection scheme in inverter-fed induction motors is in the detection of rotor asymmetry at zero speed in electric vehicles (EV and HEV). In EV, speed of the motor is zero at start-up and idle modes, in which case this scheme may be conveniently applied. As Akin *et. al.* [86] remarked, although conventional rotor asymmetry test techniques are applied when the motor is running under a known steady state speed under load and drawing stationary currents from the supply, it is difficult to get these regular test conditions for long periods of time during the daily vehicle operations. Thus, conventional online fault detection like MCSA are not suitable to be used here. [86] further asserts that in EV applications, non-uniform airgap caused by automobile vibrations are common during motor operation, thus resulting in a noisy current spectrum. So, standstill schemes such as the one proposed here overcome these problems. This technique can be applied at start-up or during idle modes of the electric vehicle.

4.5 Concluding Remarks

Varghese and Reema [16] assert that induction motor faults can be grouped into machine faults and switching faults. Common induction motor faults, inclusive of the broken rotor bar fault, were described in Chapter 2. On the contrary, switching faults are faults occurring in the DC link capacitor, rectifier diodes and IGBT/MOSFET switches of the inverter [16]. The overall focus of this work is to study the incapability of MCSA to detect broken rotor bar fault – a machine fault – in inverter-fed squirrel cage induction motor (SCIM), using the grid-connected SCIM as a bases of evaluation. Then it proposes and validates an alternative approach to supplement MCSA, based on variation of motor impedance at standstill with respect to rotor position. However, the VSI forms an integral part of the drive system. Therefore, the reliability of the VSI feeding the induction motor is also irrefutably indispensable [51] to the overall integrity, reliability, and availability of the system. Hence, in addition to the broken rotor bar fault diagnosis in an inverter-fed motor, this work also investigates the impact of some inverter switching faults on the performance of the system, along with the diagnosis of these faults. This chapter highlighted the impacts of VSI open switch faults on the VSI-fed induction motor drive system and their diagnosis using the diagnostic variables technique. It further highlighted the shortcomings of MCSA as a diagnostic tool for diagnosing broken rotor bar fault in inverter-fed squirrel cage induction motor. It derived an alternative diagnostic approach that can be used to supplement MCSA in inverter fed SCIM based on standstill impedance variation with the rotor position, especially in EV applications. The next step is to design and build the variable speed drive that will be used in these fault studies.

Chapter 5: Design and Development of Variable Speed Drive for Fault Studies

5.1 Introduction

This research generally investigates faults across the various components of an induction motor variable frequency drive. It focuses on the broken rotor bar fault on the motor end of the drive, and inverter open switch faults on the converter end of the drive. So, this chapter describes the design and development of the variable frequency drive system which is used in the study of these faults.

5.2 An overview of the Variable Frequency Drive System

Variable frequency drives (VFDs) are used to control the speed and torque of a motor. In AC motors, this control is achieved by varying the input frequency and voltage or current to the AC motor. VFDs use either AC – AC or DC – AC topologies. In this work, the AC – AC topology is used where the standard grid AC voltage is rectified, and the DC voltage is inverted back to AC voltage of the desired amplitude and frequency. As shown in Fig. 5.1 [87], a typical VFD comprises of an AC motor and main drive controller assembly.

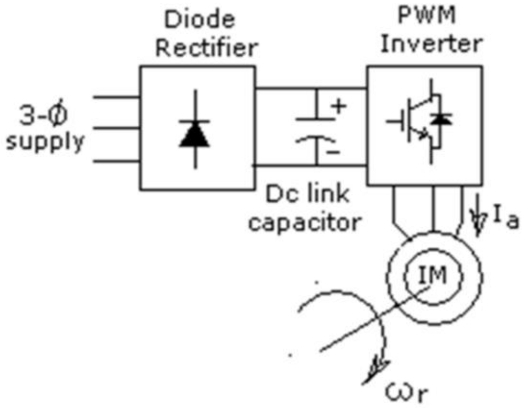

Fig. 5.1: Block diagram of VFD system [87]

It is noteworthy that the rectified voltage needs to be smoothed out to attenuate its ripple content as much as possible before its inversion. This is achieved using large capacitors shunted between the rectifier output and inverter input, as shown in Fig. 5.1. The preceding sections outline the design and development of the VFD and its control.

5.3 Variable Frequency Drive System

This section describes the design and development of the VFD system used in this project. It also describes the other auxiliary systems and subsystems like the filter and the control systems.

5.3.1 AC Motor – Test Motors

The AC motor used in this work is a 250 W, 190 V, 50 Hz and 2-pole, star-connected three-phase squirrel cage induction motor. The nameplate ratings of the motor are shown in Table 5.1.

Table 5.1: Nameplate ratings of the machines

Parameter	**Value**	**Units**
Rated voltage	190	V
Rated current	1.85	A
Connection	Wye	
Frequency	50	Hz
Speed at rated power	2850	Rpm
Rated power	248.57	W
Number of phases	3	
VA Ratings	608.82	VA
Slip at rated power	5	%
Rated torque	0.8329	Nm

Several experiments such as the no-load test, blocked rotor tests, DC tests and spin down tests were carried out to determine the parameters of this machine. These parameters are shown in Table 5.2 for the two test motors. This table gives parameters for both the healthy motor and broken rotor bar motor.

Table 5.2: Measured Machine Parameters under healthy (Healthy) and broken rotor bar (BRB) conditions

Parameter	**Value**	
	Healthy	BRB
Stator resistance R_s	4.24 Ω	5.17 Ω
Rotor resistance R_r	2.12 Ω	2.98 Ω
Magnetizing reactance X_m	76.27 Ω	78.21 Ω
Stator leakage reactance X_{ls}	3.95 Ω	4.12 Ω
Rotor leakage reactance X_{lr}	3.95 Ω	4.12 Ω
Moment of inertia J	0.0016797 kgm^2	0.0018219 kgm^2
Friction coefficient B	0.0010356 Nm.s	0.0011263Nm.s

5.3.2 VFD Controller Assembly – Components Selection and Testing

The basic design of a drive system considers the selection and sizing of the controller components as shown in Fig. 5.1. This section presents the selection and sizing of the controller components used in this work.

A. Selection and Testing of Power Semi-conductor Device

The inverter considered for this work is a two-level inverter, with three legs, one for each phase of the output. There are two electronic switches per bridge arm of the inverter. The design of inverter-driven motor drive therefore consists of selection of the three-phase rectifier, the DC-link capacitance, power electronic switch, and the drive circuit. This is done in relation to the specification of the load that is going to be fed from the inverter.

One of the key design considerations in inverter design is the selection of the power semiconductor device to use for switching. These power electronic switches enable the inverter to output an ac voltage or current by switching on and off a DC power voltage or current. First, there is commonly the thyristor and transistor switches, with transistors having the advantage of not requiring commutating techniques like their counterparts [88]. These transistor switches include the Insulated-Gate Field-Effect Transistor (IGBT), power Metal-Oxide-Semiconductor Field-Effect Transistor (MOSFET), GTO or SCR [89]. The choice of which transistor switch to use is determined by the specific attributes of the switch and the requirements of the application.

GTOs have a higher switching speed than BJTs while MOSFETs offer higher voltage and current handling capabilities, making them suitable for high power applications. However, their drawback is their high conduction losses. On the contrary, an IGBT, like a MOSFET, has high switching speed capability, but is not suitable for high voltage and high current applications. This means it has relatively low conduction losses like that of a BJT but with an advantage of high speed, making it suitable for use at relatively high frequencies [88], [90]. Given that the rated current of the test motors is 1.85 A, an IGBT will be used as the switching device in this work.

As it will be shown in the ensuing section, the expected DC-link voltage is around 475 V. So, the IGBT should be able to block a voltage as high as 475 V when it is off and should be able to conduct 1.85 A without excessive heating or destruction. The standard SKM 50 GB 123 D Semikron IGBT modules, shown in Fig. 5.2, is used in this work.

Fig. 5.2: Semikron IGBT modules

These modules have maximum reverse blocking voltage of $V_{CES} = 1200\ V$ and rated collector current of $I_C = 50\ A$. It can therefore be safely used in this application as the load current and DC-link voltage are sufficiently lower than the ratings of the device.

Each switch is tested separately before combining to form the inverter. To test the upper switch, S5 on the third bridge arm, the circuit was connected according to the schematic of Fig. 5.3(a). The gate of the bottom switch (S2) is pulled to its source to ensure that it is turned off. A resistive load (R = 10 Ω) is connected in parallel with this off switch and in series with the switch to be tested (S5). This combination is connected across a 15 V DC supply. The gate of the top switch is supplied with square wave of 5 V from a signal generator. The load voltage is monitored.

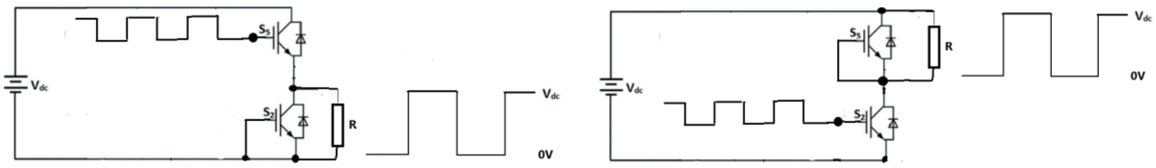

(a) **(b)**

Fig. 5.3: The schematic of a circuit used to test **(a)** top, and **(b)** bottom switch.

Likewise, to test the bottom switch, the circuit is connected as in schematic of Fig. 5.3(b), in which the top switch is kept off by pulling its gate to its source. The resistive load is connected in parallel to this gate and in series with the switch to be tested (bottom switch). Fig. 5.4(a) shows the actual circuit used to test the top switch. The load voltage, Fig. 5.4(b), is a square wave of the same frequency as the gate signal and of amplitude of 12.2 V. The difference (15 V – 12.2 V) can be associated with the voltage drop across the switch.

Fig. 5.4: **(a)** Experimental set-up for testing the top switch, **(b)** Load voltage

B. Selection and Sizing of DC-link Capacitance

Another important aspect in inverter design is the selection of the DC-link capacitance. Usually, an inverter has two capacitors connected in series and shunted across the power electronic switches. Different design approaches to select the value of the capacitance are available in the literature. Some designs go as far as enforcing the ½ line cycle hold over requirement – the drive must continue to operate smoothly even if the input power is interrupted for one half cycle [91]. Some designs put an emphasis on the size of the DC ripple current. On the contrary, this work selects the capacitance based on a predefined worst case ripple voltage. First, infinite capacitance is assumed and then the ripple voltage of the capacitor is determined. It is common knowledge that large capacitance exhibits low voltage ripple.

For a 3-phase load of 190V connected at the output of the inverter, assuming ideal switches, the required DC-link, Vdc, voltage is given by:

$$V_{dc} = \frac{2\times\sqrt{2}\times V_L}{\sqrt{3}\times M_a} = \frac{2\times\sqrt{2}\times 190V}{\sqrt{3}\times 0.85} = 365V \qquad (5.1)$$

where, M_a is the modulation index, and V_L is the line-to-line voltage. The modulation index is a constant defined as the ratio of the modulating/reference signal to the carrier signal. Its significance on the performance of the inverter will be explained in succeeding sections of this chapter. In this work, the modulation index at steady state is fixed at 0.85.

Taking 30% safety factor to increase reliability and catering for the voltage drops from the switches, the DC-link voltage can be taken as 475 V. Allowing the worst-case ripple voltage at 5%, then ripple voltage is 23.75 V. At a switching frequency of 8kHz, the DC-link capacitance can be calculated as [92],

$$C = \frac{V_{dc}}{32 \times L \times \Delta V \times f_s^2} = \frac{475}{32 \times 0.025146 \times 23.75 \times 8000^2} = 388.35\, nF \qquad (5.2)$$

Consequently, each capacitor should have a minimum value of $C_1 = C_2 = 776.7\, nF$. The Semikron model consists of two FELSIC 85/S 450V 3 300 μF capacitors connected in series as shown in Fig. 5.5. These capacitors are larger than the minimum capacitance required and therefore may be used in this application.

Fig. 5.5: DC – link Capacitors

C. Selection and Testing of Power Rectifier

The bridge rectifier is selected based on its rectified average current, I_D, and maximum reverse blocking voltage, V_D. As shown in the preceding section, the DC-link voltage is 475 V, therefore the rectifier's maximum reverse blocking voltage should be greater than this value. Likewise, the rated load current of the motor is 1.85 A, hence, the rectifier's rated average current needs to be greater than this. The selected Semikron inverter uses a Power Bridge Rectifier SKD 50/16 A3 module, which is shown in Fig. 5.6. The maximum blocking voltage of this module is V_D =1600V while its rated rectified average current is I_D = 10A, which are well above the values required. Therefore, this rectifier meets the requirements for this application.

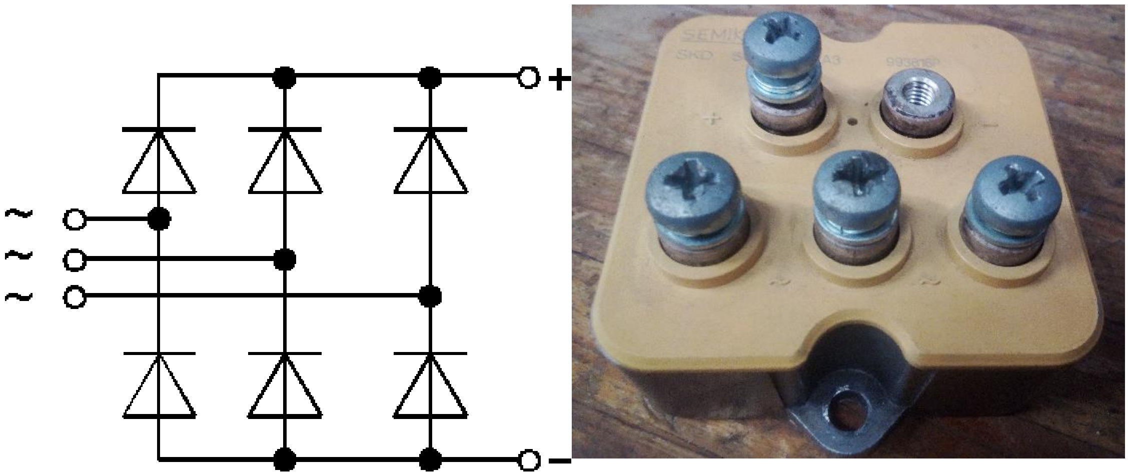

(a) **(b)**

Fig5.6: Full wave bridge rectifier SKD 50/16 A3 **(a)** schematic, **(b)** module

D. IGBT Gate Driver Circuit

The gate driver is a circuit that connects the low voltage from the microcontroller, containing software and system logic, to the requirements of the power module – IGBTs, MOSFETs, etc. To turn-on an IGBT, its gate capacitance must be charged so that current flows from its collector to emitter. The switch does not turn on until its gate capacitance charges up to a minimum turn-on voltage.

In this work, the output of the controlling microcontroller is 3.4 V, while the minimum turn-on voltage of the Semikron SKM 50 GB 123 D IGBT module is 15 V. The Semikron SKHI 21 9512 IGBT driver circuit was used to increase the output of the microcontroller to 15 V so that the generated PWM can turn the IGBT modules on and off. Each driver circuit controls two switches, the top and the bottom switch on the same bridge arm.

5.3.3 Assembly of the Main Controller Components

Once the individual components and modules have been selected and successfully tested, they were assembled to form a single subsystem – the VFD controller assembly, as shown in Fig. 5.7. These are then mounted onto a heatsink with a cooling fan for regulating thermal stress on the controller's submodules in high powered applications. Since this is a low powered application, the cooling fan was not used. As shown in the figure, this subsystem has one input – the standard three-phase grid voltage and one output, the controlled/regulated three-phase voltage. The three-phase input is at the input terminals of the rectify and the output is at the inverter terminals.

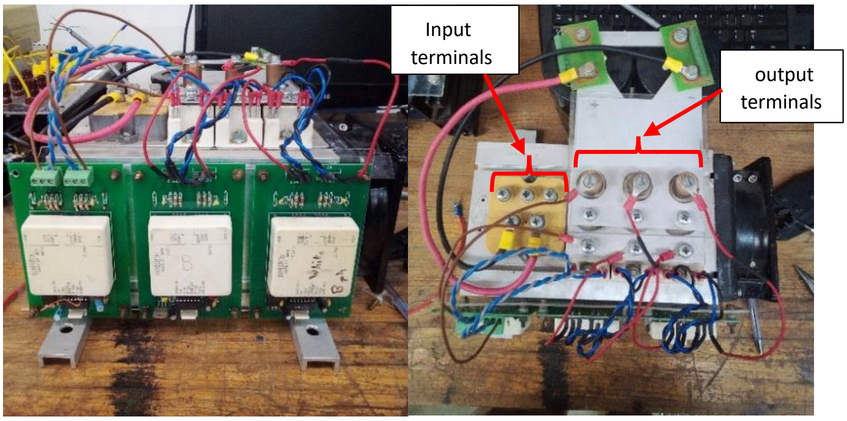

(a) **(b)**

Fig. 5.7: **(a)** Front-view and **(b)** top-view of the VFD Controller Assembly

5.4 Inverter Output Filtering

This section looks deeper into the aspect of filtering the output of the inverter. It commences by highlighting the necessity to filter the inverter output currents and voltages before impressing them onto the induction motor. It then gives a brief overview of the filtering options available in the literature, before finally designing a three-phase second-order low-pass sinusoidal LC filter for this application.

5.4.1 Need for Filtering the Output of a 2-Level Inverter

The use of three-phase power inverters in variable speed drive systems has several advantages as already mentioned in earlier chapters. However, inverters intrinsically bring some complications of their own and therefore, the overall drive system design should be able to redress such shortcomings imposed by the inverter. Firstly, the fast switching of the dc-link voltage by the electronic switches results in high dv/dt at the ac-side terminals of the inverter. The prominence of this phenomenon in most recent applications is premised on the devising of silicon carbide (SiC) power MOSFET switches which are technologically more enticing than the commonly used silicon (Si) power MOSFET. The former exhibits faster switching transitions than the latter [93]. If the inverter output is directly connected to the induction machine, the fast-changing voltage leads to the inception of several stray capacitances – capacitance between stator and frame, between rotor and frame, between stator and rotor, and capacitance of the bearings.

Electromagnetic interference (IEM) also manifests in the connected induction motor owing to the fast turn on-and-off of the switches. IEM manifestation is two-fold as shown in Fig. 5.7 [94]: common-mode IEM, blameworthy for the flow of large shaft currents (currents between motor windings and the shaft), and differential-mode IEM, giving rise to overheating of the motor [94]. Therefore, IEM resulting from high dv/dt, subjects the machine windings to high thermal stress, which could lead to insulation breakdown. It also produces current paths between the motor and ground through the bearings, by breaking down (electric discharge of) the dielectric fluid in the bearing housing. This bearing current leads to bearing damage.

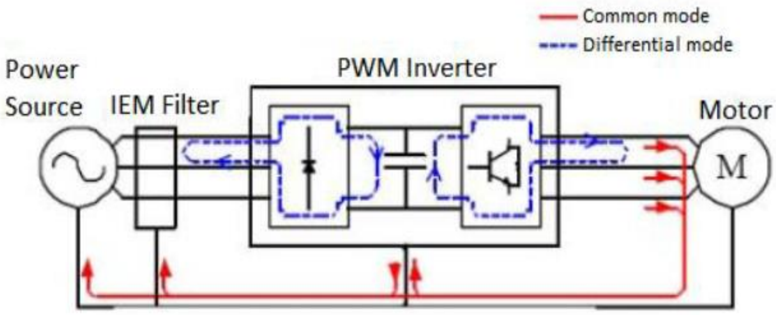

Fig. 5.7: Circulating paths of common and differential modes high frequency currents

Apart from the electrical and thermal stresses, the raw inverter output also subjects the machine to increased mechanical stresses. Since the inverter output voltage consists of square pulses, the motor current produced is not a smooth sinusoid, but has a high noise content due to switching. Consequently, the motor torque developed has a ripple or an oscillating component at the switching frequency. This breeds additional losses and acoustic noise [95] and increases mechanical stress on the machine.

Sometimes, the induction motor and the VSI are separated by a large distance, such that a long connecting cable is required. Given the impedance imbalance between the cable and the motor, voltage reflection is observed throughout the length of the cable, resulting in over-voltages of up to twice the dc bus voltage [96], or even more at the machine terminals. This overvoltage scenario increases electrical stress on the machine, leading to the aggravation of insulation breakdown, whether ground wall (winding to core frame) insulation or winding (turn-turn) insulation. These problems, however, can be reduced by connecting the output of the inverter to the machine through a filter. The filter design should take into consideration the effects of the connecting cable, if the cable is long enough that its effects cannot be ignored.

5.4.2 Three-phase Filter Options

Three common types of filters include active filters, passive filters, and hybrid filters [97]. As the name implies, hybrid filters are made of several active and passive filters. Passive filters use passive elements like resistors, inductors, and capacitors to reject unwanted signal components or to modify a signal. Likewise, active filters still modify the signal or attenuate an unwanted component of the signal. However, active filters use active elements such as transistors and operational amplifiers to achieve this. They may in addition use capacitors and resistors but never inductors. Passive filters are more suitable for high power applications and are cheaper as they are made of only passive elements, and ideally have no power consumption, as opposed to active filters. Passive filters also do not require dc power supplies in addition to the input signal, as do their active counter parts. The most popular passive filter configuration proposed in the literature is the (three-phase) second-order low-pass sinusoidal LC filter [93]. The literature also provides the numerous methods of designing the LC filter, in which the inductor (L) is connected in series with the motor and the capacitor (C) is shunted. Different methodologies investigate different aspects of the design process such as cost optimization, size of the filter, losses in the filter, effects of the filter capacitor on the drive system and many others.

5.4.3 Three-phase Second-Order Low-Pass Sinusoidal LC Filter Design

In this work, the standard LC filter design method, as outlined in [93], is used. In this method, the first step is to determine the size of the per phase filter inductance L. This is done by considering two important aspects: the size of the ripple current, Δi_{inv}, through L and the size of the voltage drop, v_L, across the inductor. In this criterion, the maximum ripple current is limited to less than 25% of the peak value of the ac-side inverter current, i_{inv}. The inductor voltage drop at rated inverter current and rated frequency is limited to less than 3% of the motor voltage. So, the governing equations are:

$$\Delta i_{inv} = \frac{V_{dc}}{8 \times f_s \times L} \tag{5.3}$$

$$v_L = i_{inv}\left(\sqrt{R^2 + (2\pi f_s L)^2}\right) \tag{5.4}$$

where, f_s denotes the switching frequency, and R is the resistance of the inductor coil. Taking the peak ac-side inverter current i_{inv} to be equal to the peak rated current of the motor, $\sqrt{2}\,I$, and considering the ripple current to be 20% of this, we obtain the expression for filter inductance as

$$L = \frac{V_{dc}}{8 \times f_s \times \Delta i_{inv}} = \frac{V_{dc}}{8 \times f_s \times 0.2 \times \sqrt{2} \times I} \tag{5.5}$$

Therefore, L = 10.9 mH for dc-link voltage of 365 V, switching frequency of 8 kHz, RMS motor current of I = 1.85 A. Three inductors with L = 9.5 mH and R_f = 0.6 Ω were used for this project. Thus, at rated current, the v_L = 1.11 V, which is 1% of the operating voltage of the motor, and less than the 3% limit.

To calculate the filter capacitor, the power circuit in Fig. 5.8 was used. In this circuit, rotor leakage reactance, L_{1r}, stator leakage reactance, L_{1s}, filtering inductance, L, and filtering capacitor, C, are used.

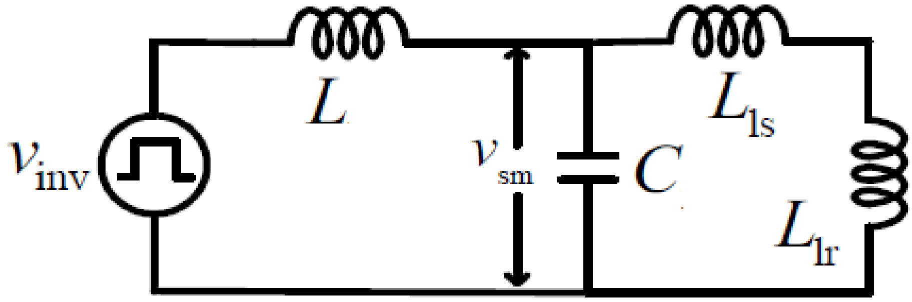

Fig. 5.8: Power circuit for calculation of filter parameters [93]

From this circuit, it follows that the expression for the resonance frequency can be expressed as:

$$f_{res} = \frac{1}{2\pi\sqrt{L_{eq}C}} = \frac{1}{2\pi}\sqrt{\frac{L+L_1}{LL_1C}} \tag{5.6}$$

Here, $L_1 = L_{1s} + L_{1r}$, and L_{eq} is the equivalent inductance as seen by the filtering capacitor. To avoid the resonance problem, the resonance frequency should be far enough from both the switching frequency and the fundamental frequency. A resonance frequency that is more 10 times away from the fundamental frequency will suffice for this work. If it chosen to be 560 Hz, which is far enough from the switching frequency, with the stator leakage reactance (L_{1s}) = rotor leakage reactance (L_{1r}) = 12.57 mH, the filtering capacitor is calculated as $C =$ 10.63 μF. This capacitance was achieved by connecting two 22 μF 450 V capacitors in series. The filter was then built and is shown in Fig. 5.9.

Fig. 5.9: Three-phase Second order LC Filter

5.5 Modulation Scheme and Microcontroller Choice

5.5.1 Modulation Schemes

Fundamental to all VFDs is a technique called the pulse width modulation (PWM), which is premised on varying the width of a fixed signal by modulating pulse duration to constitute a variable analogue signal. In VFDs, PWM is applied to the fixed DC-link voltage across the DC bus capacitors. The pulses are produced by means of fast switching of semiconductor devices like the IGBTs or MOSFETs. As shown in Fig. 5.10, through variation of the pulse widths in the output voltage waveform, an AC sine wave can be constructed [36].

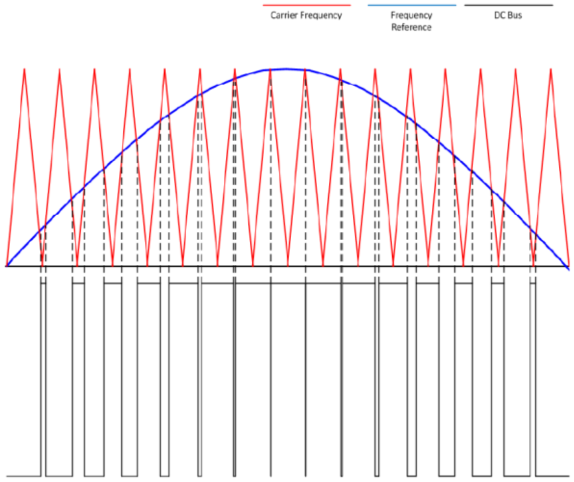

Fig. 5.10: Pulse width modulation technique [36]

It is observed in Fig. 5.10 that while the DC bus voltage is fixed, the output voltage waveform embodies square waves. However, since AC motors are inductive, the waveform of the current drawn by the motor will be sinusoidal [36].

To control the output voltage of an inverter and to reduce its inherent harmonic content, different modulation strategies are applied. These include among others the sinusoidal pulse width modulation (SPWM), space vector pulse width modulation (SVPWM), third order harmonic injection pulse width modulation (THIPWM) and selective harmonic elimination (SHE). In essence, these modulation schemes control the switching of the electronic switches to obtain the desired amplitude and frequency of output voltage with the desired quality. Their objective is to make the output voltage as close as possible to a sinewave while suppressing its harmonic content. The selection of a modulation technique depends on the specific requirements of the application and the merits of the individual technique. These merits include harmonic content in the output of the inverter (THD), DC bus voltage utilization, resulting common mode voltages and ease of implementation among others [98], [99].

In this work, two candidate modulation strategies were considered, the SPWM and SVPWM, because of their ease to implement and effectiveness. In SPWM, a sinusoidal voltage waveform is produced by filtering an output pulse waveform with varying width [100]. As shown in Fig. 5.11(a) [101], SPWM is realized by comparing a high frequency triangular signal – called the carrier signal – of amplitude V_c and a sinusoidal signal – called the reference/modulating signal – of amplitude V_r. The points of intersection of these two signals mark switch transition instants. The ratio of the amplitude V_r to V_c is called the modulation index, denoted by M_a. The modulation index controls the amplitude of the output voltage while the frequency of the reference signal determines the frequency of the output voltage signal.

On the contrary, in SVPWM as shown in Fig. 5.11(b), the desired three-phase voltages at the inverter output (reference voltages) could be represented as a rotating vector, rotating in the anti-clockwise direction [99]. The SVPWM uses this rotating synchronous reference frame to produce a special switching sequence of the three top switches. It is realized by first transforming voltages in the conventional abc reference frame to voltages in the stationary dq reference frame consisting of the vertical and horizontal axis [100] as shown in Fig. 5.11(a).

To decide on which one of these two modulation strategies to use in this work, a model of an inverter-fed squirrel cage induction motor was built in MATLAB/Simulink. The machine ratings and machine parameters were chosen to match those on the nameplate ratings of the test motors in the laboratory and their parameters as determined from the no-load test, blocked rotor test and the spin down test conducted on these machines. A 2-level, 3-legged and six-switch inverter was also built from six standard IGBT blocks available in Simulink. Two switching frequencies were considered: 5 kHz and 8 kHz. The modulation index remained fixed at 85%. They were assessed based on the THD in the output signals. The results are summarized in Table 5.3. Detailed results presentation and analysis will be presented in Chapter 7 of this report. Hence, SVPWM was chosen as the main modulation strategy in this work and 8 kHz switching frequency was used since they produced low THD.

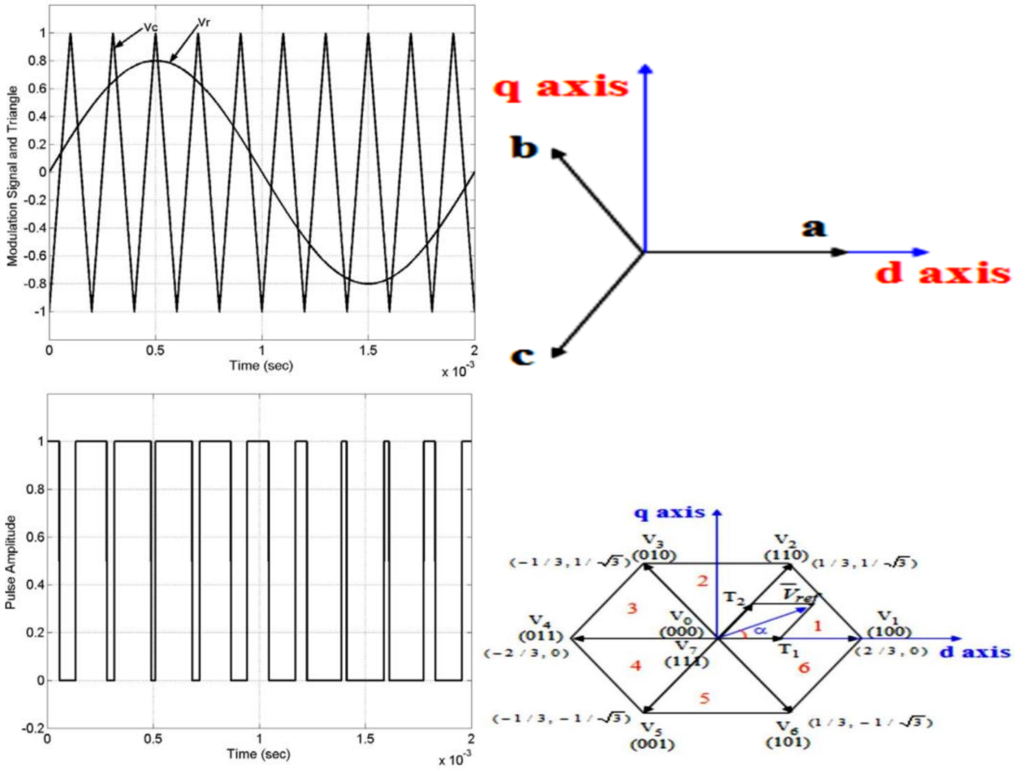

(a) **(b)**

Fig. 5.11: **(a)** SPWM and **(b)** SVPWM implementation

Table 5.3: THD comparison in SPWM and SVPWM at 5 kHz and 8 kHz

Switching Frequency	**Parameter**	**Total Harmonic Distortion (THD) (%)**	
		SPWM	SVPWM
5 kHz	Modulating signal	0.00	20.80
	Inverter voltage output	72.22	54.63
	Inverter current output	5.08	4.71
8 kHz	Modulating signal	0.00	20.80
	Inverter voltage output	64.56	49.08
	Inverter current output	3.87	3.75

5.5.2 TI C2000 F28335 Microcontroller and PWM Generation

In this work, the microcontroller TI C2000 F28335 is used. MATLAB embedded coder for the F28335 was used to enable programming and configuring the microcontroller in Simulink. It has enhanced pulse width modulator (ePWM) peripheral – a key element in generation of PWM. The ePWM peripheral performs a digital to analog (DAC) function, and the duty cycle is equivalent to a DAC value. F28335 has six (6) ePWM modules, and each module has two (2) ePWMs, A and B. So, in total, there are 12 ePWMs – ePWM1A, ePWM1B, ePWM2A, ePWM2B, …, ePWM6A and ePWM6B. Since the 2-level inverter used here has only six switches, only six ePWMs are used, ePWM1A to ePWM3B.

Fig. 5.12(a) shows one ePWM module of the microcontroller, showing constituent submodules which play critical roles in producing a PWM. The time-base submodule determines all the event timing for the ePWM module, and built-in synchronisation logic enables the time-base of multiple ePWM modules to work together as single system.

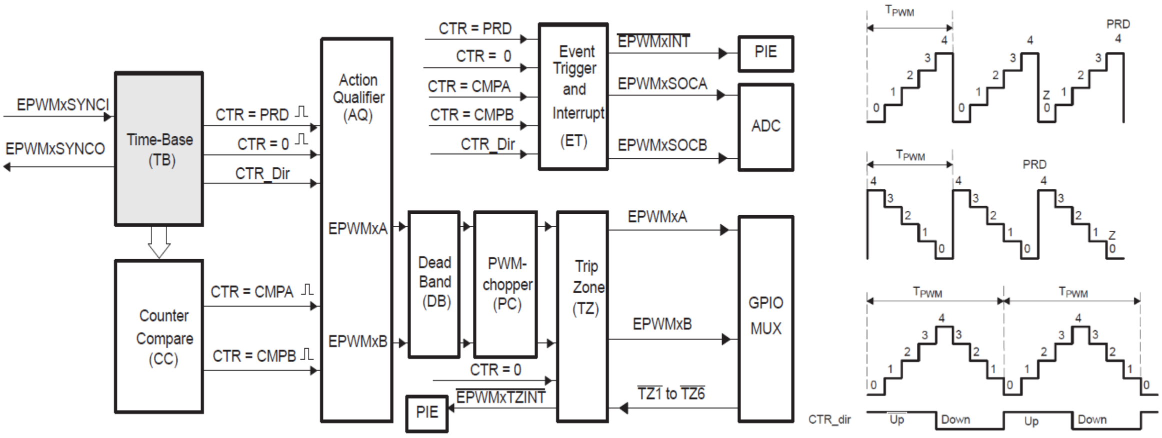

(a) **(b)**

Fig. 5.12: **(a)** ePWM module and **(b)** Counting modes of F28335

To produce the carrier triangular wave, the switching period or frequency is first set. The timer counter counts from zero to the period. F28335 offers three counting modes, as shown in Fig. 5.12(b). There is the up-count, down-count and up-down-count modes. The choice of which mode to use is application based. This work uses up-down-count mode. The counter compare submodule takes as input the time-base counter value and continuously compare it to the counter-compare A (CMPA) and counter-compare B (CMPB) registers. An appropriate event is generated by the counter-compare unit when the time-base counter is equal to one of the compare registers. So, the reference signal values are stored in the counter-compare registers and compared with time-counter (which constitute the triangular carrier signal), to generate PWM duty cycle if the action-qualify submodule is configured appropriately. The action-qualify module qualifies and generates actions like set, clear or toggle, based on values stored in the counter-compare registers relative to the time-counter values. The configuration of the ePWM modules for the different tests is shown in Appendix A3.

5.6 Open Loop V/F Control and Its Implementation

This control method was reviewed in detail under the literature review (section 2.2.3). It was deduced from equation 2.6 that the electromagnetic torque developed by the motor increases with increasing voltage supply and decrease with increasing supply frequency. It was deduced that to ensure high efficiency and prevent driving the machine into saturation, both voltage and frequency should be changed proportionately to control the speed and torque of the motor. The ratio of V and f should be kept constant for all frequencies so that the flux that produces maximum torque can be established. Fig. 5.11 [37] shows the voltage vs frequency change under this type of control.

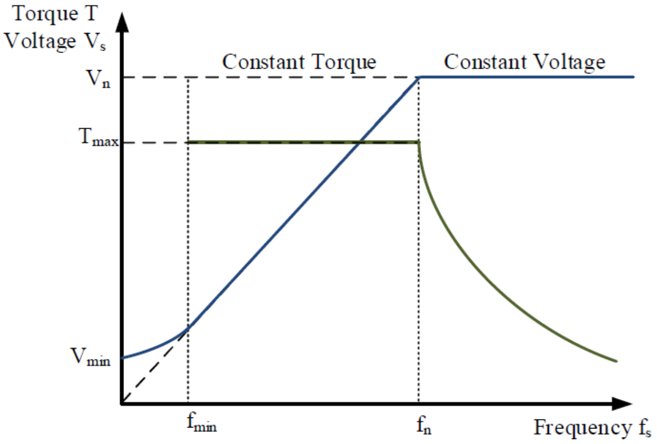

Fig. 5.11: Voltage/frequency characteristics

If the frequency is reduced to reduce the speed of the motor, then flux will have to increase to keep the induced emf the same. This drives the machine into saturation. Contrarily, if the frequency increases to increase beyond rated frequency, then the weakening of the magnetic field occurs, causing reduction in torque as shown in Fig. 5.11. It is also noteworthy that there is a minimum voltage and frequency below which a voltage higher than the specified V/f ratio need to be applied to the motor to cater for the voltage drop across the windings.

In this work, the open loop V/F control system is developed in MATLAB/Simulink environment in conjunction with F28335 microcontroller. The frequency of the reference voltages was ramped from 0 Hz to 50 Hz and limited at this value as the rated operating frequency. As the frequency of the reference voltage increase, their amplitudes increase proportionately, such that V/F is kept constant at 25 V/Hz. The diagram of this system as constructed in MATLAB/Simulink is shown in Appendix A3.

5.6 Concluding Remarks

This chapter looked at the design and development of a variable speed drive system for fault studies. It looked at the design of the VFD controller assembly along with the design of the interfacing three-phase filter. It also described how the modulation scheme used in this work was decided upon and the features of the microcontroller used. Finally, it described the implementation of the open loop scalar (*V/F*) controller for the VFD. The next chapter will describe the methodology and the test procedures used.

Chapter 6: Methodology and Test Procedures

6.1 Introduction

In this work, tests are performed on the three-phase squirrel cage induction motor and on a 2-level three-phase inverter. This chapter outlines experimental set-ups and procedures of the various tests carried out, equipment used, and data acquisition and processing procedure. The MFS-MG rig is used for the MCSA tests for both grid-connected and inverter-fed motors. It is also used to implement standstill impedance variation test for the inverter-fed motor. The standstill impedance variation test for the grid connected motor is implemented on a separate set-up.

6.2 Online Fault Diagnosis with MCSA

The schematic and the set-up for the online diagnosis with MCSA for both the grid connected and inverter fed motor is as shown in Fig. 6.1 and Fig. 6.2 respectively. The induction motor can either be fed from the grid or from an inverter by means of a toggler switch on the control panel.

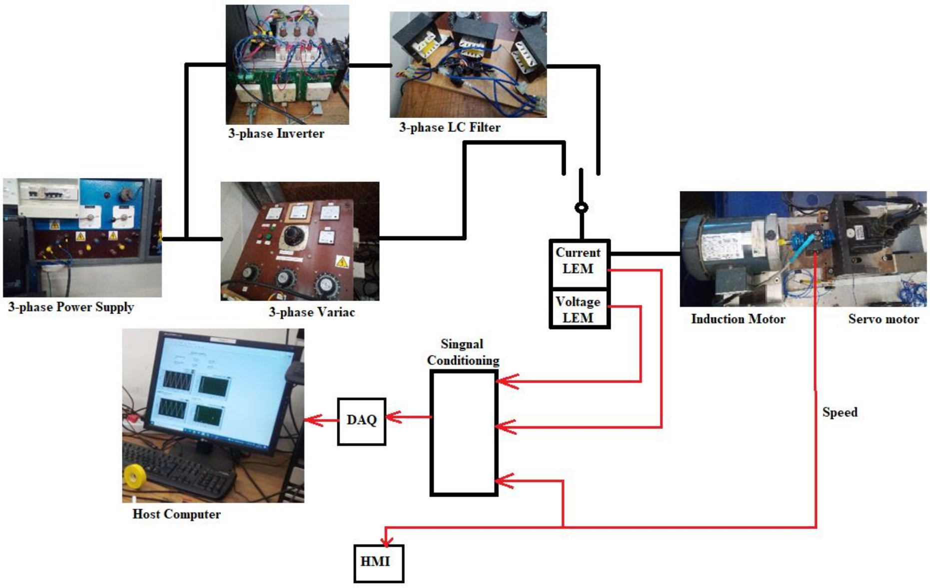

Fig. 6.1: Schematic of the set-up for Online Diagnosis with MCSA

For the grid-connected case, the motor is soft started using a three-phase variac (autotransformer). In the inverter case, a three-phase filter interfaces the inverter with motor. Current and voltage LEM modules are used to measure the voltage and current signals fed to the motor. The measured shaft speed, voltage and current signals are conditioned and captured by the DAQ modules, which send them to the host computer for observation and storage.

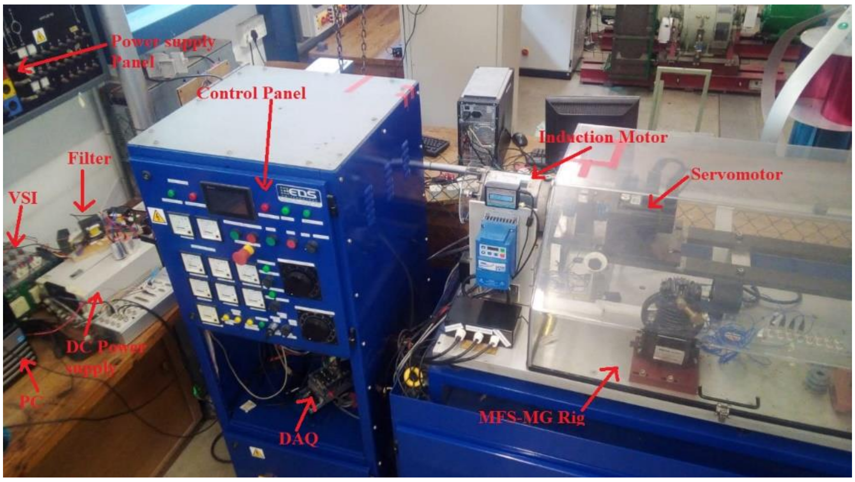

Fig. 6.2: Set-up for Online Diagnosis with MCSA

6.2.1 Instrumentation and Data Acquisition

A. Analog to Digital Converter

The data for analysis was captured using the National Instruments CompactDAQ system – a portable system that allows the connection of modular I/O such as the NI 9215 Differential Analog Input Module. The module has four differential inputs with $\pm 10V$ range. It can capture up to capture 100 000 samples per second at 16 Bit resolution, simultaneously [102]. Fig. 6.3 shows a schematic diagram of the input module.

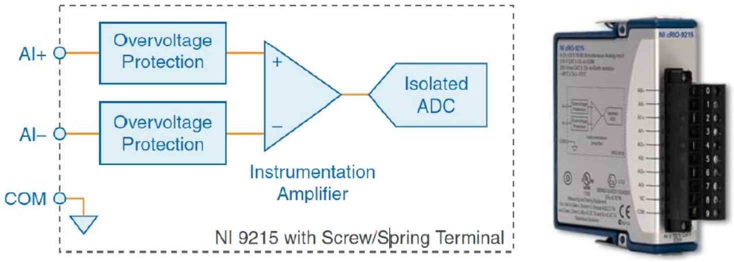

Fig. 6.3: NI9215 Analog input module [102]

This CompactDAQ system is able to connect directly to a host computer through a USB interface. In this work, LabView software tool was used to configure the three NI9215 modules and to record and visualize the data. The inputs of the motor that were measured are:

- Line voltage - v_{ab}
- Line voltage - v_{bc}
- Line voltage - v_{ca}
- Line current A - i_a
- Line current B - i_b
- Line current C - i_c
- Shaft torque - T
- Shaft speed - n
- Inverter frequency f_{inv}

The system samples at 25.6 kilo-samples per second, and the acquisition time is set at 30 seconds. Consequently, the system captures 768 000 data points per channel. The LabVIEW virtual instrument block diagram (code) used is shown in Appendix A4.

B. Voltage and Current Measurements

LEM LV25-P Hall effect voltage transducers were employed to measure the three (3) line voltages supplied to the motor. Likewise, for the three (3) line currents, measurement was done using LEM LA25-NP hall effect current transducers. These transducer outputs are then fed into an anti-aliasing low pass filter circuits after being biased to a $\pm 10V$ range. The cut-off frequency of the anti-aliasing low pass filter is 12 kHz, which is less than 50% of the sampling frequency as per Nyquist theorem. As the name suggests, this filter rejects frequencies above the range of interest. Finally, the resulting voltage inputs are calibrated and linearized using in LabView DAQ assistant function, and thus obtaining voltage and current measurements in units of Volts and Amperes.

C. Speed and Torque Measurements

Speed can be measured using either the digital tachometer or the pulse encoder. In this work, shaft speed was measured using the 20-bit rotary incremental shaft encoder of the coupled servo motor drive because it is more accurate. The encoder was set to output the maximum of 128 000 pulses per revolution, which is the highest resolution it can provide. This was achieved by using the servo drive configuration software. The voltage signal, obtained from the encoder and representative of the shaft speed is fed into NI9215 module in a similar way with the voltage signals for the measured current and voltage.

On the contrary, the motor shaft torque was measured directly using an inline Lorenz DR-2112 Torque transducer. The output of the transducer was fed into the analog input module of the data acquisition system.

6.2.2 Data Processing

For data processing, the captured data was processed using MATLAB2019a. The MATLAB code imported the data from a text file and applied the signal processing techniques – FFT and PSD – to the stator current. The different MATLAB codes produced for this study can be found in Appendix A2.

6.2.3 Test Motors

The SpectraQuest test rig is supplied with several intentionally faulted induction motors. All the motors are 3 phase, Class B and have identical ratings as detailed in Table 5.1 and Table 5.2. In this work, only two test motors were used: the healthy motor, which was used as a benchmark for diagnosing the faulty motor, with the broken rotor bars, which has a total of 34 rotor bars, 3 of which are intentionally broken, to create the broken rotor bar fault for fault diagnosis studies [103].

6.2.4 Motor Supplies and Loads

A. Grid versus Inverter supply

The squirrel cage induction motor under test can be connected to the grid/mains supply through a variac or it can be fed through an inverter. The mains voltage in the laboratory is 380 V but the motor is only rated for 190 V. Therefore, the variac is used to control this voltage to obtain the necessary rated voltage by soft starting the motor. The selection between the grid (through the variac) and the inverter is made by means of a selector switch on the drive interface control panel. The connection of these supplies to mains supply (on the wall) is through an earth leakage and isolator.

As already described in the previous chapter, the inverter, constituting one of the subsystems making up the VFD controller assembly, was configured and used in the constant-volts-per hertz operating mode as explained in section 5.6.2.

B. Resistive Load Versus Servo Load

The induction motor can be loaded in two ways, both of which require the operation of the servo machine and servo drive. Firstly, there is a resistance controlled variable load. This loading type is introduced to the motor by rectifying the servo machine outputs and dissipating the resulting dc current through the variable resistor mounted on the drive interface control panel.

Alternatively, there is loading through the servo machine in closed loop control. In this type of loading, the drive is selected to control the torque via the servo system's HMI (Human Machine Interface). The required load level is selected by inserting a negative torque in the HMI. The regenerative energy built up by the servo machine is dissipated through an external 1kW regenerative resistor [97].

In this study, the former loading method was used. The motor was loaded to four levels during the various tests according to the following table:

Table 6.1: Percentage loading and the corresponding shaft torque

Load (%)	Torque (Nm)
0	0
50	0.416
75	0.625
100	0.8329

6.2.5 Experimental Methodology

A. Baseline Conditions

Motor warm-up

The test motors were each operated at no load for a period of 10 minutes before any test can be carried out on the motor. This was done to allow the motor and drive components to reach thermal stability.

Laboratory Electrical Supply

The laboratory supply connected to the drive control interface panel was checked for balance through the use of a power analyzer. Individual phases were adjusted using a three phase variac to supply the rated voltage to the motor.

B. Experimental Procedure

The detailed experimental procedure for performing experiments to simulate and detect the broken rotor bar fault using MCSA is shown in the Appendix A1 section of this report.

6.3 Standstill Impedance Variation Test

The standstill impedance variation test was performed for both the grid connected motor and inverter fed motor. The following sections outline the experimental and testing procedures for these two cases.

6.3.1 Standstill Impedance Variation Test – Grid connected motor

The schematic and test set-up for the standstill impedance variation test for the grid connected motor is as shown in Fig. 6.4 and Fig. 6.5 respectively. In this test, the phases A and B of the induction motor are manually shorted at the end of the connecting cable and a single-phase voltage was impressed between phase A and C. This single-phase voltage was supplied through California Instrument Programmable Power Supply. The power supply is programmed to output a single-phase output voltage, which is connected between phase A and C of the motor through a 4.98Ω resistor. Two voltages are measured: the output voltage of the power supply and the terminal voltage of the motor. The difference between these voltages is the voltage drop across the connecting resistor and is used to calculate the motor current under this configuration.

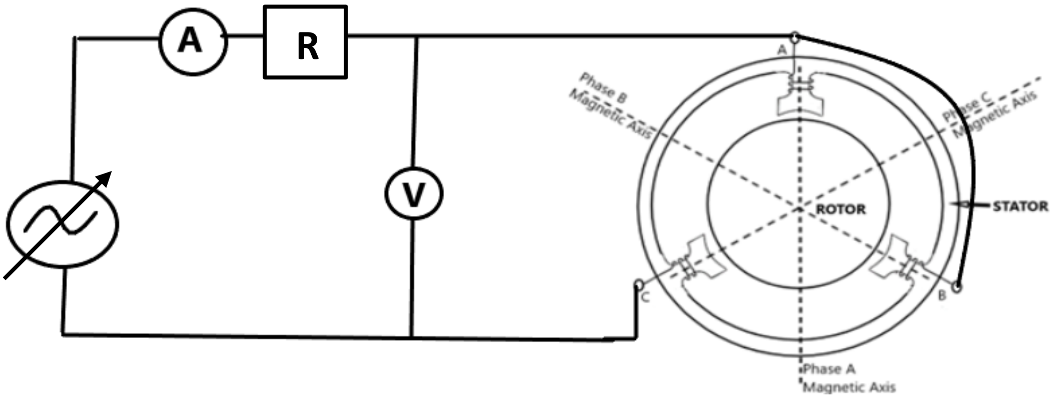

Fig. 6.4: Schematic for the grid standstill impedance variation test

The rotor angle/position is varied manually by physically changing the rotor position in 10° from 0 to 360°. This was achieved by using a circular paper with angles marked along its circumference and inserted in the shaft and sticked to the motor near the bearing point. A pointer was firmly sticked to the shaft and rotated with it and pointed to the rotor angle on the paper with angles marked in. The detailed procedure of this set up is described in appendix A1.4 of this report.

Fig. 6.5: Set-up for Grid-connected Impedance Variation Test

A. Instrumentation and Data Acquisition

The only data measured is the voltage at the terminals of the machine (across the stator windings) and at the terminals of the power supply. This measurement is done using a NI DAQ device through a BNC cable. The NI USB-6366 device used here is an 8-channel X series multifunction signal acquisition device with a 16-bit resolution. It has analog inputs with ranges $\pm 1\,V$, $\pm 12\,V$, $\pm 5\,V$ and $\pm 10\,V$. It has high signal sampling rate of up to 2.0 mega-samples per second. To capture the two voltages needed for data processing, the two channels of NI DAQ were used whose inputs were from the voltage differential probes at the machine terminals and supply terminals. The DAQ device was configured in LabView. The voltage across the stator windings and the current signals were stored on the PC for processing. The LabView configuration code for the DAQ is shown in Appendix A4.

B. Data Processing

For data processing, the captured data was processed using MATLAB2019a. The MATLAB code imported the data from a text file and applied the FFT to both the voltage and stator current signals, before calculating the impedance at the rated frequency of 50Hz. The MATLAB code produced for this study can be found in Appendix A2.

C. Test Motors

This test procedure was done, as in the previous test, on the two class B squirrel cage induction motors, one which is healthy and the other one with intentionally broken rotor bars.

D. Fault Simulation Procedure

The procedure that was followed when performing the experiment for grid-connected standstill motor impedance variation test is outlined in the Appendix A1 section of this report.

6.3.2 Standstill Impedance Variation Test – Inverter fed motor

The schematic and experimental set-up for this test is the same as the one shown in Fig. 6.1 and Fig. 6.2 respectively. The only difference is that the inverter is connected to the supply through the variac for voltage control in order to limit the current flowing in the unshorted phase to the rated current of 1.85 A. The same instrumentation and data acquisition is used as that in Fig. 6.2. Also, in this test, the shorting of two phases is done through controlled switching of the controlling microcontroller. This is realized by simultaneously turning on any two top switches along with one bottom switch or vice versa. Simulink block diagram for the configuration of the ePWMs of the microcontroller are shown in the Appendix A3, along with the fault simulation procedure for this test in Appendix A1.

6.3.4 An Advancement of Standstill in Impedance Variation Test

For the standstill impedance variation test in inverter fed motors, it is possible to utilize the geometrical orientation of the three phase windings and manipulate the switching to change the axis of the pulsating flux instead of having to manually move the rotor. In this scheme, the rotor fixed at a known position, the axis of the pulsating flux is rotated by 120º to obtain three impedances. Then the rotor is then fixed at a different position and three different impedances are obtained. This is done until the rotor has rotated by 180º (which equates to one cycle of impedance variation). The fault simulation procedure and fault detection procedure for this test is shown in the Appendix A1. The Simulink block diagram for the configuration of the ePWMs of the microcontroller for the implementation of this test are also shown in Appendix A3.

6.4 Inverter Open Switch Faults

The experimental set-up for the implementation of open switch faults is the same as the one shown in Fig. 6.1 and Fig.6.2, except that in this test, the motor is supplied through the inverter throughout. The same instrumentation and data acquisition is used as that in Fig. 6.1. The open switch fault on a given switch is implemented by depriving that switch its gate drive voltage signal as was described in section 4.2.2. This is achieved by programming the microcontroller to start outputting a constant low on its output pin controlling the gate drive of the switch in question, at the intended occurrence time of the fault. So, initially, the motor would be running under healthy conditions until when the fault occurs. The detailed fault simulation, impact observation and fault detection procedures for these tests are included in the Appendix along with the associated Simulink block diagram for the configuration of the ePWMs modules of the microcontroller for the implementation of these faults (Appendix A3).

6.5 Concluding Remarks

This chapter presented experimental and testing aspects in online fault diagnosis with MCSA for both grid-connected and inverter fed motors, standstill impedance variation test for both grid-connected and inverter fed motors, inverter open switch faults with specific focus on their impacts on the performance of the connected motor as well as their diagnosis. It presented both the hardware and software used during the conduction of the tests. It discussed the experimental procedure used in each of the tests, as well as the fault detection procedure used. The next chapter presents the results of these experimental tests, and their counterpart simulation results.

Chapter 7: Results and Analysis

7.1 Introduction

This chapter presents both experimental and simulation results. There are some parts of the work where Simulink models are used to predict the response of the system prior to carrying out the experimental work.

7.2 Selection of Modulation Strategy and Switching Frequency

In selecting the modulation strategy and switching, the system was first modelled and simulated in MATLAB Simulink using different candidate modulation schemes and switching frequencies. The choice was made based on the resulting total harmonic distortion (THD) in the voltage and current signals. This section presents the description of the model used and the simulation results.

7.2.1 Description of the Simulated VFD system

The system was built in MATLAB Simulink. The induction motor was modelled with the standard asynchronous motor block found in MATLAB Simulink. A 0.6088kVA, 190V, 50Hz, 2-pole induction motor was used. The machine parameters were assigned as follows:

Stator resistance, R1 = 4.24 Ω, stator inductance, L1 = 12.573 mH
Rotor resistance, R2’ = 2.12 Ω, rotor inductance, L2’ = 12.573 mH
Mutual Inductance, L_m = 242.77 mH
Inertia factor were, J = 0.0016797 kgm^2 and,
Friction factor, F = 0.0010356 Nms

The machine ratings and parameters were chosen based on the name plate ratings of the test motors in the laboratory and their parameters as determined from the no-load test, blocked rotor test and the spin down test conducted on these machines.

A 2-level, 3-legged and six-switch inverter was also built from six standard IGBT blocks available in Simulink, and this was supplied from a constant DC voltage. The output of the inverter was connected directly to the induction motor, without a filter.

7.2.2 Modulation Scheme and Switching frequency

The choice of switching frequency was based on the sampling capabilities of the DAQ device in the laboratory and Nyquist theorem. The DAQ has a limited sampling frequency of 25600 samples/s and according to Nyquist theorem, the switching frequency cannot exceed 50% of the sampling frequency – 12.8 kHz. So, the minimum switching frequency was chosen to be 10 times the fundamental frequency. For practical consideration, the highest considered switching frequency needed to be less than that required by the Nyquist theorem. Consequently, a switching frequency of 5 kHz and 8 kHz were tested for their contribution in the distortion of the output current signal.

Regarding modulation scheme, two candidate modulation strategies were put to test and assessed based on the resulting total harmonic distortion in the inverter output voltage and current. These were the sinusoidal pulse width modulation (SPWM) and the space vector pulse width modulation (SVPWM). In each case, the induction motor, the inverter topology, and the frequency of the triangular carrier wave remained fixed, with the only change being the modulating/reference signal. Likewise, the modulation index remained fixed at 85%. The simulation was repeated for both 5 kHz and 8 kHz switching frequencies.

Fig. 7.1(a) and (b) shows the FFT of the reference signals used in SPWM and SVPWM, respectively, at 8 kHz switching frequency. It shows FFT over one cycle of the signals, the frequency components present in the signals, and a measure of the amount of distortion in the signals (THD).

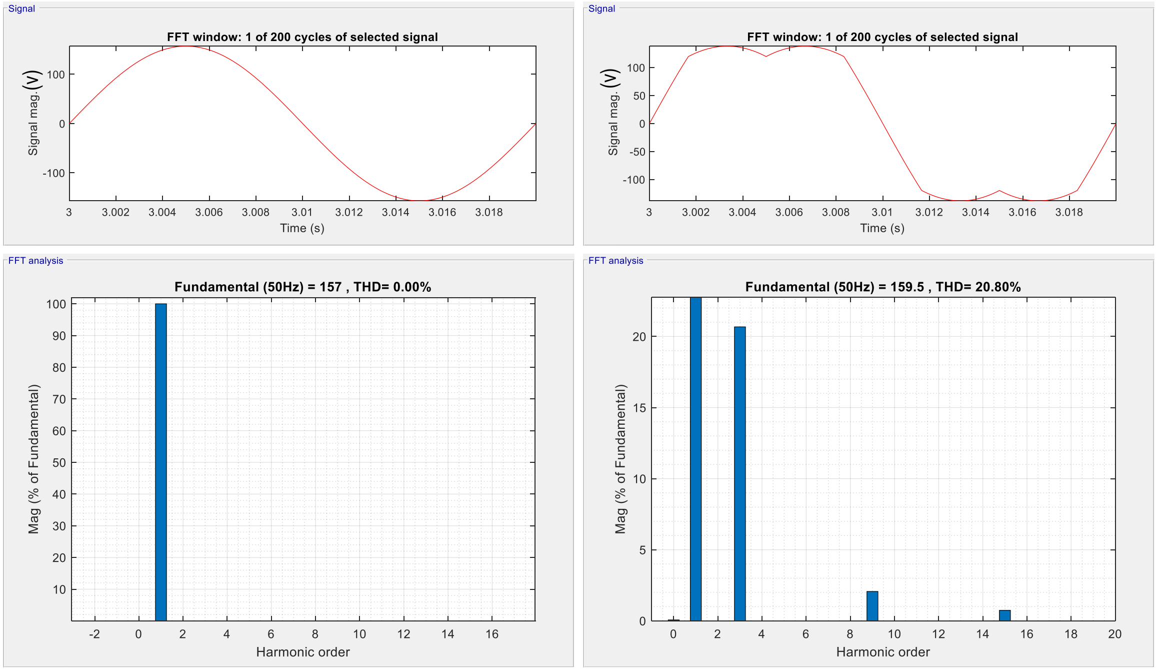

(a) **(b)**

Fig. 7.1: FFT of the modulating signal in **(a)** SPWM, **(b)** SVPWM

The reference signal in SPWM is a pure sinusoid with no distortion at all, since THD = 0.00%. On the contrary, in SVPWM, the reference signal is not a pure sinusoid. It has a special shape as seen in Fig. 7.1(b). In addition to the fundamental harmonic component, it has noticeable odd harmonic components – 3rd, 9th and 15th order harmonics, with 3rd order being the most dominant of the three. This give rise to a THD of 20.80%. The same results were obtained with a switching frequency of 5 kHz.

Likewise, Fig. 7.2(a) and (b) show the FFT of the resulting output phase voltages in SPWM and SVPWM, respectively, at 8 kHz switching frequency. It shows FFT over one cycle of the signals, the frequency components present in the signals, and a measure of the amount of distortion in the signals (THD). The FFT of the output phase voltage in SPWM shows that it has a fundamental component at 50 Hz and contains a lot of harmonic distortion, that amounts to a THD of 64.56% of the fundamental component. The dominant odd harmonics are the 5th, 7th and 11th order harmonics constituting 1.08%, 0.8% and 0.31% of the fundamental respectively. All these other harmonic components, though many, each contribute less than 0.2% of the fundamental component.

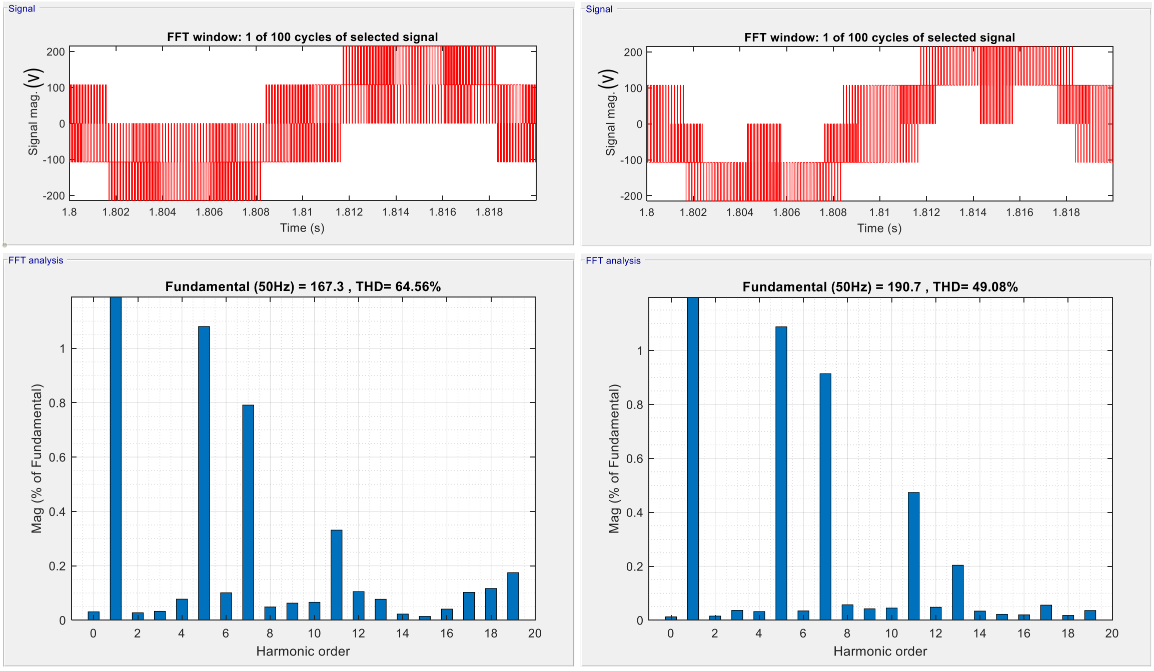

(a) **(b)**

Fig. 7.2: FFT of the inverter voltage output in **(a)** SPWM and **(b)** SVPWM modulation

On the contrary, the SVPWM modulated inverter output voltage still has fundamental component at 50Hz but exhibits a relatively lower harmonic distortion than in the case of SPWM. Here the THD is 49.08%, which is less than the 64.56% observed in SPWM. This is desirable because if the voltage has a great deal of distortion due to the inverter switching harmonics, it will subject the motor to large electrical and thermal stress, which will in turn aggravate the stator insulation degradation. The 5th, 7th, 11th and 13th order harmonics are still dominant here contributing 1.08%, 0.92%, 0.47% and 0.2% of the fundamental component respectively. Also notable is that SVPWM increased the amplitude of the fundamental component by 14%, which is consistent with theory since Rao *et. al* [100] remarked that SVPWM can increase the fundamental by as high as 27.3% relative to SPWM.

Finally, Fig. 7.3(a) and (b) depict the FFT of the inverter output current over one cycle along with the corresponding THD for SPWM and SVPWM modulated inverter, respectively, at a switching frequency of 8 kHz. The current drawn by the motor in SPWM modulation is also rich in harmonics, resulting in a THD of 3.87%. Apart from the fundamental component at 50Hz, it also has 5th, 7th and 11th order harmonics constituting 2%, 1.15% and 0.3% of the fundamental component. All other harmonics contribute less than 0.2% each. Also evident is a DC component contributing up to 0.7% of the fundamental component.

Expectedly, the harmonic distortion in the current spectrum in SVPWM modulation is also slightly reduced from 3.87% in the case of SPWM to 3.75% (about 3.2% reduction). Evident harmonic components include the 5th and 7th order harmonics contributing 2.3% and 1. 4% respectively. All other harmonics are less than 0.45%. There is still a DC component which is about 1.8% of the fundamental component.

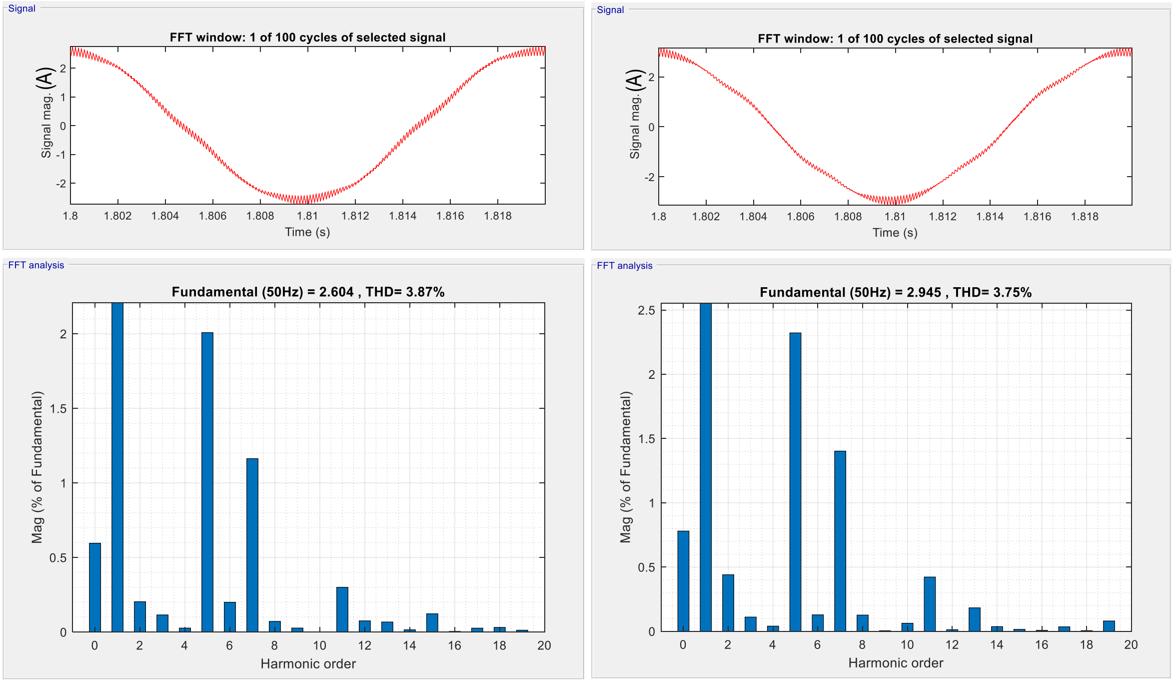

(a) **(b)**

Fig. 7.3: FFT of the inverter output current in **(a)** SPWM and **(b)** SVPWM modulation

7.2.3 Concluding Remarks

This section presented a description of the VFD system modelled and simulated in MATLAB Simulink to compare SPWM and SVPWM modulation schemes at 5 kHz and 8 kHz switching frequencies. The comparison between SPWM and SVPWM at these two frequencies can therefore be summarized as shown in Table 7.1, based on the results of the simulations presented above.

Table 7.1: THD comparison in SPWM and SVPWM at 5 kHz and 8 kHz

Switching Frequency	Parameter	Total Harmonic Distortion (THD) (%)	
		SPWM	SVPWM
5 kHz	Modulating signal	0.00	20.80
	Inverter voltage output	72.22	54.63
	Inverter current output	5.08	4.71
8 kHz	Modulating signal	0.00	20.80
	Inverter voltage output	64.56	49.08
	Inverter current output	3.87	3.75

It can therefore be concluded that SVPWM is the better modulation scheme to use in comparison with SPWM. Furthermore, the higher switching frequency of 8 kHz give results will less harmonic distortion than the low switching frequency of 5 kHz. Therefore, SVPWM modulation scheme and 8 kHz are chosen and will be implemented in all experimental tests of this work. It should be noted, however, that these are not the only modulation schemes available in literature. There are several other modulation schemes, but these two were considered because they are relatively simple to implement and effective in comparison with other modulation schemes.

7.3 Impact of the Designed 3-Phase LC Filter

A three-phase second-order sinusoidal LC filter was designed and was used to interface the unloaded motor with the inverter, to reduce the harmonic content of the inverter output before feeding it into the induction motor. The design process for this filter was outlined in chapter 5. This section presents both simulation and experimental results in which the inverter was tested of effectiveness in attenuating the inverter switching noise.

7.3.1 Simulation Results

For simulation purposes, the designed filter was implemented in Simulink using standard inductor (L) and capacitor (C) elements. It was used to interface the motor – at no-load – to the inverter to filter the inverter switching noise. The system was simulated with and without the filter, and in each case the characteristic parameters like voltage and current output of the filter were examined for distortion. Fig. 7.4(a) and (b) shows the voltage and current signals prior to filtering.

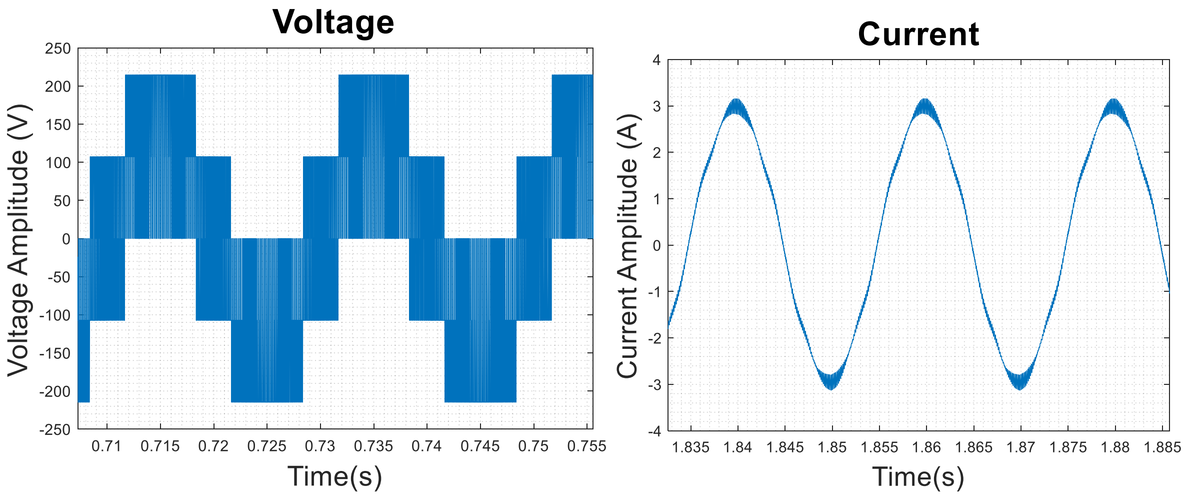

(a) **(b)**

Fig. 7.4: Unfiltered inverter output **(a)** voltage and **(b)** current

As expected, the output voltage signal consists of a square waves or spikes resulting from the switching on and off of the DC voltage. On the other hand, the current is a sinusoid but very noisy. The current is somewhat sinusoidal due to the inductive nature of the induction motor, acting like a filter. Nonetheless, these signals are not ideal for feeding into an induction motor as they quicken degradation and ageing of the induction motor. A filter needs to be connected to the output of the inverter to attenuate most of the low order voltage and current harmonics.

When a three-phase LC filter interfaces the motor to the inverter, the same signals appear smoother and cleaner at the output of the filter and are suitable for driving the induction motor. Fig. 7.5 shows the same voltage and current signals at the output of the filter. For the voltage signal, the THD has been reduced substantially from 49.08% prior to filtering to 0.34% after filtering. The FFT of the voltage showed that the odd switching harmonics are still present, but their amplitudes have been greatly reduced to a negligible value.

Likewise, the filter output current spectrum (FFT) still shows a large reduction in harmonic content in the presence of the filter, relative to when there is no filter. The THD has reduced from 3.75% to less than 1%. This demonstrates the effectiveness of the filter in filtering out and reducing switching harmonics and noise.

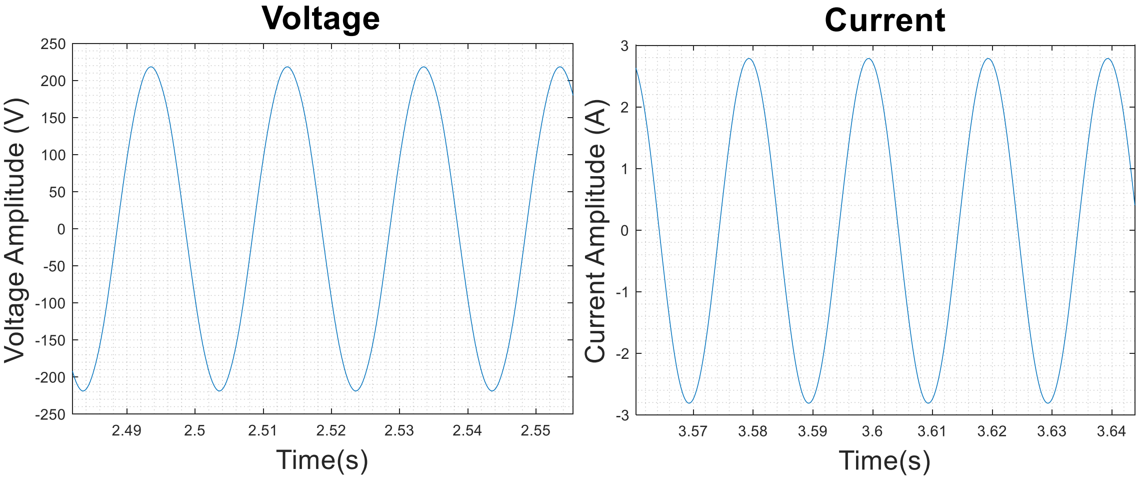

(a) **(b)**

Fig. 7.5: Filtered inverter output **(a)** voltage and **(b)** current

Based on the analysis of the simulation results with respect to the harmonic content of the current and voltage signals at the output of the filter, it is concluded that the designed filter is effective and able to attenuate the inverter switching harmonics to an acceptable level, that is low enough not to cause overheating of the motor. The next step was to assess its effectiveness experimentally, and the next subsection presents the results of the assessment.

7.3.2 Experimental Results

The effectiveness of the filter was tested on a balanced 3-phase star-connected *RL* load with $R = 33.3\ \Omega$ per phase and $L = 66.6$ mH per phase. Although these *R* and *L* values are larger than the motor's resistance and inductance values, its purpose was to serve as a guide of its effectiveness. Fig. 7.6 shows the output line voltage V_{ab} and line current I_a of the inverter as seen by the *RL* load without the three-phase filter.

It is observed that the voltage in this case consists of square pulses, as it was the case in the simulation, with the only difference being that here is the RL load and not the motor. Likewise, the current is a sinusoid but contains noise.

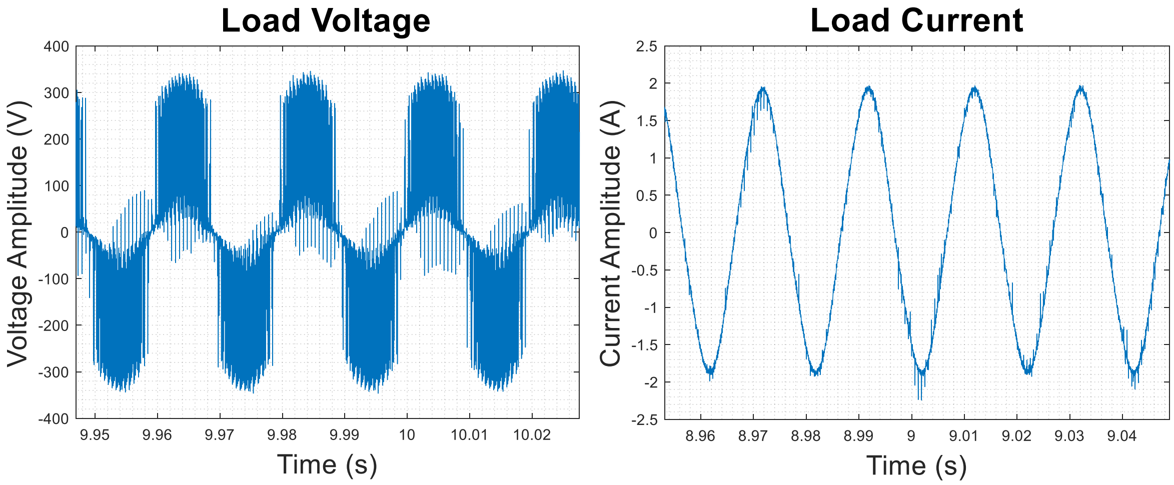

(a) **(b)**

Fig. 7.6: Pre-filtered line **(a)** Voltage and, **(b)** Current

On the contrary, if the designed 3-phase filter is used to interface the 3-phase RL load with the inverter, the same line voltage and line current waveforms take the form shown in Fig. 7.7. With the filter in place, the waveforms are cleaner with less noise and interference.

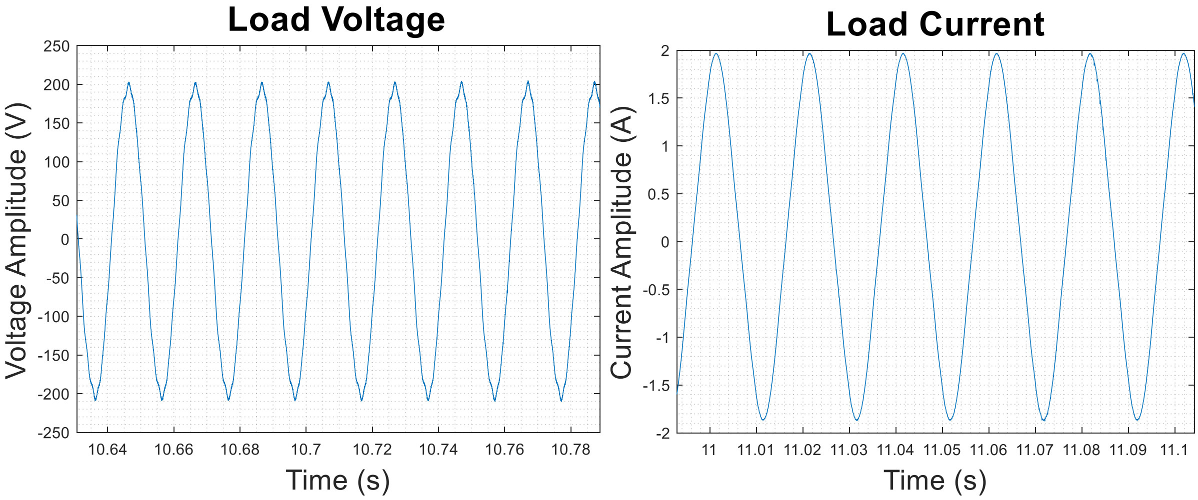

(a) **(b)**

Fig. 7.7: The filtered line **(a)** Voltage and, **(b)** Current

In terms of THD, the pre-filtered voltage and current signals have THD of -38.32 dB and -29.93 dB respectively. After filtering, the THD decreased to -37.32 dB and -28.12 dB for voltage and current respectively. The decrease is not as prominent here since the inductance of the load was large compared to that of the motor for which the filter was designed. The expectation is that the attenuation of the harmonics will greatly improve for the motor.

7.4 V/F (Scalar) Control Results

In this method, the terminal voltage of the machine is varied alongside the supply frequency such that the ratio of terminal voltage to frequency remains constant throughout. Here, the frequency was ramped up linearly from 0 Hz to 50Hz, which is the operating frequency of the motor. This section presents both the simulation and experimental results from V/F control implementation.

7.4.1 Simulation Results

In the simulation studies, the frequency was ramped over a period of 1 second. The time-domain graphs show, the voltage, current, speed and torque response of the induction motor in an open-loop V/F control configuration. Presented first in Fig. 7.8 is the three-phase voltage time-domain response of the motor under this control method. The figure shows the evolution of frequency and voltage amplitude over time. As the frequency increases, the voltage also proportionately increase in amplitude until the frequency remains constant at 50 Hz. In a similar manner, the amplitude of the voltage remain constant without any further increase.

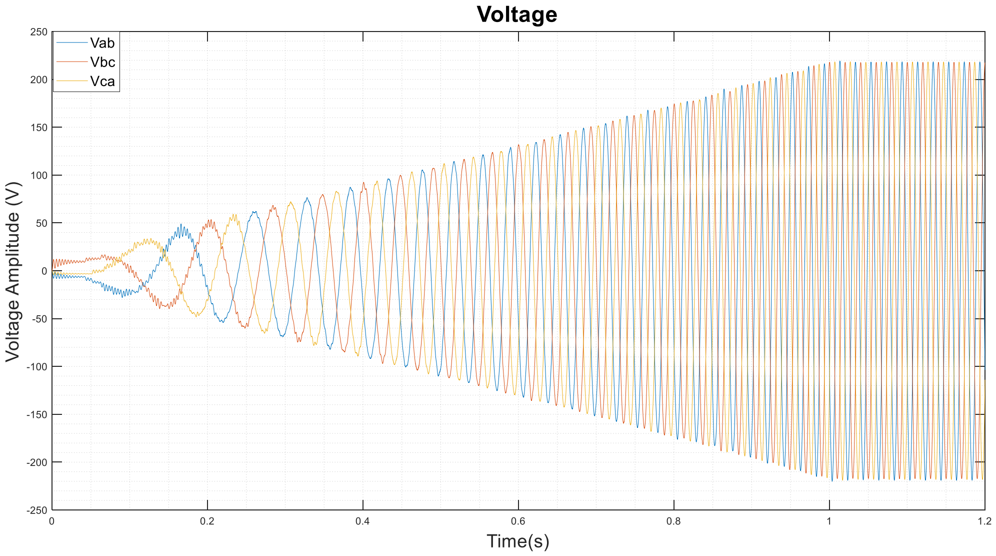

Fig. 7.8: Three-phase voltage response of the motor in V/F control mode

The evolution of the graph over time is such that the change in voltage amplitude over a defined time interval as ratio of the change in frequency over that same interval is constant, as outlined in the literature and in section 5.6.2 of this work. A similar behaviour is observed in the response of the motor current over time, as shown in Fig. 7.9. The amplitude increases as the frequency increases, until maximum no-load current is reached.

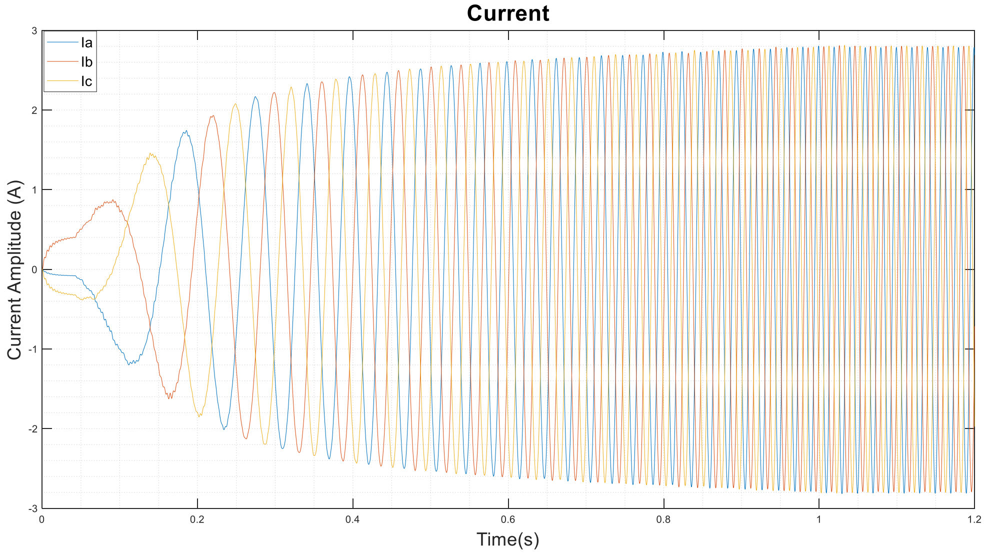

Fig. 7.9: Three-phase current response of the motor in V/F control

On the other hand, the speed and torque response of the unloaded motor under V/F control are shown in Fig. 7.10. The speed of the machine increases almost steadily from zero up to a steady state speed of 2 987 rpm (or 312.8 rad/s). The machine is not loaded, and hence the steady state torque is low (0.16 Nm on average). To accelerate the motor, the torque increases to overcome the reactionary torque until steady state is reached, after which it falls to a value close to zero.

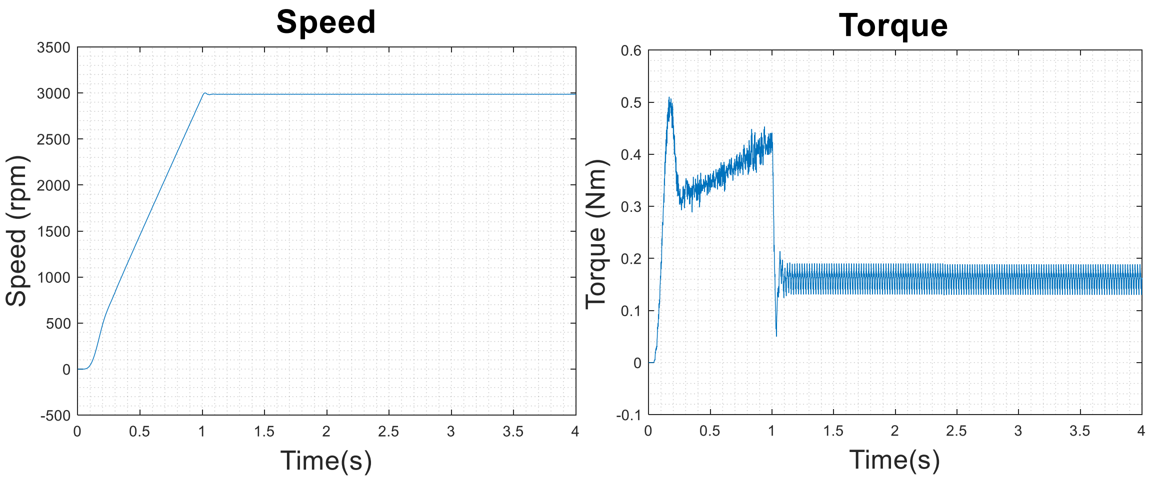

(a) **(b)**

Fig. 7.10: **(a)** Speed and **(b)** Torque response of the motor in V/F control

7.4.2 Experimental Results

In the development of the system, the *V/F* control was first tested on a balanced three phase *RL* load, as described in section 7.3.2, to ensure proper operation before being applied to the induction motor. From start, the frequency is ramped up (linearly increased) from 0 Hz to 50 Hz over a period of 10 seconds, after which it is kept constant. Fig. 7.11 shows the three-phase voltage and current response when V/F control was applied to the three-phase RL load, the characteristics of which are described in section 7.3.2.

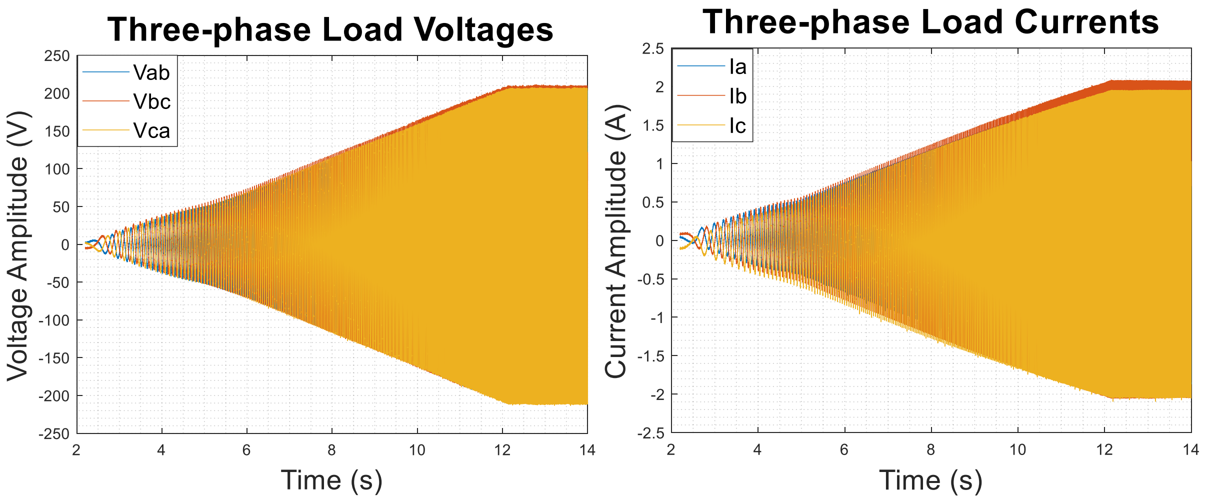

(a) **(b)**

Fig. 7.11: **(a)** Voltage and **(b)** Current response of the RL load in V/F control

It is observed from Fig. 7.11(a) that the load voltage increases in amplitude and frequency, until the steady state is reached 10 seconds later (at 12 seconds). Both voltage and frequency remain constant from 12 seconds onwards. Expectedly, the current waveform is very similar to that of voltage. As depicted in Fig. 7.11(b), the current starts increasing in amplitude, from 0 A to 1.4 A, as the frequency is ramped from 0 Hz to 50 Hz. The current of 1.4 A was chosen here because the no-load current of the test motor used in this work is 1.4 A. So, as the frequency of current increases, its amplitude also increases until the frequency stops increasing at 50 Hz, and the current remains constant at 1.4 A. Both voltage and current responses were as expected based on the simulation results presented earlier. The negligibly small differences noted in the measurements in Fig. 7.11 are due to small offset in the phase measurements because of slight miscalibrations.

Having successfully assessed the developed V/F control on a RL load, it was then applied and tested on the 3-phase induction motor with slight changes made. Here the frequency was still ramped from 0 Hz to 50 Hz as before, but this was done over a period of 2 seconds (from 2.2 seconds to 4.2 seconds). The voltage response and current response of the motor are shown in Fig. 7.12.

It is observed from Fig. 7.12(a) that the voltage increases in both amplitude and frequency. The voltage increases from 0 V to approximately 190 V, and this increase is proportionate to the increase in frequency. Beyond 4.2 seconds, the voltage as well as its frequency remain constant throughout. Likewise, the three phase currents flowing through the stator windings of the motor under V/F control mode are shown in Fig. 7.12(b). The inverter started switching at 2.2 seconds. It is observed that the current increases in amplitude and frequency. The amplitude increases to a maximum of about 4.8 A before dropping again until it reaches a steady state value of 1.9 A, which corresponds to the RMS value of 1.4 A, which is the no-load current of the motor. The steady state current and frequency is reached after 4.2 seconds.

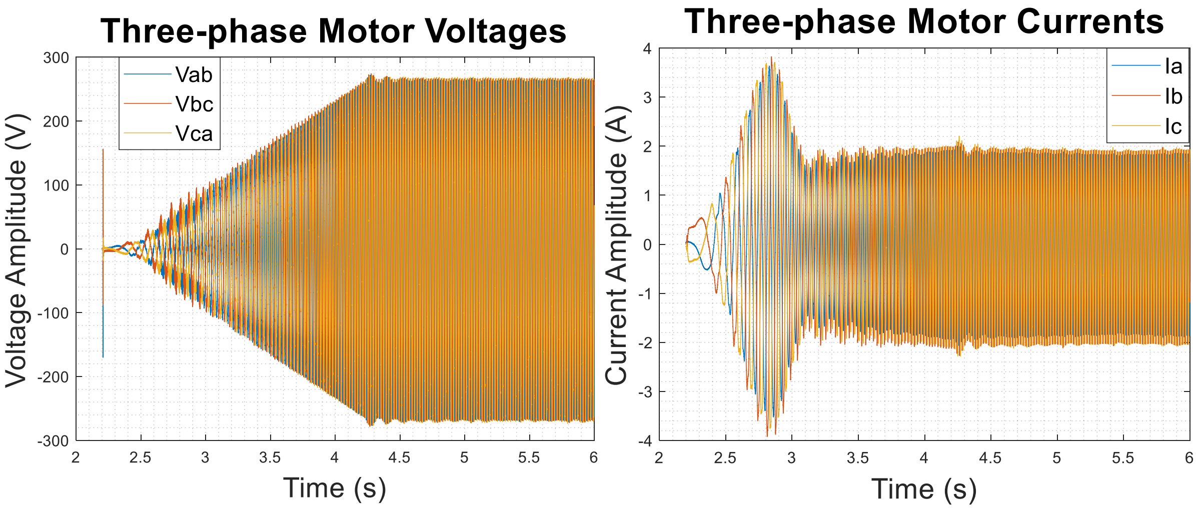

(a) **(b)**

Fig. 7.12: **(a)** Three-phase line voltage and **(b)** Current response of the motor in *V*/*F* control mode

An induction motor has high starting current since its impedance is slip dependent, hence why the amplitude of the starting current increased to as high as 4.8 A (because of low starting impedance due to high slip value) to provide the necessary starting torque in accelerating the motor.

Finally, the speed and torque response of the motor under *V*/*F* control at no-load are presented. The results for speed and torque are shown in Fig. 7.13(a) and (b) respectively. It is observed that the speed of the motor increases almost linearly as the frequency of the reference/modulating signal is ramped up from 0 Hz to 50 Hz. The speed increases from 0 rpm at the time when the inverter starts switching at time t = 2.2 seconds, until it reaches a steady state speed that is very close to 3000rpm at time t = 4.2 seconds.

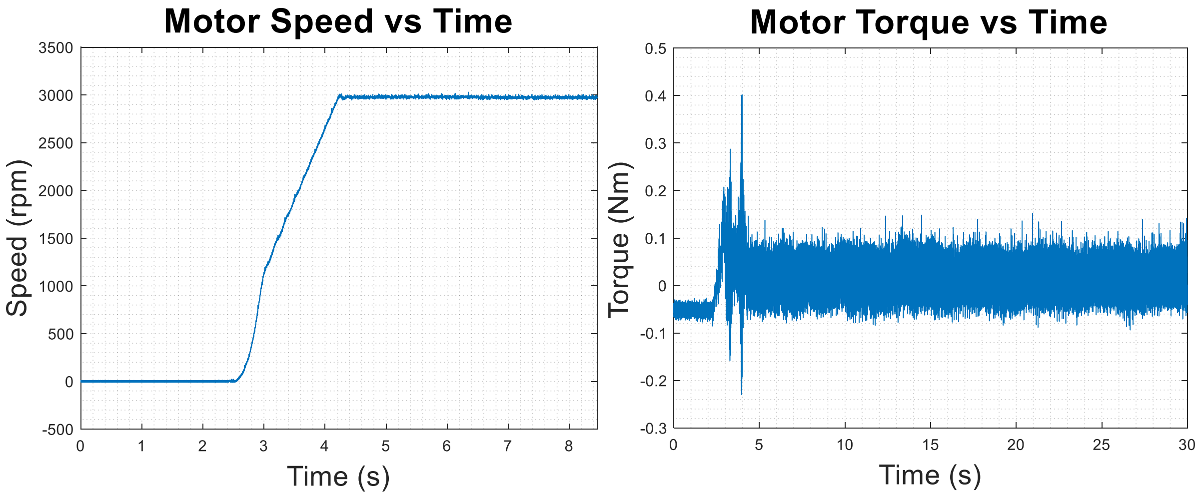

(a) **(b)**

Fig. 7.13: **(a)** Speed and **(b)** Torque response of the motor in V/F control

This is expected since the speed of the induction motor is depended on the supply frequency – the frequency of the inverter output voltage in this case. So, as the frequency of the output of the inverter increases, so does the speed of the motor. The torque also shows an increase in torque at the beginning, up to a value around 0.4 Nm, however, the torque eventually decreases back to zero after the transition time.

7.5 Impact of Inverter Open-Switch Faults

This section presents the results for the open-switch faults on the inverter. These faults were first simulated in MATLAB Simulink environment before being implemented in the laboratory on the actual electric drive. In this study, only three distinct faulty switch operations were considered: single switch open-switch fault, two open-switch faults on the same bridge arm (single phasing), and two open-switch faults on two separate bridge arms. Therefore, both simulation and experimental results are presented here. In each case, the time domain analysis is performed to deduce what happens to the motor voltage, current, speed and torque when one of these three faults manifest in the inverter. Since the objective is to study its impact on the motor, only the healthy motor is used here, and is operated under no-load conditions.

7.5.1 Simulation Results

In MATLAB Simulink, open switch faults were simulated by removing the gate signal of the switch in question. This was done by feeding the gate signals to the respective gates through switches that pull the gate drive voltage to zero at a specified time. The gate drive remains zero after this time. This way, two responses in each simulation are obtained – the response prior to the occurrence of the fault and the response after the occurrence of the fault. This subsection presents the simulation results for the respective open switch faults implemented.

A. Single Switch Open-switch Fault

To implement this type of a fault, any one of the three top switches (S1, S3 and S5) or any one of the bottom switches (S4, S6 and S2) is opened while the machine is operating in steady state. The voltage and current signals, along with the speed and torque signals are captured and analysed for pre- and post-fault response. In this work, S1 was open circuited. Fig. 7.14(a) and (b) show the time-domain voltage and current response of the motor under the influence of this fault. S1 was open circuited at t = 1 second and remained open.

It is observed that before the switch fails to close, steady state has been reached. The time-domain response shows that when switch S1 is open, both line voltages V_{ab} and V_{ca} become significantly distorted while line voltage V_{bc} is less affected. This could be because switch S1 (alongside S4) is responsible for the pole voltage V_a from which both V_{ab} and V_{ca} are calculated. Before the fault occurs, the THD of the three line-voltages V_{ab}, V_{bc} and V_{ca} are 0.72%, 1.06% and 0.73% of the fundamental respectively. However, post fault, these THDs increased to 23.47%, 1.41% and 27.70% respectively. While these THDs may not be the absolute value of the distortion since some of the low ordered harmonics are attenuated by the filter, they are for relative comparison of the impact on the individual line voltages and serve to confirm what is seen in the time-domain analysis of Fig. 7.14(a).

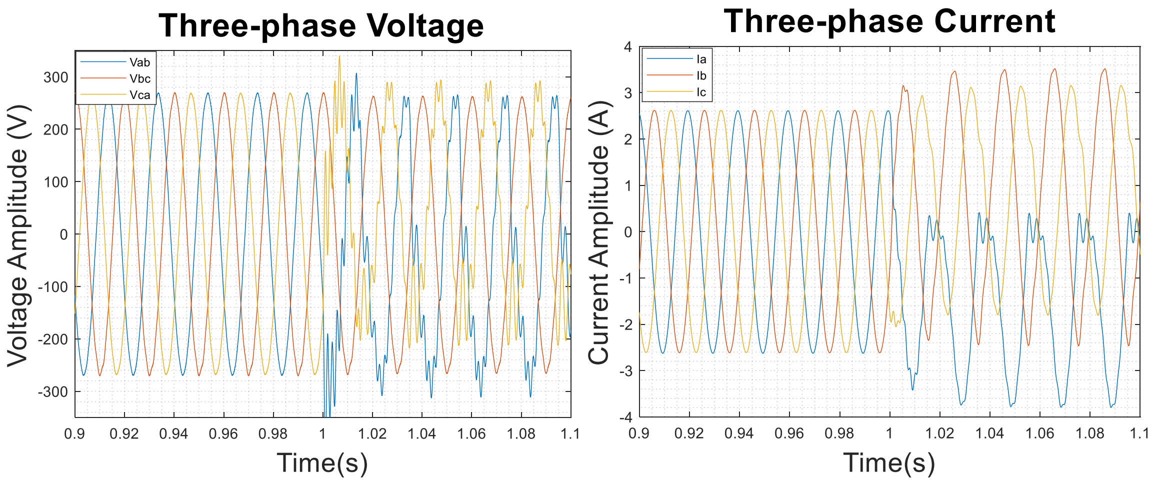

(a) **(b)**

Fig. 7.14: Three-phase **(a)** voltage and **(b)** current response when S1 is open-circuited

The DC offset voltages of -14.5% and 16.8% of the fundamental voltage are observed on the line voltages V_{ab} and V_{ca} respectively. Also evident is the decline in the amplitude of the fundamental due to this fault, with 4.12%, 2.02% and 17.9% decrease observed in V_{ab}, V_{bc} and V_{ca} respectively. Finally, the calculated voltage unbalance due to this fault amounts to 10.3%. These characteristics are summarized in Table 7.1.

In terms of current (Fig. 7.14(b)), all three line-currents are distorted differently when switch S1 is open. Top half of I_a waveform is eliminated leaving the lower half, with an increased amplitude, and increased distortion. The other two line-currents (I_b and I_c) remain distorted, and their amplitude is increased in the top half, opposite to that of line current I_a. This is the same response that was obtained by Cui [15], shown in chapter 4 of this report. Due to the occurrence of this fault, the THD increased by 21%, 7.54% and 8.69% for phase currents I_a, I_b and I_c respectively. Each of the phase currents also experienced an increase in its DC component (DC offset), with I_a having the greatest DC offset of -59.1% of the fundamental component. I_b and I_c have 27.2% and 29.4% respectively. The current unbalance resulting from this fault is 17.68%. These results are summarized in Table 7.1.

Table 7.1: Voltage and current response of the motor when S1 is open circuited

Assessment Parameter	**Voltage**			**Current**		
	V_{ab}	V_{bc}	V_{ca}	I_a	I_b	I_c
% Increase in THD	22.8	0.35	27.0	21	7.54	8.69
% DC offset	-14.5	0	16.8	-59.1	27.2	29.4
% Change in amplitude of the fundamental	-4.12	-2.02	-17.9	-22.2	8.62	-8.25
% Unbalance	10.3			17.68		

Finally, Fig. 7.15 shows the speed and torque response of the induction motor when switch S1 is open circuited. When switch S1 is open circuited, the speed of the motor decreases slightly from 2990.3 rpm to 2946.1 rpm (about 1.5%) and start to oscillate with an amplitude of 142.60 rpm. Likewise, before the occurrence of the fault, the motor develops a torque of 0.14265 Nm since the motor is unloaded.

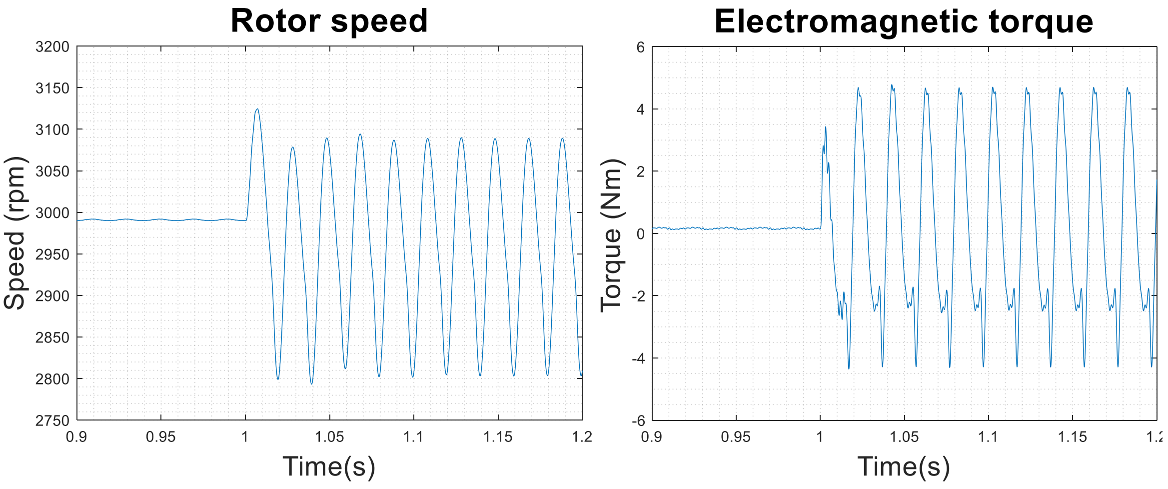

(a) **(b)**

Fig. 7.15: **(a)** Speed and **(b)** torque response of the motor with S1 open

However, the torque starts to oscillate with a peak-to-peak amplitude of 9.0 Nm centred around 0.2811 Nm. The frequency of oscillation for both speed and torque is the same as the frequency of the supply (50 Hz). These results are summarized in Table 7.2.

Table 7.2: Speed and Torque response of the motor when S1 is open circuited

Assessment Parameter	Speed	Torque
% Change in amplitude	-1.5	97.06
Amplitude of oscillation	146.60 rpm	4.7843 Nm
Frequency of oscillation (Hz)	50	50

B. Single-phasing Open-Switch fault

This is a case where there is a double-switch fault in the same bridge arm. In this work, both switch S1 and S4 were open circuited simultaneously by cutting of their gates' signals at t = 1.0 s. The time domain analysis of motor voltages and currents under the influence of this fault are analysed, alongside the electromagnetic torque and speed of the motor. Fig. 7.16 shows the voltage and current responses when switches S1 and S4 are open circuited simultaneously. Fig. 7.17 shows speed and torque response of the motor under the same fault conditions.

It is observed from Fig. 7.16(a) that pre-fault, the three-phase voltages are at steady state and balanced. However, when the fault occurs, the voltages become distorted, with line voltages V_{ab} and V_{ca} decreasing suddenly in amplitude in comparison to line voltage V_{bc}. The amplitudes of V_{ab} and V_{ca} have decreased by 32.9% and 54.8% respectively, while V_{bc} only decreased by 4.07%. This could, as before, be attributed to the fact that switches S1 and S4 are responsible for the pole voltage V_a from which the two affected line voltages are determined. It can also be noted that the voltage amplitude is still symmetrical about the x-axis (time-axis) even after the occurrence of this kind of fault, thus implying no DC offset.

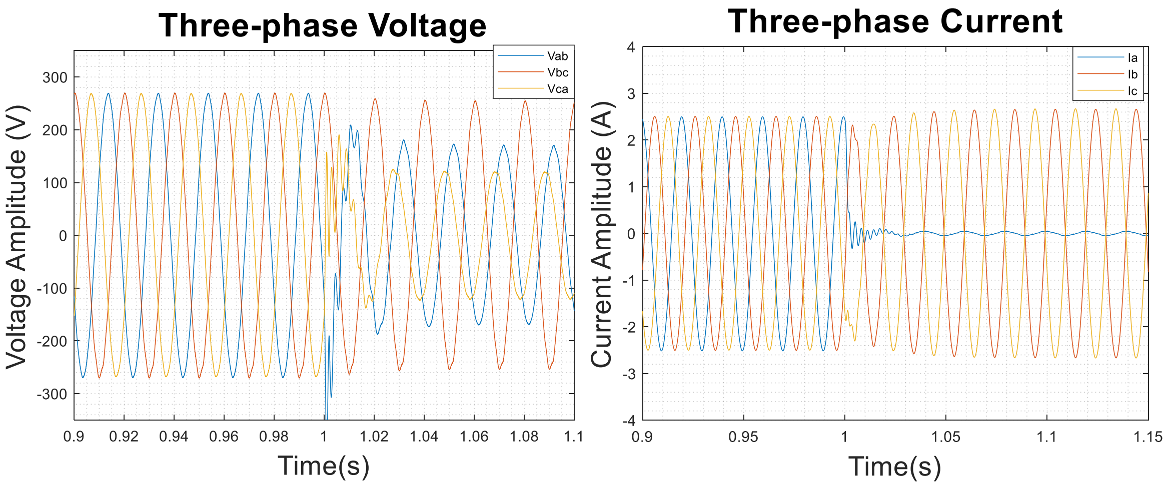

(a) **(b)**

Fig. 7.16: **(a)** Three-phase voltage and **(b)** current response when S1 and S4 are open-circuited

The individual line voltages experienced small THD increases of 0.4%, 0.09% and 1.0% for V_{ab}, V_{bc} and V_{ca} respectively. So, except for the substantial decrease in amplitude, there isn't much of a distortion brought by this fault since the THD before and after the fault are almost the same. So, the only notable change is the decrease in amplitude. The voltage unbalance here is 38.40%.

Similarly, Fig. 7.16(b) shows the time-domain response of the three-phase motor currents under the influence of this type of fault. It is evident that when this type of fault occurs, phase A current, I_a, drops to zero while the other two phase-currents initially drop slightly before gradually increasing until they are slightly greater than the pre-fault steady state value. The amplitudes of phase currents I_b and I_c increased by 6.00% and 6.24% respectively. There is not much observable distortion or noise in the current spectrum since the average THD increase is 0% for both phase currents I_b and I_c. The resulting current unbalance caused by the fault is 49.2%. So, it is conclusive that when this type of fault occurs, say, S1 and S4 are open circuited, phase A current, I_a is lost, while the other phase currents increase slightly without any distortion. The overall current and voltage response of the motor under the influence of this fault are summarized in Table 7.3.

Table 7.3: Voltage and current response of the motor under single-phasing fault

Assessment Parameter	**Voltage**			**Current**		
	V_{ab}	V_{bc}	V_{ca}	I_a	I_b	I_c
% Increase in THD	0.4	0.09	1.0	0	0	0
% DC offset	0	0	0	0	0	0
% Change in amplitude of the fundamental	-32.9	-4.07	-54.8	-100	6.00	6.24
% Unbalance	38.4			49.2		

On the speed and torque front, Fig. 7.17(a) shows that both torque and speed decrease slightly and start to oscillate at 50 Hz, the frequency of the supply, about this reduced steady stead value.

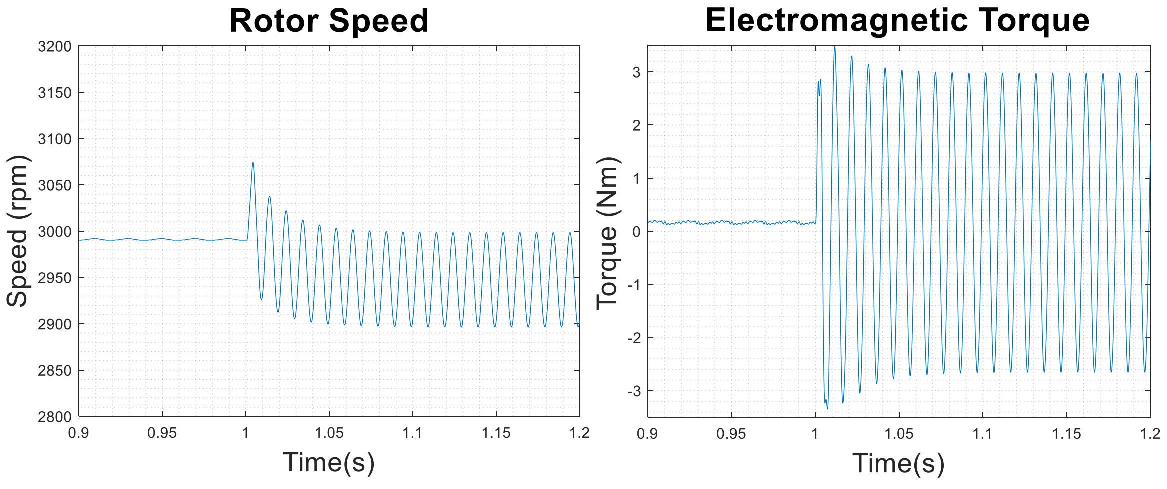

(a) **(b)**

Fig. 7.17: **(a)** Speed and **(b)** torque response of the motor with S1 and S4 open

The speed dropped from a steady state value of 2990.3 rpm (before the fault) to 2947.7 rpm after the fault, thus giving rise to 1.4% drop in speed. Similarly, the torque decreased from 0.179 to 0.159 Nm, thus giving rise to 11.2% decrease in torque. Also notable is that, as opposed to the case of a single switch open-switch fault, both the torque and speed oscillations in this case, are smooth (like pure sinusoidal) about the new steady state value. These results are summarized in Table 7.4.

Table 7.4: Speed and Torque response of the motor under single-phasing fault

Assessment Parameter	Speed	Torque
% Change in amplitude	-1.4	-11.2
Amplitude of oscillation	50.7 rpm	2.8097 Nm
Frequency of oscillation (Hz)	50	50

C. Two switches open on two separate bridge arms

This section presents the results of double open switch faults on different arms but at the same bridge position. This fault was implemented in Simulink by depriving switches S1 and S3 of their gate drive signals. The voltage and current response of the motor under this fault are shown in Fig. 7.18(a) and (b) respectively. Fig. 7.18(a) shows that all three line-voltages become severely distorted. The relative increase in THD is 52.07%, 31.93% and 33% for voltages V_{ab}, V_{bc} and V_{ca} respectively. There is also an increase in DC offset in the voltages, in which V_{ab} and V_{ca} experienced 1.66% and 20.3% increase in DC offset voltage while V_{bc} has -21.9% percentage DC offset. The relative decrease in the amplitude of the fundamental are 33.5%, 17.4% and 26.0% for V_{ab}, V_{bc} and V_{ca} respectively. The resulting voltage unbalance is 11.0%.

It is evident from the figure that simultaneously open circuiting the top two switches (e.g. S1 and S3 in this case) will remove the top half-cycle of the waveforms of currents which are derived from pole voltages (V_a and V_b in this case) controlled by the faulted switches. So current I_a and I_b both have their top half cycle removed. The opposite is true for the other line current.

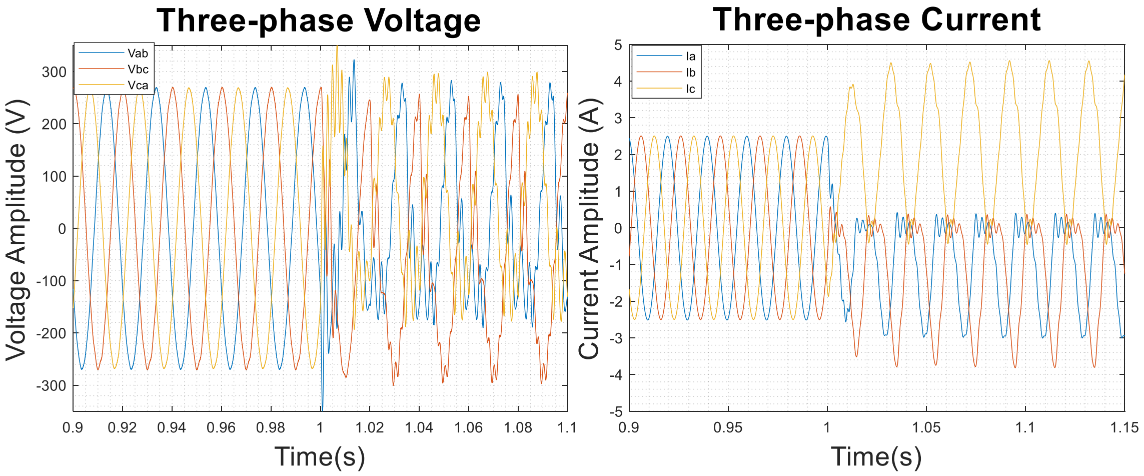

Fig. 7.18: Three-phase **(a)** voltage and **(b)** current response with S1 and S3 open

Consequently, the frequency-domain analysis showed an equivalent increase in distortion and in DC component in all the currents in this case. The increase in THD due to the fault is 38.5%, 34.4% and 12% in phase currents I_a, I_b and I_c respectively. There is a DC offset of -38.4% and -50.5% in I_a and I_b respectively while I_c has DC offset of 90.3%. The amplitude of I_a, I_b and I_c increased by 20.5%, 51.8% and 82.1% respectively. The current unbalance resulting from this fault is 20.3%. These results are summarized in Table 7.5.

Table 7.5: Voltage and current response of the motor when S1 and S3 are open.

Assessment Parameter	**Voltage**			**Current**		
	V_{ab}	V_{bc}	V_{ca}	I_a	I_b	I_c
% Increase in THD	52.7	31.9	33.0	38.5	34.4	12.0
% DC offset	1.66	-21.9	20.3	-39.4	-50.5	90.3
% Change in amplitude of the fundamental	-33.5	-17.4	-26.0	20.5	51.8	82.1
% Unbalance	11.0			20.3		

Finally, Fig. 7.19 shows the speed and torque response of the motor when both S1 and S3 are open circuited. It is observed here that, as before, both speed and torque start to oscillate. However, oscillations are more erotic than before and are not smooth, with amplitude of oscillation increasing on the opposite site to the open circuited switches. Speed drops from 2991.4 rpm to 2892.3 rpm, which is a 3.31% decrease in speed. The amplitude of speed oscillation about this new steady state speed is 143.6 rpm. Similarly, the torque developed decrease from 0.145 Nm to -0.846 Nm. The amplitude of oscillation of the torque is 5.64 rpm. Table 7.6 shows the summary of speed and torque response of the motor under the influence of this fault.

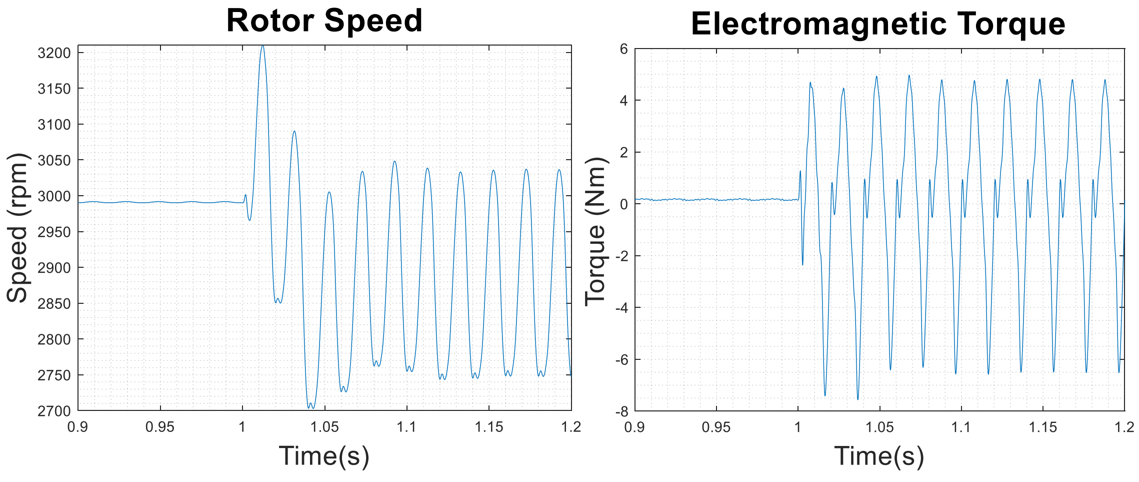

(a) **(b)**

Fig. 7.19: **(a)** Speed and **(b)** torque response of the motor when S1 and S3 are open circuited.

Table 7.6: Speed and Torque response of the motor when S1 and S3 are open circuited.

Assessment Parameter	Speed	Torque
% Change in amplitude	-3.31	-683
Amplitude of oscillation	143.60 rpm	5.64 Nm
Frequency of oscillation (Hz)	50	50

D. Concluding Remarks

This section presented simulation results for three distinctive faults: single switch open switch fault, single phasing fault and double switch open switch fault on the inverter. Their impact on the motor was analysed by studying the changes in voltage, current, speed and torque. Double switch open switch fault resulted in the largest increase in voltage distortion and largest increase in DC offset voltage than the other two faults, while single phasing experiences the least changes in these parameters than the other two faults. In fact, single phasing fault shows negligible increase in distortion and DC offset for both current and voltage. The only aspect evident is its highest change in the amplitude of the fundamental component for both voltage and current. It is also observed that for each of the fault, current unbalance is always greater than voltage unbalance, which is constituent with the literature. There relative severity of the faults portrayed by the changes in the characteristics of voltage and current of the motor is reinforced by the speed and torque responses of the motor under the respective faults. In each case, the fault causes the speed and torque to slightly decrease and to start pulsating at the frequency of the fundamental component (50 Hz). However, double switch open switch fault shows relatively high drop in speed and torque and a relatively high amplitude of oscillation than the other two faults. However, single phasing fault shows the least drop in speed and torque and the lowest amplitude of oscillation compared to the other faults. These impacts can be expected to be worse if the motor is loaded, since it would already be drawing more current and rotating at a rated speed while delivering rated torque. So, this type of faults could lead to the damage of winding insulation and accelerate aging of the motor. The next section presents experimental results of the same faults analysed here.

7.5.2 Experimental Results

Open switch faults were implemented in the laboratory using the procedure described in section 4.4.2 of this report and outlined in section 6.4. The results obtained are presented in this section. Three faults were implemented – Single switch open switch fault, double switch open switch fault on the same bridge arm (single-phasing) fault and double switch open switch fault.

A. Single Switch Open-switch Fault

In this work, switch S1 was open circuited at approximately t = 14.5 seconds. Before then, the motor is operating under steady state conditions, at rated voltage and no-load current. Fig. 7.20 shows the three-phase voltage and current response of the motor pre- and post-fault. This response is similar to the one obtained from simulations and presented in Fig. 7.14. From the time-domain representation of Fig. 7.20(a), it is observed that before the fault, the voltages are smooth sinusoid but become distorted when the fault occurs. This is also confirmed by Table 7.7 which gives a measure of the amount of distortion in each of the line voltages. Similar to Table 7.1, Table 7.7 shows that all line voltages experienced an increase in distortion. However, line voltages $V_a b$ and V_{ca} are the most distorted since they have the largest percentage increase in THD. This can be associated with the fact that switch S1 controls pole voltage V_a which used in the determination of both V_{ab} and V_{ac}. These results are consistent with the simulation.

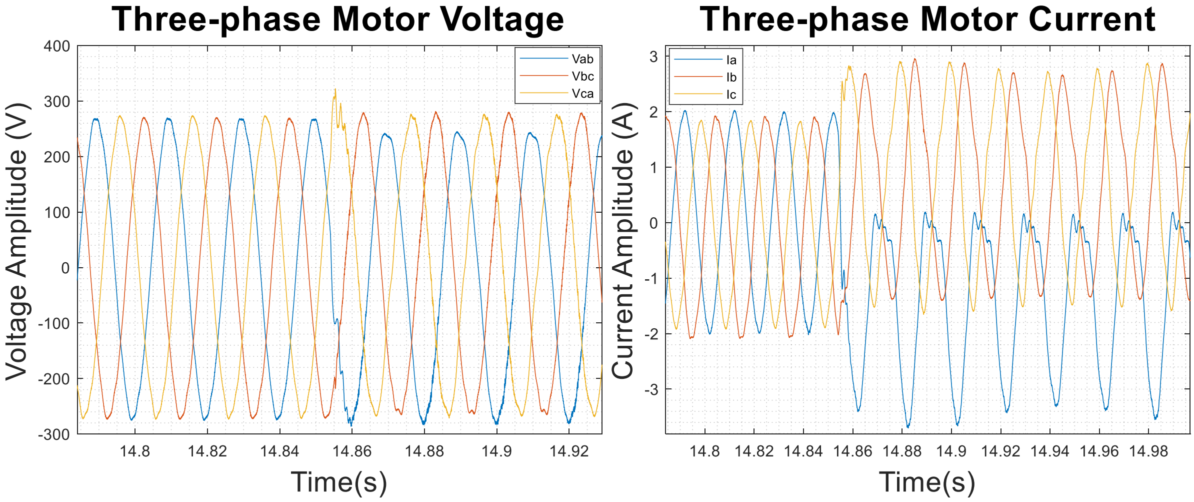

(a) **(b)**

Fig. 7.20: Three-phase **(a)** voltage and **(a)** current response of the motor when S1 is open circuited.

In addition to the extensive distortion in V_{ab} and V_{ca} relative to V_{bc}, there is also an increase in the DC offset voltage of approximately equal magnitude but opposite polarity between the two line voltages, while no DC offset is experienced by line voltage V_{bc}. The amplitude of fundamental component of V_{ca} decreased significantly while that of V_{ab} and V_{bc} decreased only slightly. These results are similar to the simulation results presented in Table 7.1.

It is also observed from Fig. 7.20(b) and Table 7.7 that under this fault, the phase current I_a become increasingly distorted, and the top (positive) half cycle of its waveform is eliminated. Consequently, I_a has relatively high DC offset current Also noteworthy is that the positive amplitude of the other phase currents (I_b and I_c) increases while their negative amplitude decrease.

Table 7.7: Voltage and current response of the motor when S1 is open circuited.

Assessment Parameter	**Voltage**			**Current**		
	V_{ab}	V_{bc}	V_{ca}	I_a	I_b	I_c
% Increase in THD	27.5	11.8	29.1	61.5	32.7	36.2
% DC offset	-3.80	-0.04	3.96	-71.4	39.5	39.9
% Change in amplitude of the fundamental	-3.20	-1.24	-11.3	77.8	48.8	55.9
% Unbalance	5.68			63.4		

The pattern of this experimental results is consistent with what was observed in the simulation results of this type of a fault. The increased pulsating DC current and the increased current amplitude leads to increased heating of the machine windings which could lead to the possible damage of winding insulation and the total destruction of machine. This is more so if this fault occurs while the machine is loaded, and already drawing rated current.

Similarly, Fig. 7.21(a) and (b) shows the speed and torque response of the machine under this type of fault. Table provides a summary of the characteristic changes that happen to both torque and speed and torque when this fault occurs. Before the occurrence of the fault, both speed and torque had reached their average steady state values of 2964 rpm and 0.03 Nm respectively. However, when the fault occurs, they both decrease slightly, as shown in Table 7.8, and start oscillating with a frequency of 50 Hz, the frequency of input voltage and currents. The pulsations are not smooth or purely sinusoidal but are rather rigorous as shown clearly in Fig. 7.21(b). Even the sound produced by the machine changes to mimic this torque and speed pulsations. This subjects the machine under enormous mechanical stress and can lead to accelerated wear and tear of machine parts.

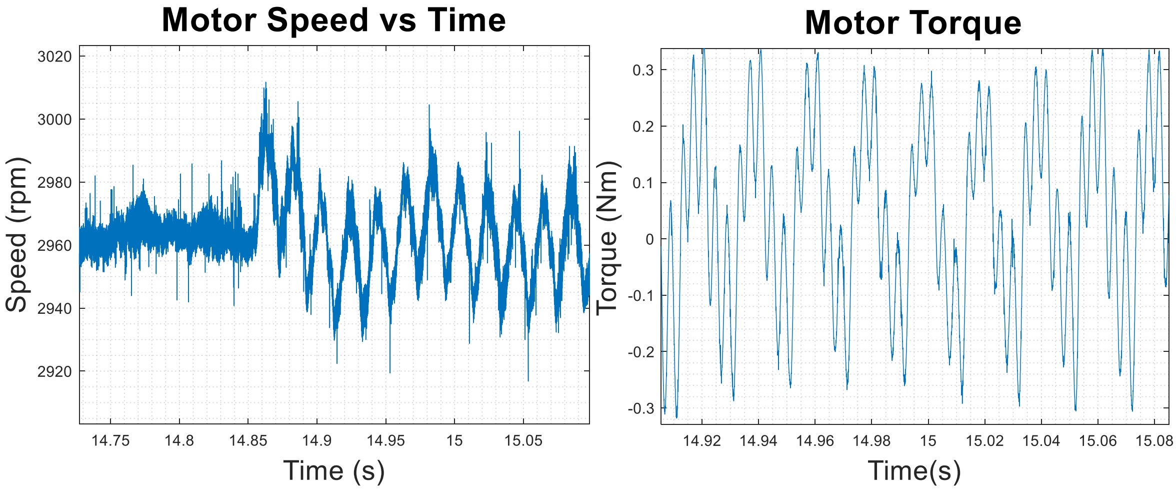

(a) **(b)**

Fig. 7.21: **(a)** Speed and **(b)** torque response when S1 is open circuited

Table 7.8: Speed and Torque response of the motor when S1 is open circuited.

Assessment Parameter	Speed	Torque
% Change in amplitude	-0.30	-20.0
Amplitude of oscillation	20.0 rpm	0.31 Nm
Frequency of oscillation (Hz)	50	50

B. Single-phasing Open-Switch fault

Here, switches S1 and S4 were simultaneously open circuited while the motor was running under steady state operating conditions, at no-load. These switches were simultaneously open circuited at approximately $t = 14.675$ seconds. Before then, the motor was running under steady state conditions, at rated voltage and no-load current. Fig. 7.22(a) and (b) show the time-domain voltage and current response of the motor, respectively.

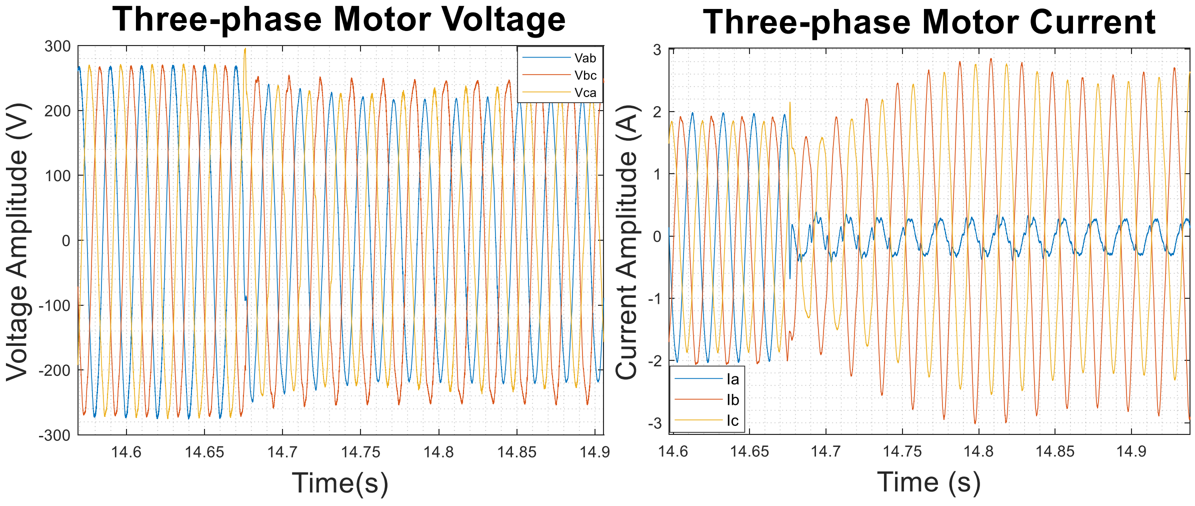

(a) **(b)**

Fig. 7.22: Three-phase voltage response with S1 and S4 open circuited

It is observed that upon the occurrence of the fault, the amplitude (both positive and negative) of the line voltages decreases slightly. Also noticeable, though seemingly mild is the distortion in the waveform of the voltages, with V_{ca} having the highest percentage increase in distortion of 25.1%. Table 7.9 provides a summary of the characteristic changes in voltage and current due to the occurrence of this fault. Notable from Fig. 7.22(a) is that the voltage signals are still symmetrical about the time-axis (or x-axis), hence why Table 7.9 shows no DC offset in each of the line voltage. Line voltages V_{ab} and V_{ca} show the highest decline in the amplitude of the fundamental component. The voltage unbalance resulting from this fault is 7.44%.

Table 7.9: Voltage and current response of the motor under single-phasing fault

Assessment Parameter	Voltage			Current		
	V_{ab}	V_{bc}	V_{ca}	I_a	I_b	I_c
% Increase in THD	7.5	22.1	25.1	58.1	20.9	19.4
% DC offset	0	0	0	0	0	0
% Change in amplitude of the fundamental	-18.0	-7.61	-17.1	-85.5	39.2	41.3
% Unbalance	7.44			84.6		

Fig. 7.22(a) shows that prior to the fault, the current has reached its steady state. When the fault occurs, phase A current, I_a, is significantly reduced to an amplitude of less than 0.3 A, alongside being distorted. However, the other two currents, I_b and I_c initially decrease as the fault occur, but gradually increase to a value higher than the steady state amplitude of the healthy motor. It should be noted that before the new steady state is reached, the current shows an interim period of oscillation in amplitude about the new steady state value. Table 7.9 shows changes brought by the fault to some characteristics of the individual currents. There is no DC offset current and the current unbalance, as can be expected, is way higher than voltage unbalance. These results are consistent with the simulation results, presented earlier, of the same fault.

Finally, Fig. 7.23 shows speed and torque response of the motor under this fault. Before occurrence of this fault at t = 14.675 seconds, the motor has reached a steady state speed of close to 2970 rpm and a stead state torque of 0.0139 Nm. However, when the switches S1 and S4 are open circuited, the speed of the motor drops slightly to 2964 rpm and starts oscillating about this value. The frequency of this oscillation is 50 Hz as before.

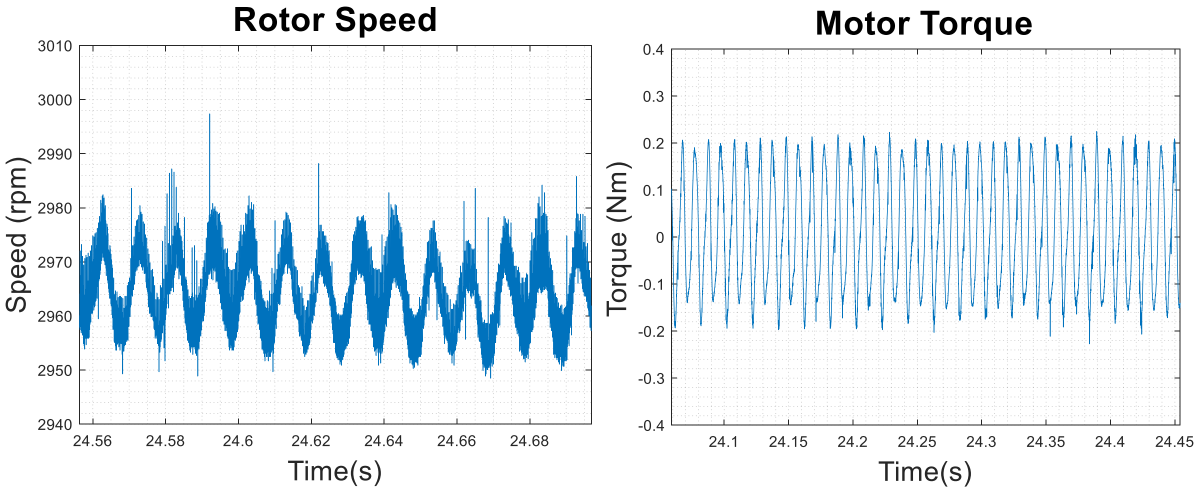

(a) **(b)**

Fig. 7.23: **(a)** Speed and **(b)** torque response when S1 and S4 are open circuited

Likewise, Fig. 7.23(b) shows the same behaviour for the torque of the motor. The torque drops slightly and start to pulsate. The pulsations here are relatively smoother and not rigorous in the case of a single switch open circuit fault. Nonetheless, the frequency of oscillation is still 50 Hz which is the same as the frequency of the supply. These characteristics changes in speed and torque are summarized in Table 7.10, which is consistent with the Table 7.4 depicting simulation results of the same fault.

Table 7.10: Speed and Torque response of the motor under single phasing

Assessment Parameter	**Speed**	**Torque**
% Change in amplitude	-0.19	-1.44
Amplitude of oscillation	14.8 rpm	0.19 Nm
Frequency of oscillation (Hz)	50	50

C. Two switches open on two separate bridge arms

Double-switch fault in different bridge arms can either involve two switches on separate bridge arms but at the same arm position or at different arm positions. In this work, the former is tested by simultaneously removing gate signals for the switches S1 and S3. Prior to the occurrence of this fault, the motor is running under steady state operating conditions, at no-load. This section presents the results of voltage, current, speed and torque response of the motor under this fault.

Fig. 7.24 shows the time-domain response of both voltage and current when the motor is subjected to this type of fault at t = 12.46 seconds after data acquisition has started.

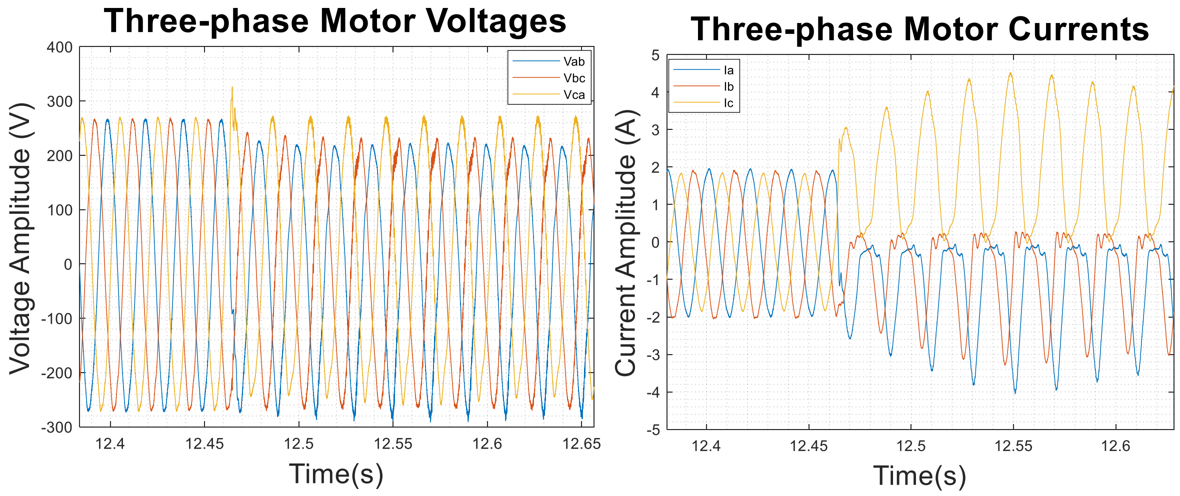

(a) **(b)**

Fig. 7.24: Three-phase **(a)** voltage and **(b)** current response with S1 and S3 open circuited

It is evident from the time domain representation of the voltages that the occurrence of the fault has caused changes in amplitudes and brought about unbalance in both line voltages and currents. From Fig. 7.24(b) it is observed that the positive half cycles of waveforms of currents I_a and I_b have been eliminated leaving only the negative half cycles with increased amplitudes. Consequently, the negative half cycle of the waveform of I_c is eliminated. The overall characteristic changes in current and voltages are presented in Table 7.11. There is an increase in distortion in all line voltages and currents with V_{ab} and I_a experiencing the greatest distortion.

Table 7.11: Voltage and current response of the motor when S1 and S2 are open circuited

Assessment Parameter	**Voltage**			**Current**		
	V_{ab}	V_{bc}	V_{ca}	I_a	I_b	I_c
% Increase in THD	50.8	31.2	37.9	78.8	74.9	36.4
% DC offset	-0.61	-5.18	6.08	-65.4	-43.7	112
% Change in amplitude of the fundamental	-16.6	-12.8	0.22	89.5	54.7	139
% Unbalance	11.7			100		

There is slight increase in DC component in line voltages V_{bc} and V_{ca} of approximately equal magnitude but opposite polarity. Similarly, there is also increase in DC offset current in I_a and I_b but it is not as substantial as that in I_c. It is this increased DC current that will result in excessive heating of the motor, leading to winding insulation breakdown and the likely total damage of the motor if this fault is not addressed in time.

Finally, Fig. 7.25(a) and (b) show speed and torque response, respectively, of the motor under this fault. It shows both the pre-fault and post-fault response. From Fig. 7.24(a), it is observed that before the occurrence of the fault, the motor is rotating at steady state speed of about 2973 rpm. When the fault occurs, speed drops to an average angular speed of 2963 rpm, and starts pulsating about this value. The amplitude and frequency of the speed pulsations is approximately 31.82 rpm and 50 Hz respectively.

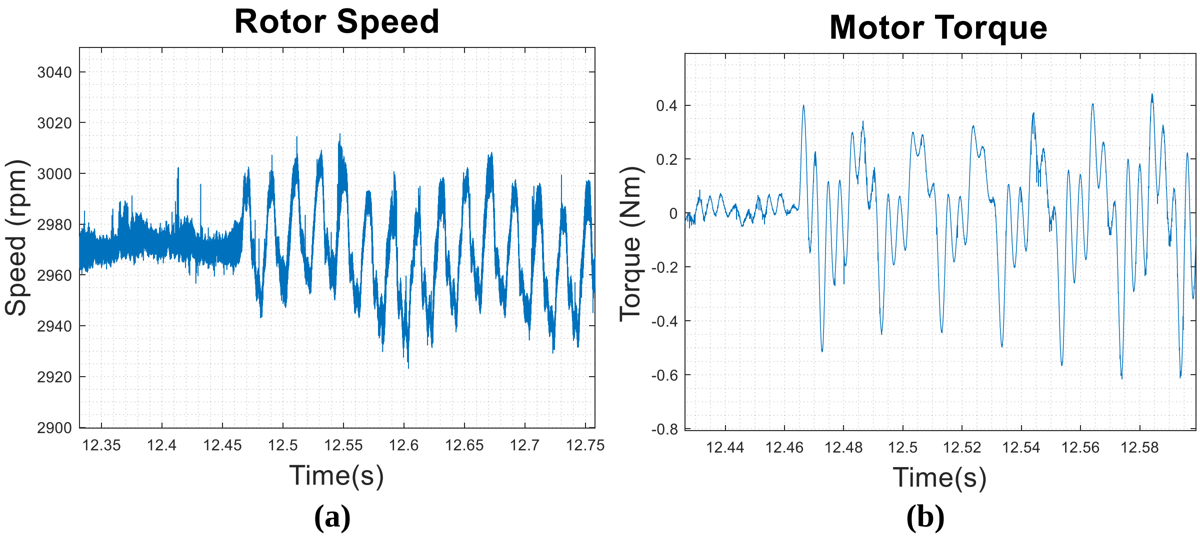

Fig. 7.25: **(a)** Speed and **(b)** torque response when S1 and S3 are open circuited

The same can be said about the torque of the motor. The motor is unloaded, so before the fault, its steady state torque is 0.0119 Nm. However, when the fault occurs, the torque drops slightly and start pulsating at 50 Hz frequency and with an average amplitude of approximately 0.50 Nm, which is about 60% of the motor's rated torque. The torque pulsations are more rigorous that in the case of a single switch open switch fault. These characteristics changes in motor speed and torque caused by this fault are summarized in Table 7.12.

Table 7.12: Speed and Torque response of the motor when S1 and S3 are open circuited.

Assessment Parameter	Speed	Torque
% Change in amplitude	-0.32	-3.5
Amplitude of oscillation	31.82 rpm	0.506 Nm
Frequency of oscillation (Hz)	50	50

D. Concluding Remarks

In this section, the experimental results for single switch open switch fault, single phasing fault and double switch open switch fault were presented to analyse their impact on the operation of the induction motor. Variables studied were the voltage, current, speed and torque of the motor. In reference to the motor voltage and current, the single phasing fault is the least severe fault of the three, in terms of the increase in distortion, increase in DC offset, changes in the amplitude of the fundamental component. The most severe fault, showing excessively high increase in THD, voltage and current unbalance and increase in DC offset is the double switch open switch fault. This assertion is more so when we consider the impact of these faults on the speed and torque of the motor. It is observed across the three faults that both torque and speed decrease slightly before they start to pulsate when each of the faults occurs. However, double switch open switch fault showed relatively greatest drop in speed and torque coupled with the largest amplitude of oscillations for both of these variables than the other two faults. Despite the increased amplitude of torque pulsations, the torque pulsations in double switch open switch fault were vigorous than in the other two faults. In single phasing fault, the torque pulsations were rather smooth with less noise. It is also worth noting that the experimental results are consistent with the simulation results for all of these faults. The next section presents the diagnosis of these three faults.

7.6 Inverter Open-Switch Fault Diagnosis

Finally, inverter open-switch fault diagnosis is carried out on both simulation and experimental data to detect inverter open-switch faults and identify the faulty switch. The diagnosis method employed here uses the measured motor current to detect and localise an open-switch fault. This method was described in detail in section 4.4.3 of this report. This section presents both simulation and experimental results using this diagnosis method.

7.6.1 Simulation Results

Three distinct fault scenarios were simulated in MATLAB Simulink: Single switch open switch fault, single phasing fault, and double switch open switch fault. This section presents the simulation results.

A. Single Switch Open-circuit Fault

Fig. 7.26 shows the diagnostic results of what happens to the diagnostic variables and the normalized currents average values when a single switch is open circuited. For the purposes of comparing the results for the top and bottom switches, Fig. 7.26(a) and (b) are the results of opening switches S1 and S4 respectively. For the respective switches, open-circuit fault is introduced by removing the corresponding gate signals at t = 2.5 s. From Fig. 7.26(a), the diagnostic variable of the faulted phase e_a increases and reaches 0.119 while the other diagnostic variables, e_b and e_c, decrease and converge to -0.022 and -0.072 respectively. So, $k_f \leq e_a < k_d$. Consequently, from equation (4.8), $E_a = P$, while $E_b = E_c = N$. Fig. 7.26(a) also shows a large negative average current in phase A (labelled IaNA). Hence, from equation (4.9), $M_a = L$ since average current, $\langle i_{aN} \rangle < 0$. These two conditions corresponds to the second row of Table 4.1. Therefore, S1 is open circuited.

By similar analysis, in Fig. 7.26(b), $e_a = 0.12$, $e_b = -0.021$ and $e_c = -0.059$. Therefore, $E_a = P$ and $E_b = E_c = N$ as before. However, IaNA $= \langle i_{aN} \rangle > 0$, which means $M_a = H$. Consequently, this combination correspond to row 5 of Table 4.1. Consequently, S4 is open circuited.

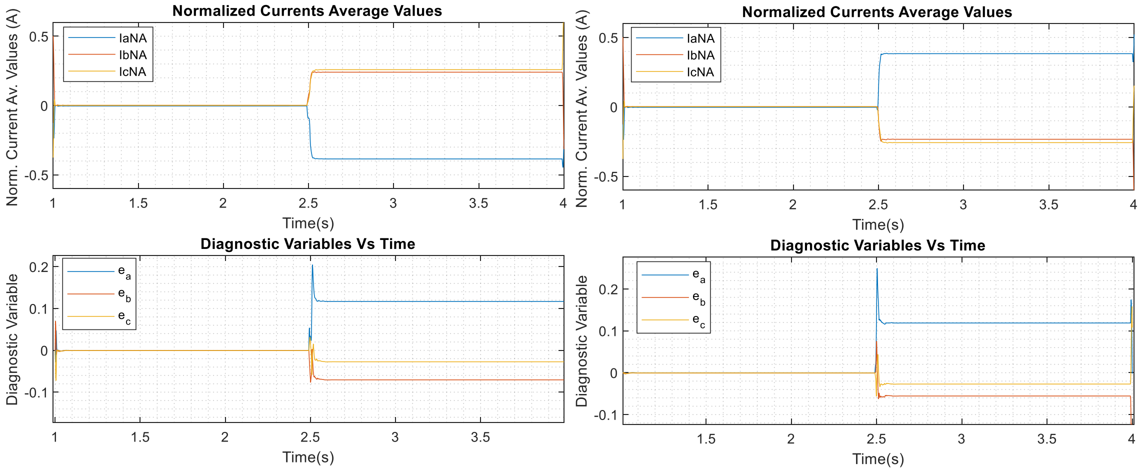

(a) **(b)**

Fig. 7.26: Normalised currents average values and diagnostic variables for single switch open circuit in switch **(a)** S1 and **(b)** S4

B. Single-phase Open-circuit Fault

Fig. 7.27 shows the diagnostic results of having both S1 and S4 open circuited. Similarly, the gate pulses are removed at t = 2.5s. This effectively results in an open-circuit fault in phase A.

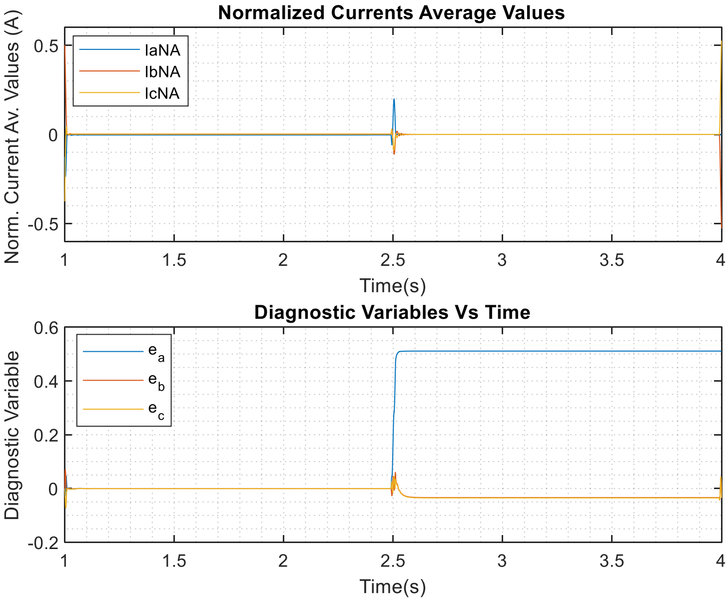

Fig. 7.27: Normalised Currents Average values and Diagnostic variables for single-phase open-circuit Fault

When this fault occurs, the diagnostic variable, e_a increases and reaches a final value of 0.501 while the other two diagnostic variables both decrease to a value of -0.04. The value of $e_a = 0.501$ is greater than the threshold $k_d = 0.32$. Therefore, $E_a = D$. So, according to row 8 of Table 4.1, this means that S1 and S4 are open circuited.

C. Double Switch Open-circuit Fault

Finally, Fig. 7.28 shows the diagnostic variables along with the normalised currents average values when both S1 and S3 are open circuited, thus establishing a double switch open-circuit fault. The fault is still introduced by the removal of the gate signals of the respective switches at time t = 2.5s. It is observed that the diagnostic variables for the affected phases, e_a and e_b increase, attaining final values higher than the threshold, $k_f = 0.08$, while e_c decreases to a value of -0.225. So, based on equation (4.8), $E_a = E_b = P$ and $E_c = N$.

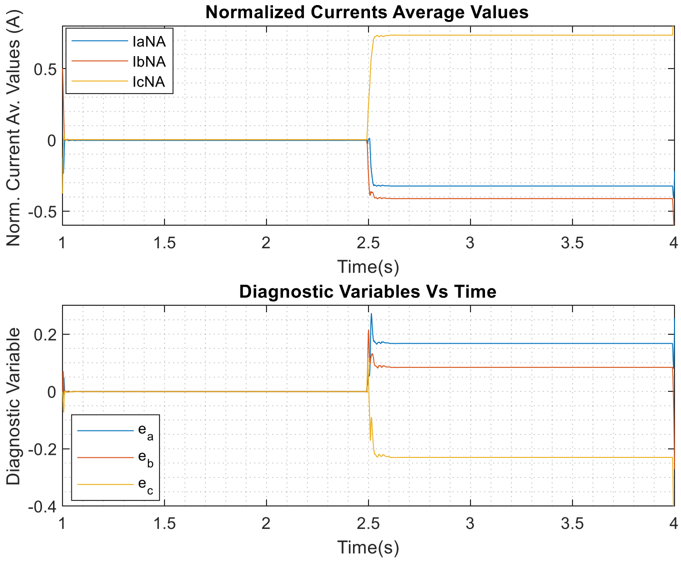

Fig. 7.28: Normalised Currents Average values and Diagnostic variables for double switch open-circuit Fault

On the contrary, the normalised currents’ average values for phases A and B are negative while it is positive for phase C. Therefore, from equation (4.9), $M_a = M_b = L$ and $M_c = H$. Therefore, according to Table 4.1, this combination means that both S1 and S3 are open circuited.

7.6.2 Experimental Results

In this work, the switch faults are user-controlled using F28335 microcontroller. The faults are realized by removing the gate signal of the corresponding switch. The experimental results presented here are for three distinct fault scenarios: single switch open-circuit fault, single-phase open-circuit fault, and double switch open-circuit fault.

A. Single Switch Open-circuit Fault

Fig. 7.29(a) and (b) show the experimental results for the normalized current average values and the diagnostic variables open circuit fault in S1 and S4 respectively. These experimental results are similar to the results obtained through simulations and depicted in Fig. 7.26.

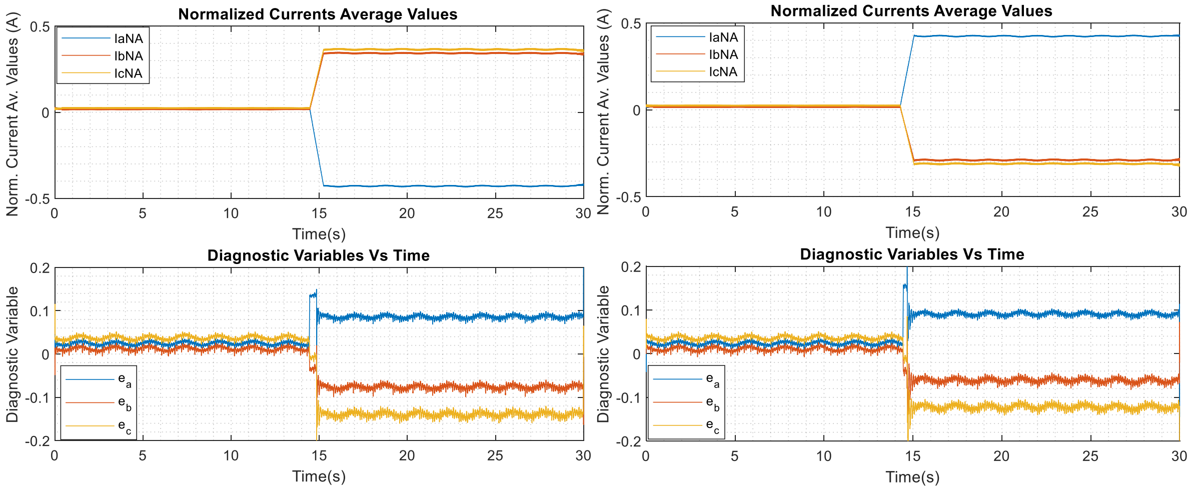

(a) **(b)**

Fig. 7.29: Normalised Currents Average values and Diagnostic variables for single switch open circuit in switch **(a)** S1 and **(b)** S4

Before the occurrence of the fault, it is observed that both the diagnostic variables and the normalised current average values are approximately equal to zero. However, when the fault is introduced at approximately 14.5446 seconds, all the variables show the same behavioural pattern that was reflected by the simulation results. Therefore, using the defined threshold alongside the diagnostic fault signatures provided in Table 4.1, the faulty switch is identified. In Fig. 7.29(a), the diagnostic variable, e_a, rises to a positive value of 0.091773 while the other diagnostic variables e_b and e_c drop to a final value of -0.058278 and -0.12064, respectively. Thus, $E_a = P$ and $E_b = E_c = N$. Meanwhile, the normalised current average value for phase A, $\langle |I_{aNA}| \rangle$, is negative. Thus, $M_a = L$. Hence, according to Table 4.1, switch S1 is, admittedly, open circuited.

B. Single-phase Open-circuit Fault

Likewise, Fig. 7.30 shows the experimental results for the normalized currents average values along with the three diagnostic variables when switches S1 and S4 are open circuited, thus creating a single-phasing fault.

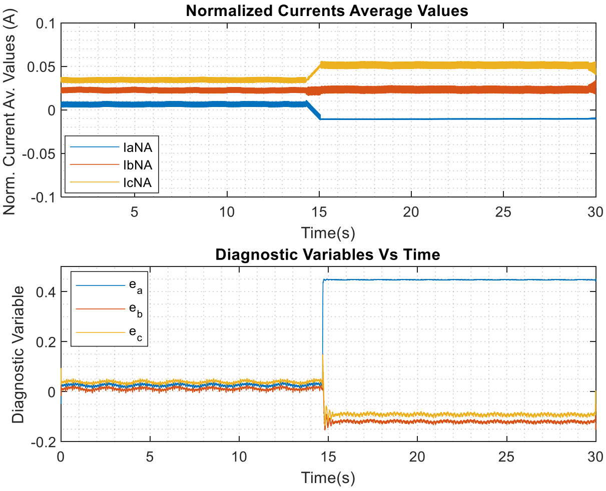

Fig. 7.30: Normalised Currents Average values and Diagnostic variables for single-phase open-circuit Fault

It is observed here that the normalized current average values are negligibly small, indicating that there is negligibly small DC component of current. However, the diagnostic variable for phase A, e_a, increases to a positive value of 0.44726, which is greater than the defined threshold $k_d = 0.32$. Hence, $E_a = D$. The other errors, e_b and e_c decreased to the negative values of -0.08991 and -0.11703 respectively. In reference to the diagnostic signatures of Table 4.1, these indicate a single-phase open circuit on phase A (i.e., both S1 and S4 are open circuited).

C. Double Switch Open-circuit Fault

Finally, Fig. 7.31 shows the normalised current average values and the three diagnostic variables for double switch open-circuit fault on S1 and S3. These results agree with the simulated results. Following the occurrence of the fault in phases A and B, the diagnostic variables for these phases increase and reach approximately the same final positive value, which is greater than the threshold $k_f = 0.08$, while the e_c decreases and assumes a negative value. The normalized current's average values are also similar to their simulated counterparts. So, the observed fault signature from Table 4.1 is the same, indicating that the faulty switches are S1 and S3.

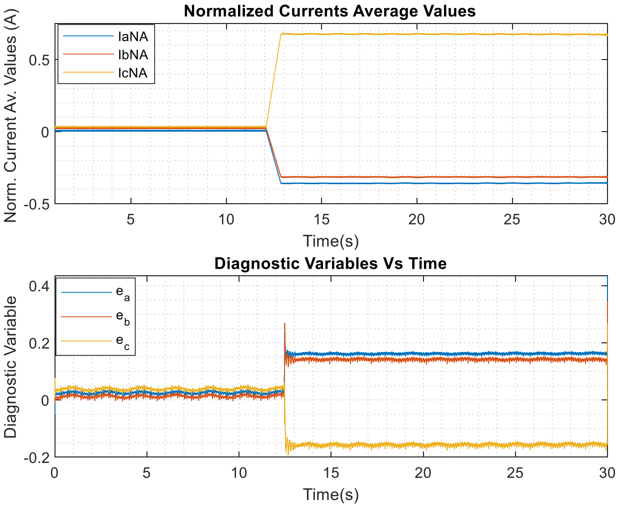

Fig. 7.31: Normalised Currents Average values and Diagnostic variables for double switch open-circuit Fault

7.6.3 Concluding Remarks

This section presented the diagnosis of inverter open switch faults using both simulation and experimental data. The results obtained from both simulations and experimental data for the diagnosis of inverter open switch faults using the diagnostic variables technique concur and are consistent with the results presented in [17], [20] and [21] and reviewed in section 4.2.3 of these report. The diagnosis method used here employed both diagnostic variables and normalized average current values to detect and localise open switch faults. Therefore, the method of diagnostic variables is valid for the detection of inverter open switch faults of the test induction motor drive. The next section presents the results of MCSA applied in grid-connected induction motors.

7.7 MCSA in Grid-Connected Induction Motors

Two test induction motors, one healthy and one with broken rotor bar are tested. This section presents experimental results when these motors are connected to the grid, and the acquired data is analysed using MCSA. The tests examine the capabilities of MCSA in detecting broken rotor bar faults with varying load.

7.7.1 MCSA No-Load Versus Full-Load – Experimental Results

The faulty motor was tested under no-load and full load conditions to investigate the ability to detect the fault sideband harmonics using MCSA in each loading condition. This section presents the results of the tests when the motor is supplied from the grid. The healthy motor is used to benchmark the results of the faulty motor.

A. Unloaded motor

The PSD of phase A current, I_a, for both the healthy and broken rotor bar motors under no load condition are shown in Fig. 7.32. Under the no-load condition, it is observed that the first order fault sideband harmonics are unidentifiable as they overlap the fundamental component. Under this loading condition, the left and right sideband harmonics are 49.5 Hz and 50.5 Hz as determined from the value of slip.

The inability to confidently detect or identify these fault sideband harmonics for unloaded faulty motors poses a problem since it defeats the very objective of condition monitoring, which is to detect faults at their incipient stages so that they are addressed before they become severe.

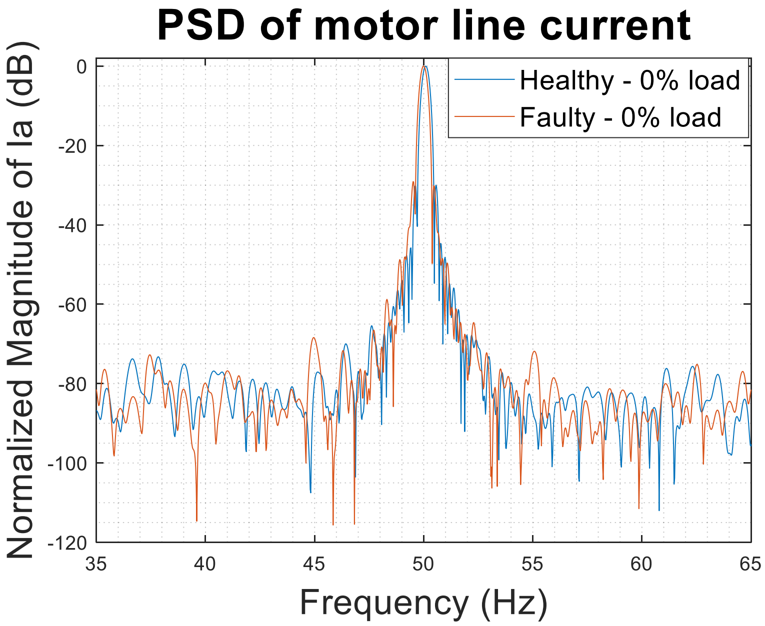

Fig. 7.32: PSD results of unloaded healthy and faulty motor

B. Fully loaded motor

On the contrary, if the machine is heavily loaded, the first order sideband harmonics are seen to spread out and are further from the fundamental component, making them easily detectable. Fig. 7.33 shows the PSD of phase A current, I_a, for the healthy and broken rotor bar motor at full load. The sideband in the faulty motor are greatly amplified in comparison with the healthy motor. The first order sideband harmonics are located at 47.5 Hz and 52.5 Hz. Three subsequent fault sideband harmonics are at 45.0 Hz, 42.5 Hz and 40.0 Hz on the left-hand side of the fundamental harmonic, and at 55.0 Hz, 57.5 Hz and 60.0 Hz on the right-hand side of the fundamental component.

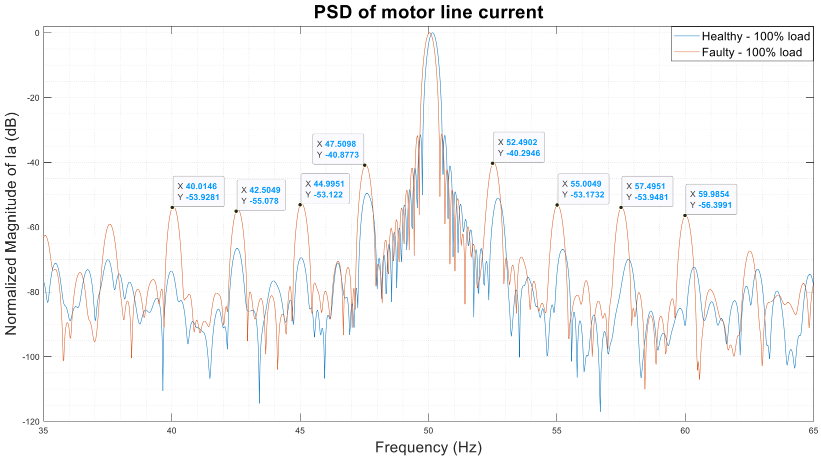

Fig. 7.33: PSD results of loaded healthy and faulty motor

Under full load conditions, the speed of the machine is relatively lower than the speed at no-load, resulting in a relatively larger slip value, hence sideband harmonics that are further away from the fundamental component.

7.7.2 Effect of Load Level Variation on MCSA

The broken rotor bar motor was loaded with different loads to observe ability to detect the sideband harmonics at different loads. The slip changes as the load on the motor changes, and so does the position of sideband harmonics. Fig. 7.34 shows the evolution of the first order sideband harmonics as the load increases from 0% to 50%, to 75%, to 88% and finally to 100%.

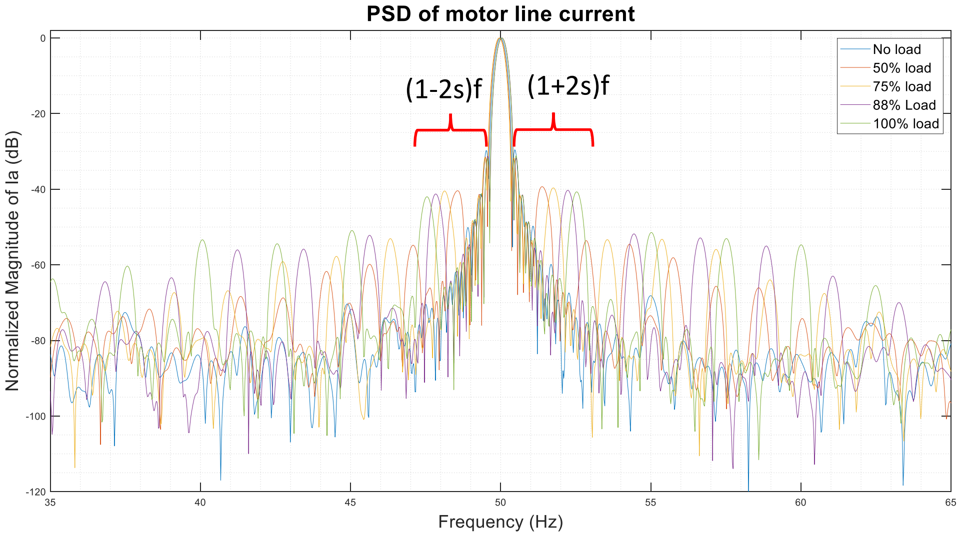

Fig. 7.34: PSD of current at different load levels – faulty motor

From Fig.7.34, at no-load the sidebands overlap with the fundamental harmonic component (as before) and hence are difficult to identify. However, at 50% of the rated torque, the harmonics are well amplified and very visible, as they become spread out. The left and right first order ($k = 1$) sideband harmonics are at frequencies 48.6 Hz and 51.4 Hz respectively. As the load changes to 75%, 88% and finally to 100%, these fault sidebands harmonics become more and more spread out, going further away from the fundamental component and become positioned at 48.2 Hz and 51.8 Hz, 47.8 Hz and 52.2 Hz, and 47.5 Hz and 52.5 Hz for the respective load levels. So, as the load is increased, the sidebands move outwards proportionately.

7.7.3 Concluding Remarks

This section presented MCSA results for the grid connected motor. At no load, due to small operating slip, the first order sideband harmonics overlap the fundamental component, hence are unidentifiable. These results are consistent with the results presented in [6], [11], [74], [76] and reviewed in detail in section 4.3 of this report. When the load is gradually increased, the sideband harmonics move further from the fundamental component and are well amplified. At full load, they are furthest from the fundamental component. This is consistent with the results presented in [19], [65] and [74] and reviewed in section 4.3. The next represents the results when the same tests are performed on an inverter-fed induction motor.

7.8 MCSA in Inverter-Fed Induction Motors

Likewise, one healthy and one with broken rotor bar are tested here. They are fed through the inverter, and the acquired data is analysed using MCSA. The results are presented in this section. As in the previous section, the tests examine the capabilities of MCSA in detecting broken rotor bar fault when the machine is unloaded (or lightly loaded), and when the motor is fully loaded. It also analyses the impact of gradually increasing the load level in the ability to detect the broken rotor bar fault.

7.8.1 MCSA No-Load Versus Full-Load – Experimental Results

The faulty motor was tested under no-load and full load conditions, and MCSA technique applied to the stator current in each case. This section presents the results for the respective cases.

A. Unloaded Motor Results

Fig. 7.35 shows the PSD results of phase A current, I_a, for both the healthy and broken rotor bar motors under no load. Relative to the case of grid-connected motor (Fig. 7.32), it is observed here that the spectrum contains a lot of noise.

Under the no-load condition, it is observed that first order fault sideband harmonics are unidentifiable as they are too close to the fundamental component and hence are masked by the fundamental and inverter switching noise. Based on the operating value of slip at no-load, the first order sideband harmonics should be at frequencies 49.1 Hz and 50.9 Hz for the left and right sideband harmonics, respectively.

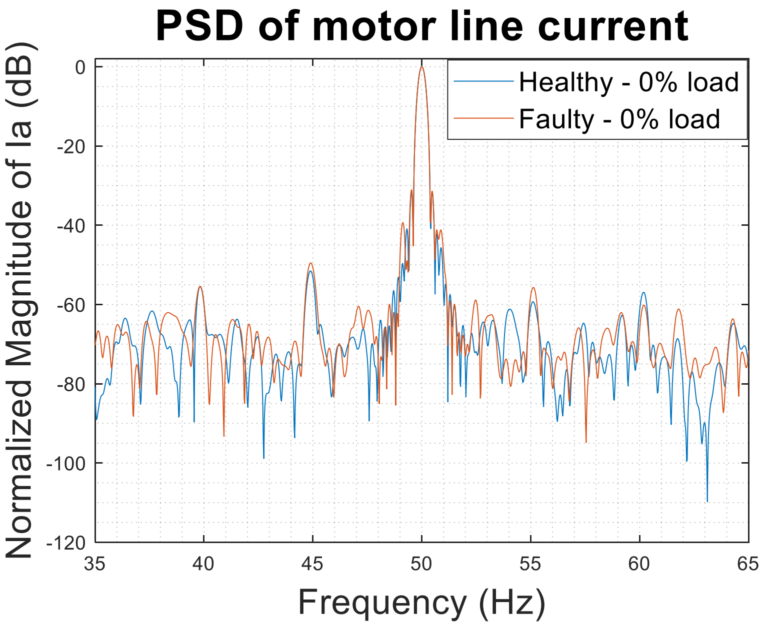

Fig. 7.35: PSD of current of inverter-fed motor at no-load

B. Fully Loaded Motor Results

On the contrary, if both the healthy and the broken rotor bar machines are fully loaded, their PSD is as shown in Fig. 7.36.

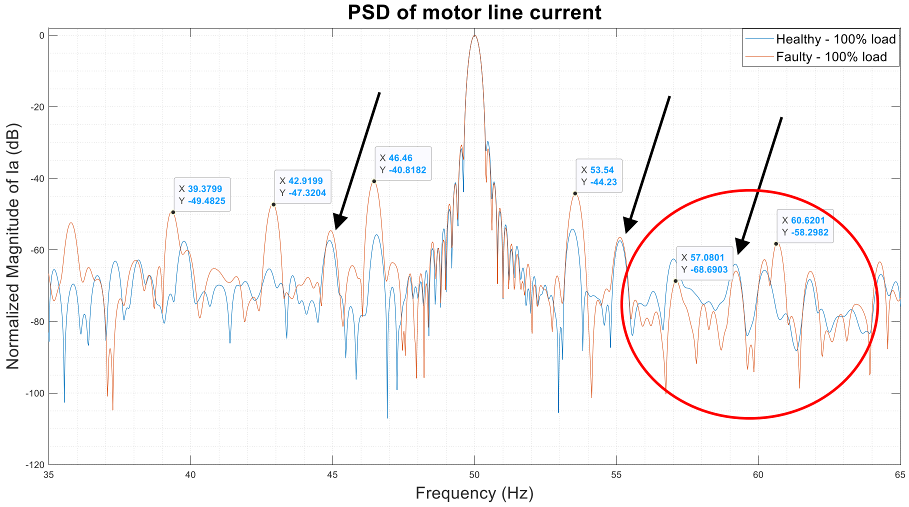

Fig. 7.36: PSD of current of inverter-fed motor at Full load

Under full load conditions, the first order left and right sideband harmonics are appreciably far from the fundamental component and are clearly recognizable. They are at approximately at frequencies 46.5 Hz and 53.5 Hz respectively. There is a lot of interference from the inverter switching harmonics when higher order sideband harmonics (k > 1) are considered, as indicated by the arrows in Fig. 7.36. In this higher order sideband, the degree of amplification of the sidebands in the broken rotor bar motor is low as in the case of circled harmonics.

7.8.2 Effect of Load Level Variation on MCSA

The broken rotor bar motor was loaded with different loads to observe ability to detect the sideband harmonics at different loads when the motor is fed through a voltage source inverter. This section presents the results for this test.

The PSD of phase A current, I_a, at different load levels is shown in Fig. 7.37. Four load levels – no load, 50% load, 75% load and full (100%) load are considered.

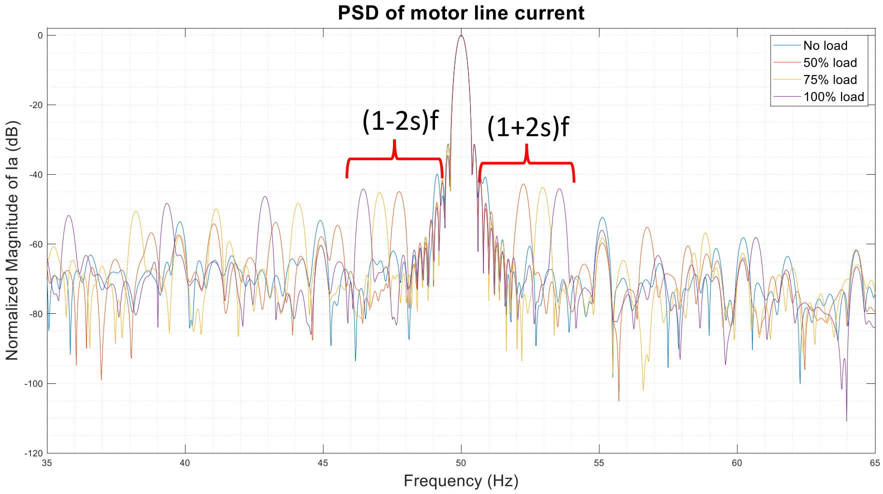

Fig. 7.37: FFT of current at different load levels – faulty motor

At no-load, the sidebands are not easily identifiable since they overlap with the fundamental component. When the load is increased to 50% of the rated load, they move outwards to frequencies 47.7 Hz and 52.3 Hz. When the load is increased slightly from 50% to 75%, the outward movement of the sidebands is also slightly less than it was when the load increased from 0% to 50% load. In this case, the distance of the sidebands from the fundamental increased slightly, as they are now positioned at 47.0 Hz and 53.0 Hz. Finally, as the load increases to 100%, the fault sideband harmonics move farther away from the fundamental and are positioned at frequencies 46.5 Hz and 53.5 Hz. It is therefore conclusive that, with PSD, the sideband harmonics are visible at all load levels, and they spread out as the load is increased. The sideband harmonics at no-load overlap the fundamental component and at full load, the sideband harmonics are the farthest from the fundamental component. Despite the increasing load, the sideband harmonics seem to have approximately the same amplitude (magnitude). So, the amplitude of the sidebands is not load dependent.

7.8.3 Concluding Remarks

In this section, the results of MCSA for inverter-fed broken rotor bar faulted motor were presented. Similar to grid connected motors, at no load, the first order sideband harmonics overlap the fundamental component and are unidentifiable. However, as the load increases, the sidebands move outwards from the fundamental component and can easily be identified as it was reviewed in section 4.3. The higher the load, the further they are from the fundamental, just as it was the case with the grid connected motor. Contrary to the results of the grid-connected faulty motor, there is a lot of interference from switching harmonics when higher order harmonics are considered, and the degree of amplification of these higher order harmonics is not large enough to characterise the fault. As a result, it is difficult to confidently diagnose the motor as faulty based on these MCSA results alone. The next section represents the results of an alternative technique that can be used to supplement MCSA for inverter-fed induction motors.

7.9 Standstill Impedance Variation Test – Grid-Connected Motor

The experimental test is set up as shown in Fig. 6.5 and the circuit schematic shown in Fig. 6.4. The rotor position was then manually varied from 0 through to 360 degrees. The corresponding time-domain voltage and current signals under this configuration and with rotor angle at position 0 degrees are shown in Fig. 7.38.

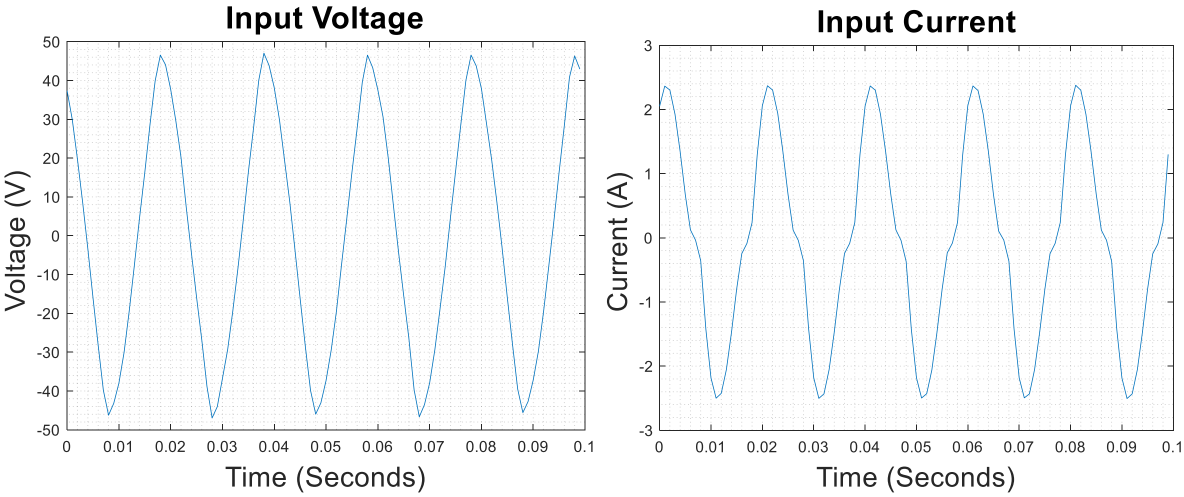

(a) **(b)**

Fig. 7.38: Current and voltage signals with 2 phases shorted; **(a)** voltage, **(b)** current

These voltage and current signals are clean and do not contain much noise. However, the current signal is distorted and does not reflect a perfect sinusoidal signal.

From these profiles of the current and voltage signals, captured at different rotor angles, impedance is calculated for each rotor position for both the healthy and the broken rotor bar motors. The results are shown in Fig. 7.39. It is evident that the impedance of the healthy motor is relatively constant for all rotor positions.

However, the impedance of a broken rotor motor varies almost sinusoidally with the rotor position, just as it was shown in [73], [84] and [85], while that of the healthy motor is constant. This variation of impedance with rotor position is characteristic of rotor asymmetry associated with the broken rotor bars. As seen from Fig. 7.39, the maximum and minimum impedance registered is 18.2297 Ω and 16.8626 Ω, giving rise to a total change of 1.3671 Ω – 7.79% of the average impedance of the motor, which is characteristic of the broken rotor bar fault. These results will be used as benchmark to assess the effectiveness of this approach in its application to inverter fed squirrel cage motors.

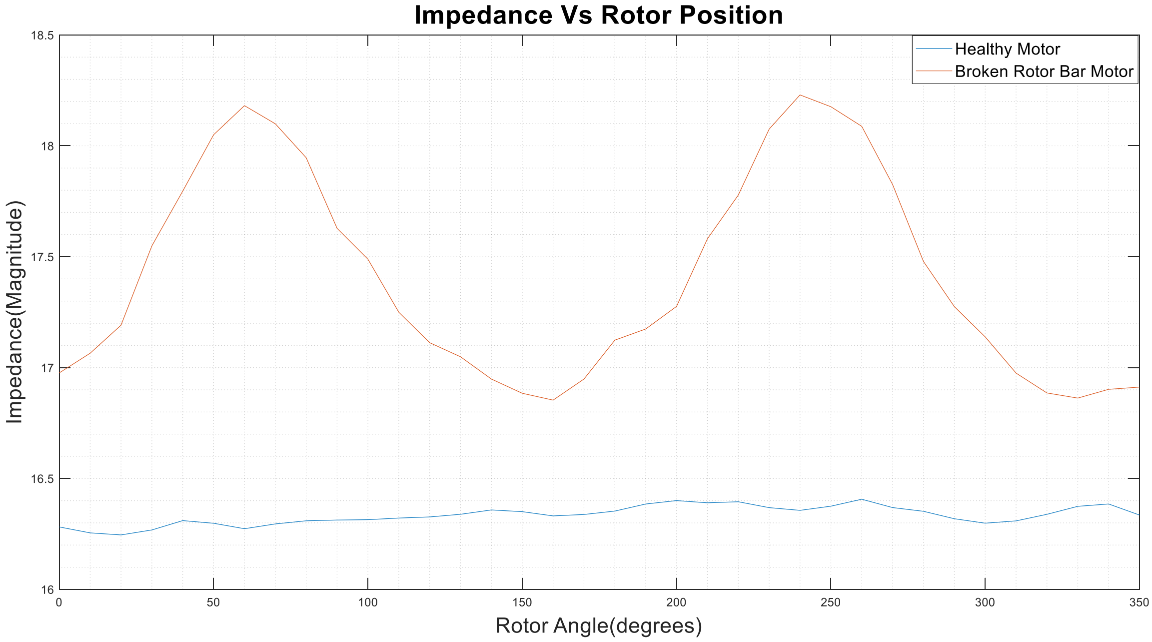

Fig. 7.39: Standstill Impedance variation for grid-connected motor

7.10 Standstill Impedance Variation Test – Inverter-Fed Motor

This section presents experimental results for two distinct tests scenarios. In the first scenario, a fixed pulsating magnetic flux is produced through the use of inverter switching as described in section 4.3.3, and the rotor is rotated in steps from 0º to 360º. In the second scenario, the rotor is fixed, while the orientation of the pulsating flux is rotated by 120º twice by utilizing the 120º spatial displacement of 3-phase windings of the 2-pole machine to obtain sets of 3 impedances for each rotor orientation as described in section 4.4.3.

7.10.1 Scenario 1: Fixed Pulsating Magnetic Flux and Rotating Rotor

Standstill impedance variation test using the inverter switching configuration is implemented as already described in section 4.4.3 of this report. In this case, phases A and B were shorted and supplied through phase C, and rotor position varied from 0 to 360 degrees in steps of 10° increment. The time-domain voltage and current signals under this configuration and with rotor angle at position 0 degrees are shown in Fig. 7.40.

It is observed from Fig. 7.40(a) that V_{ab} is zero, while the other line voltages are non-zero but are greatly distorted and noisy. Likewise, the current is also distorted, and as expected, the phase current I_c is twice the other two phase currents, which are approximately equal. Except for the increased noise in the voltage and from a single-phase point of view, these results are similar to the results presented in Fig. 7.38 for grid-connected standstill impedance variation test.

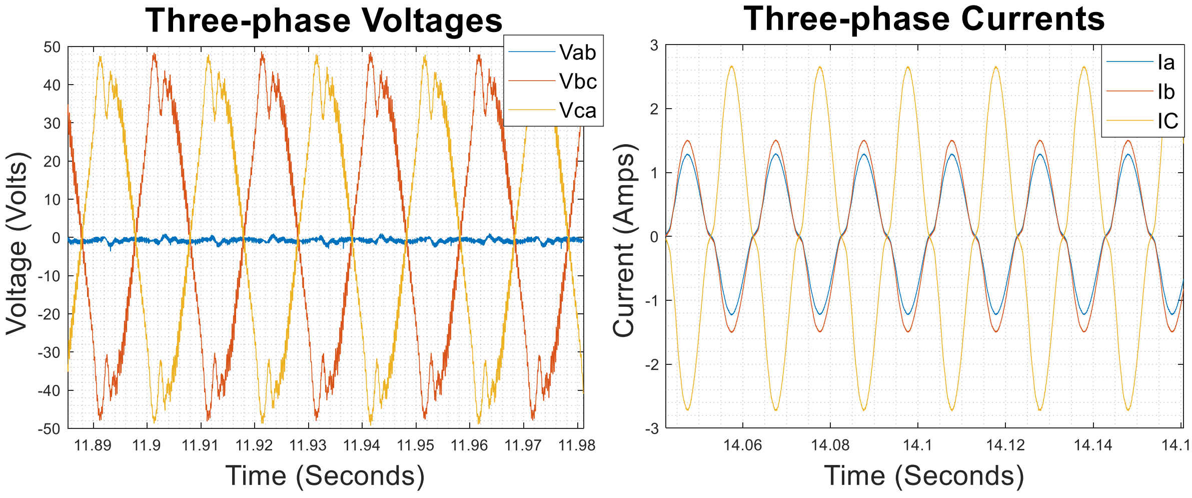

(a) **(b)**

Fig. 7.40: Current and voltage signals with phase A and B shorted; **(a)** voltage, **(b)** current

Fig. 7.41 shows the impedance variation of the healthy and broken rotor bar motor with the rotor position. Evidently, despite the presence of switching noise in both voltage and current signals, the results show that the impedance pattern is as expected in both motors – constant for the healthy motor, and sinusoidally varying for the broken rotor bar motor.

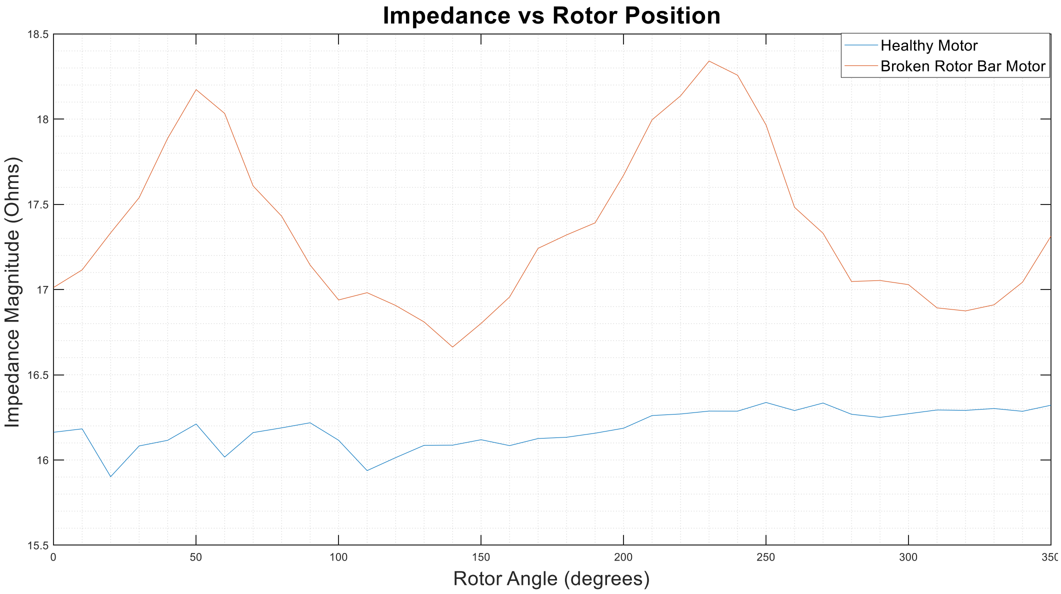

Fig. 7.41: Standstill Impedance variation for Inverter-fed motor

This means the inverter harmonics do not seem to have a noticeable impact on the variation of impedance with rotor position. They do not mask this variation at all. A closer look at Fig. 7.41 depicts that the maximum impedance reached is 18.3407Ω while the minimum value is 16.6625Ω. This gives rise to a change in impedance of 1.6782Ω – 9.59%, characteristic of the broken rotor bar fault as described in section 4.4.1. Likewise, these results are similar to the results presented in Fig. 7.39 for the grid-connected standstill impedance variation test.

7.10.2 Scenario 2: Fixed Rotor and Rotating Pulsating Magnetic Flux

In this test, the rotor is fixed, but the orientation of the pulsating magnetic field is changed by changing the phases which are shorted as described in section 4.4.3. Three respective impedances, Z_a, Z_b and $Z_{c,}$ at each rotor position are determined are then determined. Fig. 7.42 shows a plot of these impedances against rotor position.

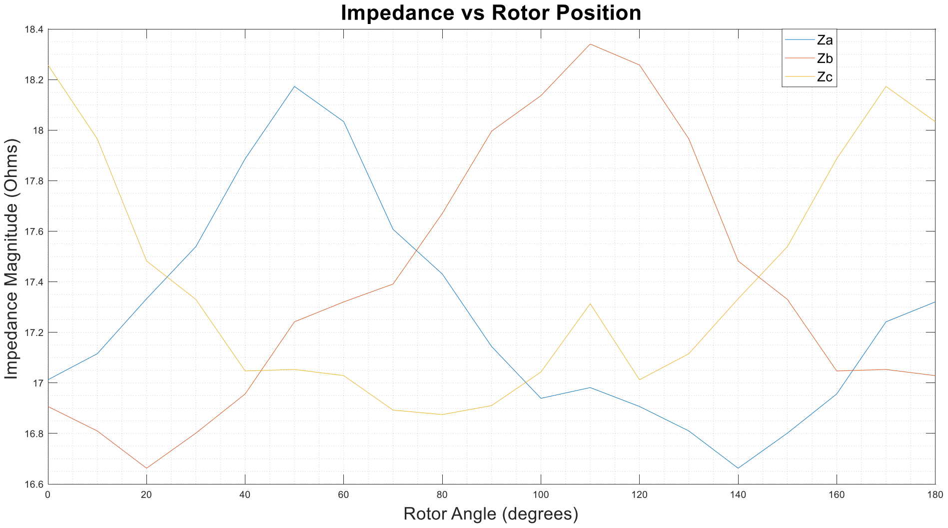

Fig. 7.42: Phase impedance at various rotor positions

It is observed that the three impedances profiles are 120º out of phase as it was deduced in section 4.4.3 and shown in Fig. 4.15(a). The average of the absolute values of the difference in impedances obtained for each rotor orientation is calculated and plotted against the rotor position. This is shown in Fig. 7.43. These results are similar to the analytical results presented in Fig. 4.15 in chapter 4. The critical rotor positions are at 30°, 70° and 150° as highlighted by the red circles.

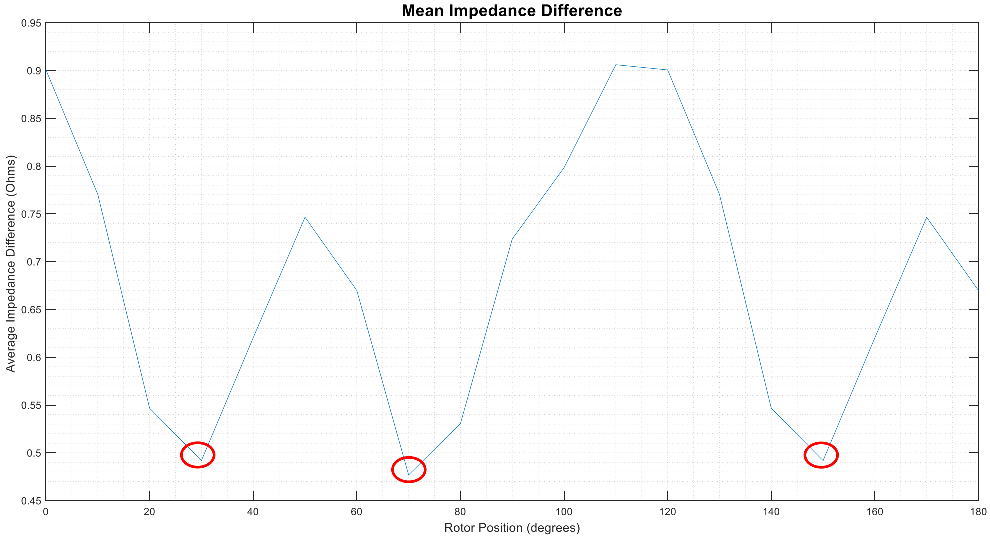

Fig. 7.43: Critical Rotor Positions for Standstill Impedance variation Test

These are orientations/positions of the rotor at which there is no significant changes in impedance along each of the three-magnetic axis associated with the stator windings. These positions are circled red in the figure above. It is noteworthy that the rotor positions here are taken from 0° to 180° because that covers one cycle of impedance variation.

7.10.3 Concluding Remarks

This section (7.10) presented the results of two test scenarios for the standstill impedance variation test for the inverter-fed induction motor. In scenario 1, the flux was kept pulsating along the magnetic axis of phase C and the rotor position was changed/varied. Despite the evidence of distortion in the voltage and current signals at each rotor position (Fig. 7.40), the impedance varies sinusoidally with rotor position in the broken rotor bar motor, just as it was the case in the grid connected case, whereas it is constant in the healthy motor. The variation in impedance is large enough to characterize the presence of the broken rotor bar fault. These results are similar to those obtained in [73], [84], [85] and in this work for the grid-connected case. Thus, the presence of inverter switching harmonics do not mask the variation of impedance with the rotor position.

In scenario 2, the rotor position is momentarily fixed at an arbitrary position and the axis of the pulsating flux is rotated three times, by 120º each time, in accordance with the magnetic axis of the three-phase windings. The rotor is then momentarily fixed in a different position and the procedure repeated, until the rotor has been rotated through 180º, thus covering one cycle of impedance variation. The results show that at each rotor position, the three impedances obtained along each magnetic axis show mean large differences to characterize the fault except at when the rotor is at 30°, 70° and 150° relative to the chosen reference position. These positions are described as critical rotor positions since, at these positions, the variation in impedance is quite small to confidently characterize the broken rotor bar fault, which could lead to the possible misdiagnosis of the fault.

Chapter 8: Conclusions and Recommendations

8.1 Conclusions

The squirrel-cage induction motor is greatly admired and preferred in industry and regarded as the workhorse of the industry. Nonetheless, most industrial applications requiring accurate speed and torque control require the induction motor to be fed through an inverter, thus constituting a variable speed induction motor drive.

A variable frequency drive was designed and built in this study. The drive was configured for open-loop constant Volt/Hertz control. Two main components of the drive – the inverter and the induction motor – were investigated for faults. Inverter open switch faults were investigated for their impacts on the performance of the connected induction motor and the method of diagnostic variables was investigated for its viability in the diagnosis, detection, and localisation of these faults. The induction motor was star connected and was studied for broken rotor bar fault. The MCSA technique was investigated for some of its shortcomings in detecting this fault for both grid-connected and inverter-fed motors. The suitability of a complimentary method, referred as standstill impedance variation method, was investigated for the detection of the broken rotor bar fault in grid-connected squirrel cage induction motor. This method is based on the variation of impedance with the rotor position. Finally, the applicability of this method in the detection of broken rotor bar fault in inverter-fed squirrel cage induction motor is investigated for use as a supplementary technique to MCSA.

In addition to increasing THD of the current and voltage signal fed to the motor, inverter open switch faults resulted in the injection of DC currents in the motor, the consequence of which is pulsating torque and speed. When these faults occur, they are accompanied by a slight drop in the amplitude of torque and speed, followed by pulsations of these quantities at a frequency of 50 Hz (the fundamental frequency). These faults also results in changes in the amplitudes of the fundamental components of current and voltage for different phases, which may result in heating up of the motor and hence damage to the insulation of the windings. They also increase voltage and current unbalance in the motor resulting in accelerated aging of the motor. In terms of relative severity, double switch open switch faults are the most severe, resulting in the most distortion and unbalance of the voltage and current signals, coupled with the most vigorous torque and speed pulsations. Single phasing fault is the least severe of all three in terms of increase in THD and torque and speed pulsations.

Despite MCSA’s robustness, some complexities of employing MCSA as a diagnostic tool in inverter-fed induction machines with broken rotor bar faults have been highlighted in this work. It is shown that at no-load, first order sideband harmonics associated with the broken rotor bar, overlap the fundamental component and are undetectable. This is because, under such loading levels, the slip is quite small, resulting in the first order sidebands that overlap with the fundamental component. This is true for both grid-connected and inverter-fed broken rotor bar motors. This may be more pronounced in its industrial applications where the set-ups are not ideal, and there are likelihood of low sampling frequencies, short acquisition times and other factors which may result in low data samples for processing with MCSA. It is only in heavily loaded conditions that the sideband harmonics move farther outwards from the fundamental component and are easily identifiable. Furthermore, in inverter-fed broken rotor bar motor, the higher ordered harmonics ($k > 1$) are difficult to identify due to interference from switching harmonics. These compromise the reliability of MCSA in the fault diagnosis of broken rotor bar faults for inverter-fed induction motors. Thus, alternative diagnostic techniques are needed to confirm the presence of broken rotor bar fault following diagnosis of this fault with MCSA.

This work further proposed a supplementary scheme, the standstill impedance variation test, could be used to verify whether there is some form of asymmetry introduced by the broken rotor bar fault. The standstill impedance variation test performed on the inverter-fed motor shows a large enough variation in impedance for different rotor positions, which can be used to supplement MCSA in detecting broken rotor bar faults for the inverter-fed motors. This was implemented in two ways. One way, was to fix the airgap flux pulsating along a known axis and vary the rotor position, calculating the impedance at each rotor position and then observe the variation in impedance as a function of rotor position. Another way was to fix the rotor and align the pulsating magnetic flux along each of the three magnetic axis of the three-phase windings and calculate the impedance along each magnetic axis. This showed a large change in impedance except when the rotor was fixed at positions 30°, 70° and 150° relative to the chosen reference position.

8.2 Recommendations

This work studied inverter open switch faults for a star connected squirrel cage induction motor controlled by an open loop Volts/Hertz method. This work can be extended by considering a closed loop Volts/Hertz control, and further studying the response of the motor when it is delta connected instead of open loop V/F control. Furthermore, in this work, the thresholds k_f and k_d, used in the diagnostic variables method, were chosen based on the work done by [21]. This work can be further extended by doing more research on the determination of these thresholds for the test motor.

REFERENCES

[1] K. T. Chau, "Induction Motor Drives," in *Electric Vehicle Machines and Drives: Design, Analysis and Application*, 1st ed., Wiley-IEEE Press, 2015, pp. 39–68. doi: 10.1002/9781118752555.ch3.

[2] H. Mohan, S. K. Dwivedi, and M. Kumar Pathak, "Control of Induction Motor Drives -Technological Advancements," *India Int. Conf. Power Electron. IICPE*, vol. 2018-Decem, 2018, doi: 10.1109/IICPE.2018.8709467.

[3] Y. Liu, L. Ralikalakala, P. Barendse, and P. Pillay, "Power Hardware-in-the-Loop based Emulation of An Induction Machine with Stator Winding Faults," *IECON 2021 – 47th Annu. Conf. IEEE Ind. Electron. Soc.*, pp. 1–6, doi: 10.1109/IECON48115.2021.9589711.

[4] Y. Liu, L. Ralikalakala, P. Barendse, and P. Pillay, "Power Electronic Converter Based Induction Motor Emulator With Stator Winding Faults," *IEEE Trans. Ind. Electron.*, vol. 70, no. 5, pp. 4440–4449, 2022, doi: 10.1109/TIE.2022.3189099.

[5] P.C. Sen, "Induction (Asynchronous) Machines," in *Principles of Electric Machines and Power Electronics*, Third., Jolene Ling, Ed. United States: John Wiley & Sons, Inc, 2014, pp. 207–291.

[6] J. Antonino-Daviu, M. Riera-Guasp, J. Roger-Folch, F. Martínez-Giménez, and A. Peris, "Application and optimization of the discrete wavelet transform for the detection of broken rotor bars in induction machines," *Appl. Comput. Harmon. Anal.*, vol. 21, no. 2, pp. 268–279, Sep. 2006, doi: 10.1016/j.acha.2005.12.003.

[7] F. J. T. E. Ferreira and A. T. De Almeida, "Overview on energy saving opportunities in electric motor driven systems - Part 1: System efficiency improvement," *Conf. Rec. - Ind. Commer. Power Syst. Tech. Conf.*, vol. 2016-June, pp. 1–8, 2016, doi: 10.1109/ICPS.2016.7490219.

[8] P. Waide and C. U. Brunner, "Energy-Efficiency Policy Opportunities for Electric Motor-Driven Systems," *Int. energy agency*, vol. na, no. na, p. 132, 2011.

[9] M. R. Mehrjou *et al.*, "Wavelet-Based Analysis of MCSA for Fault Detection in Electrical Machine," in *Wavelet Transform and Some of Its Real-World Applications*, InTech, 2015. doi: 10.5772/61532.

[10] L. Maraaba, Z. Al-Hamouz, and M. Abido, "An efficient stator inter-Turn fault diagnosis tool for induction motors," *Energies*, vol. 11, no. 3, Feb. 2018, doi: 10.3390/en11030653.

[11] , D. G., W. G. Aguilar, D. Arcos-Aviles, and D. Sotomayor, "Broken Bar Diagnosis for Squirrel Cage Induction Motors Using Frequency Analysis Based on MCSA and Continuous Wavelet Transform," *Math. Comput. Appl.*, vol. 22, no. 2, p. 30, Apr. 2017, doi: 10.3390/mca22020030.

[12] A. Choudhary, D. Goyal, S. L. Shimi, and A. Akula, "Condition Monitoring and Fault Diagnosis of Induction Motors: A Review," *Arch. Comput. Methods Eng.*, vol. 26, no. 4, pp. 1221–1238, Sep. 2019, doi: 10.1007/s11831-018-9286-z.

[13] H. Keskes and A. Braham, “Recursive Undecimated Wavelet Packet Transform and DAG SVM for Induction Motor Diagnosis,” *IEEE Trans. Ind. Informatics*, vol. 11, no. 5, pp. 1059–1066, Oct. 2015, doi: 10.1109/TII.2015.2462315.

[14] K. N. Gyftakis, J. A. Antonino-Daviu, R. Garcia-Hernandez, M. D. McCulloch, D. A. Howey, and A. J. M. Cardoso, “Comparative Experimental Investigation of Broken Bar Fault Detectability in Induction Motors,” *IEEE Trans. Ind. Appl.*, vol. 52, no. 2, pp. 1452–1459, 2016, doi: 10.1109/TIA.2015.2505663.

[15] B. Cui, “Simulation of inverter with switch open faults based on switching function,” *Proc. IEEE Int. Conf. Autom. Logist. ICAL 2007*, pp. 2774–2778, 2007, doi: 10.1109/ICAL.2007.4339053.

[16] S. E. Varghese and N. Reema, “Effects of Switching Faults on Induction Motor Drive System,” *Int. Res. J. Eng. Technol.*, pp. 607–611, 2016.

[17] J. O. Estima and A. J. M. Cardoso, “A novel diagnostic method for single power switch open-circuit faults in voltage-fed PWM motor drives,” *SPEEDAM 2010 - Int. Symp. Power Electron. Electr. Drives, Autom. Motion*, pp. 535–540, 2010, doi: 10.1109/SPEEDAM.2010.5545024.

[18] M. D. Kumar, S. F. Kodad, and B. Sarvesh, “Simplified Fault Detection Algorithm for Voltage Source Fed Induction Motor,” *Mater. Today Proc.*, vol. 5, no. 1, pp. 1401–1410, 2018, doi: 10.1016/j.matpr.2017.11.226.

[19] H. Douglas, P. Pillay, and A. K. Ziarani, “Broken Rotor Bar Detection in Induction Machines With Transient Operating Speeds,” *IEEE Trans. Energy Convers.*, vol. 20, no. 1, pp. 135–141, 2005.

[20] H. Merabet, T. Bahi, K. Bedoud, and D. Drici, “Real-time switches fault diagnosis for voltage source inverter driven induction motor drive,” *Int. J. Electr. Electron. Eng. Telecommun.*, vol. 8, no. 2, pp. 103–107, 2019, doi: 10.18178/ijeetc.8.2.103-107.

[21] J. O. Estima and A. J. M. Cardoso, “A new approach for real-time multiple open-circuit fault diagnosis in voltage-source inverters,” *IEEE Trans. Ind. Appl.*, vol. 47, no. 6, pp. 2487–2494, 2011, doi: 10.1109/TIA.2011.2168800.

[22] J. Faiz and S. M. M. Moosavi, “Eccentricity fault detection - From induction machines to DFIG - A review,” *Renewable and Sustainable Energy Reviews*, vol. 55. Elsevier Ltd, pp. 169–179, Mar. 01, 2016. doi: 10.1016/j.rser.2015.10.113.

[23] G. I. Sainz Palmero, J. Juez Santamaria, E. J. Moya De La Torre, and J. R. Perán González, “Fault detection and fuzzy rule extraction in AC motors by a neuro-fuzzy ART-based system,” *Eng. Appl. Artif. Intell.*, vol. 18, no. 7, pp. 867–874, Oct. 2005, doi: 10.1016/j.engappai.2005.02.005.

[24] G. Singh, C. Anil Kumar, and V. N. A. Naikan, “Effectiveness of Current Envelope analysis to detect broken rotor bar and inter turn faults in an inverter fed induction motor drive,” in *Proceedings of the 2015 IEEE International Conference on Power and Advanced Control Engineering, ICPACE 2015*, Sep. 2015, pp. 191–194. doi: 10.1109/ICPACE.2015.7274941.

[25] D. Morinigo-Sotelo, L. A. Garcia-Escudero, O. Duque-Perez, and M. Perez-Alonso, “Practical aspects of mixed-eccentricity detection in PWM voltage-source-inverter-fed induction motors,” *IEEE Trans. Ind. Electron.*, vol. 57, no. 1, pp. 252–262, Jan. 2010,

doi: 10.1109/TIE.2009.2024654.

[26] G. Rajamany, S. Srinivasan, K. Rajamany, and R. K. Natarajan, "Induction Motor Stator Interturn Short Circuit Fault Detection in Accordance with Line Current Sequence Components Using Artificial Neural Network," *J. Electr. Comput. Eng.*, vol. 2019, 2019, doi: 10.1155/2019/4825787.

[27] S. Janiga, S. N. Syed, S. K. Tummala, and P. Srinivasa Varma, "Speed control of an induction motor fed by an inverter using dSPACE controller," in *E3S Web of Conferences*, Feb. 2019, vol. 87. doi: 10.1051/e3sconf/20198701002.

[28] Devraj Jee (109EE0039) and Nikhar Patel (109EE0087), "Vf CONTROL OF INDUCTION MOTOR DRIVE," Odisha, India, May 2013.

[29] A. Garg and A. Tomar, "Starting Time Calculation for Induction Motor," *J. Electr. Electron. Syst.*, vol. 4, no. 2, pp. 2–5, 2015, doi: 10.4172/2332-0796.1000149.

[30] Hassan H. Eldeeb, Haisen Zhao, and Osama Mohammed, "Wavelet Transformation-Based Diagnosis of Turn-to-Turn Faults in Vector Control Drive system," Nov.

[31] H. Hafezi and A. Jalilian, "Design and construction of induction motor thermal monitoring system," in *41st International Universities Power Engineering Conference, UPEC 2006, Conference Procedings*, 2006, vol. 2, pp. 674–678. doi: 10.1109/UPEC.2006.367564.

[32] J. P. . aul, Arun.S, "Voltage Source Inverter Fed Induction Motor Drive," *Int. J. Adv. Res. Electr. Electron. Instrum. Eng.*, vol. 04, no. 06, pp. 5020–5027, Jun. 2015, doi: 10.15662/ijareeie.2015.0406018.

[33] Kharagpur, "Module 7: Electrical Machine and Drives. Lesson 34 Electrical Actuators: Induction Motor Drives," *LinkedIn Slideshare*, Aug. 04, 2013.

[34] Emojong Eenen Eric, "DESIGN OF INVERTER DRIVE FOR AC INDUCTION MOTOR," Nairobi, Kenya, May 2009.

[35] J. M. Pena and E. V. Diaz, "Implementation of V/f scalar control for speed regulation of a three-phase induction motor," *Proc. 2016 IEEE ANDESCON, ANDESCON 2016*, 2017, doi: 10.1109/ANDESCON.2016.7836196.

[36] S. Petersen, "White Paper: Variable Frequency Drive Control Methods," Waukegan, Illinois, WP.AFD.13, 2014. [Online]. Available: https://www.yaskawa.com/downloads/search-index/details?showType=details&docnum=WP.AFD.13

[37] Z. B. Duranay, H. Guldemir, and S. Tuncer, "Implementation of a V/f Controlled Variable Speed Induction Motor Drive," *Emit. Int. J. Eng. Technol.*, vol. 8, no. 1, pp. 35–48, 2020, doi: 10.24003/emitter.v8i1.490.

[38] M. A. W. Begh and Hans-Georg Herzog, "Comparison of Field Oriented Control and Direct Torque Control for PMSM," *World Acad. Sci. Eng. Technol.*, vol. 21, no. April, pp. 209–304, 2019, doi: 10.13140/RG.2.2.21677.59360/1.

[39] X. del T. Garcia, B. Zigmund, A. A. Terlizzi, R. Pavlanin, and L. Salvatore, "Comparison between FOC and DTC Strategies for Permanent Magnet Synchronous Motors," *Adv. Electr. Electron. Eng.*, vol. 5, no. 1, pp. 76–81, 2006.

[40] E. Strangas and S. Aviyente, “Failure prognosis methods in electrical drives - State of the art and future directions,” in *Proceedings - 2015 IEEE Workshop on Electrical Machines Design, Control and Diagnosis, WEMDCD 2015*, Aug. 2015, pp. 254–260. doi: 10.1109/WEMDCD.2015.7194538.

[41] V. Hegde and M. G. Sathyanarayana Rao, “Detection of Stator Winding Inter-Turn Short Circuit Fault in Induction Motor Using Vibration Signals by MEMS Accelerometer,” *Electr. Power Components Syst.*, vol. 45, no. 13, pp. 1463–1473, Aug. 2017, doi: 10.1080/15325008.2017.1358777.

[42] N. R. Devi, D. V. S. S. Siva Sarma, and P. V. Ramana Rao, “Detection of stator incipient faults and identification of faulty phase in three-phase induction motor - simulation and experimental verification,” *IET Electr. Power Appl.*, vol. 9, no. 8, pp. 540–548, Sep. 2015, doi: 10.1049/iet-epa.2015.0024.

[43] C.S.Sharma and N. Tali, “Simulation and Analysis of PWM Inverter Fed Induction Motor Drive,” *Int. J. Sci. Eng. Technol. Res.*, vol. 2, no. 2, pp. 359–366, 2013.

[44] J. O. Estima and A. J. M. Cardoso, “Impact of inverter faults in the overall performance of permanent magnet synchronous motor drives,” *2009 IEEE Int. Electr. Mach. Drives Conf. IEMDC ’09*, pp. 1319–1325, 2009, doi: 10.1109/IEMDC.2009.5075374.

[45] A. R. Abdullah, N. S. Ahmad, E. F. Shair, and A. Jidin, “Open switch faults analysis in voltage source inverter using spectrogram,” *Proc. 2013 IEEE 7th Int. Power Eng. Optim. Conf. PEOCO 2013*, no. June, pp. 438–443, 2013, doi: 10.1109/PEOCO.2013.6564588.

[46] S. Oommen, “Fault Analysis in Inverter Fed Induction Motor Drive System due to Switch Failures,” *J. Xi’an Univ. Archit. Technol.*, vol. XII, no. Iv, pp. 3936–3944, 2020.

[47] Y. K. Priya and M. V. Kumar, “Analysis of various switch faults of the Three level Neutral point clamped inverter feeding induction motor drive,” *Proceeding IEEE - 2nd Int. Conf. Adv. Electr. Electron. Information, Commun. Bio-Informatics, IEEE - AEEICB 2016*, pp. 580–586, 2016, doi: 10.1109/AEEICB.2016.7538357.

[48] R. Yan, R. X. Gao, and X. Chen, “Wavelets for fault diagnosis of rotary machines: A review with applications,” *Signal Processing*, vol. 96, no. PART A, pp. 1–15, 2014, doi: 10.1016/j.sigpro.2013.04.015.

[49] D. Goyal and B. S. Pabla, “Condition based maintenance of machine tools-A review,” *CIRP Journal of Manufacturing Science and Technology*, vol. 10. Elsevier Ltd, pp. 24–35, 2015. doi: 10.1016/j.cirpj.2015.05.004.

[50] R. Kechida, A. Menacer, H. Talhaoui, and H. Cherif, “Discrete wavelet transform for stator fault detection in induction motors,” in *Proceedings - SDEMPED 2015: IEEE 10th International Symposium on Diagnostics for Electrical Machines, Power Electronics and Drives*, Oct. 2015, pp. 104–109. doi: 10.1109/DEMPED.2015.7303676.

[51] F. Khater, M. I. Abu El-Sebah, and M. Osama, “Fault diagnostics in an inverter feeding an induction motor using fuzzy logic,” *J. Electr. Syst. Inf. Technol.*, vol. 4, no. 1, pp. 10–17, 2017, doi: 10.1016/j.jesit.2016.10.005.

[52] M. Alavi, M. Luo, D. Wang, and D. Zhang, “Fault diagnosis for power electronic inverters: A model-based approach,” *SDEMPED 2011 - 8th IEEE Symp. Diagnostics Electr. Mach. Power Electron. Drives*, pp. 221–228, 2011, doi: 10.1109/DEMPED.2011.6063627.

[53] J. A. Reyes-Malanche, F. J. Villalobos-Pina, E. Cabal-Yepez, R. Alvarez-Salas, and C. Rodriguez-Donate, “Open-Circuit Fault Diagnosis in Power Inverters through Currents Analysis in Time Domain,” *IEEE Trans. Instrum. Meas.*, vol. 70, 2021, doi: 10.1109/TIM.2021.3082325.

[54] U. R. Mala, R. B. Dhumale, and S. D. Lokhande, “Open Switch Fault Diagnosis in Three Phase Inverter Using Diagnostic Variable Method,” *Int. J. Res. Eng. Technol.*, vol. 02, no. 12, pp. 636–640, 2013, doi: 10.15623/ijret.2013.0212108.

[55] D. Goyal and B. S. Pabla, “The Vibration Monitoring Methods and Signal Processing Techniques for Structural Health Monitoring: A Review,” *Arch. Comput. Methods Eng.*, vol. 23, no. 4, pp. 585–594, Dec. 2016, doi: 10.1007/s11831-015-9145-0.

[56] M. R. Mehrjou, N. Mariun, M. H. Marhaban, and N. Misron, “Evaluation of Fourier and wavelet analysis for efficient recognition of broken rotor bar in squirrel- cage induction machine,” *PECon2010 - 2010 IEEE Int. Conf. Power Energy*, pp. 740–743, 2010, doi: 10.1109/PECON.2010.5697678.

[57] S. A. Fulambarkar and D. V Jadhav, “EMPIRICAL MODE DECOMPOSITION: A METHOD FOR ANALYZING NON-STATIONARY SIGNALS,” *Int. J. Eng. Sci. Res. Technol.*, vol. 5, no. 7, 2016, [Online]. Available: http://www.ijesrt.com

[58] Martin Blodt, “Condition Monitoring of Mechanical Faults in Variable Speed Induction Motor Drives - Application of Stator Current Time-Frequency Analysis and Parameter Estimation,” Toulouse, France, Sep. 2006.

[59] Signal and Systems Lab Manual, “EXPERIMENT NO.:1 Study of types of signals Deterministic and Stochastic (Continuous) Contents,” Haryana, India, Jan. 2020.

[60] M. Abdesh Shafiel Kafiey Khan and M. Azizur Rahman, “Wavelet Based Diagnosis and Protection of Electric Motors,” in *Fault Detection*, W. Zhang (Ed.)., Wei Zhang, Ed. London, United Kingdom: IntechOpen, 2010 [Online], 2010. doi: http://dx.doi.org/10.5772/9068.

[61] G. A. Ambaye, “Time and Frequency Domain Analysis of Signals: A Review,” *Int. J. Eng. Res. Technol.*, vol. 9, no. 12, Dec. 2020, [Online]. Available: www.ijert.org

[62] M. S. Othman, M. Z. Nuawi, and R. Mohamed, “Experimental comparison of vibration and acoustic emission signal analysis using kurtosis-based methods for induction motor bearing condition monitoring,” *Prz. Elektrotechniczny*, vol. 92, no. 11, pp. 208–212, 2016, doi: 10.15199/48.2016.11.51.

[63] R. K. Patel and V. K. Giri, “Condition monitoring of induction motor bearing based on bearing damage index,” *Arch. Electr. Eng.*, vol. 66, no. 1, pp. 105–119, Mar. 2017, doi: 10.1515/aee-2017-0008.

[64] M. Misiti, Y. Misiti, G. Oppenheim, and J.-M. Poggi, “For Use with MATLAB ® User’s Guide Wavelet Toolbox,” 3 Apple Hill Drive, Natick, United States, Mar. 1997. [Online]. Available: www.mathworks.com

[65] W. Li and C. K. Mechefske, “Detection of induction motor faults: A comparison of

stator current, vibration and acoustic methods," *JVC/Journal Vib. Control*, vol. 12, no. 2, pp. 165–188, Feb. 2006, doi: 10.1177/1077546306062097.

[66] K. Salloum and H. Wooi, "Wavelet Fault Diagnosis of Induction Motor," in *MATLAB for Engineers - Applications in Control, Electrical Engineering, IT and Robotics*, InTech, 2011. doi: 10.5772/19584.

[67] D. J. Jwo, I. H. Wu, and Y. Chang, "Windowing Design and Performance Assessment for Mitigation of Spectrum Leakage," *E3S Web Conf.*, vol. 94, 2019, doi: 10.1051/e3sconf/20199403001.

[68] R. M. P. Teate, "Window Functions and Subqueries," *SQL Data Sci.*, pp. 97–112, 2021, doi: 10.1002/9781119669388.ch7.

[69] F. Lindsten, "A remark on zero-padding for increased frequency resolution," 2010.

[70] E. Z. M. Salem, A. Haitham Z, A. G. Saad F, and M. M. Elkholy, "Open gate fault diagnosis and tolerant for voltage source inverter fed speed sensorless induction motor drive," *Int. J. Electron.*, vol. 107, no. 11, pp. 1754–1772, 2020, doi: 10.1080/00207217.2020.1756434.

[71] B. Akin, U. Orguner, H. A. Toliyat, and M. Rayner, "Low order PWM inverter harmonics contributions to the inverter-fed induction machine fault diagnosis," *IEEE Trans. Ind. Electron.*, vol. 55, no. 2, pp. 610–619, 2008, doi: 10.1109/TIE.2007.911954.

[72] J. C. Hernandez, J. Antonino-Daviu, F. Martinez-Gimenez, and A. Peris, "Comparison of different wavelet families for broken bar detection in induction motors," in *Proceedings of the IEEE International Conference on Industrial Technology*, Jun. 2015, vol. 2015-June, no. June, pp. 3220–3225. doi: 10.1109/ICIT.2015.7125574.

[73] V. Ambrozic, R. Fiser, M. Nemec, and K. Drobnic, "Dynamic Model of Induction Machine with Faulty Cage in Rotor Reference Frame," in *Proceedings - 2011 IEEE Ninth International Conference on Power Electronics and Drive Systems*, 2011, no. December, pp. 77–82. doi: 10.1109/PEDS.2011.6147227.

[74] B. Asad, T. Vaimann, A. Kallaste, and A. Belahcen, "Broken rotor bar fault detection of the grid and inverter-fed induction motor by effective attenuation of the fundamental component," *IET Electr. Power Appl.*, vol. 13, no. 12, pp. 2005–2014, 2019, doi: 10.1049/iet-epa.2019.0350.

[75] L. Ralikalakala and P. Barendse, "Impact of Inverter Switching Harmonics in Detecting Changes in Impedance Due to Broken Rotor Bars," in *2022 IEEE Energy Conversion Congress and Exposition (ECCE), Detroit, MI, USA*, 2022, pp. 1–6. doi: 10.1109/ECCE50734.2022.9947928.

[76] J. A. Antonino-Daviu, S. Bin Lee, and E. Wiedenbrug, "Reliable detection of rotor bar failures in induction motors operating in petrochemical plants," 2014. doi: 10.1109/PCICEurope.2014.6900065.

[77] J. Antonino-daviu *et al.*, "Detection of Broken Outer-Cage Bars for Double-Cage Induction Motors Under the Startup Transient," *IEEE Trans. Ind. Appl.*, vol. 48, no. 5, pp. 1539–1548, 2012.

[78] A. Garcia-Perez, R. J. Romero-Troncoso, D. Camarena-Martinez, R. A. Osornio-Rios, and J. P. Amezquita-Sanchez, "Broken rotor bar detection in inverter-fed induction

motors by time-corrected instantaneous frequency spectrogram," *Proc. 2017 IEEE 11th Int. Symp. Diagnostics Electr. Mach. Power Electron. Drives, SDEMPED 2017*, vol. 2017-Janua, pp. 280–285, 2017, doi: 10.1109/DEMPED.2017.8062368.

[79] V. Fernandez-Cavero, L. A. García-Escudero, J. Pons-Llinares, M. A. Fernández-Temprano, O. Duque-Perez, and D. Morinigo-Sotelo, "Diagnosis of broken rotor bars during the startup of inverter-fed induction motors using the dragon transform and functional anova," *Appl. Sci.*, vol. 11, no. 9, 2021, doi: 10.3390/app11093769.

[80] M. Akar, "Detection of rotor bar faults in field oriented controlled induction motors," *J. Power Electron.*, vol. 12, no. 6, pp. 982–991, 2012, doi: 10.6113/JPE.2012.12.6.982.

[81] T. A. Garcia-Calva, D. Morinigo-Sotelo, V. Fernandez-Cavero, A. Garcia-Perez, and R. de J. Romero-Troncoso, "Early detection of broken rotor bars in inverter-fed induction motors using speed analysis of startup transients," *Energies*, vol. 14, no. 5, pp. 1–16, 2021, doi: 10.3390/en14051469.

[82] V. Fernandez-Cavero, D. Morinigo-Sotelo, O. Duque-Perez, and J. Pons-Llinares, "A Comparison of Techniques for Fault Detection in Inverter-Fed Induction Motors in Transient Regime," *IEEE Access*, vol. 5, pp. 8048–8063, 2017, doi: 10.1109/ACCESS.2017.2702643.

[83] K. Drobnič, M. Nemec, R. Fišer, and V. Ambrožič, "Influence of broken rotor bars on magnetic quantities in induction machine," *Int. Conf. Compat. Power Electron. , CPE*, pp. 231–234, 2013, doi: 10.1109/CPE.2013.6601160.

[84] K. Drobnič, M. Nemec, D. Makuc, R. Fišer, and V. Ambrožič, "Pseudo-salient model of induction machine with broken rotor bars," *SDEMPED 2011 - 8th IEEE Symp. Diagnostics Electr. Mach. Power Electron. Drives*, pp. 213–220, 2011, doi: 10.1109/DEMPED.2011.6063626.

[85] V. Ambrozic, R. Fiser, M. Nemec, and K. Drobnic, "Dynamic model of induction machine with faulty rotor in field reference frame," *Proc. - 2013 9th IEEE Int. Symp. Diagnostics Electr. Mach. Power Electron. Drives, SDEMPED 2013*, pp. 142–149, 2013, doi: 10.1109/DEMPED.2013.6645709.

[86] B. Akin, S. B. Ozturk, H. A. Toliyat, and M. Rayner, "DSP-Based sensorless electric motor fault-diagnosis tools for electric and hybrid electric vehicle powertrain applications," *IEEE Trans. Veh. Technol.*, vol. 58, no. 6, pp. 2679–2688, 2009, doi: 10.1109/TVT.2009.2012430.

[87] K. Subramanian, V. Kavitha, and R. Saravanakumar, "Implementation of V/F control for variable speed drive of a 3- ΦInverter fed induction motor," *Int. J. Appl. Eng. Res.*, vol. 9, no. 22, pp. 13027–13046, 2014.

[88] A. Aligbe, E. Oluwasogo, and O. Ignatius, "Design and Implementation of Three Phase Variable Voltage Igbt Design and Implementation of Three Phase Variable Voltage Igbt Inverter for the Control of Induction," *Am. Int. J. Res. Sci. Technol. Eng. Math.*, vol. 11, no. 1, pp. 37–46, 2015.

[89] A. A. Faleh and A. H. Al-mukhtar, "Designing and implementing 7 . 5kW three phase inverter for Electrical Vehicle," *Int. J. Curr. Eng. Technol.*, vol. 7, no. 6, pp. 2003–2008, 2017.

[90] A. Merza, "Design And Implementation Of Three Phase Inverter Based On

Microcontroller,” 2019.

[91] P. L. Schimel, “Design Considerations for using IGBT modules in Inverters and Drives Apicaction Note AN1202,” *Infineon Technol. Co.*, pp. 1–30, 2016, [Online]. Available: www.infineon.com/hirel

[92] F. Fürst, “Design of a 48 V three-phase inverter,” 2015. [Online]. Available: http://publications.lib.chalmers.se/records/fulltext/224623/224623.pdf

[93] P. Mishra and R. Maheshwari, “Design, Analysis, and Impacts of Sinusoidal LC Filter on Pulsewidth Modulated Inverter Fed-Induction Motor Drive,” *IEEE Trans. Ind. Electron.*, vol. 67, no. 4, pp. 2678–2688, 2020, doi: 10.1109/TIE.2019.2913824.

[94] R. R. Riehl, C. H. B. De Souza, H. B. De Morais, and B. Albuquerque, “Analysis and Simulation of Common-Mode Current Filtering in PWM-fed Induction Motor Drives,” in *THE 13th LATIN-AMERICAN CONGRESS ON ELECTRICITY GENERATION AND TRANSMISSION - CLAGTEE 2019*, 2019, no. April 2020.

[95] J. Salomäki and J. Luomi, “Vector control of an induction motor fed by a PWM inverter with output LC filter,” *EPE J. (European Power Electron. Drives Journal)*, vol. 16, no. 1, pp. 37–43, 2006, doi: 10.1080/09398368.2006.11463611.

[96] L. Wang, Y. Zhang, M. S. Ali, G. Chen, J. M. Guerrero, and J. C. Vasquez, “High-frequency modeling and filter design for PWM drives with long cables,” *Energies*, vol. 14, no. 4, pp. 1–18, 2021, doi: 10.3390/en14041155.

[97] S. Z. Mohammad Noor, N. Rosmizi, N. Aminudin, and F. A.H, “Investigation of Passive Filter Performance on Three Phase DC to AC Converter,” *Int. J. Power Electron. Drive Syst.*, vol. 9, no. 3, p. 1016, 2018, doi: 10.11591/ijpeds.v9.i3.pp1016-1028.

[98] M. Inverters, J. R. G. I, and P. N. Kapi, “Analysis of Different Modulation Techniques for Multilevel Inverters,” *1st IEEE Int. Conf. Power Electron. Intell. Control Energy Syst. Anal.*, no. 1, p. 6, 2016.

[99] P. Naveenchandran and Vijayaraghavan, “MODULATION TECHNIQUES IN SWITCHING DEVICES,” *Int. J. Pure Appl. Math.*, vol. 116, no. 13, pp. 137–142, 2017.

[100] R. K. Rao, P. Srinivas, and M. V Suresh Kumar, “Design and Analysis of Various Inverters Using Different Pwm Techniques,” *Int. J. Eng. Sci. ISSN*, pp. 2319–1813, 2014.

[101] “CHAPTER 2 SINGLE PHASE PULSE WIDTH MODULATED INVERTERS,” *Tennessee Tech.*

[102] N. Instruments, “NI 9215 Datasheet,” *Natl. Instruments*.

[103] SpectraQuest Inc., “User Operating Manual for Machinery Fault Simulator,” *SpectraQuest Inc.*.

APPENDIX

A1. Fault Simulation and Detection Procedures for the Various Tests

These section of the appendix outlines the various fault simulation procedures for the different tests performed, along with the diagnosis and detection of these faults using different fault detection techniques.

A1.1 Fault Simulation Procedure and Detection using MCSA

Fault simulation Procedure

The following procedure was followed when performing the experiments to simulate and detect the motor faults:

1. First the main's breaker on the wall was open to ensure no electric supply to the test rig and then the desired motor to be tested was installed.
2. The motor test rig was then reconnected to electrical supply by closing the breaker.
3. The motor was then de-isolated from the mains supply by means of a toggler isolator switch on the control panel.
4. Select the supply to the motor, i.e. grid or inverter supply.
5. Select the mode of the dynamometer.
6. Start the induction motor and allow at least 20 minutes for the machine to warm up.
7. Select the required load level using the variable resistor knob on the control panel.
8. Run LabView's Instrument Block Diagram and start a recording the data. Save the data with your preferred filename when prompted to. Always check that the data is what is expected by observing the graphs prior to saving.
9. This procedure is repeated chronologically when varying the load or selecting a different supply.

MCSA Procedure for Motor Fault Detection

The fault detection procedure involved loading data into the MATLAB data processing programs and running these programs to observe fault signatures. The programs' execution followed the following sequence:

1. Start by import the data for both healthy and faulty motor.
2. Definition of parameters such as sampling frequency, F_s, number of samples, N, time, and frequency vectors.
3. Application of the Hanning window function to the current data.
4. Pad zeros to the windowed data to increase the length of the sample to the next power of two for smoother FFT output.
5. Application of the FFT function to the modified data and creation of a single sided spectrum.
6. Calculation of the Power Spectral Density and its normalization.
7. Plot the PSD of current for the healthy versus faulty under the selected load condition.
8. Calculate the expected frequencies of the fault sideband harmonics for both the healthy and faulty motors.
9. Analysis of the obtained spectra at frequencies around calculated sideband harmonic frequencies and identify the fault harmonics and their relative amplification due to fault.
10. Repetition of this process for different supply types or loads conditions.

A1.2. Standstill Impedance Variation Test Procedure for Grid Connected Motor

1. The power supply to the California Instrument is first switched off by opening its contact breaker.
2. Terminal of phases A and B were shorted by means of a short cable.
3. Connect the terminals of the California Instrument to the phases A and C of the motor through the resistor and an ammeter (a multimeter is used here).
4. Measure the voltage output at the terminals of the California Instrument supply with a differential probe and feed it into one input port of NI DAQ (e.g., a0+).
5. Measure the input voltage at the terminals of the motor (between phase A and C) with another differential probe and feed it into a different input port of NI DAQ (e.g., a1+).
6. Switch on the California Instrument power supply and set the frequency to 50Hz.
7. While monitoring the current on the multimeter, gradually increase the voltage on the California Instrument until a rated current of 1.8A is flowing.
8. Run LabView's Instrument Block Diagram and start a recording the data. Save the data with your preferred filename when prompted to. Always check that the data is what is expected by observing the graphs prior to saving.
9. Decrease the voltage to zero and rotate the rotor over an angle of 10 degrees
10. Repeat the process from step 7 until you have rotated the rotor through 360 degrees.

A1.3. Standstill Impedance Variation Test Procedure for Inverter-fed Motor

The following procedure was followed when performing the experiment for the inverter fed motor impedance variation test:

1. First the supply main's breaker on the wall was open to ensure no electric supply to the test rig and then the desired motor to be tested was installed.
2. The motor test rig was then reconnected to electrical supply by closing the breaker.
3. The motor was then de-isolated from the mains supply by means of a toggler isolator switch on the control panel.
4. Inverter supply was selected by a means of toggler switch on the control panel.
5. Program the microcontroller to configure the 3-phase inverter to output a single-phase by simultaneously turning any two top switches along with one bottom switch, or vice versa. Bear in mind that two switches on the same bridge arm should not be turned on at the same time lest the occurrence of a short circuit. Say for instance, we want to short phase A and B as we have been doing and impress a single-phase supply between phases A and C of the motor. The algorithm of programming the microcontroller would be:
    a. Drive the switches 1, 2 and 3 with the same PWM gate signal simultaneously.
    b. With the compliment of this PWM gate signal, drive switches 4, 5 and 6.
    c. The result is a single-phase output current injection into phase C and dividing phase A and B (since the windings are now connected in parallel because of the shorting).
6. Start the induction motor with the rotor in a specific known position (Note: the rotor won't be rotating since there is no rotating flux in the airgap, rather a flux pulsating in a certain arbitrary axis).

7. While observing the current on the power analyser, increase the output voltage of the inverter by increasing its input through the variac. Increase the voltage until the rated current (1.8A) is flowing in phase C.
8. Run LabView's Instrument Block Diagram and start a recording the data. Save the data with your preferred filename when prompted to. Always check that the data is what is expected by observing the graphs prior to saving. In this case, current in phase C should be equal to the sum of currents in phases A and B, which are approximately the same.
9. Now turn down the variac to zero and rotate the rotor through an angle of 10 degrees (say in a clockwise direction).
10. Repeat the process from step 7 until you have rotated the rotor through 360 degrees.

A1.4. Fault Detection Procedure for Standstill Impedance Variation Test

The fault detection procedure involved loading data into the MATLAB data processing programs and running these programs to observe fault signatures. The programs' execution followed the following sequence:

1. Start by importing the data for both healthy and faulty motor at rotor angle of 0 degrees.
2. Definition of parameters such as sampling frequency, F_s, number of samples, N, time, and frequency vectors.
3. Application of the FFT function to the captured stator current and creation of a single sided spectrum.
4. Application of the FFT function to the captured terminal voltage and creation of a single sided spectrum.
5. Extraction of voltage and current amplitudes at 50Hz frequency.
6. Determination of impedance by dividing voltage amplitude by current amplitude at 50Hz. Store this impedance in an array.
7. Repeat this process for rotor angles 10, 20, 30, …,350 degrees.
8. Plot the impedance vs rotor angle graph.
9. Analysis of the obtained impedance vs rotor position graph, and determination of impedance variation by subtracting the lowest impedance amplitude from the largest amplitude obtained from the graph.

A1.5. Fault Simulation and Detection Procedure for Inverter Fed Motor – Advancement

A. Fault Simulation Procedure

The following procedure was followed when performing the experiment for the inverter fed motor impedance variation with rotor position fixed and axis of pulsating flux rotated by 120º.

1. First the supply main's breaker on the wall was open to ensure no electric supply to the test rig and then the motor with broken rotor bars was installed.
2. The motor test rig was then reconnected to electrical supply by closing the breaker.
3. The motor was then de-isolated from the mains supply by means of a toggler isolator switch on the control panel.
4. Inverter supply was selected by a means of toggler switch on the control panel.
5. Program the microcontroller to configure the 3-phase inverter to output a single-phase by simultaneously turning any two top switches along with one bottom switch, or vice

versa. Bear in mind that two switches on the same bridge arm should not be turned on at the same time lest the occurrence of a short circuit. Say for instance, we want to short phase A and B and impress a single-phase supply between phases A and C of the motor. The algorithm of programming the microcontroller would be:

   a) Drive the switches 1, 2 and 3 with the same PWM gate signal simultaneously.
   b) With the compliment of this PWM gate signal, drive switches 4, 5 and 6.
   c) The result is a single-phase output current injection into phase C and dividing into phases A and B (since the windings are now connected in parallel because of the shorting).

6. Start the induction motor with the rotor in a specific known position (Note: the rotor won't be rotating since there is no rotating flux in the airgap, rather a flux pulsating in a certain arbitrary axis).
7. While observing the current on the power analyser, increase the output voltage of the inverter by increasing its input through the variac. Increase the voltage until the rated current (1.8A) is flowing in phase C.
8. Run LabView's Instrument Block Diagram and start a recording the data. Save the data with your preferred filename when prompted to. Always check that the data is what is expected by observing the graphs prior to saving. In this case, current in phase C should be equal to the sum of currents in phases A and B, which are approximately the same.
9. Now turn down the variac to zero and rotate the rotor through an angle of 10^o (say in a clockwise direction).
10. For the same rotor position, repeat the process from step 5 but now short phases B and C, and supply through phase A. Repeat the process again but now shorting phases C and A and supplying through B.
11. Rotate the rotor through an angle, say 10^o and repeat the process from step 5. Do this until rotor has been rotated by 180^o from the starting point.

B. Fault Detection Procedure

The fault detection procedure involved loading data into the MATLAB data processing programs and running these programs to observe fault signatures. The programs' execution followed the following sequence:

1. Start by importing the data at rotor angle of 0 degrees, which will be three pairs of current and voltage profiles.
2. Definition of parameters such as sampling frequency, F_s, number of samples, N, time, and frequency vectors.
3. For each pair:
   (a) Apply the FFT function to the captured stator current and create a single sided spectrum.
   (b) Apply the FFT function to the captured terminal voltage and create a single sided spectrum.
   (c) Extract voltage and current amplitudes at 50Hz frequency.
   (d) Calculate impedance by dividing voltage amplitude by current amplitude at 50Hz.
   (e) Calculate the average of the absolute impedance differences. That is if our three impedances are Z_a, Z_b and Z_c, we calculate as,

$$\bar{Z}_0 = \frac{|Z_a - Z_b| + |Z_b - Z_c| + |Z_c - Z_a|}{3}$$

(f) Store the result in an array.

4. Repeat this process for rotor angles 10, 20, 30, …,180 degrees.
5. Plot the impedance vs rotor angle graph.
6. Analysis of the obtained impedance vs rotor position graph, and determination of critical rotor angle position(s) as the lowest point(s) in the graph.

A1.6. Fault Simulation, Impact Observation and Detection Procedures for Inverter Open Switch Faults

A. Fault Simulation Procedure

The following procedure was followed when performing the experiment for the inverter open switch fault:

1. First the supply main's breaker on the wall was open to ensure no electric supply to the test rig and the healthy motor was installed.
2. The motor test rig was then reconnected to electrical supply by closing the breaker.
3. The motor was then de-isolated from the mains supply by means of a toggler isolator switch on the control panel.
4. Inverter supply was selected by a means of toggler switch on the control panel.
5. Program the microcontroller according to the following algorithm:
    a) At turn-on, generate the necessary PWM signals to control the gate drives to the IGBTs to generate the rated balanced three-phase voltages and currents at the output of the inverter.
    b) 2 minutes and 30 seconds after turn-on, pull the output pin of the microcontroller controlling that switch to a constant low. This means the inception of the fault is set to 2.5 minutes after start.
6. Start the induction motor and simultaneously start a stopwatch.
7. After 2 minutes and 15 seconds, run LabView's Instrument Block Diagram and start a recording the data. This will capture approximately 15 seconds of healthy operation and 15 seconds of faulty operation, for comparison. Save the data with your preferred filename when prompted to. Always check that the data is what is expected by observing the graphs prior to saving.
8. Now switch off the motor.
9. Repeat the process with open switch fault on the top switch (say S1), bottom switch (say S4) and two switches (say S1 and S4).

B. Fault Impact Observation and Detection Procedure

The observation of the impacts of the fault and its detection procedures involved loading data into the MATLAB data processing programs and running these programs to observe fault signatures. The programs' execution followed the following sequence:

1. Start by importing the previously saved data for healthy motor.
2. Definition of parameters such as sampling frequency, F_s, number of samples, N, time, and frequency vectors.

3. To observe the impacts of the fault:
    a) Plot current vs time and voltage vs time graphs for the different phases and observe the difference between the pre- and post-fault signals.
    b) Plot speed vs time and torque vs time graphs and observe the pre- and post-fault responses.
    c) Application of the FFT function to the stator current and voltage before and after the fault, and determination of the THD in each case. Comparison of the THDs before and after the occurrence of the fault.
4. To detect the open switch faults, process the loaded motor stator current according to the following algorithm:
    a) Normalise the three currents by dividing by the Park's modulus.
    b) Know that the average absolute value of the normalised phase currents for a healthy inverter is constant and equal to 0.5198.
    c) Calculate the motor currents average values.
    d) Calculate the average absolute values of the normalised motor currents.
    e) Calculate diagnostic variables e_n, defined as the errors of average absolute values of the normalised currents for healthy and faulty currents.
    f) Plot the graphs of current average values and diagnostic variables.
    g) If one or more of the diagnostic variables has a positive value, then there is an open switch fault.
    h) Localize the fault by observing both diagnostic variables and the motor current average values and using a lock-up table as described in section 4.4.3.
5. Repeat this for a single open switch fault, single phasing, and double open switch faults.

A2. MATLAB Code for the Different Tests Analysis

A. MCSA at Full-load (broken rotor bar vs healthy Motor)

```
function MCSA
healthy_data = load('HNoload_2992.txt');
fault_data = load('BNoload.txt');

f_sampling = 25600; % Sampling frequency
T = 1/f_sampling; % Sampling period
N = 768000; % Number of samples
t = (0:N-1)*T; % Time Vector

ia_healthy = healthy_data(:,5); % read phase A current of
healthy motor
ia_fault = fault_data(:,5); % read phase A current of
faulted motor 512000

ia_healthy = ia_healthy(640000:end);
ia_fault = ia_fault(640000:end);
Nn = length(ia_healthy);
```

```
% speedH = mean(healthy_data(:,9))
% torqueH = mean (healthy_data(:,8))
% speedF = mean(fault_data(:,9))
% torqueF = mean(fault_data(:,8))

%w = hann(N); % apply window function
% Nh = 1:N; % number of windows for Hann Window
Nh = 1:Nn;
Nhr = rot90(Nh); % rotated window vector
% Window(Nhr) = 0.5*(1-cos(2*pi*(Nhr)/N)); % manually
perform Hann Window
Window(Nhr) = 0.5*(1-cos(2*pi*(Nhr)/Nn)); % manually
perform Hann Window
Window_rot = rot90(Window); % rotate Window vector to
perform multiplication

ia_hann_healthy = ia_healthy.*Window_rot; % multiply
current vector by rotated window vector
ia_hann_fault = ia_fault.*Window_rot; % multiply current
vector by rotated window vector

NFFT = 2^nextpow2(N); % zero padding
f = (f_sampling/NFFT)*(0:NFFT/2-1); %create a frequency
vector

FFT_Ia = fft(ia_hann_healthy,NFFT); % run FFT...
FFT_Ia = FFT_Ia(1:NFFT/2); % creates single sided
spectrum

FFT_Ia_2 = fft(ia_hann_fault,NFFT); % run FFT...
FFT_Ia_2 = FFT_Ia_2(1:NFFT/2); % creates single sided
spectrum

% Temp = FFT_Ia_2/max(FFT_Ia_2);
% Y = mag2db(Temp);
% plot(f, Y);xlabel('Frequency/Hz')

P_Ia = (1/NFFT) * abs(FFT_Ia).^2; % calculating power for
each freq comp
P_Ia_Norm = P_Ia./max(P_Ia); % Normalizing

P_Ia_2 = (1/NFFT) * abs(FFT_Ia_2).^2; % calculating power
for each freq comp
P_Ia_2_Norm = P_Ia_2./max(P_Ia_2); % Normalizing

%P_I = FFT_Ia_2.*conj(FFT_Ia_2)/NFFT;% calculates PSD
(hamming)
%P_I_n = P_I./max(P_I); %normalise
```

```
figure(2);
plot(f,10*log10(P_Ia_Norm));hold on
plot(f,10*log10(P_Ia_2_Norm));hold on

xlabel('Frequency
(Hz)','FontSize',18,'FontWeight','normal');
ylabel('Normalized Magnitude of Ia
(dB)','FontSize',18,'FontWeight','normal');
title('PSD of motor line
current','FontSize',22,'FontWeight','bold');
%title('PSD of motor line current');
legend('Healthy - 100% load','Faulty - 100%
load','FontSize',14);
axis([35 65 -120 2]);
grid minor
```

B. MCSA – broken rotor bar at different loads

```
function MCSA1
Noload_data = load('BNoLoad_2976vsi.txt');
Load2p_data = load('BLoad_2932vsi.txt');
Load4p_data = load('BLoad_2910vsi.txt');
% Load6p_data = load('BLoad_2938.txt');
Load8p_data = load('BLoad_2893vsi.txt');
Load10p_data = load('BLoad_2926.txt');

f_sampling = 25600; % Sampling frequency
T = 1/f_sampling; % Sampling period
N = 768000; % Number of samples
t = (0:N-1)*T; % Time Vector

ia_Noload = Noload_data(:,7); % read phase A current of
healthy motor
ia_Load2p = Load2p_data(:,7); % read phase A current of
healthy motor
ia_Load4p = Load4p_data(:,7); % read phase A current of
healthy motor
% ia_Load6p = Load6p_data(:,7); % read phase A current of
healthy motor
ia_Load8p = Load8p_data(:,7); % read phase A current of
healthy motor
ia_Load10p = Load10p_data(:,7); % read phase A current of
healthy motor

ia_Noload = ia_Noload(640000:end);
ia_Load2p = ia_Load2p(640000:end);
```

```
ia_Load4p = ia_Load4p(640000:end);
ia_Load8p = ia_Load8p(640000:end);
ia_Load10p = ia_Load10p(640000:end);
Nn = length(ia_Noload);
%w = hann(N); % apply window function
% Nh = 1:N; % number of windows for Hann Window
Nh = 1:Nn;
Nhr = rot90(Nh); % rotated window vector
Window(Nhr) = 0.5*(1-cos(2*pi*(Nhr)/Nn)); % manually
perform Hann Window
Window_rot = rot90(Window); % rotate Window vector to
perform multiplication

ia_hann_Noload = ia_Noload.*Window_rot; % multiply
current vector by rotated window vector
ia_hann_Load2p = ia_Load2p.*Window_rot; % multiply
current vector by rotated window vector
ia_hann_Load4p = ia_Load4p.*Window_rot; % multiply
current vector by rotated window vector
% ia_hann_Load6p = ia_Load6p.*Window_rot; % multiply
current vector by rotated window vector
ia_hann_Load8p = ia_Load8p.*Window_rot; % multiply
current vector by rotated window vector
ia_hann_Load10p = ia_Load10p.*Window_rot; % multiply
current vector by rotated window vector
% ia_hann_Loadres = ia_Loadres.*Window_rot; % multiply
current vector by rotated window vector

NFFT = 2^nextpow2(N); % zero padding
f = (f_sampling/NFFT)*(0:NFFT/2-1); %create a frequency
vector

% FFT_Ia = fft(ia_hann_healthy,NFFT); % run FFT...
% FFT_Ia = FFT_Ia(1:NFFT/2); % creates single sided
spectrum
% FFT_Ia_2 = fft(ia_hann_fault,NFFT); % run FFT...
% FFT_Ia_2 = FFT_Ia_2(1:NFFT/2); % creates single sided
spectrum

FFT_Ia = fft(ia_hann_Noload,NFFT); % run FFT...
FFT_Ia = FFT_Ia(1:NFFT/2); % creates single sided
spectrum
FFT_Ia2 = fft(ia_hann_Load2p,NFFT); % run FFT...
FFT_Ia2 = FFT_Ia2(1:NFFT/2); % creates single sided
spectrum
FFT_Ia4 = fft(ia_hann_Load4p,NFFT); % run FFT...
```

```
FFT_Ia4 = FFT_Ia4(1:NFFT/2); % creates single sided
spectrum
% FFT_Ia6 = fft(ia_hann_Load6p,NFFT); % run FFT...
% FFT_Ia6 = FFT_Ia6(1:NFFT/2); % creates single sided
spectrum
FFT_Ia8 = fft(ia_hann_Load8p,NFFT); % run FFT...
FFT_Ia8 = FFT_Ia8(1:NFFT/2); % creates single sided
spectrum
FFT_Ia10 = fft(ia_hann_Load10p,NFFT); % run FFT...
FFT_Ia10 = FFT_Ia10(1:NFFT/2); % creates single sided
spectrum
% FFT_IaR = fft(ia_hann_Loadres,NFFT); % run FFT...
% FFT_IaR = FFT_IaR(1:NFFT/2); % creates single sided
spectrum
P_Ia = (1/NFFT) * abs(FFT_Ia).^2; % calculating power for
each freq comp
P_Ia_Norm = P_Ia./max(P_Ia); % Normalizing
P_Ia2 = (1/NFFT) * abs(FFT_Ia2).^2; % calculating power
for each freq comp
P_Ia2_Norm = P_Ia2./max(P_Ia2); % Normalizing
P_Ia4 = (1/NFFT) * abs(FFT_Ia4).^2; % calculating power
for each freq comp
P_Ia4_Norm = P_Ia4./max(P_Ia4); % Normalizing
% P_Ia6 = (1/NFFT) * abs(FFT_Ia6).^2; % calculating power
for each freq comp
% P_Ia6_Norm = P_Ia6./max(P_Ia6); % Normalizing
P_Ia8 = (1/NFFT) * abs(FFT_Ia8).^2; % calculating power
for each freq comp
P_Ia8_Norm = P_Ia8./max(P_Ia8); % Normalizing
P_Ia10 = (1/NFFT) * abs(FFT_Ia10).^2; % calculating power
for each freq comp
P_Ia10_Norm = P_Ia10./max(P_Ia10); % Normalizing
% P_IaR = (1/NFFT) * abs(FFT_IaR).^2; % calculating power
for each freq comp
% P_IaR_Norm = P_IaR./max(P_IaR); % Normalizing

% P_Ia = (1/NFFT) * abs(FFT_Ia).^2; % calculating power
for each freq comp
% P_Ia_Norm = P_Ia./max(P_Ia); % Normalizing
%
% P_Ia_2 = (1/NFFT) * abs(FFT_Ia_2).^2; % calculating
power for each freq comp
% P_Ia_2_Norm = P_Ia_2./max(P_Ia_2); % Normalizing

%P_I = FFT_Ia_2.*conj(FFT_Ia_2)/NFFT;% calculates PSD
(hamming)
%P_I_n = P_I./max(P_I); %normalise
```

```
% figure(1); %
plot(f(7200:9200),10*log10(P_Ia_Norm(7200:9200)),'g');
hold on,
% plot(f(7200:9200),10*log10(P_Ia_2_Norm(7200:9200)));
%
% xlabel('Frequency (Hz)')
% ylabel('Normalized Magnitude of Ia (dB)');
% title('Single Sided PSD of Ia using a Hann Window');
% %legend('Healthy Motor No load (inverter)','Motor with
4 shorted turns, 100% load (inverter)');
% legend('Healthy Motor, no load','Motor with 4 shorted
turns, no load');

figure(2);
plot(f,10*log10(P_Ia_Norm));hold on
plot(f,10*log10(P_Ia2_Norm));hold on
plot(f,10*log10(P_Ia4_Norm));hold on
% plot(f,10*log10(P_Ia6_Norm));hold on
plot(f,10*log10(P_Ia8_Norm));hold on
% plot(f,10*log10(P_Ia10_Norm));hold on

xlabel('Frequency
(Hz)','FontSize',18,'FontWeight','normal');
ylabel('Normalized Magnitude of Ia
(dB)','FontSize',18,'FontWeight','normal');
title('PSD of motor line
current','FontSize',22,'FontWeight','bold');
title('PSD of motor line current');
legend('No load','50% load','75% load','100%
load','FontSize',14);
axis([35 65 -120 2]);
grid minor
% legend({'Healthy motor,inverter driven, 100%
load','Motor with 4 shorted turns, inverter driven, 100%
load'},'FontSize',18,'FontWeight','normal');
```

C. Inverter Open switch Faults Analysis

```
function InverterFaults
%%Load simulation data
% load('IauF.mat'); Ia = I.Data; Ti = I.Time;
% load('VauF.mat'); Va = V.Data; Tv = V.Time;
% load('Ia2.mat'); IA = ia.Data; Ti = ia.Time;
% load('Vab2.mat'); Vab = Va.Data; Tv = Va.Time;
% load('Ib2.mat'); IB = ib.Data; Ti = ib.Time;
% load('Vbc2.mat'); Vbc = Vb.Data; Tv = Vb.Time;
% load('Ic2.mat'); IC = ic.Data; Ti = ic.Time;
```

```
% load('Vca2.mat'); Vca = Vc.Data; Tv = Vc.Time;
% load('Sp2.mat'); sp = S.Data; Ts = S.Time;
% load('Tor2.mat'); tor = T.Data; Tt = T.Time;

%%voltage, current, speed or torque against time for
simulation data
% sp = sp * 60/(pi);
% plot(Tt,sp); axis([0.9 1.2 2700 3210])
% xlabel('Time(s)','FontSize',18,'FontWeight','normal');
% % ylabel('Current Amplitude
(A)','FontSize',18,'FontWeight','normal');
% ylabel('Speed
(rpm)','FontSize',18,'FontWeight','normal');
% title('Rotor Speed','FontSize',22,'FontWeight','bold');
% % legend('Vab','Vbc','Vca','FontSize',14);
% % legend('Ia','Ib','Ic','FontSize',14);


filename = 'MyInverterOCtop0.txt';
% % filename = 'MyInverterOCbottom0.txt';
% filename = 'MyInverter2SwitchesSameArm.txt';
% % filename = 'MyInverter2SwitchesDifferentArms.txt';
% filename = 'MyInverter2SwitchesSamePosition.txt';

FileID = fopen(filename,'r');
C = textscan(FileID,'%f %f %f %f %f %f %f %f %f %f %f %f
%f %f','HeaderLines',23,'delimiter',',');
fclose(FileID);

T = C{1}.'; Tr = C{8}.'; S = C{9}.';
Vab = C{3}.'; Vbc = C{2}.'; Vca = C{4}.';
Ia = C{7}.'; Ib = C{6}.'; Ic = C{5}.';

%%voltage, current, speed or torque against time for
experimental data
% plot (T,Vab,T,Vbc,T,Vca);
% plot(T,Ia,T,Ib,T,Ic)
plot(T,Tr)
xlabel('Time(s)','FontSize',18,'FontWeight','normal');
% ylabel('Current Amplitude
(A)','FontSize',18,'FontWeight','normal');
ylabel('Torque
(Nm)','FontSize',18,'FontWeight','normal');
title('Motor Torque','FontSize',22,'FontWeight','bold');
% title('Three-phase Motor
Current','FontSize',22,'FontWeight','bold');
% % legend('Vab','Vbc','Vca','FontSize',14);
```

```
% legend('Ia','Ib','Ic','FontSize',14);

%%Calculation of the mean values of line voltage and
current and plotting
Iam = movmean(Ia,512); Ibm = movmean(Ib,512); Icm =
movmean(Ic,512);
Vabm = movmean(Vab,512); Vbcm = movmean(Vbc,512); Vcam =
movmean(Vca,512);
% plot(T,Vabm,T,Vbcm,T,Vcam); axis([0 30 -15 15])
% plot (T,Iam, T,Ibm, T,Icm)
% xlabel('Time(s)','FontSize',18,'FontWeight','normal');
% ylabel('Current Average
(A)','FontSize',18,'FontWeight','normal');
% title('Three-phase Average
Current','FontSize',22,'FontWeight','bold');
% legend('Ia','Ib','Ic','FontSize',14);
% % legend('Vab','Vbc','Vca','FontSize',14);

%%Calculation of the THD values for line voltage and
currents
% VabH = thd(Vab(1:379200))
% VabF = thd(Vab(382060:768000))
% VbcH = thd(Vbc(1:379200))
% VbcF = thd(Vbc(382060:768000))
% VcaH = thd(Vca(1:379200))
% VcaF = thd(Vca(382060:768000))

% IaH = thd(Ia(1:379200))
% IaF = thd(Ia(382060:768000))
% IbH = thd(Ib(1:379200))
% IbF = thd(Ib(382060:768000))
% IcH = thd(Ic(1:379200))
% IcF = thd(Ic(382060:768000))

%%Normalization of the line currents
% % Im = max(Ia(1:1400000));
% Ima = max(Ia(1:256000)); Imb = max(Ib(1:256000)); Imc =
max(Ic(1:256000));
% Im = (Ima + Imb + Imc)/3;
% is = Im * sqrt(3/2);
% IaN = Ia/is; IbN = Ib/is; IcN = Ic/is;
% % plot(T,IaN,T,IbN,T,IcN)
% % legend("IaN","IbN","IcN")

%%Absolute values of the normalized currents
% IaN_abs = abs(IaN); IbN_abs = abs(IbN); IcN_abs =
abs(IcN);
```

```
% % plot(T,IaN_abs,T,IbN_abs,T,IcN_abs)
% % legend("IaN_abs","IbN_abs","IcN_abs")

%%Calculation of mean of the the absolute values of the
normalized currents
% % IaN_abs_A = movmean(IaN_abs,20000); IbN_abs_A =
movmean(IbN_abs,20000); IcN_abs_A =
movmean(IcN_abs,20000);
% IaN_abs_A = movmean(IaN_abs,512); IbN_abs_A =
movmean(IbN_abs,512); IcN_abs_A = movmean(IcN_abs,512);
% Aver = (IaN_abs_A + IbN_abs_A + IcN_abs_A)/3;
% % plot(T,IaN_abs_A,T,IbN_abs_A,T,IcN_abs_A);
% % legend("IaN_abs_A","IbN_abs_A","IcN_abs_A")

%%Calculation of the diagnostic variables
% e_a = 0.5198 - IaN_abs_A; e_b = 0.5198 - IbN_abs_A; e_c
= 0.5198 - IcN_abs_A;
% % e_a = Aver - IaN_abs_A; e_b = Aver - IbN_abs_A; e_c =
Aver - IcN_abs_A;

%%Plotting of current averages and diagnostic variables
% subplot(2,1,1)
% plot(T,IaNA,T,IbNA,T,IcNA);
% legend("IaNA","IbNA","IcNA")
% title("Normalized Currents Average Values")
% xlabel("Time(s)")
% ylabel("Norm. Current Av. Values (A)")
% axis([1 30 -0.5 0.75])
% grid minor

% subplot(2,1,2)
% plot(T,e_a,T,e_b,T,e_c);
% legend("e_a","e_b","e_c");
% title("Diagnostic Variables Vs Time")
% xlabel("Time(s)")
% ylabel("Diagnostic Variable")
% % axis([0 30 -0.2 0.5])
% % axis([1 4 -0.4 0.3])
grid minor
```

D. Grid-connected Standstill Impedance variation

```
function StandStillG
filename = 'hrb_impe.txt';
FileID = fopen(filename,'r');
C = textscan(FileID,'%f %f %f','delimiter','\t');
fclose(FileID);
```

```
filename = 'brb_impe.txt';
FileID = fopen(filename,'r');
D = textscan(FileID,'%f %f %f','delimiter','\t');
fclose(FileID);

Impedh = C{3}.';
Impedb = D{3}.';
Angle =
[0,10,20,30,40,50,60,70,80,90,100,110,120,130,140,150,160
,170,180,190,200,210,220,230,240,250,260,270,280,290,300,
310,320,330,340,350];
plot(Angle,Impedh,Angle,Impedb)
xlabel('Rotor
Angle(degrees)','FontSize',18,'FontWeight','normal');
ylabel('Impedance(Magnitude)','FontSize',18,'FontWeight',
'normal');
title('Impedance Vs Rotor
Position','FontSize',22,'FontWeight','bold');
legend('Healthy Motor','Broken Rotor Bar
Motor','FontSize',14);
grid minor
```

E. Inverter-fed standstill impedance test and its advancement

```
function LockedRotor
PhaseB = ["P00S.txt" "P10S.txt" "P20S.txt" "P30S.txt"
"P40S.txt" "P50S.txt" "P60S.txt" "P70S.txt" "P80S.txt"
"P90S.txt" "P100S.txt" "P110S.txt" "P120S.txt"
"P130S.txt" "P140S.txt" "P150S.txt" "P160S.txt"
"P170S.txt" "P180S.txt" "P190S.txt" "P200S.txt"
"P210S.txt" "P220S.txt" "P230S.txt" "P240S.txt"
"P250S.txt" "P260S.txt" "P270S.txt" "P280S.txt"
"P290S.txt" "P300S.txt" "P310S.txt" "P320S.txt"
"P330S.txt" "P340S.txt" "P350S.txt"];
PhaseC = ["BP00S10.txt" "BP10S10.txt" "BP20S10.txt"
"BP30S10.txt" "BP40S10.txt" "BP50S10.txt" "BP60S10.txt"
"BP70S10.txt" "BP80S10.txt" "BP90S10.txt" "BP100S10.txt"
"BP110S10.txt" "BP120S10.txt" "BP130S10.txt"
"BP140S10.txt" "BP150S10.txt" "BP160S10.txt"
"BP170S10.txt" "BP180S10.txt" "BP190S10.txt"
"BP200S10.txt" "BP210S10.txt" "BP220S10.txt"
"BP230S10.txt" "BP240S10.txt" "BP250S10.txt"
"BP260S10.txt" "BP270S10.txt" "BP280S10.txt"
"BP290S10.txt" "BP300S10.txt" "BP310S10.txt"
"BP320S10.txt" "BP330S10.txt" "BP340S10.txt"
"BP350S10.txt"];
Za = 0; Zb = 0; Zc = 0; x = (0.866-0.5i)*sqrt(3);
```

```
% for m = 1:36
%     filename = PhaseB(m);
%     FileID = fopen(filename,'r');
%     C = textscan(FileID,'%f %f %f %f %f %f %f %f %f %f
%f %f %f %f','HeaderLines',23,'delimiter',',');
%     fclose(FileID);
%
%     Vab = C{2}.'; Vbc = C{3}.'; Vca = C{4}.';
%     Ia = C{5}.'; Ib = C{6}.'; Ic = C{7}.';
%     T = C{1}.';
%
%     Fs = 25600;
%
%     XIb = fft(Ib)/length(Ib);
%     XIb = (XIb(1:length(Ib)/2+1))*2;
%
%     XVbc = fft(Vbc)/length(Vbc);
%     XVbc = (XVbc(1:length(Vbc)/2+1))*2;
%
%     F = 0:Fs/length(Ib):Fs/2;
%     i = 0;
%     for n = 1:length(F)
%         if abs(XIb(n))== max(abs(XIb))
%             i = n;
%             break
%         end
%     end
%     Zb(m) = XVbc(i)./XIb(i);
% end

% for m = 1:36
%     filename = PhaseC(m);
%     FileID = fopen(filename,'r');
%     C = textscan(FileID,'%f %f %f %f %f %f %f %f %f %f
%f %f %f %f','HeaderLines',23,'delimiter',',');
%     fclose(FileID);
%
%     Vab = C{2}.'; Vbc = C{3}.'; Vca = C{4}.';
%     Ia = C{5}.'; Ib = C{6}.'; Ic = C{7}.';
%     T = C{1}.';
%
%     Fs = 25600;
%
%     XIc = fft(Ic)/length(Ic);
%     XIc = (XIc(1:length(Ic)/2+1))*2;
%
```

```
%       XVca = fft(Vca)/length(Vca);
%       XVca = (XVca(1:length(Vca)/2+1))*2;
%
%       F = 0:Fs/length(Ic):Fs/2;
%       i = 0;
%       for n = 1:length(F)
%           if abs(XIc(n))== max(abs(XIc))
%               i = n;
%               break
%           end
%       end
%       Zc(m) = XVca(i)./XIc(i);
% end
% Zb = abs(Zb)- 1.0913; Zc = abs(Zc)- 1.2413;
% Zc(1) = 17.0125;

filename = 'input2.txt';
% FID = fopen(filename, 'w');
% % fwrite(FID, Zc, 'char');
% fprintf(FID, '%f\n', Zc);
% fclose(FID);

FileID = fopen(filename,'r');
Zc = fscanf(FileID,'%f');
fclose(FileID);

Z1=[Zc(1),Zc(13),Zc(25)];Z2=[Zc(2),Zc(14),Zc(26)];Z3=[Zc(
3),Zc(15),Zc(27)];Z4=[Zc(4),Zc(16),Zc(28)];Z5=[Zc(5),Zc(1
7),Zc(29)];
Z6=[Zc(6),Zc(18),Zc(30)];Z7=[Zc(7),Zc(19),Zc(31)];Z8=[Zc(
8),Zc(20),Zc(32)];Z9=[Zc(9),Zc(21),Zc(33)];Z10=[Zc(10),Zc
(22),Zc(34)];
Z11=[Zc(11),Zc(23),Zc(35)];Z12=[Zc(12),Zc(24),Zc(36)];Z13
=[Zc(13),Zc(25),Zc(1)];Z14=[Zc(14),Zc(26),Zc(2)];Z15=[Zc(
15),Zc(27),Zc(3)];Z16=[Zc(16),Zc(28),Zc(4)];
Z17=[Zc(17),Zc(29),Zc(5)];Z18=[Zc(18),Zc(30),Zc(6)];Z19=[
Zc(19),Zc(31),Zc(7)];


A =
[0,10,20,30,40,50,60,70,80,90,100,110,120,130,140,150,160
,170,180];
Z =
[Z1;Z2;Z3;Z4;Z5;Z6;Z7;Z8;Z9;Z10;Z11;Z12;Z13;Z14;Z15;Z16;Z
17;Z18;Z19];
Zl = 0;
for n = 1:19
```

```
    m = Z(n,:);
    a = abs(m(1)-m(2));
    b = abs(m(2)-m(3));
    c = abs(m(3)-m(1));
    Z1(n)=(a+b+c)/3;
    Zaa(n) = m(1); Zbb(n) = m(2); Zcc(n) = m(3);
end
length(Zc)
% Angle =
[0,10,20,30,40,50,60,70,80,90,100,110,120,130,140,150,160
,170,180,190,200,210,220,230,240,250,260,270,280,290,300,
310,320,330,340,350];
% % plot(Angle, abs(Zb), Angle, abs(Zc))
% plot(Angle, Zb, Angle, Zc)
plot(A,Z1)
% plot(A,Zaa, A,Zbb, A, Zcc)
% legend("Za","Zb","Zc", 'FontSize',14)
% title("Impedance vs Rotor
Position",'FontSize',22,'FontWeight','bold')
title("Mean Impedance
Difference",'FontSize',16,'FontWeight','bold')
% ylabel("Impedance Magnitude (Ohms)
",'FontSize',18,'FontWeight','normal')
ylabel("Average Impedance Difference (Ohms)
",'FontSize',12,'FontWeight','normal')
xlabel("Rotor Position
(degrees)",'FontSize',12,'FontWeight','normal')
% xlabel("Rotor Angle
(degrees)",'FontSize',18,'FontWeight','normal')
grid minor
```

A3. Simulink Blocks for System Simulation and ePWM Module configuration

A. V/F control implementation block

i. Complete Simulink model

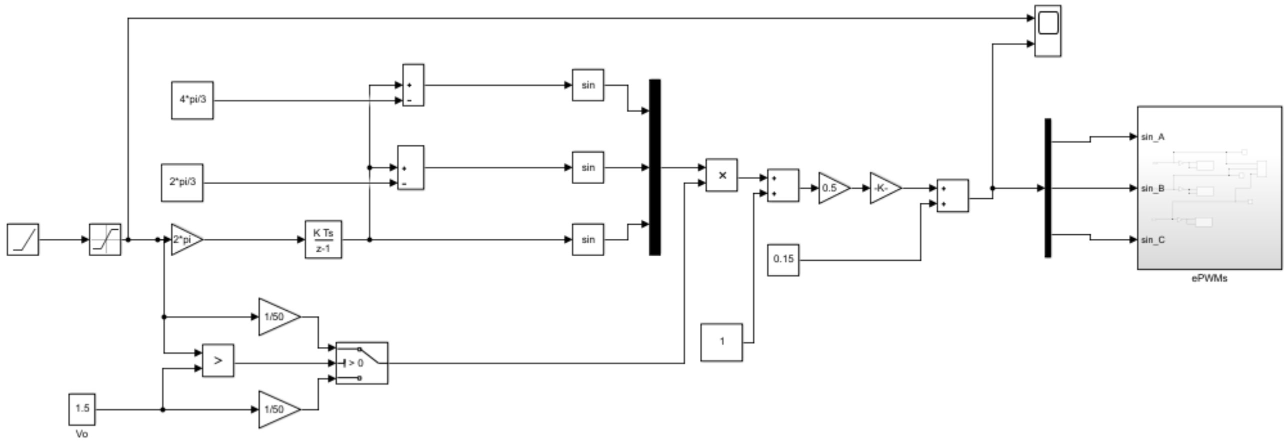

ii. ePWM Blocks

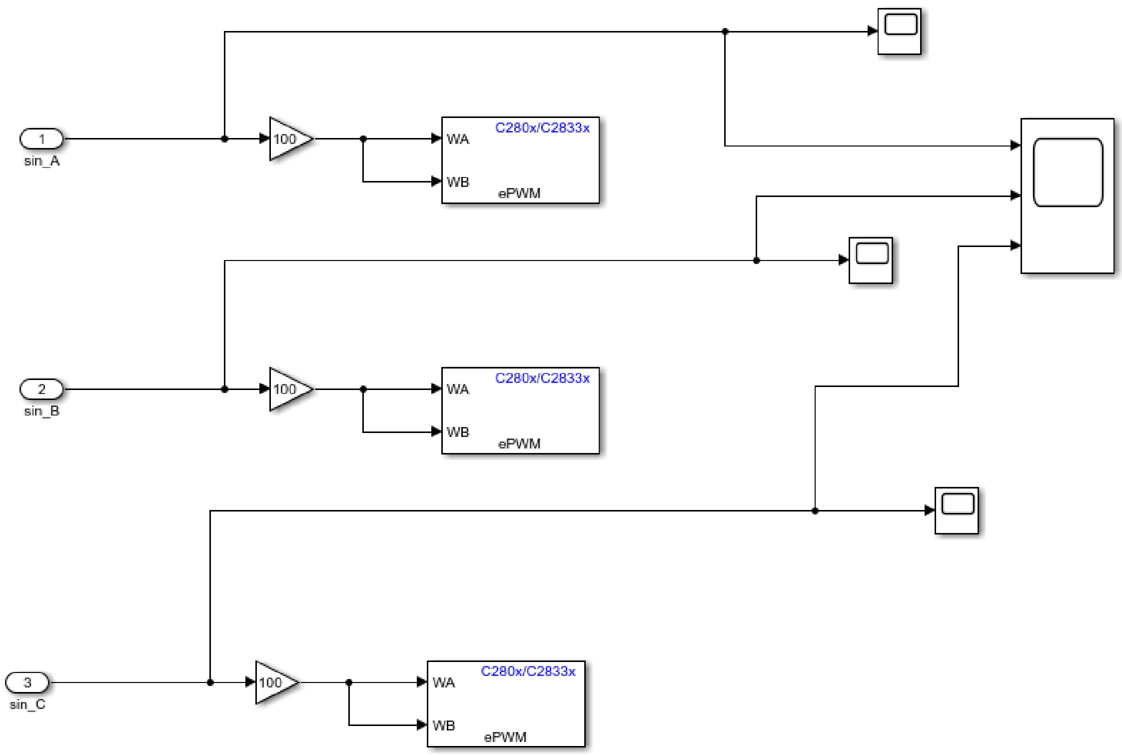

iii. ePWM block Configuration

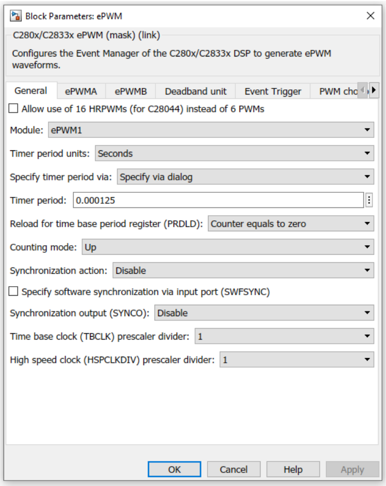

C280x/C2833x ePWM (mask) (link)

Configures the Event Manager of the C280x/C2833x DSP to generate ePWM waveforms.

☐ Allow use of 16 HRPWMs (for C28044) instead of 6 PWMs

Module: ePWM1

Timer period units: Seconds

Specify timer period via: Specify via dialog

Timer period: 0.000125

Reload for time base period register (PRDLD): Counter equals to zero

Counting mode: Up

Synchronization action: Disable

☐ Specify software synchronization via input port (SWFSYNC)

Synchronization output (SYNCO): Disable

Time base clock (TBCLK) prescaler divider: 1

High speed clock (HSPCLKDIV) prescaler divider: 1

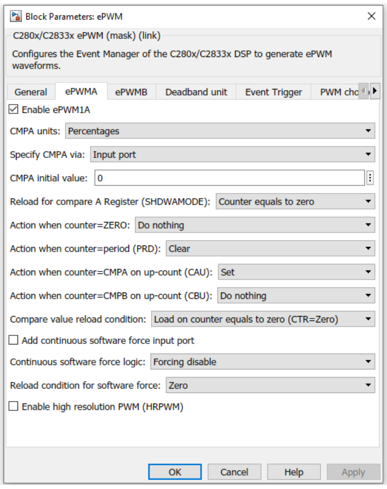

C280x/C2833x ePWM (mask) (link)

Configures the Event Manager of the C280x/C2833x DSP to generate ePWM waveforms.

☑ Enable ePWM1A

CMPA units: Percentages

Specify CMPA via: Input port

CMPA initial value: 0

Reload for compare A Register (SHDWAMODE): Counter equals to zero

Action when counter=ZERO: Do nothing

Action when counter=period (PRD): Clear

Action when counter=CMPA on up-count (CAU): Set

Action when counter=CMPB on up-count (CBU): Do nothing

Compare value reload condition: Load on counter equals to zero (CTR=Zero)

☐ Add continuous software force input port

Continuous software force logic: Forcing disable

Reload condition for software force: Zero

☐ Enable high resolution PWM (HRPWM)

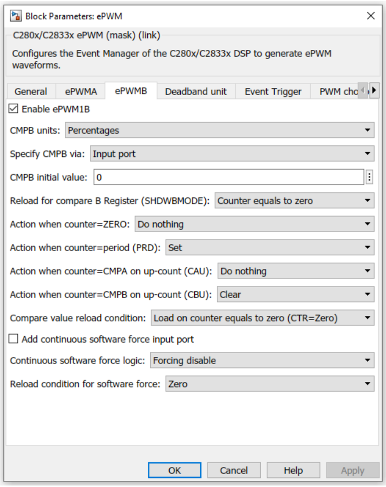

C280x/C2833x ePWM (mask) (link)

Configures the Event Manager of the C280x/C2833x DSP to generate ePWM waveforms.

☑ Enable ePWM1B

CMPB units: Percentages

Specify CMPB via: Input port

CMPB initial value: 0

Reload for compare B Register (SHDWBMODE): Counter equals to zero

Action when counter=ZERO: Do nothing

Action when counter=period (PRD): Set

Action when counter=CMPA on up-count (CAU): Do nothing

Action when counter=CMPB on up-count (CBU): Clear

Compare value reload condition: Load on counter equals to zero (CTR=Zero)

☐ Add continuous software force input port

Continuous software force logic: Forcing disable

Reload condition for software force: Zero

B. ePWM Blocks for Implementation of Open Switch faults

i. S1 Open

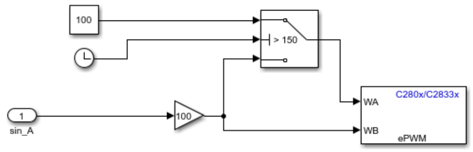

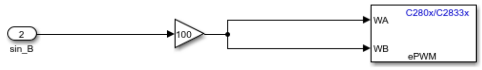

ii. S4 Open

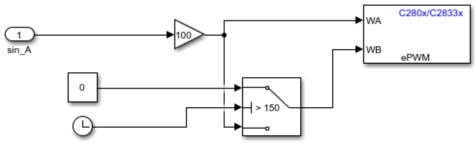

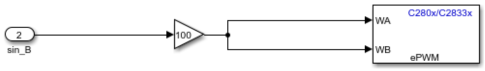

iii. S1 and S4 open

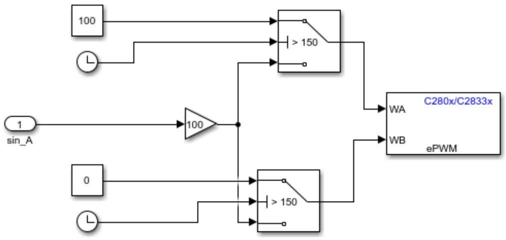

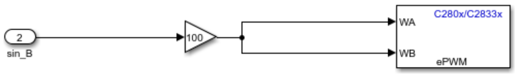

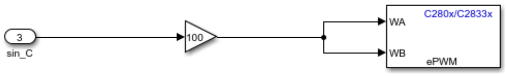

iv. S1 and S3 Open

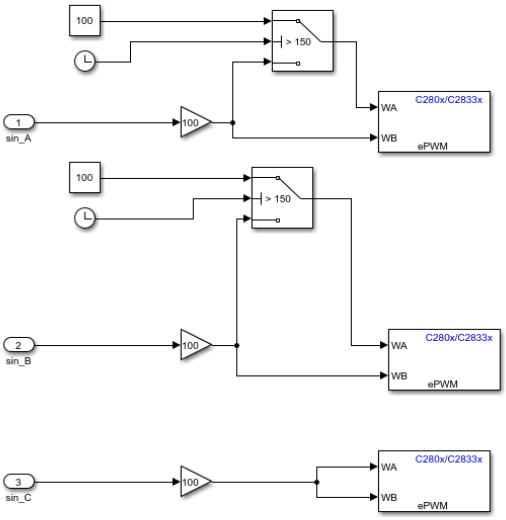

C. Configuration of ePWM in standstill impedance test

i. Simulink Model used

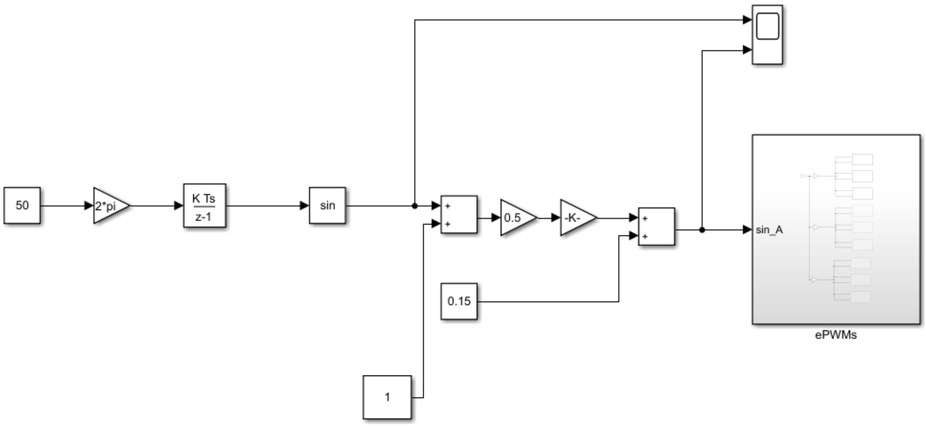

ii. Aligning the pulsating flux along the magnetic axis of phase A

(a) Configuration of the first bridge arm

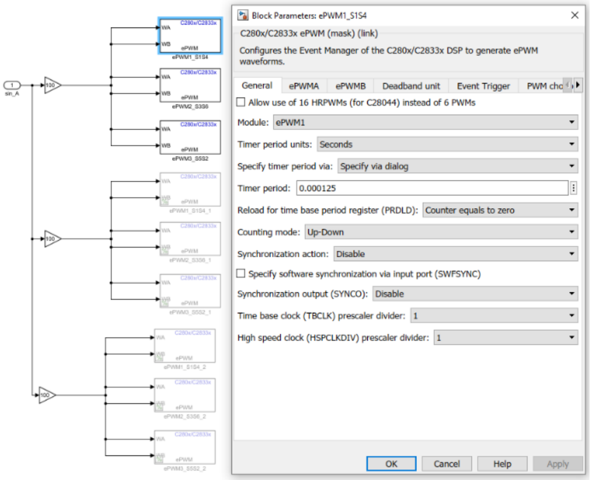
Block Parameters: ePWM1_S1S4

C280x/C2833x ePWM (mask) (link)

Configures the Event Manager of the C280x/C2833x DSP to generate ePWM waveforms.

☐ Allow use of 16 HRPWMs (for C28044) instead of 6 PWMs

Module: ePWM1

Timer period units: Seconds

Specify timer period via: Specify via dialog

Timer period: 0.000125

Reload for time base period register (PRDLD): Counter equals to zero

Counting mode: Up-Down

Synchronization action: Disable

☐ Specify software synchronization via input port (SWFSYNC)

Synchronization output (SYNCO): Disable

Time base clock (TBCLK) prescaler divider: 1

High speed clock (HSPCLKDIV) prescaler divider: 1

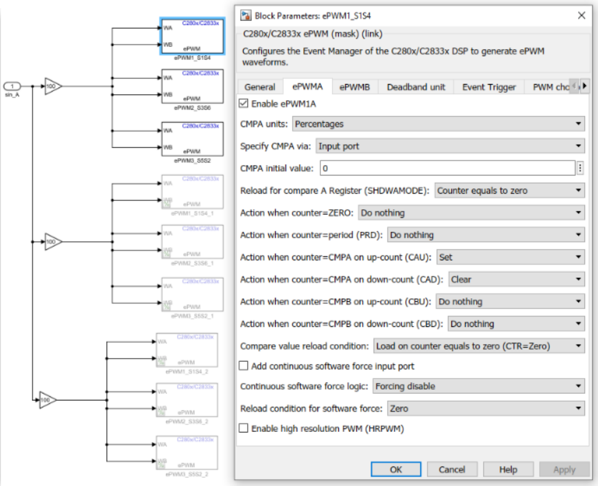
Block Parameters: ePWM1_S1S4

C280x/C2833x ePWM (mask) (link)

Configures the Event Manager of the C280x/C2833x DSP to generate ePWM waveforms.

☑ Enable ePWM1A

CMPA units: Percentages

Specify CMPA via: Input port

CMPA initial value: 0

Reload for compare A Register (SHDWAMODE): Counter equals to zero

Action when counter=ZERO: Do nothing

Action when counter=period (PRD): Do nothing

Action when counter=CMPA on up-count (CAU): Set

Action when counter=CMPA on down-count (CAD): Clear

Action when counter=CMPB on up-count (CBU): Do nothing

Action when counter=CMPB on down-count (CBD): Do nothing

Compare value reload condition: Load on counter equals to zero (CTR=Zero)

☐ Add continuous software force input port

Continuous software force logic: Forcing disable

Reload condition for software force: Zero

☐ Enable high resolution PWM (HRPWM)

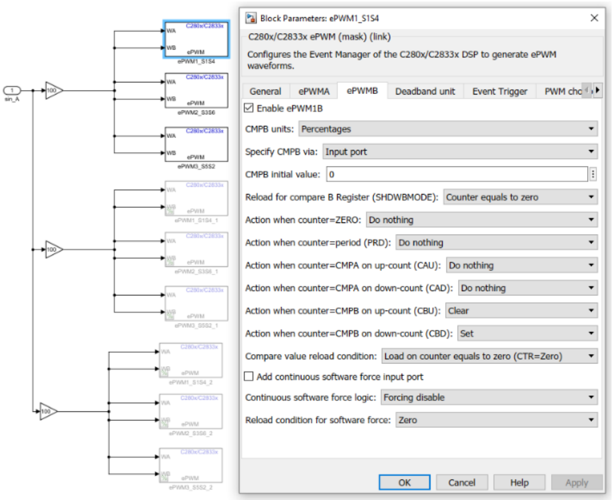

Block Parameters: ePWM1_S1S4

C280x/C2833x ePWM (mask) (link)

Configures the Event Manager of the C280x/C2833x DSP to generate ePWM waveforms.

☑ Enable ePWM1B

CMPB units: Percentages

Specify CMPB via: Input port

CMPB initial value: 0

Reload for compare B Register (SHDWBMODE): Counter equals to zero

Action when counter=ZERO: Do nothing

Action when counter=period (PRD): Do nothing

Action when counter=CMPA on up-count (CAU): Do nothing

Action when counter=CMPA on down-count (CAD): Do nothing

Action when counter=CMPB on up-count (CBU): Clear

Action when counter=CMPB on down-count (CBD): Set

Compare value reload condition: Load on counter equals to zero (CTR=Zero)

☐ Add continuous software force input port

Continuous software force logic: Forcing disable

Reload condition for software force: Zero

(b) Configuration of the second bridge arm

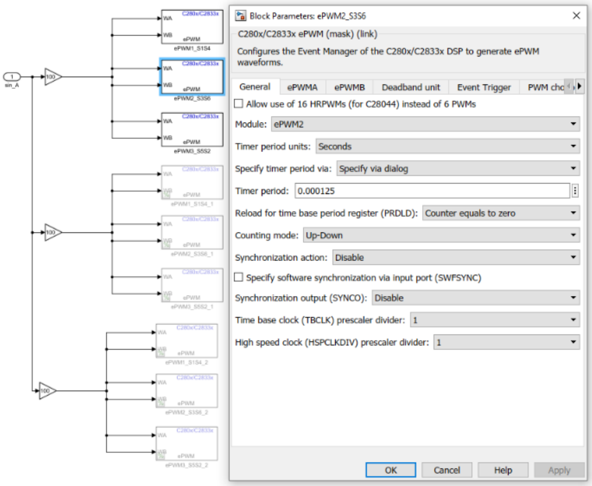

Block Parameters: ePWM2_S3S6

C280x/C2833x ePWM (mask) (link)

Configures the Event Manager of the C280x/C2833x DSP to generate ePWM waveforms.

☐ Allow use of 16 HRPWMs (for C28044) instead of 6 PWMs

Module: ePWM2

Timer period units: Seconds

Specify timer period via: Specify via dialog

Timer period: 0.000125

Reload for time base period register (PRDLD): Counter equals to zero

Counting mode: Up-Down

Synchronization action: Disable

☐ Specify software synchronization via input port (SWFSYNC)

Synchronization output (SYNCO): Disable

Time base clock (TBCLK) prescaler divider: 1

High speed clock (HSPCLKDIV) prescaler divider: 1

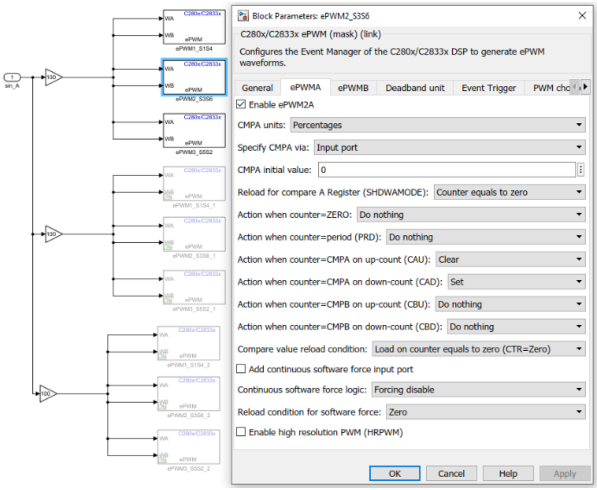

Block Parameters: ePWM2_S3S6

C280x/C2833x ePWM (mask) (link)

Configures the Event Manager of the C280x/C2833x DSP to generate ePWM waveforms.

☑ Enable ePWM2A

CMPA units: Percentages

Specify CMPA via: Input port

CMPA initial value: 0

Reload for compare A Register (SHDWAMODE): Counter equals to zero

Action when counter=ZERO: Do nothing

Action when counter=period (PRD): Do nothing

Action when counter=CMPA on up-count (CAU): Clear

Action when counter=CMPA on down-count (CAD): Set

Action when counter=CMPB on up-count (CBU): Do nothing

Action when counter=CMPB on down-count (CBD): Do nothing

Compare value reload condition: Load on counter equals to zero (CTR=Zero)

☐ Add continuous software force input port

Continuous software force logic: Forcing disable

Reload condition for software force: Zero

☐ Enable high resolution PWM (HRPWM)

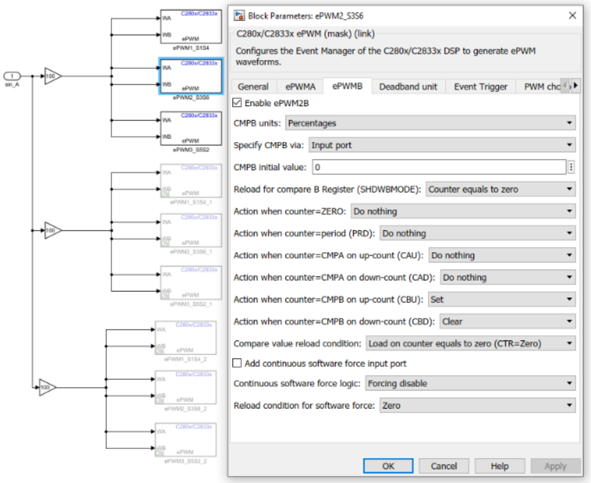

Block Parameters: ePWM2_S3S6

C280x/C2833x ePWM (mask) (link)

Configures the Event Manager of the C280x/C2833x DSP to generate ePWM waveforms.

☑ Enable ePWM2B

CMPB units: Percentages

Specify CMPB via: Input port

CMPB initial value: 0

Reload for compare B Register (SHDWBMODE): Counter equals to zero

Action when counter=ZERO: Do nothing

Action when counter=period (PRD): Do nothing

Action when counter=CMPA on up-count (CAU): Do nothing

Action when counter=CMPA on down-count (CAD): Do nothing

Action when counter=CMPB on up-count (CBU): Set

Action when counter=CMPB on down-count (CBD): Clear

Compare value reload condition: Load on counter equals to zero (CTR=Zero)

☐ Add continuous software force input port

Continuous software force logic: Forcing disable

Reload condition for software force: Zero

(c) Configuration of the third bridge arm

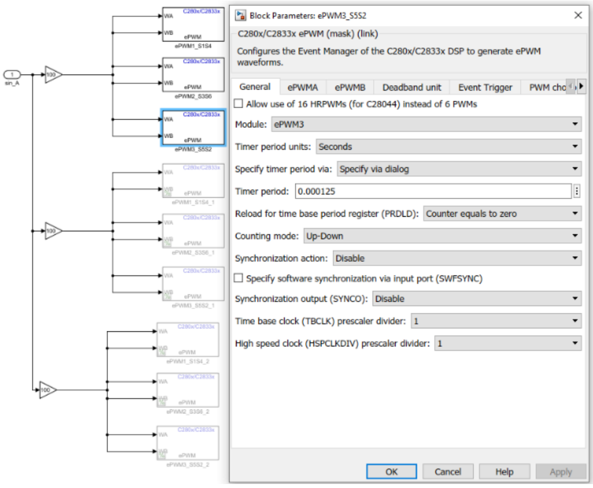

Block Parameters: ePWM3_S5S2

C280x/C2833x ePWM (mask) (link)

Configures the Event Manager of the C280x/C2833x DSP to generate ePWM waveforms.

☐ Allow use of 16 HRPWMs (for C28044) instead of 6 PWMs
Module: ePWM3
Timer period units: Seconds
Specify timer period via: Specify via dialog
Timer period: 0.000125
Reload for time base period register (PRDLD): Counter equals to zero
Counting mode: Up-Down
Synchronization action: Disable
☐ Specify software synchronization via input port (SWFSYNC)
Synchronization output (SYNCO): Disable
Time base clock (TBCLK) prescaler divider: 1
High speed clock (HSPCLKDIV) prescaler divider: 1

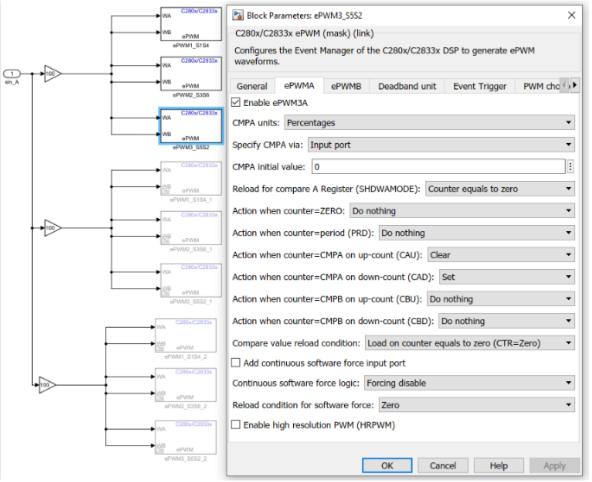

Block Parameters: ePWM3_S5S2

C280x/C2833x ePWM (mask) (link)

Configures the Event Manager of the C280x/C2833x DSP to generate ePWM waveforms.

☑ Enable ePWM3A
CMPA units: Percentages
Specify CMPA via: Input port
CMPA initial value: 0
Reload for compare A Register (SHDWAMODE): Counter equals to zero
Action when counter=ZERO: Do nothing
Action when counter=period (PRD): Do nothing
Action when counter=CMPA on up-count (CAU): Clear
Action when counter=CMPA on down-count (CAD): Set
Action when counter=CMPB on up-count (CBU): Do nothing
Action when counter=CMPB on down-count (CBD): Do nothing
Compare value reload condition: Load on counter equals to zero (CTR=Zero)
☐ Add continuous software force input port
Continuous software force logic: Forcing disable
Reload condition for software force: Zero
☐ Enable high resolution PWM (HRPWM)

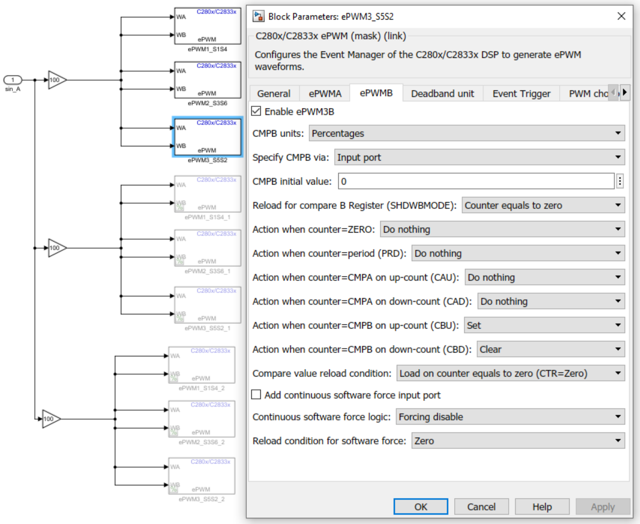

Block Parameters: ePWM3_S5S2

C280x/C2833x ePWM (mask) (link)

Configures the Event Manager of the C280x/C2833x DSP to generate ePWM waveforms.

☑ Enable ePWM3B
CMPB units: Percentages
Specify CMPB via: Input port
CMPB initial value: 0
Reload for compare B Register (SHDWBMODE): Counter equals to zero
Action when counter=ZERO: Do nothing
Action when counter=period (PRD): Do nothing
Action when counter=CMPA on up-count (CAU): Do nothing
Action when counter=CMPA on down-count (CAD): Do nothing
Action when counter=CMPB on up-count (CBU): Set
Action when counter=CMPB on down-count (CBD): Clear
Compare value reload condition: Load on counter equals to zero (CTR=Zero)
☐ Add continuous software force input port
Continuous software force logic: Forcing disable
Reload condition for software force: Zero

iii. Aligning the pulsating flux along the magnetic axis of phase B

(a) Configuration of ePWM for the first bridge arm

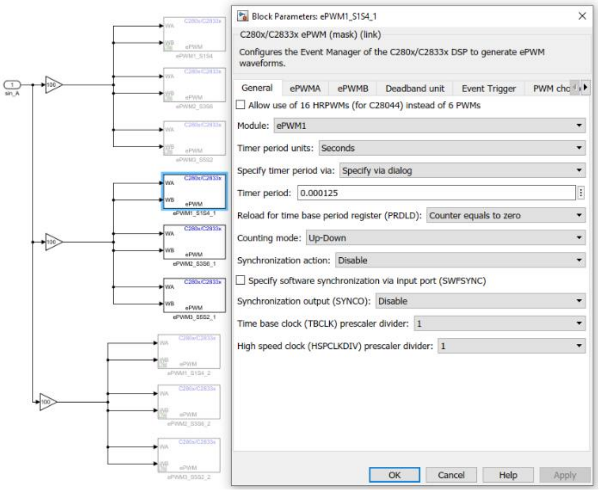

Block Parameters: ePWM1_S1S4_1

C280x/C2833x ePWM (mask) (link)

Configures the Event Manager of the C280x/C2833x DSP to generate ePWM waveforms.

☐ Allow use of 16 HRPWMs (for C28044) instead of 6 PWMs
Module: ePWM1
Timer period units: Seconds
Specify timer period via: Specify via dialog
Timer period: 0.000125
Reload for time base period register (PRDLD): Counter equals to zero
Counting mode: Up-Down
Synchronization action: Disable
☐ Specify software synchronization via input port (SWFSYNC)
Synchronization output (SYNCO): Disable
Time base clock (TBCLK) prescaler divider: 1
High speed clock (HSPCLKDIV) prescaler divider: 1

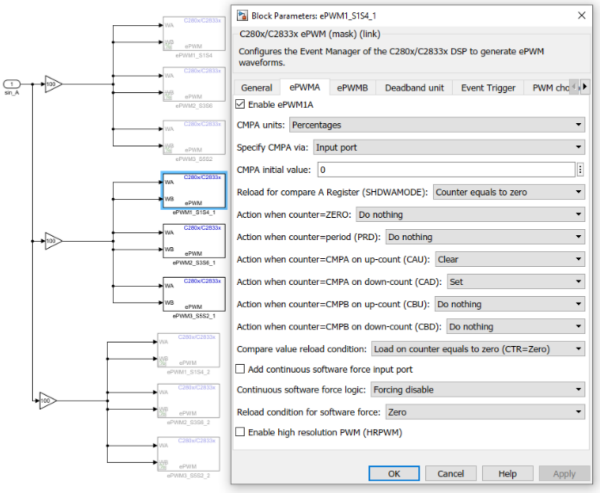

Block Parameters: ePWM1_S1S4_1

C280x/C2833x ePWM (mask) (link)

Configures the Event Manager of the C280x/C2833x DSP to generate ePWM waveforms.

☑ Enable ePWM1A
CMPA units: Percentages
Specify CMPA via: Input port
CMPA initial value: 0
Reload for compare A Register (SHDWAMODE): Counter equals to zero
Action when counter=ZERO: Do nothing
Action when counter=period (PRD): Do nothing
Action when counter=CMPA on up-count (CAU): Clear
Action when counter=CMPA on down-count (CAD): Set
Action when counter=CMPB on up-count (CBU): Do nothing
Action when counter=CMPB on down-count (CBD): Do nothing
Compare value reload condition: Load on counter equals to zero (CTR=Zero)
☐ Add continuous software force input port
Continuous software force logic: Forcing disable
Reload condition for software force: Zero
☐ Enable high resolution PWM (HRPWM)

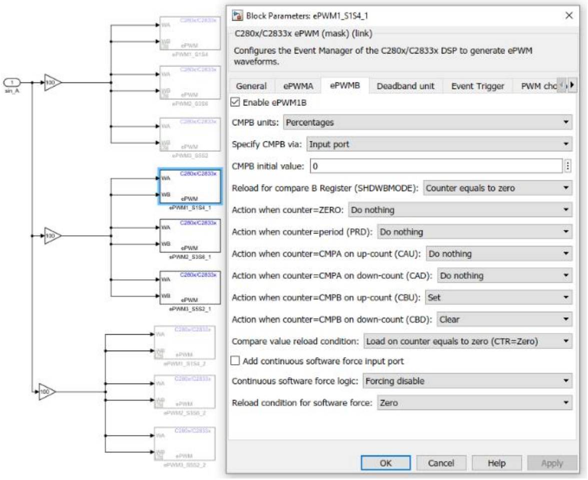

Block Parameters: ePWM1_S1S4_1

C280x/C2833x ePWM (mask) (link)

Configures the Event Manager of the C280x/C2833x DSP to generate ePWM waveforms.

☑ Enable ePWM1B

CMPB units: Percentages

Specify CMPB via: Input port

CMPB initial value: 0

Reload for compare B Register (SHDWBMODE): Counter equals to zero

Action when counter=ZERO: Do nothing

Action when counter=period (PRD): Do nothing

Action when counter=CMPA on up-count (CAU): Do nothing

Action when counter=CMPA on down-count (CAD): Do nothing

Action when counter=CMPB on up-count (CBU): Set

Action when counter=CMPB on down-count (CBD): Clear

Compare value reload condition: Load on counter equals to zero (CTR=Zero)

☐ Add continuous software force input port

Continuous software force logic: Forcing disable

Reload condition for software force: Zero

(b) Configuration of ePWM for the second bridge arm

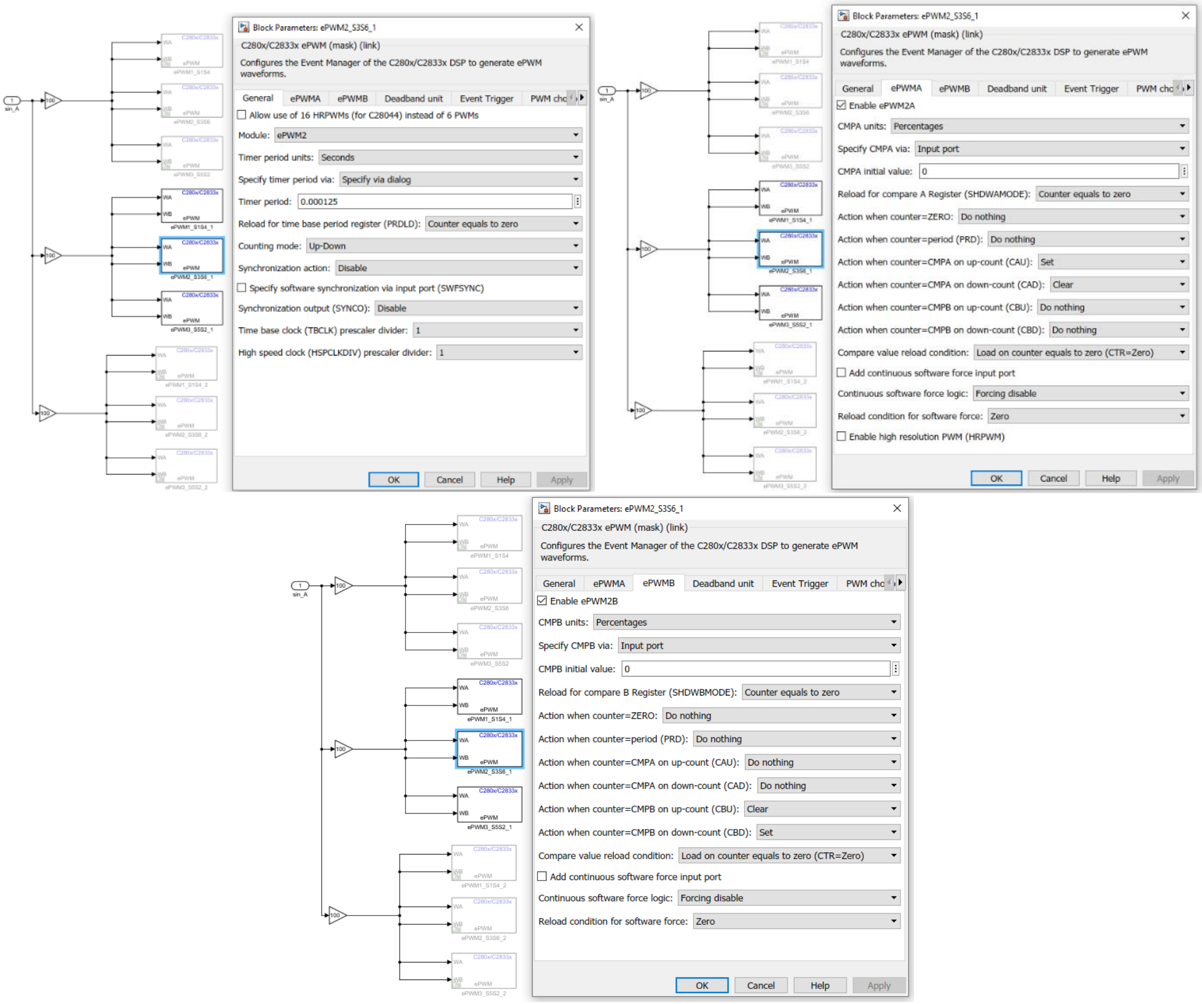

Block Parameters: ePWM2_S3S6_1

C280x/C2833x ePWM (mask) (link)

Configures the Event Manager of the C280x/C2833x DSP to generate ePWM waveforms.

☐ Allow use of 16 HRPWMs (for C28044) instead of 6 PWMs

Module: ePWM2

Timer period units: Seconds

Specify timer period via: Specify via dialog

Timer period: 0.000125

Reload for time base period register (PRDLD): Counter equals to zero

Counting mode: Up-Down

Synchronization action: Disable

☐ Specify software synchronization via input port (SWFSYNC)

Synchronization output (SYNCO): Disable

Time base clock (TBCLK) prescaler divider: 1

High speed clock (HSPCLKDIV) prescaler divider: 1

Block Parameters: ePWM2_S3S6_1

C280x/C2833x ePWM (mask) (link)

Configures the Event Manager of the C280x/C2833x DSP to generate ePWM waveforms.

☑ Enable ePWM2A

CMPA units: Percentages

Specify CMPA via: Input port

CMPA initial value: 0

Reload for compare A Register (SHDWAMODE): Counter equals to zero

Action when counter=ZERO: Do nothing

Action when counter=period (PRD): Do nothing

Action when counter=CMPA on up-count (CAU): Set

Action when counter=CMPA on down-count (CAD): Clear

Action when counter=CMPB on up-count (CBU): Do nothing

Action when counter=CMPB on down-count (CBD): Do nothing

Compare value reload condition: Load on counter equals to zero (CTR=Zero)

☐ Add continuous software force input port

Continuous software force logic: Forcing disable

Reload condition for software force: Zero

☐ Enable high resolution PWM (HRPWM)

Block Parameters: ePWM2_S3S6_1

C280x/C2833x ePWM (mask) (link)

Configures the Event Manager of the C280x/C2833x DSP to generate ePWM waveforms.

☑ Enable ePWM2B

CMPB units: Percentages

Specify CMPB via: Input port

CMPB initial value: 0

Reload for compare B Register (SHDWBMODE): Counter equals to zero

Action when counter=ZERO: Do nothing

Action when counter=period (PRD): Do nothing

Action when counter=CMPA on up-count (CAU): Do nothing

Action when counter=CMPA on down-count (CAD): Do nothing

Action when counter=CMPB on up-count (CBU): Clear

Action when counter=CMPB on down-count (CBD): Set

Compare value reload condition: Load on counter equals to zero (CTR=Zero)

☐ Add continuous software force input port

Continuous software force logic: Forcing disable

Reload condition for software force: Zero

(c) Configuration of ePWM for the third bridge arm

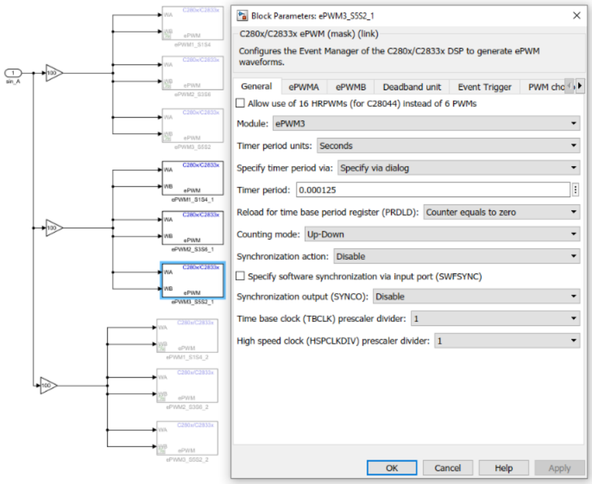

Block Parameters: ePWM3_S5S2_1

C280x/C2833x ePWM (mask) (link)

Configures the Event Manager of the C280x/C2833x DSP to generate ePWM waveforms.

☐ Allow use of 16 HRPWMs (for C28044) instead of 6 PWMs
Module: ePWM3
Timer period units: Seconds
Specify timer period via: Specify via dialog
Timer period: 0.000125
Reload for time base period register (PRDLD): Counter equals to zero
Counting mode: Up-Down
Synchronization action: Disable
☐ Specify software synchronization via input port (SWFSYNC)
Synchronization output (SYNCO): Disable
Time base clock (TBCLK) prescaler divider: 1
High speed clock (HSPCLKDIV) prescaler divider: 1

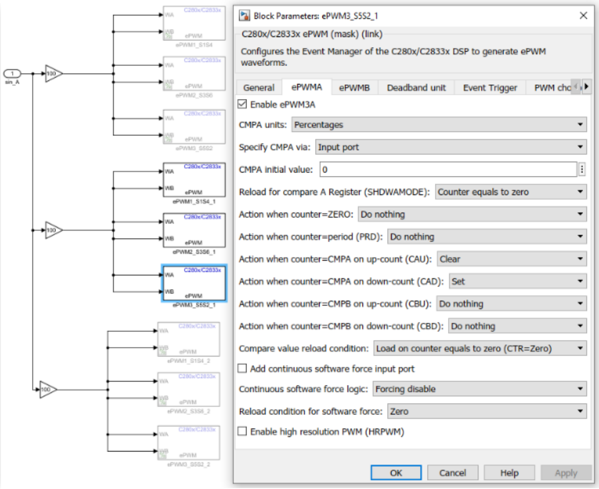

Block Parameters: ePWM3_S5S2_1

C280x/C2833x ePWM (mask) (link)

Configures the Event Manager of the C280x/C2833x DSP to generate ePWM waveforms.

☑ Enable ePWM3A
CMPA units: Percentages
Specify CMPA via: Input port
CMPA initial value: 0
Reload for compare A Register (SHDWAMODE): Counter equals to zero
Action when counter=ZERO: Do nothing
Action when counter=period (PRD): Do nothing
Action when counter=CMPA on up-count (CAU): Clear
Action when counter=CMPA on down-count (CAD): Set
Action when counter=CMPB on up-count (CBU): Do nothing
Action when counter=CMPB on down-count (CBD): Do nothing
Compare value reload condition: Load on counter equals to zero (CTR=Zero)
☐ Add continuous software force input port
Continuous software force logic: Forcing disable
Reload condition for software force: Zero
☐ Enable high resolution PWM (HRPWM)

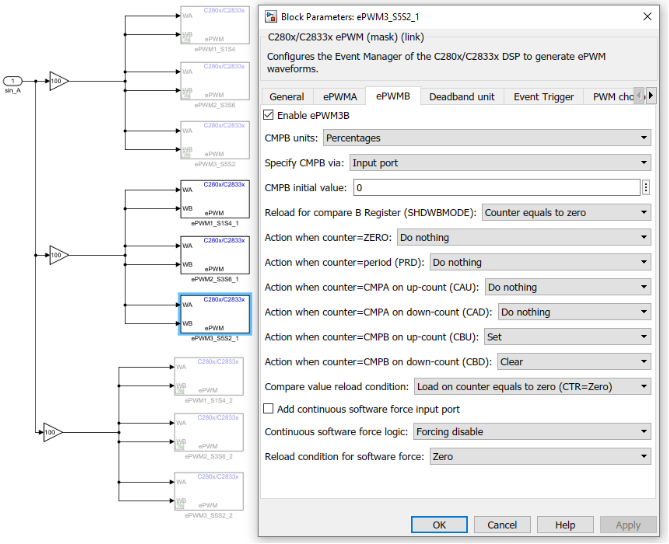

Block Parameters: ePWM3_S5S2_1

C280x/C2833x ePWM (mask) (link)

Configures the Event Manager of the C280x/C2833x DSP to generate ePWM waveforms.

☑ Enable ePWM3B
CMPB units: Percentages
Specify CMPB via: Input port
CMPB initial value: 0
Reload for compare B Register (SHDWBMODE): Counter equals to zero
Action when counter=ZERO: Do nothing
Action when counter=period (PRD): Do nothing
Action when counter=CMPA on up-count (CAU): Do nothing
Action when counter=CMPA on down-count (CAD): Do nothing
Action when counter=CMPB on up-count (CBU): Set
Action when counter=CMPB on down-count (CBD): Clear
Compare value reload condition: Load on counter equals to zero (CTR=Zero)
☐ Add continuous software force input port
Continuous software force logic: Forcing disable
Reload condition for software force: Zero

iv. Aligning the pulsating flux along the magnetic axis of phase C

(a) Configuration of ePWM for the first bridge arm

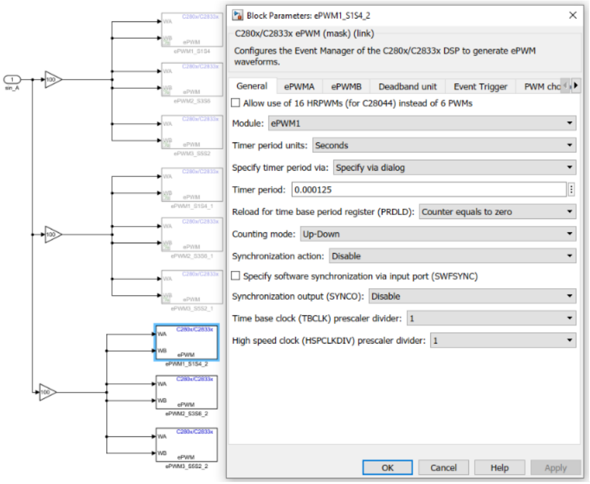

Block Parameters: ePWM1_S1S4_2

C280x/C2833x ePWM (mask) (link)

Configures the Event Manager of the C280x/C2833x DSP to generate ePWM waveforms.

☐ Allow use of 16 HRPWMs (for C28044) instead of 6 PWMs
Module: ePWM1
Timer period units: Seconds
Specify timer period via: Specify via dialog
Timer period: 0.000125
Reload for time base period register (PRDLD): Counter equals to zero
Counting mode: Up-Down
Synchronization action: Disable
☐ Specify software synchronization via input port (SWFSYNC)
Synchronization output (SYNCO): Disable
Time base clock (TBCLK) prescaler divider: 1
High speed clock (HSPCLKDIV) prescaler divider: 1

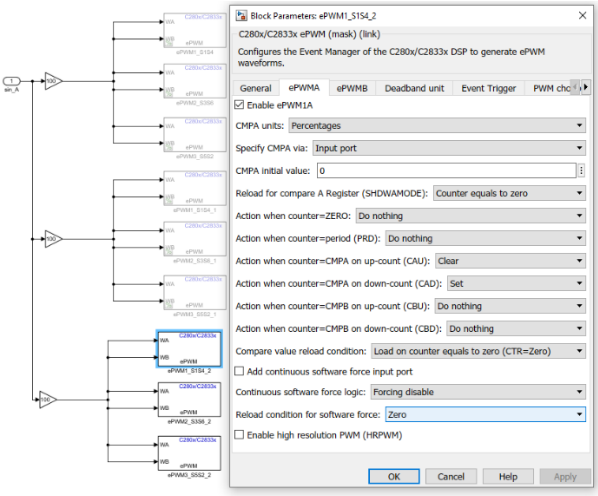

Block Parameters: ePWM1_S1S4_2

C280x/C2833x ePWM (mask) (link)

Configures the Event Manager of the C280x/C2833x DSP to generate ePWM waveforms.

☑ Enable ePWM1A
CMPA units: Percentages
Specify CMPA via: Input port
CMPA initial value: 0
Reload for compare A Register (SHDWAMODE): Counter equals to zero
Action when counter=ZERO: Do nothing
Action when counter=period (PRD): Do nothing
Action when counter=CMPA on up-count (CAU): Clear
Action when counter=CMPA on down-count (CAD): Set
Action when counter=CMPB on up-count (CBU): Do nothing
Action when counter=CMPB on down-count (CBD): Do nothing
Compare value reload condition: Load on counter equals to zero (CTR=Zero)
☐ Add continuous software force input port
Continuous software force logic: Forcing disable
Reload condition for software force: Zero
☐ Enable high resolution PWM (HRPWM)

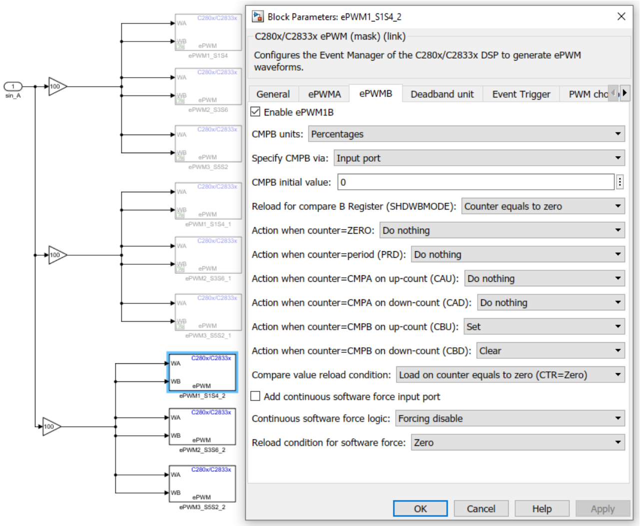

Block Parameters: ePWM1_S1S4_2

C280x/C2833x ePWM (mask) (link)

Configures the Event Manager of the C280x/C2833x DSP to generate ePWM waveforms.

☑ Enable ePWM1B

CMPB units: Percentages

Specify CMPB via: Input port

CMPB initial value: 0

Reload for compare B Register (SHDWBMODE): Counter equals to zero

Action when counter=ZERO: Do nothing

Action when counter=period (PRD): Do nothing

Action when counter=CMPA on up-count (CAU): Do nothing

Action when counter=CMPA on down-count (CAD): Do nothing

Action when counter=CMPB on up-count (CBU): Set

Action when counter=CMPB on down-count (CBD): Clear

Compare value reload condition: Load on counter equals to zero (CTR=Zero)

☐ Add continuous software force input port

Continuous software force logic: Forcing disable

Reload condition for software force: Zero

(b) Configuration of ePWM for the second bridge arm

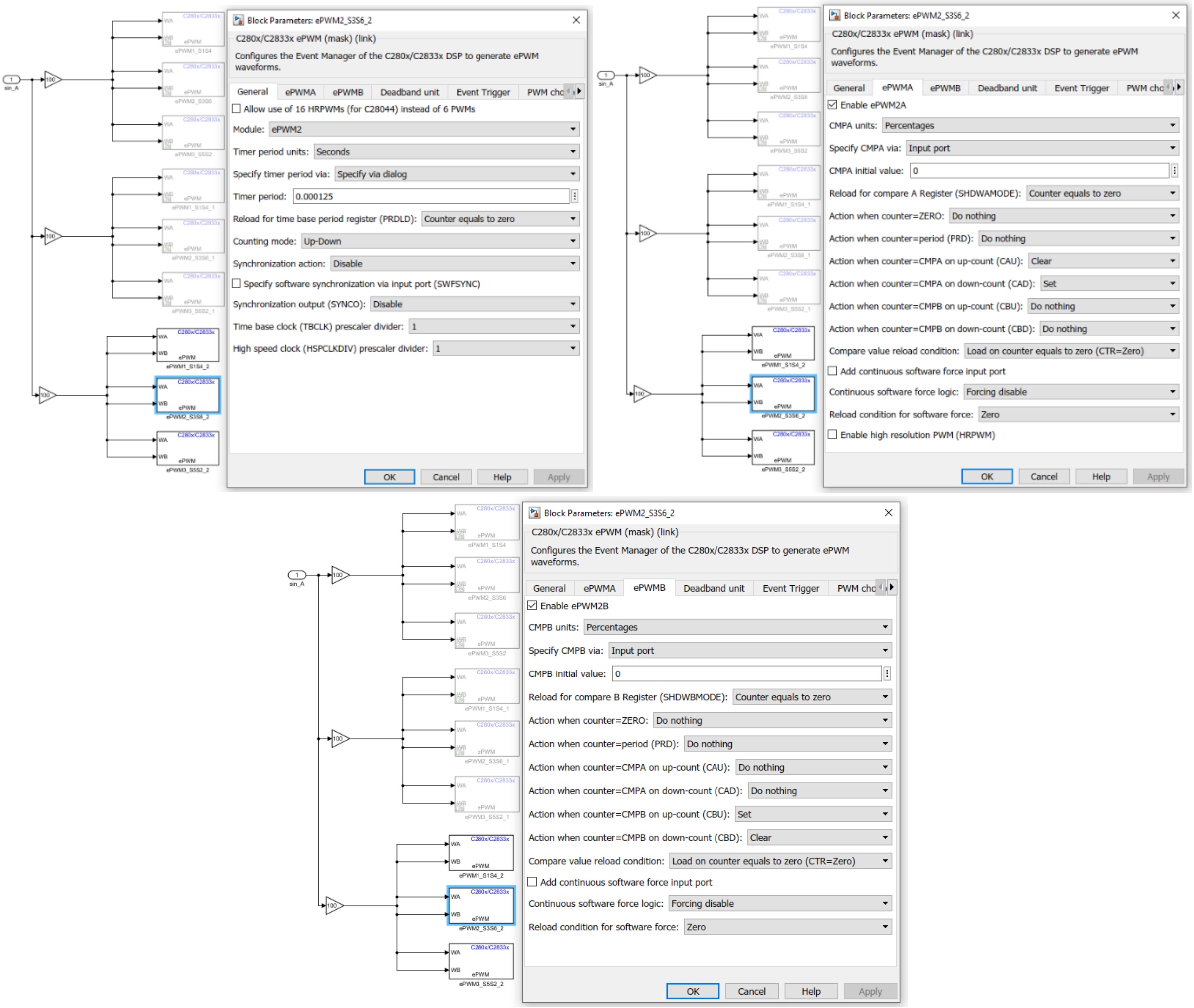

Block Parameters: ePWM2_S3S6_2

C280x/C2833x ePWM (mask) (link)

Configures the Event Manager of the C280x/C2833x DSP to generate ePWM waveforms.

☐ Allow use of 16 HRPWMs (for C28044) instead of 6 PWMs

Module: ePWM2

Timer period units: Seconds

Specify timer period via: Specify via dialog

Timer period: 0.000125

Reload for time base period register (PRDLD): Counter equals to zero

Counting mode: Up-Down

Synchronization action: Disable

☐ Specify software synchronization via input port (SWFSYNC)

Synchronization output (SYNCO): Disable

Time base clock (TBCLK) prescaler divider: 1

High speed clock (HSPCLKDIV) prescaler divider: 1

Block Parameters: ePWM2_S3S6_2

C280x/C2833x ePWM (mask) (link)

Configures the Event Manager of the C280x/C2833x DSP to generate ePWM waveforms.

☑ Enable ePWM2A

CMPA units: Percentages

Specify CMPA via: Input port

CMPA initial value: 0

Reload for compare A Register (SHDWAMODE): Counter equals to zero

Action when counter=ZERO: Do nothing

Action when counter=period (PRD): Do nothing

Action when counter=CMPA on up-count (CAU): Clear

Action when counter=CMPA on down-count (CAD): Set

Action when counter=CMPB on up-count (CBU): Do nothing

Action when counter=CMPB on down-count (CBD): Do nothing

Compare value reload condition: Load on counter equals to zero (CTR=Zero)

☐ Add continuous software force input port

Continuous software force logic: Forcing disable

Reload condition for software force: Zero

☐ Enable high resolution PWM (HRPWM)

Block Parameters: ePWM2_S3S6_2

C280x/C2833x ePWM (mask) (link)

Configures the Event Manager of the C280x/C2833x DSP to generate ePWM waveforms.

☑ Enable ePWM2B

CMPB units: Percentages

Specify CMPB via: Input port

CMPB initial value: 0

Reload for compare B Register (SHDWBMODE): Counter equals to zero

Action when counter=ZERO: Do nothing

Action when counter=period (PRD): Do nothing

Action when counter=CMPA on up-count (CAU): Do nothing

Action when counter=CMPA on down-count (CAD): Do nothing

Action when counter=CMPB on up-count (CBU): Set

Action when counter=CMPB on down-count (CBD): Clear

Compare value reload condition: Load on counter equals to zero (CTR=Zero)

☐ Add continuous software force input port

Continuous software force logic: Forcing disable

Reload condition for software force: Zero

(c) Configuration of ePWM for the third bridge arm

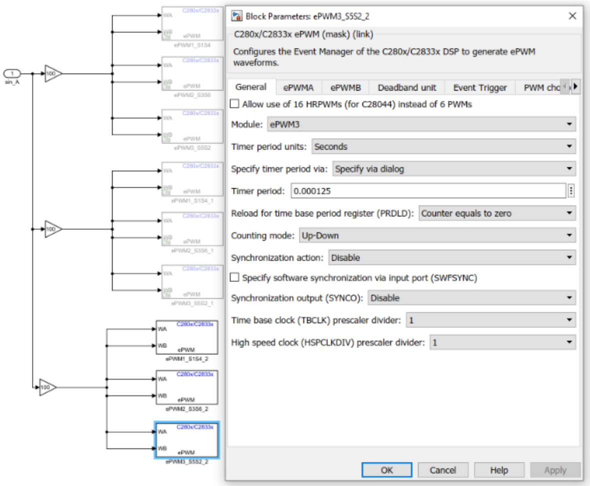

Block Parameters: ePWM3_S5S2_2

C280x/C2833x ePWM (mask) (link)

Configures the Event Manager of the C280x/C2833x DSP to generate ePWM waveforms.

☐ Allow use of 16 HRPWMs (for C28044) instead of 6 PWMs

Module: ePWM3

Timer period units: Seconds

Specify timer period via: Specify via dialog

Timer period: 0.000125

Reload for time base period register (PRDLD): Counter equals to zero

Counting mode: Up-Down

Synchronization action: Disable

☐ Specify software synchronization via input port (SWFSYNC)

Synchronization output (SYNCO): Disable

Time base clock (TBCLK) prescaler divider: 1

High speed clock (HSPCLKDIV) prescaler divider: 1

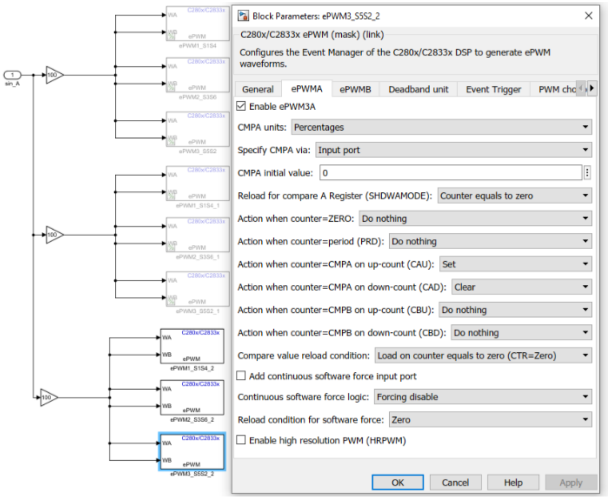

Block Parameters: ePWM3_S5S2_2

C280x/C2833x ePWM (mask) (link)

Configures the Event Manager of the C280x/C2833x DSP to generate ePWM waveforms.

☑ Enable ePWM3A

CMPA units: Percentages

Specify CMPA via: Input port

CMPA initial value: 0

Reload for compare A Register (SHDWAMODE): Counter equals to zero

Action when counter=ZERO: Do nothing

Action when counter=period (PRD): Do nothing

Action when counter=CMPA on up-count (CAU): Set

Action when counter=CMPA on down-count (CAD): Clear

Action when counter=CMPB on up-count (CBU): Do nothing

Action when counter=CMPB on down-count (CBD): Do nothing

Compare value reload condition: Load on counter equals to zero (CTR=Zero)

☐ Add continuous software force input port

Continuous software force logic: Forcing disable

Reload condition for software force: Zero

☐ Enable high resolution PWM (HRPWM)

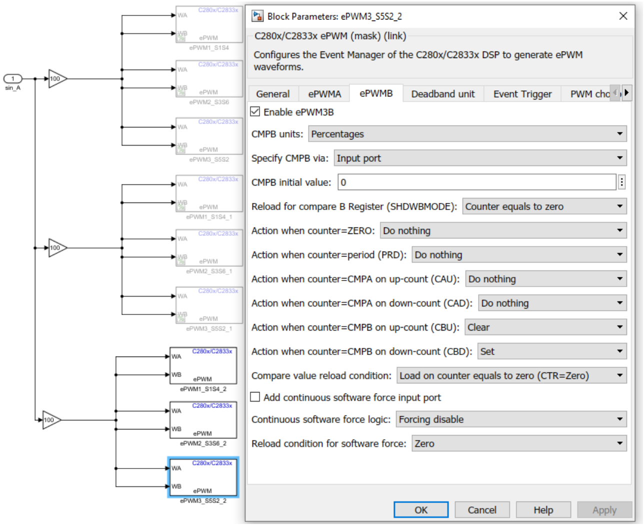

Block Parameters: ePWM3_S5S2_2

C280x/C2833x ePWM (mask) (link)

Configures the Event Manager of the C280x/C2833x DSP to generate ePWM waveforms.

☑ Enable ePWM3B

CMPB units: Percentages

Specify CMPB via: Input port

CMPB initial value: 0

Reload for compare B Register (SHDWBMODE): Counter equals to zero

Action when counter=ZERO: Do nothing

Action when counter=period (PRD): Do nothing

Action when counter=CMPA on up-count (CAU): Do nothing

Action when counter=CMPA on down-count (CAD): Do nothing

Action when counter=CMPB on up-count (CBU): Clear

Action when counter=CMPB on down-count (CBD): Set

Compare value reload condition: Load on counter equals to zero (CTR=Zero)

☐ Add continuous software force input port

Continuous software force logic: Forcing disable

Reload condition for software force: Zero

A4. LabView Code

A4.1 LabView Code for broken rotor bar fault detection with MCSA and Standstill impedance variation test for inverter-fed induction motor.

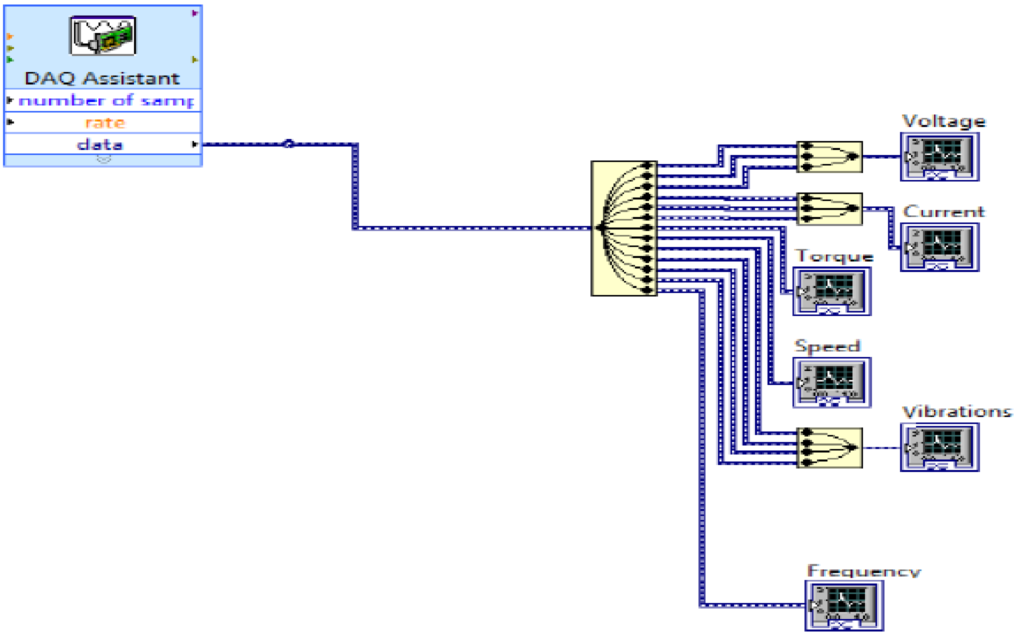

A4.2 LabView Code for Standstill variation test for grid-connected induction motor.